

# LOAN DOCUMENT

PHOTOGRAPH THIS SHEET

DTIC ACCESSION NUMBER

LEVEL

INVENTORY

**AFRL-ML-WP-TR-2000-4085**

DOCUMENT IDENTIFICATION

## DISTRIBUTION STATEMENT A

Approved for Public Release  
Distribution Unlimited

## DISTRIBUTION STATEMENT

ACCESSION BY	
NTIS	GRAM
DTIC	TRAC
UNANNOUNCED	
JUSTIFICATION	
BY	
DISTRIBUTION/	
AVAILABILITY CODES	
DISTRIBUTION	AVAILABILITY AND/OR SPECIAL
A-1	

DISTRIBUTION STAMP

DATE ACCESSIONED

DATE RETURNED

**20001031 078**

DATE RECEIVED IN DTIC

REGISTERED OR CERTIFIED NUMBER

PHOTOGRAPH THIS SHEET AND RETURN TO DTIC-FDAC

H  
A  
N  
D  
L  
E  
  
W  
I  
T  
H  
  
C  
A  
R  
E

**AFRL-ML-WP-TR-2000-40**<sup>85</sup>



**CONSORTIUM FOR THE  
DEVELOPMENT OF SILICON  
CARBIDE FOR ELECTRONICS  
APPLICATIONS**

James A. Cooper, Jr  
A. Rohatgi  
A. Doolittle  
P. Pirousz

AUBURN UNIVERSITY  
AUBURN AL 36849-5320

**FEBRUARY 2000**

**FINAL REPORT FOR 09/21/94 – 11/29/99**

**PUBLIC RELEASE; DISTRIBUTION UNLIMITED**

This paper is declared a work of the U.S. Government and as such is not subject to copyright protection in the United States

**MATERIALS AND MANUFACTURING DIRECTORATE  
AIR FORCE RESEARCH LABORATORY  
AIR FORCE MATERIEL COMMAND  
WRIGHT-PATTERSON AIR FORCE BASE, OH 45433-7750**

REPORT DOCUMENTATION PAGE			Form Approved OMB No. 0704-0188	
<small>Public reporting burden for this collection of information is estimated to average 1 hour per response, including the time for reviewing instructions, searching existing data sources, gathering and maintaining the data needed, and completing and reviewing the collection of information. Send comments regarding this burden estimate or any other aspect of this collection of information, including suggestions for reducing this burden, to Washington Headquarters Services, Directorate for Information Operations and Reports, 1215 Jefferson Davis Highway, Suite 1204, Arlington, VA 22202-4302, and to the Office of Management and Budget, Paperwork Reduction Project (0704-0188), Washington, DC 20503.</small>				
1. AGENCY USE ONLY (Leave blank)		2. REPORT DATE 28 February 2000		3. REPORT TYPE AND DATES COVERED Final Technical Report: 09/21/1994 - 11/29/1999
4. TITLE AND SUBTITLE A Consortium for the Development of Silicon Carbide for Electronics Applications			5. FUNDING NUMBERS C: 33615-94-2-5407 PE: 62102 PR: 2423 TA: 70 WU: 02	
6. AUTHOR(S) James A. Cooper, Jr., A. Rohatgi, A. Doolittle, P. Pirousz				
7. PERFORMING ORGANIZATION NAME(S) AND ADDRESS(ES) Purdue University    Georgia Inst. of Technology    Case Western Reserve University West Lafayette, IN    Atlanta, GA    Cleveland, OH  Managed By: Auburn University Auburn, AL			8. PERFORMING ORGANIZATION REPORT NUMBER	
9. SPONSORING/MONITORING AGENCY NAME(S) AND ADDRESS(ES) MATERIALS & MANUFACTURING DIRECTORATE AIR FORCE RESEARCH LABORATORY AIR FORCE MATERIEL COMMAND WPAFB OH 45433-7750 POC: LAURA S. REA, AFRL/MLPO, 937-255-4474 x3213			10. SPONSORING/MONITORING AGENCY REPORT NUMBER  AFRL-ML-WP-TR-2000-4085	
11. SUPPLEMENTARY NOTES  This paper is declared a work of the U.S. Government and as such is not subject to copyright protection in the United States.				
12a. DISTRIBUTION AVAILABILITY STATEMENT  APPROVED FOR PUBLIC RELEASE; DISTRIBUTION UNLIMITED			12b. DISTRIBUTION CODE	
13. ABSTRACT (Maximum 200 words) The US Air Force SiC Consortium was established as a partnership of industry and government to invest in university research supporting the expansion of the technical base for this emerging compound semiconductor material. SiC has a wide bandgap, relative to more conventional compound semiconductors (2.9 eV) and high thermal conductivity (5 W/cm-K. These properties make SiC uniquely suited for high temperature, high power and high frequency operation, with higher package density and reduced cooling subsystem requirements. In addition, the high temperature nature of SiC permits the development of a host of harsh environment electronic devices. SiC-based electronics will be the enabling technology for on-engine sensors for advanced turbine engines, and will provide high-power solid state radars for future tactical systems. While some commercial and military products based on SiC have emerged over the past several years, there was a lack of fundamental understanding of some critical aspects of the material, which could ultimately hinder full exploitation of the advantageous material properties of SiC. The SiC Consortium, jointly funded by the US Air Force and three industrial partners, focused world-class university research teams on three of these areas: 1) High Field Electron Transport in 6H and 4H SiC 2) Minority Carrier Lifetime Measurements of SiC 3) Critical Resolved Shear Stress Measurements of SiC				
14. SUBJECT TERMS			15. NUMBER OF PAGES 243	
			16. PRICE CODE	
17. SECURITY CLASSIFICATION OF REPORT  UNCLASSIFIED	18. SECURITY CLASSIFICATION OF THIS PAGE  UNCLASSIFIED	19. SECURITY CLASSIFICATION OF ABSTRACT  UNCLASSIFIED	20. LIMITATION OF ABSTRACT  SAR	


## NOTICE

USING GOVERNMENT DRAWINGS, SPECIFICATIONS, OR OTHER DATA INCLUDED IN THIS DOCUMENT FOR ANY PURPOSE OTHER THAN GOVERNMENT PROCUREMENT DOES NOT IN ANY WAY OBLIGATE THE US GOVERNMENT. THE FACT THAT THE GOVERNMENT FORMULATED OR SUPPLIED THE DRAWINGS, SPECIFICATIONS, OR OTHER DATA DOES NOT LICENSE THE HOLDER OR ANY OTHER PERSON OR CORPORATION; OR CONVEY ANY RIGHTS OR PERMISSION TO MANUFACTURE, USE, OR SELL ANY PATENTED INVENTION THAT MAY RELATE TO THEM.

THIS TECHNICAL REPORT HAS BEEN REVIEWED AND IS APPROVED FOR PUBLICATION.



LAURA S. REA, Project Engineer  
Sensor Materials Branch  
Survivability & Sensor Materials Division  
Division



ROBERT L. DENISON, Chief  
Sensor Materials Branch  
Survivability & Sensor Materials



WILLIAM R. WOODY, Chief  
Survivability & Sensor Materials Division  
Materials & Manufacturing Directorate

Do not return copies of this report unless contractual obligations or notice on a specific document requires its return.



**Consortium for the Development of Silicon Carbide for  
Electronics Applications**

**US Air Force Cooperative Agreement No: F33615-94-2-5407**

**Final Report:  
28 February 2000**

**Period of Performance: 29 Sept 1994 - 30 Nov 1999**

**Consortium Management Provided by:  
Auburn University  
Space Power Institute  
Office of the Director  
231 Leach Center  
Auburn University, Alabama 36849-5320**

**Industrial Partners:  
ATMI, Inc. (Danbury, CT)  
Cree, Inc. (Durham, NC)  
Northrop Grumman (Pittsburgh, PA)**

**University Subcontractors:  
Purdue University (West Lafayette, IN)  
Georgia Institute of Technology (Atlanta, GA)  
Case Western Reserve University (Cleveland, OH)**

## **Consortium for the Development of Silicon Carbide for Electronics Applications**

**US Air Force Cooperative Agreement No: F33615-94-2-5407**

### Executive Summary:

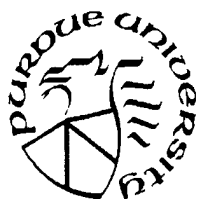
The US Air Force SiC Consortium was established as a partnership of industry and government to invest in university research supporting the expansion of the technical base for this emerging compound semiconductor material. SiC has a wide bandgap, relative to more conventional compound semiconductors (2.9 eV) and high thermal conductivity (5 W/cm-K. These properties make SiC uniquely suited for high temperature, high power and high frequency operation, with higher package density and reduced cooling subsystem requirements. In addition, the high temperature nature of SiC permits the development of a host of harsh environment electronic devices. SiC-based electronics will be the enabling technology for on-engine sensors for advanced turbine engines, and will provide high-power solid state radars for future tactical systems. Additionally, SiC electronics have numerous commercial applications. The automotive industry needs reliable materials and devices for the high temperature, corrosive, dirty environments in engine compartments.

While some commercial and military products based on SiC have emerged over the past several years, there was a lack of fundamental understanding of some critical aspects of the material, which could ultimately hinder full exploitation of the advantageous material properties of SiC. The SiC Consortium, jointly funded by the US Air Force and three industrial partners, focused world-class university research teams on three of these areas:

- 1) High Field Electron Transport in 6H and 4H SiC
- 2) Minority Carrier Lifetime Measurements of SiC
- 3) Critical Resolved Shear Stress Measurements of SiC

Through close collaboration between the three university subcontractors and the three industrial partners, over 30 publications in refereed technical journals were generated, along with an equivalent number of presentations at technical workshops, symposia and conferences. This work resulted in advancing the state of the art, and the overall knowledge-base, supporting the entire SiC community. Results from each university research effort are summarized in the attached document.

# An Investigation of High-Field Electron Transport in 6H and 4H Silicon Carbide



Contract No. 95-SPI-420757-PRF  
from Auburn University to Purdue Research Foundation  
a subagreement to the  
Silicon Carbide Consortium Program  
pursuant to  
Cooperative Agreement No. F33615-94-25407  
awarded by the U.S. Air Force

**Final Technical Report  
December 27, 1999**

**James A. Cooper, Jr., P. I.**

School of Electrical and Computer Engineering  
Purdue University  
1285 EE Building, West Lafayette, IN 47907-1285

cooperj@ecn.purdue.edu  
(765) 494-3514  
FAX: 494-6441

## **Abstract**

We have performed improved measurements of the high-field drift velocity of electrons parallel to the basal plane in 4H and 6H-SiC as a function of temperature. The electron saturation drift velocity at room temperature is  $1.9(2.2) \times 10^7$  cm/s in 6H(4H) SiC. At 320 °C the electron saturation drift velocity is  $1.0(1.6) \times 10^7$  cm/s in 6H(4H) SiC.

## **Organization of This Report**

This report consists of three parts. Part I is a brief narrative overview and summary of the project, including background information, motivation for the work, experimental procedure, and the most recent experimental results. Part II is a detailed description of the first part of the experiment (i.e. measurement of devices with a 1  $\mu$ m n-type epilayer), in the form of a Masters thesis written by Mr. Imran Khan. Part III is a paper that will appear in the February 2000 issue of *IEEE Transactions on Electron Devices* describing the final results of the experiment, including the most recent and most accurate data on devices with a 4  $\mu$ m thick n-type epilayer.

## **PART I. NARRATIVE OVERVIEW AND SUMMARY OF RESULTS**

### **Introduction**

Silicon Carbide is attracting widespread attention because of its superior electronic and thermal properties, particularly its high breakdown field, low intrinsic carrier concentration, and high thermal conductivity. One area of concern is the low electron and hole mobilities in the material. These low mobilities, combined with the short minority carrier lifetimes, result in short minority carrier diffusion lengths which limit the gain of bipolar devices such as the bipolar junction transistor (BJT) and the thyristor. The low mobility also reduces the transconductance of unipolar field-effect devices such as the MOSFET, JFET, and MESFET.

In spite of its importance, there is surprisingly little data on electron velocity in SiC. The most reliable data was taken in 1977 by V. Muench and Pettenpaul [1], who measured the drift velocity of electrons in the basal plane of n-type 6H-SiC platelets grown by the Lely method. They found the electron velocity saturated at a value of  $2 \times 10^7$  cm/s at a field of  $2 \times 10^5$  V/cm. No data is available on electron velocity in wafers grown by the modified sublimation process, and no data is available on electron velocity in the 4H polytype of SiC. No data is available on the temperature dependence of electron velocity in either polytype. In this work, we have conducted new measurements of electron velocity in both 6H and 4H-SiC as a function of temperature.

### **Measurement Technique**

The measurement technique employed by v. Muench and Pettenpaul, and also used here, consists of measuring the current-voltage relationship of a narrow constriction of n-type SiC material at high fields. The experimental device, illustrated in Fig. 1, consists of an n-type epilayer of doping  $1 \times 10^{17}$  cm<sup>-3</sup> grown on a lightly doped p-type epilayer on a heavily-doped p-type substrate. The n-type epilayer is patterned by reactive ion etching, forming a constriction of dimensions on the order of  $5 \times 5$   $\mu$ m. Ohmic contacts are established on either side of the constriction by annealed Ni. Probe contact is made to the four ohmic contacts, and a pulsed bias is applied using the apparatus shown in Fig. 2. To prevent surface arcing, the samples are immersed in Flourinert™. Bias pulses are applied to outer contacts  $L_1$  and  $L_4$  using a Directed Energy, Inc. GRX 1.5 K-E pulse generator, and the voltage drop across the inner contacts  $L_2$  and  $L_3$  is measured using the 1 M $\Omega$  inputs of a Tektronix 11401 digitizing oscilloscope. The current through the constriction is obtained from the voltage drop across the 50  $\Omega$  input of the oscilloscope in series with  $L_4$ . The electron drift velocity is calculated from the current using the relation

$$v = \frac{I}{q w n t} \quad (1)$$

where  $w$  is the width of the constriction,  $n$  is the electron density per unit volume, and  $t$  is the thickness of the undepleted portion of the n-type epilayer. The corresponding electric field is calculated from the voltage drop between the high impedance probes attached to  $L_2$  and  $L_3$ , with corrections for the end resistances between the inner ohmic contacts and the constriction.

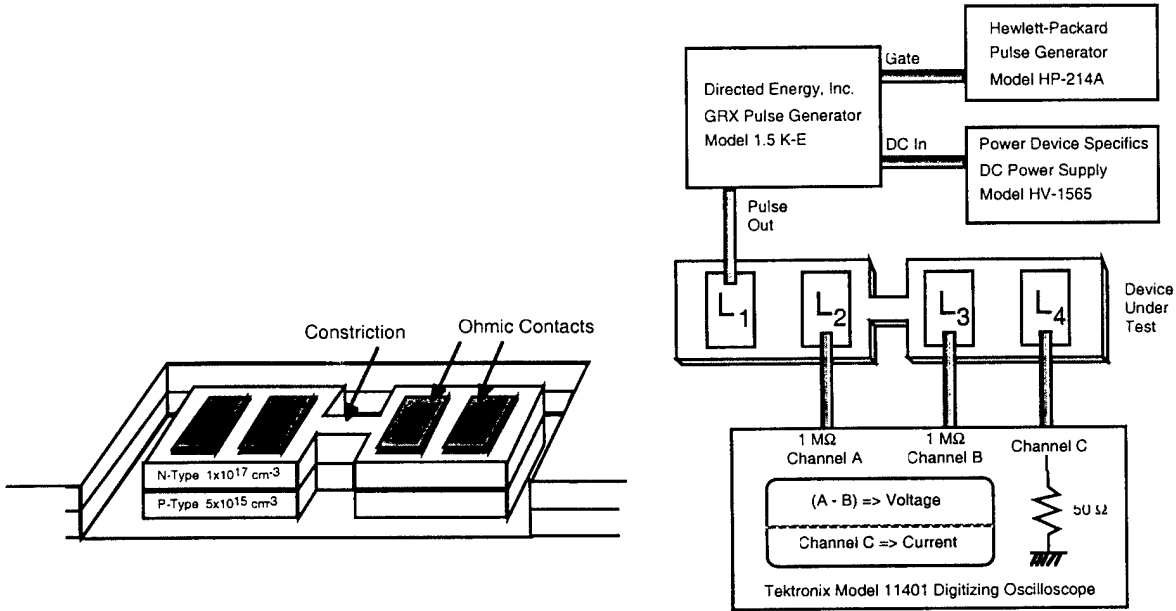


Figure 1. Isometric view of the experimental device. In most devices, the n-type epilayer is 4  $\mu\text{m}$  thick.

Figure 2. Schematic diagram of the test apparatus.

Figure 3 shows transient current waveforms for several different pulse conditions of increasing applied voltage. As seen, for electric fields above about 20 kV/cm the current decreases during the bias pulse due to transient heating at the constriction. To minimize this effect, we record the current at the earliest possible point in the bias pulse, typically within the first 50 ns. The transient response of the circuit becomes a limitation at the highest fields. The transient response is degraded by the parasitic capacitance of the probes, so at fields above 30 kV/cm we remove the two inner probes and calculate the voltage drop across the constriction using the equivalent circuit of Fig. 4. The elements in Fig. 4 represent the contact impedances and the spreading resistances of the n-type. Resistances  $(R_{C1} + R_1)$  and  $(R_{C4} + R_4)$  are obtained from four-probe measurements at low fields (no current flows through  $R_{C2}$  and  $R_{C3}$  due to the high impedance probes on  $L_2$  and  $L_3$ ). At high fields, the probes on  $L_2$  and  $L_3$  are removed and

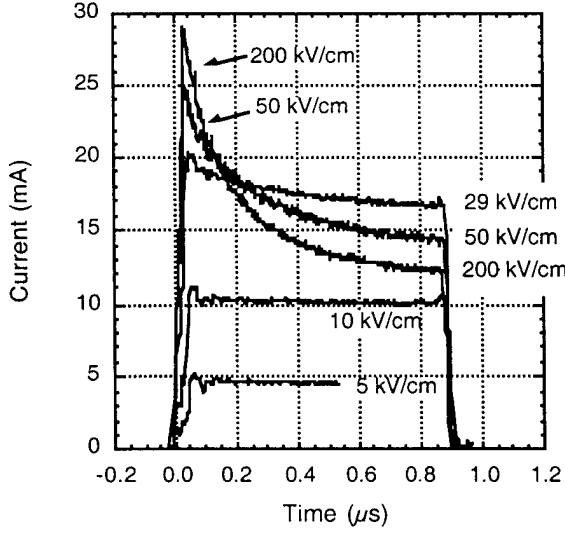


Figure 3. Transient current waveforms at various fields.

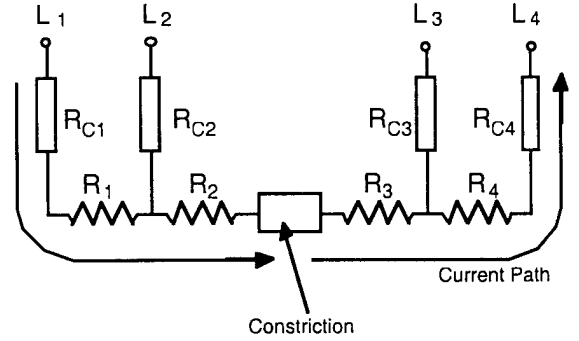


Figure 4. Equivalent circuit showing parasitic resistances.

the voltage drops across  $(R_{C1} + R_1)$  and  $(R_{C4} + R_4)$  are calculated from the measured current and known resistances. These voltage drops are then subtracted from the voltage between probes  $L_1$  and  $L_4$  to obtain the equivalent inner probe voltage drop.

### Device Details

In the experiments reported in 1997 [2], the n-type epilayer thickness was  $1 \mu\text{m}$ . This raised a concern about narrowing of the undepleted n-type channel due to the depletion region from the underlying pn junction. In the present experiments [3] we increased the thickness of the n-type epilayer to  $4 \mu\text{m}$  to minimize this effect, and we also included an analytical correction to the channel thickness  $t$  to account for the depletion. A variety of constriction sizes are also included, with dimensions (width x length) =  $5 \times 5$ ,  $5 \times 10$ ,  $5 \times 15$ ,  $10 \times 10$ , and  $10 \times 15 \mu\text{m}$ . To insure low resistance ohmic contacts, a high dose ( $1 \times 10^{19} \text{ cm}^{-3}$ ) nitrogen implant is performed in the contact regions and annealed at  $1400^\circ\text{C}$  for 18 minutes in argon. The doping-thickness ( $n \cdot t$ ) products for the n-type epilayers obtained from Hall measurements on each sample are  $2.4$  ( $3.6$ )  $\times 10^{13} \text{ cm}^{-2}$  for the 4H (6H) samples, respectively. In these calculations, the Hall scattering factor  $r_H$  is taken to be unity [4]. These ( $n \cdot t$ ) values agree well with separate TLM measurements on each sample. The lateral dimensions of the constrictions are determined within an accuracy of  $\pm 10\%$  from SEM photographs of the completed structures. Epilayer thickness and the uniformity of doping with depth are verified by SIMS.

## Experimental Results

Figures 5 and 6 show velocity-field data on the 4H and 6H samples at room temperature, 135, and 320 °C. Measurements on constrictions of various sizes are included at each temperature. The lines represent empirical fits to the equation

$$v(E) = \frac{\mu E}{\left[ 1 + \left( \frac{\mu E}{v_s} \right)^\alpha \right]^{\frac{1}{\alpha}}} \quad (2)$$

where  $\mu$  is the low field mobility,  $v_s$  is the saturation velocity, and  $\alpha$  is a shape parameter.

Values of the fit parameters are listed in Table 1. Saturation velocities of  $2.2 (1.9) \times 10^7$  cm/s are obtained for 4H (6H) SiC at room temperature. These values decrease to  $1.6 (1.0) \times 10^7$  cm/s for 4H (6H) SiC at 320 °C.

## Summary

We have reported new measurements of high field drift velocity of electrons parallel to the basal plane in 4H and 6H-SiC at room temperature, 135, and 320 °C. The saturation drift velocity in 6H-SiC at room temperature is  $1.9 \times 10^7$  cm/s, very close to the value reported by v. Muench and Pettenpaul [1] in 1977. The saturation drift velocity in 4H-SiC is  $2.2 \times 10^7$  cm/s. Saturation velocities decrease with temperature, reaching  $1.6 (1.0) \times 10^7$  cm/s in 4H (6H) SiC at 320 °C.

## References

- [1] W. v. Muench and E. Pettenpaul, J. Appl. Phys. 48 (1977), p. 4823.
- [2] I. A. Khan and J. A. Cooper, Jr., Silicon Carbide, III-Nitrides and Related Materials; G. Pensl, H. Morkoc, B. Monemar, and E. Janzen, Eds.; Trans. Tech. Publications (1998), p. 509.
- [3] I. A. Khan and J. A. Cooper, Jr., to appear in *IEEE Trans. Electron Devices*, Feb., 2000.
- [4] G. Rutsch, R. P. Devaty, D. W. Langer, L. B. Rowland, and W. J. Choyke, Mat'ls. Sci. Forum, 264-268 (1998), p. 517.



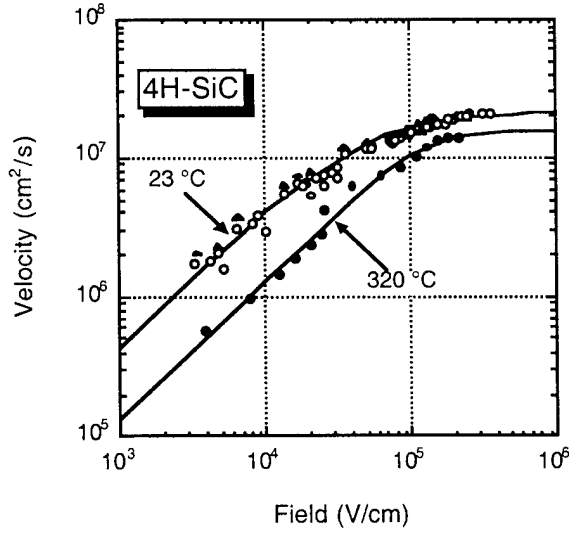


Figure 5. Velocity-field relation for electrons parallel to the basal plane in 4H-SiC.

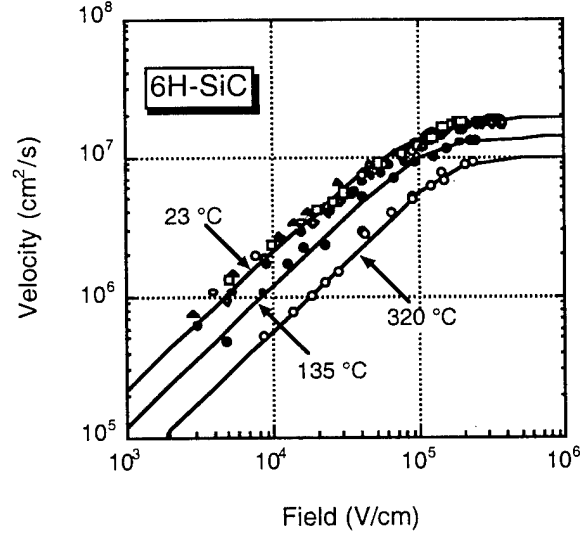


Figure 6. Velocity-field relation for electrons parallel to the basal plane in 6H-SiC.

Temperature	Parameter	6H-SiC	4H-SiC	Units
23 °C	$\mu$	215	450	cm <sup>2</sup> /Vs
	$v_s$	$1.9 \times 10^7$	$2.2 \times 10^7$	cm/s
	$\alpha$	1.7	1.2	--
135 °C	$\mu$	120	-	cm <sup>2</sup> /Vs
	$v_s$	$1.4 \times 10^7$	-	cm/s
	$\alpha$	2.5	-	--
320 °C	$\mu$	56	130	cm <sup>2</sup> /Vs
	$v_s$	$1.0 \times 10^7$	$1.6 \times 10^7$	cm/s
	$\alpha$	4.0	2.2	--

Table 1. Parameters used in (2) to fit the experimental velocity-field data.

**PART II. DETAILED DESCRIPTION OF THE FIRST PART  
OF THE EXPERIMENT (MASTER'S THESIS OF IMRAN KHAN)**

**VELOCITY FIELD MEASUREMENT OF ELECTRONS  
IN  
SILICON CARBIDE**

A Thesis  
Submitted to the Faculty

of

Purdue University

by

Imran A. Khan

In Partial Fulfillment of the  
Requirements for the degree

of

Masters of Electrical Engineering

March 1998

## TABLE OF CONTENTS

LIST OF TABLES .....	Page v
LIST OF FIGURES.....	vi
ABSTRACT.....	viii
INTRODUCTION.....	1
Introduction.....	1
Thesis Overview.....	4
FABRICATION.....	7
Epilayers.....	7
Mask.....	8
Fabrication.....	12
MEASUREMENT SETUP.....	15
Measurement Technique.....	15
TLM Measurement.....	20
Hall Measurement .....	25
VELOCITY FIELD DATA.....	33
Initial Velocity Field Data.....	33
End Resistance.....	39
Measurement Setup Revisited .....	42
Depletion Region.....	44
Velocity Field Data.....	44
CONCLUSION AND RECOMMENDATIONS FOR FUTURE WORK.....	54
Conclusion.....	54
Future Recommendations.....	54
REFERENCES.....	57

## LIST OF TABLES

Table	Page
Table 2.0: Intended doping profile for the sample.....	7
Table 3.1: Carrier concentrations obtained from TLM measurement using the pulsed System.....	21
Table 3.2: Combinations of magnetic fields and voltages used in the Hall analysis.....	27
Table 3.3: Carrier concentrations obtained using different measurement techniques.....	28
Table 4.0: Average length and width of the channels.....	36
Table 4.1: List of the average spacing between the inner contact and the constriction....	40
Table 4.2: Computed correction factors for the two polytypes.....	41
Table 4.3: List of parameters used in the empirical relation for Figs 4.8 and 4.9.....	52
Table 4.4: List of parameters used in the empirical relation for Figs 4.12 and 4.13.....	52

## LIST OF FIGURES

Figure	Page
Fig. 1.1. A piece of semiconductor with known dimensions used to calculate the Current.....	3
Fig. 1.2. Charge packet under the influence of electric field in Time of Flight.....	3
Fig. 2.1. Illustrating the depletion width growth into the n epilayer at steady state.....	8
Fig. 2.2. Mask used to fabricate the trenches using the reactive ion etching in $\text{SF}_6$ .....	10
Fig. 2.3. The final die structure with nickel contacts.....	11
Fig. 2.4. Highlights of the processing steps involved in fabricating the test Structures...	14
Fig. 3.1. Experimental setup used in performing the conductivity measurement on 4H and 6H SiC.....	17
Fig. 3.2. Construction of the custom probe used in the conductivity measurement.....	19
Fig. 3.3. TLM structure used to deduce sheet resistance in the conductivity Experiment.....	22
Fig. 3.4. The above figure illustrates how to extract the sheet resistance and contact resistance from resistance versus spacing plot.....	22
Fig. 3.5 The I-V curve obtained for 4H TLM structure using the HP 4145. Each curve corresponds to a certain contact spacing.....	23
Fig. 3.6. Total resistance versus contact spacing. The sheet resistance was $2857\Omega$ (corresponding to slope of $28.57\Omega/\text{m}$ ). And contact resistance of $255\Omega$ (intercept at $d=0$ of $510\Omega$ ).....	24
Fig. 3.7. Demonstrating the Hall effect in the n-type material.....	26
Fig. 3.8. Circuit used in measuring the Hall voltage. Carrier concentration of the n-epilayer will be determined from this measurement.....	29
Fig. 3.9. CV profile for 4H.....	30
Fig. 3.10. CV profile for 6H.....	30
Fig. 3.11. Uncalibrated SIMS data for 4H .....	31
Fig. 3.12. Uncalibrated SIMS data for 6H.....	32
Fig. 4.1. Degradation of current through the channel (6H, $10\times 10$ constriction) in the time domain for different voltages applied over the channel.....	35
Fig. 4.2. SEM pictures of the $10\times 10$ and $5\times 5$ channels.....	37
Fig. 4.3. Inaccurate Velocity-Field relationship for electrons in both 6H(*) and 4H(all other symbols) SiC.....	38
Fig. 4.4. Model used to compute the magnitude of the end resistance.....	39
Fig. 4.5. Shows the current spreading around the channel and subsequently the end resistance correction required to account for this voltage drop.....	41
Fig. 4.6. Isometric view of the test structure.....	43

Fig. 4.7. The various components over which the voltage drop needs to be subtracted from the applied voltage in order to determine the field over the channel.....	43
Fig. 4.8. Velocity Field relationship in 4H SiC. Solid line, best fit to data using equation (11). Circles represent data from 5x5 channels the rest from 10x10 channels.....	45
Fig. 4.9. Velocity Field relationship in 6H SiC. Solid line, best fit to data using equation (11). Circles represent data from 5x5 channels the rest from 10x10 channels.....	46
Fig. 4.10. Velocity Field relationship in 4H SiC. Solid line, best fit to data using equation (11). Circles represent data from 5x5 channels the rest from 10x10 channels.....	47
Fig. 4.11. Velocity Field relationship in 6H SiC. Solid line, best fit to data using equation (11). Circles represent data from 5x5 channels the rest from 10x10 channels.....	48
Fig. 4.12. Velocity Field relationship in 4H SiC with no depletion correction. Solid line, best fit to data using equation (11). Circles represent data from 5x5 channels the rest from 10x10 channels.....	49
Fig. 4.13. Velocity Field relationship in 6H SiC with no depletion correction. Solid line, best fit to data using equation (11). Circles represent data from 5x5 channels the rest from 10x10 channels.....	50
Fig. 4.14. Plot of the percentage increase in velocity ( $100 \cdot r/1-r$ of (9)) as a function of applied field.....	51
Fig. 5.1. Variation of end resistance with width and length of the channel for a given spacing.....	56
Fig. 5.2. Variation of correction factor with width and length of the channel for a given spacing.....	56

## ABSTRACT

Khan, Imran A. MSEE Purdue University, March 1998. Velocity Field measurements on silicon carbide. Major Professor: James A. Cooper.

Silicon carbide has become the material of choice for a wide range of applications. High power and S-to-X microwave, to name a few, are some of the applications that are being extensively researched. The prevalence of silicon carbide is primarily due to its superior thermal and electrical properties. However, many of the fundamental electrical parameters of the material have not been accurately measured as yet. This also presents a serious problem for device engineers, since it is difficult to predict the performance of device structures if the basic electrical parameters are not known. One of the most important electrical parameters is the relationship between electron drift velocity and electric field. At low fields, velocity is proportional to field. At higher fields, the velocity increases sub-linearly with field, and at sufficiently high fields the velocity saturates, becoming essentially independent of field. Saturated electron drift velocity is of interest especially for microwave application. In the present study, we report the recent measurements of the drift velocity of electrons in 6H and 4H silicon carbide. The highest measured drift velocity at room temperature is about  $1.8(1.7) \times 10^7$  cm/s in 6H(4H)-SiC. A saturated drift velocity of  $2 \times 10^7$  cm/s for electrons in 4H and 6H can be estimated by fitting data with an empirical velocity-field relation.



## 1. INTRODUCTION

### 1.1 Introduction

Silicon carbide has become the material of choice for a wide range of applications. High power and S-to-X band microwave, to name a few, are some of the applications that are being extensively researched. The prevalence of silicon carbide is primarily due to its superior thermal and electrical properties. One of the properties of interest especially for high speed application is the saturated electron drift velocity. For this purpose, two figures of merit have been developed to evaluate semiconductors for high speed applications namely,

$$z_j = (E_c v_s)^2 / 4\pi$$

by Johnson, [1] and

$$z_k = \lambda (c v_s / 4\pi\epsilon)^{1/2}$$

by Keys[2], where  $\lambda$  is the thermal conductivity,  $E_c$  is the critical field,  $c$  is the speed of light,  $\epsilon$  is the dielectric constant and  $v_s$  is the saturated drift velocity. For accurate evaluation of the FOM, the precise saturated drift velocity is required.

At present there are two major techniques available for the determination of the drift velocities as a function of the applied electric field in semiconductors[3]:

- (a) The conductance technique.
- (b) The time - of - flight (ToF) measurement.

In the former technique, conductivity measurements are performed in the neutral region. Consider a slab of semiconductor, as illustrated in Fig. 1.1. From basic device physics, the current through a piece of n type semiconductor with known dimensions can be written as follows[4]:

$$I = Aen\mu E \quad (1)$$

where  $A(= wt)$  is the cross sectional area,  $e$  is the electronic charge,  $n$  is the number of carriers per unit volume,  $\mu$  is the mobility of the carriers and  $E$  is the applied electric field

the carriers are experiencing. Ohm's law can be easily obtained from the above equation in a couple of steps.

$$I = Aen\mu V/d$$

where  $V$  is the applied voltage and  $d$  is the lateral separation between the points where the voltage is applied.

$$I = (Aen\mu/d)V$$

At low fields, mobility is a constant and the quantity in brackets is replaced by  $G$  the conductance with units of  $1/\text{ohms}$ .

From (1), the velocity  $v$  of the carriers can be obtained as:

$$v = I/(Ane) \quad (2)$$

The above equation is valid in both high and low fields. At low fields, the velocity of the carriers is proportional to the applied field and is given by

$$v = \mu E$$

The time-of-flight measurement relies on observing the flight of charge packets under the influence of an electric field. The packet of charge is introduced by electrical or optical means. The charge packet then travels a distance  $l$ , under the influence of an electric field in time  $t_i$ , through the space charge region. The drift velocity is obtained by

$$v = l/t_i$$

The ionizing source must create charge pairs in a time short compared to  $t_i$  and in a region of thickness  $i$  much smaller than  $l$ , as shown in Fig. 1.2. The two types of charges move in opposite direction due to the electric field. One type of carrier will be collected immediately after having traveled a distance  $l$ , while the other will travel a distance  $l$ , inducing a displacement current pulse of duration  $t_i$  at the terminals. The connecting leads, the sample, and the input to the voltage sensing circuit all contain capacitors. These are lumped into  $C$ .  $R$  is the load resistance in Fig. 1.2. For sharp falling and rising edges of the current pulse, the  $RC$  time constant must be much smaller than the time it takes for the charge packet to transverse the space charge region[5]. With this technique, the velocity-field characteristics of both types of carriers can be determined in the same sample. It is worth mentioning that the ToF technique is similar to the Haynes-Shockley experiment except that the latter allows for the measurement of only the minority carriers, in a neutral region, in low-resistivity materials[6]. When the excess minority carriers exit the sample in the Haynes-Shockley experiment, the carriers produce a current pulse in the external voltage sensing circuit. This current pulse can be monitored on an oscilloscope.

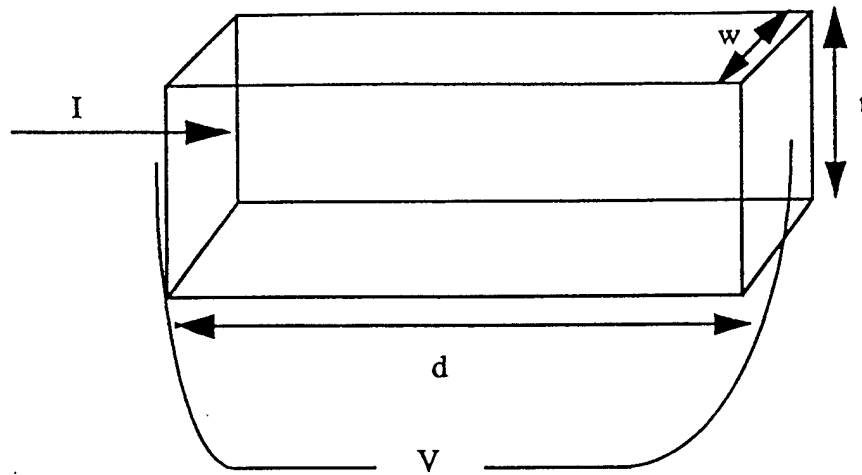


Fig.1.1. A piece of semiconductor with known dimensions used to calculate the current

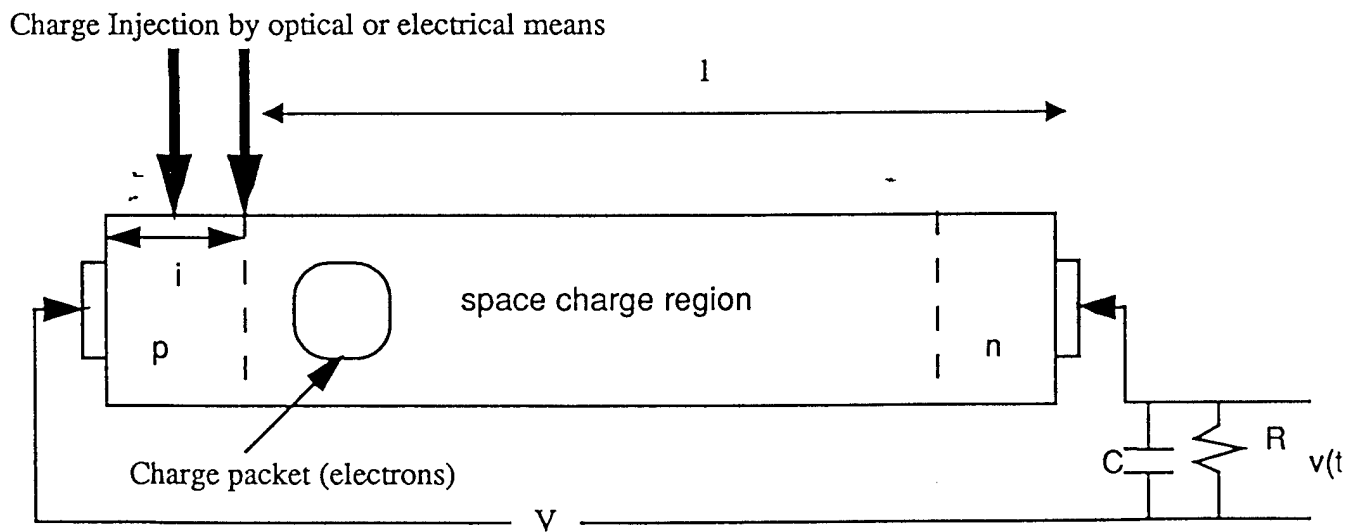


Fig.1.2. Charge packet under the influence of electric field in Time of Flight

Successful application of the ToF technique requires certain criteria to be met. Firstly, the material must be of high resistivity so that the joule heating is a minimum. Secondly, the dielectric relaxation time  $\rho\epsilon$  must be greater than  $t_1$  [7]. Finally, the mean lifetime of the carrier should not be less than  $t_1$  [8].

From a historical perspective, conductivity experiments emerged from the requirement to study the nonlinear behavior of electron and hole mobility at high fields and a possible saturation of drift velocity at higher fields. Shockley's modification of the scattering theory was the primary cause for such investigations, because the new theory predicted non-ohmic behavior at high fields [9]. In 1951 and '53, Ryder performed experiments on silicon and germanium to determine the velocity of holes and electrons as a function of applied electric field. He was able to measure the saturated drift velocities using the conductivity method [10]. The saturated electron velocities he recorded for silicon was  $1 \times 10^7$  cm/s and  $6 \times 10^6$  cm/s for germanium. In 1956, Gunn independently confirmed the previous measurements on germanium. He used the conductivity method with a slight variation to improve the computation of the applied field [11]. Due to lack of modern day processing technology in the 1950's, such experiments were performed on large bulk materials.

The only extensive study on the dependence of electron drift velocity on the applied field in silicon carbide was done by von Munech and Pettenpaul in 1977[3]. Von Munech and Pettenpaul utilized the conductivity technique to measure the dependence of electron drift velocity, parallel to the basal plane, on electric field in 6H silicon carbide. They utilized modern day processing technology to fabricate structures on SiC substrates. The p-type substrates were grown by the Lely method (sublimation at  $2500^\circ\text{C}$ ) in the form of platelets with flat surfaces perpendicular to the c-axis. The present work is similar to von Munech's experiment. The conductance technique is selected in view of its much simpler electronic equipment as compared to the time-of-flight technique. Furthermore, it provides a direct comparison between the velocity-field data of electrons in epilayers grown over substrates grown by the Lely method versus those grown by the present modified sublimation technique.

## 1.2 Thesis Overview

In Chapter 2 some background information is presented on the design of the masks for the test structures, followed by a detailed description of the critical processing steps taken to successfully fabricate the test structures. Chapter 3 will provide the description of the measurement technique used in order to extract the drift velocity of the carriers. Preliminary data taken by the measurement described in Chapter 3 with its discussion will be presented in Chapter 4. Chapter 4 will also describe in detail the adjustments made to the measurement technique described earlier. Chapter 5 will present the final electrical characterization of the structures from which the drift velocity of the carriers will be extracted. Finally, Chapter 5 will also provide the conclusion and suggestions on future

work within the domain of the conductivity measurements. The appendix at the end contains the source code of the matlab programs that facilitated data acquisition and analysis.

## 2. FABRICATION

The first half of this chapter provides information on the test structures, followed by the description of the processing steps to fabricate these structures. Section 2.0 provides information on the epilayers. The detailed description of the mask used for fabrication is included in Section 2.1, while Section 2.2 contains the information on fabrication of these devices.

### 2.0 Epilayers

Velocity field measurements were to be performed on 4H and 6H polytype SiC. The drift velocity of electrons, as a function of the applied field, was to be determined in the basal plane perpendicular to the c-axis of SiC. For this purpose two wafers, a 4H and 6H SiC, were ordered from Cree Research Durham, NC. A p type epilayer was grown on the p-type substrate and finally the n-type epilayer was grown over the p-type epilayer. The final n epilayer was used for the measurement of the drift velocity of the electrons. The table below specifies the dopant and the intended doping concentration.

Table 2.0  
Intended doping profile for the sample.

	Dopant type	Intended concentration /cm <sup>3</sup>
2nd epilayer n	Nitrogen	1e17
1st epilayer p	Aluminum	5e15
Substrate p+	Aluminum	~3e18

The thickness of the n epilayer was specified to be 1 $\mu$ m while the thickness of the p epilayer was 13 $\mu$ m. The choice of the thickness and the concentration was such as to take into account the depletion width that would grow into the channel being used for the conductivity experiment as shown in Fig. 2.1. To perform the conductivity measurement, high positive voltages would be applied to the n epilayer to create high fields. This in turn reverse biases the pn junction and creates a depletion region. For the above concentration and assuming a reverse bias of 500V, we can calculate the depletion region that grows into the n channel. Using the following relation[5]

$$W = [2\epsilon_s V (N_a + N_d) / e N_a N_d]^{1/2} \quad (3)$$

where  $W$  is the depletion width,  $\epsilon_s$  is the permittivity of SiC,  $N_a$  and  $N_d$  are the acceptor and donor concentrations. The total depletion region is  $10\mu\text{m}$  and  $0.51\mu\text{m}$  grows into the channel. 500V applied over a  $10\mu\text{m}$  channel yields a field of  $5 \times 10^5 \text{ V/cm}$ . If the resistance of the channel between the contacts of the applied voltage is a constant, then the distribution of the depletion will diminish towards the ground end in a parabolic form. See Fig. 2.1 below.

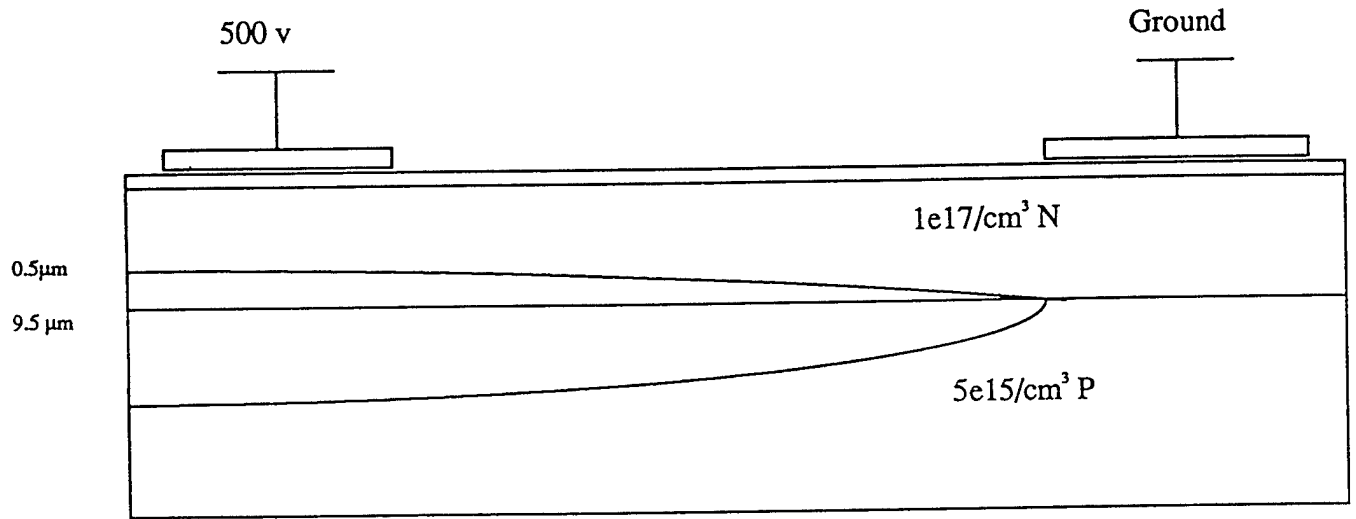


Fig. 2.1. Illustrating the depletion width growth into the n epilayer at steady state.

## 2.1 Mask

A two level mask set was created using MentorGraphic's IC station. The first mask was used to isolate the test structures on the wafer. Isolation, as will be described in the fabrication section, was accomplished with mesa etches. The width of the trench was  $30\mu\text{m}$ , while the depth was in excess of  $1.5\mu\text{m}$ . From (1), it is obvious that the determination of the drift velocity is dependent on the accurate determination of the carrier concentration, hence Hall structures were designed on the masks. TLM structures are also present on the masks. Figure 2.2 shows the first isolation mask. As can be seen from the figure, a  $5 \times 5$  and a  $10 \times 10$  constriction were isolated in each test structure. These constrictions effectively form the channels on which the conductivity experiment will be performed. Test structures were placed perpendicular to each other to notice any difference in the velocity-field characteristics in different directions in the basal plane.

The second mask was the contact mask. Figure 2.3 shows the contact mask superimposed on the trench mask. A circular Hall structure was used with semicircular contacts. The dimensions of the contacts for TLM structures was  $20 \times 100\mu\text{m}$ . The distance between the

contacts progressively increased from  $10\mu\text{m}$ , in steps of  $5\mu\text{m}$ , to a maximum of  $80\mu\text{m}$ . Four contacts were fabricated for each channel, two contacts were shared between the two channels. As will be described later in the measurement chapter, the two extra contacts were used for voltage monitoring on the oscilloscope. Furthermore, in the eventuality that one of the contacts was not working due to processing errors then at least one will be available for the conductivity experiment.



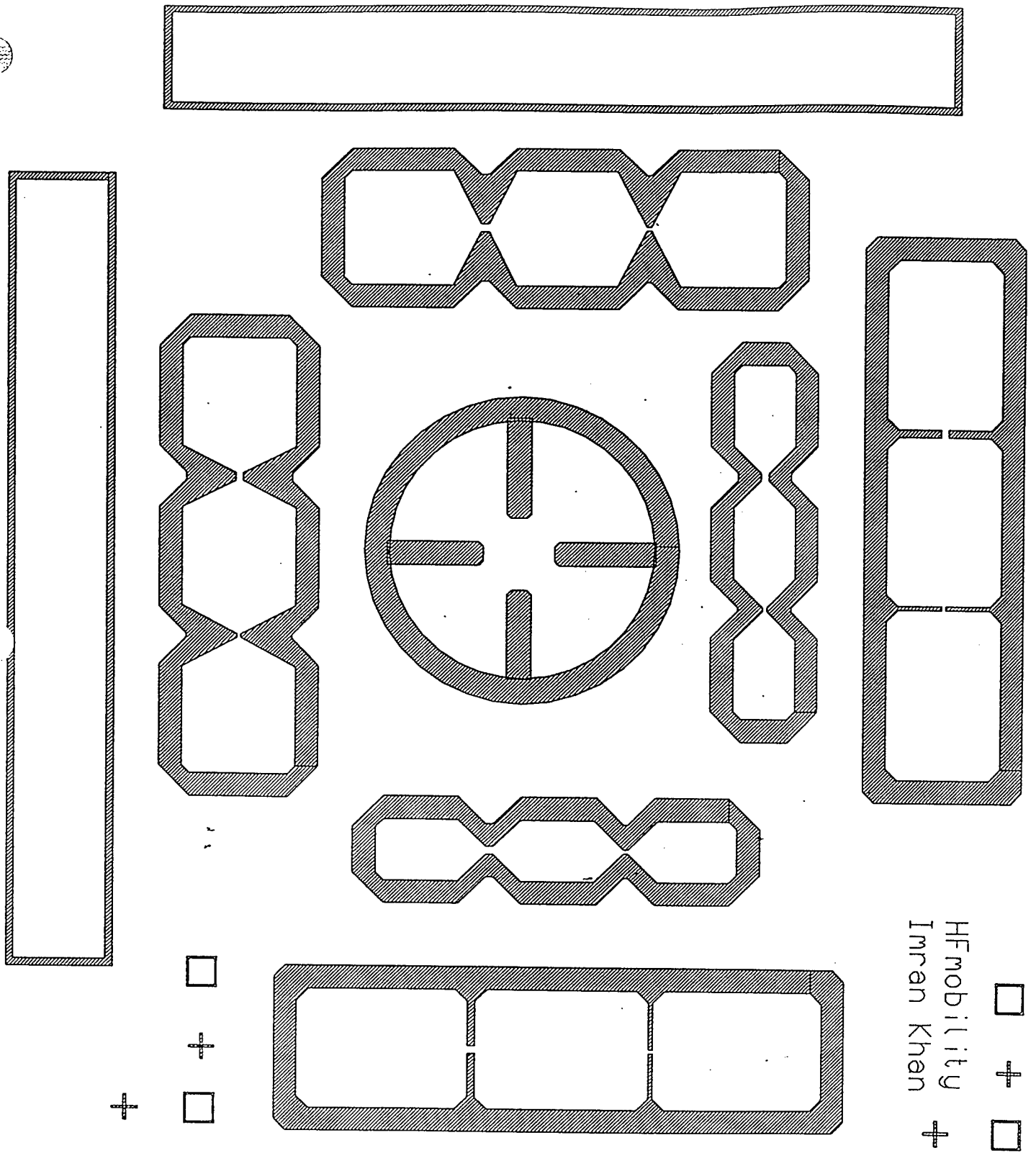


Fig. 2.2. Mask used to fabricate the trenches using reative ion etching in  $SF_6$ .

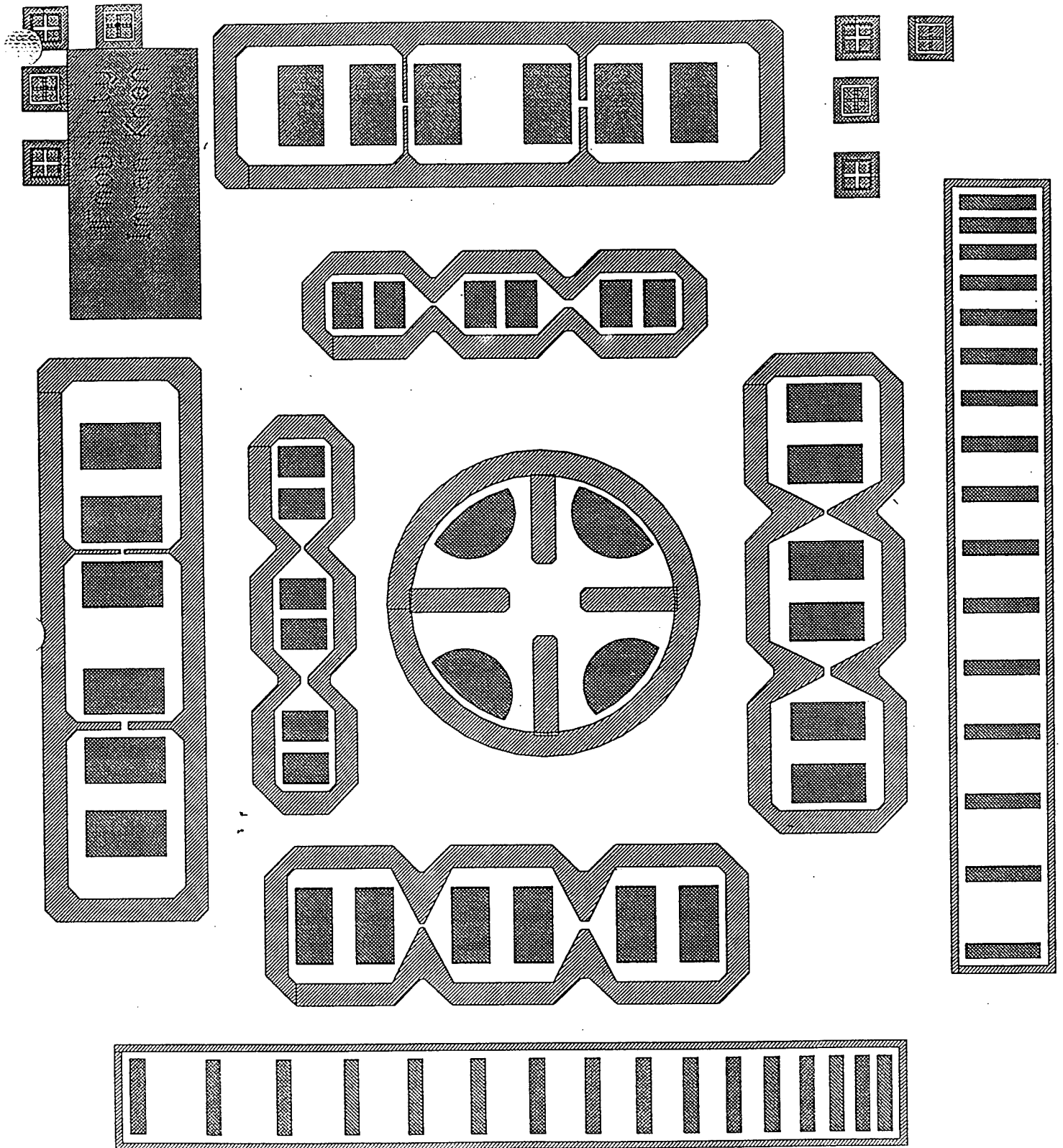


Fig. 2.3. The final die structure with nickel contacts.

## 2.2 Fabrication

This section discusses the critical steps involved in the fabrication of the test structures. The complete run sheet is attached in the appendix section. The main processing steps involved in this run are single-step optical lift-off, reactive ion etching (RIE), and metal deposition.

Lift-off is an additive metalization technique, as opposed to the etching process involved in photolithography. It was developed with the advent of electron-beam lithography in the late 1960's [13]. In this technique the surface of the photoresist film is modified by a soak in chlorobenzene either before or after uv exposure[13]. The thickness of the modified surface depends on the prebake time of the resist and the soaking time in chlorobenzene. Soaks after exposure require longer times for the same results as soaks before exposure. The modified surface has lower dissolubility than the unmodified resist, however the modified surface exposed to uv dissolves faster than that which has not been exposed. This creates an overhang, see Fig. 2.4, with an undercut after developing. Once metal has been deposited, or any other material, the overhang separates the metal on top of the resist from the metal on the substrate. During the removal of the resist, the metal on top of the resist is also "lifted-off" leaving only the metal on the substrate with the desired pattern. The main disadvantage to this process is that it can leave a fine string of metal at the edges that can be detrimental.

In this fabrication, the lift-off technique was used to pattern a metal mask for etching the isolation trenches, and it was also used to pattern the metal contacts of the devices. AZ 1518 positive photoresist was spun on the substrate at speeds of about 5000 rpm for 30 seconds. This gave a film with effective thickness of  $2\mu\text{m}$ . After the prebake step, the sample was exposed to uv light in a Suss MJB-3 mask aligner for 7 seconds using the light field isolation mask. This was followed by a soak in chlorobenzene for 17 minutes. The sample was thoroughly dried with dry nitrogen gas before developing the pattern. Photoresist covered the substrate where isolation trenches would be fabricated. At this point the sample is ready for deposition of metal. Aluminum was used to mask the substrate where etching is prohibited. Aluminum was deposited using the NRC thermal evaporator. The sample is placed facing downward above the aluminum source in the NRC chamber. Evaporation commences when the pressure in the chamber falls below  $4 \times 10^{-7}$  torr to ensure a successful and uniform deposition. During evaporation, care is taken not to hardbake/burn the photoresist on the substrate. Otherwise, the photoresist does not dissolve in the solvent, resulting in an unsuccessful lift-off. After a successful lift-off, the substrate is covered with aluminum except where mesa trenches are needed.

As stated earlier, for effective isolation, mesa trenches with depth of over  $1.5\mu\text{m}$  are required. In order to keep track of the cross sectional area of the channel, the walls of the isolation trenches were needed straight. For this purpose, anisotropic etching of SiC was required. Reactive ion etching in  $\text{SF}_6$  ensured trenches with vertical walls because of its anisotropic nature. The etch was performed in a Plasma Technology "Plasmalab" RIE system. To etch between 1.5 and  $2\mu\text{m}$  of SiC, about  $0.8\mu\text{m}$  of aluminum was required to

effectively protect the unexposed substrate. The thickness of the aluminum mask and the depth of the trenches was verified with the profilometer (Alpha Step 200, manufactured by Tencor Instruments). The remaining aluminum after RIE was etched in a solution of piranha ( $\text{H}_2\text{O}_2:\text{H}_2\text{SO}_4$ ). This also ensured a clean surface for the next step of depositing metal contacts. The Piranha clean however, leaves a thin layer of oxide on the surface. This surface oxide was removed by soaking the sample in the BHF (buffered oxide etch) for about half a minute. Note that not much can be done about the thin film of native oxide that forms after the wafer is exposed to the atmosphere. However, since it is a very thin film it is not very detrimental to the contacts.

Lift-off is once again repeated, but this time the dark field mask for the metal contacts is used. The surface is cleaned just like in the previous steps. A Varian E-beam system is used to deposit nickel on to the substrate. A beam of electrons is focused on the nickel source to evaporate it. The pressure of the chamber is kept below  $4 \times 10^{-7}$  torr for uniform deposition. Low pressure also ensures that high quality nickel is deposited for better contacts.  $0.1 \mu\text{m}$  of nickel was deposited for the metal contacts. Greater thicknesses were avoided to prevent any spiking effects. After successful deposition of nickel, the photoresist was removed and patterned metal contacts were left on the substrate.

The last step in the fabrication is to anneal the nickel contacts. For this purpose, the samples were sent to Cree Research. The contacts were annealed in Argon at 900 degrees celsius for 2 minutes. The samples are now ready for electrical tests.

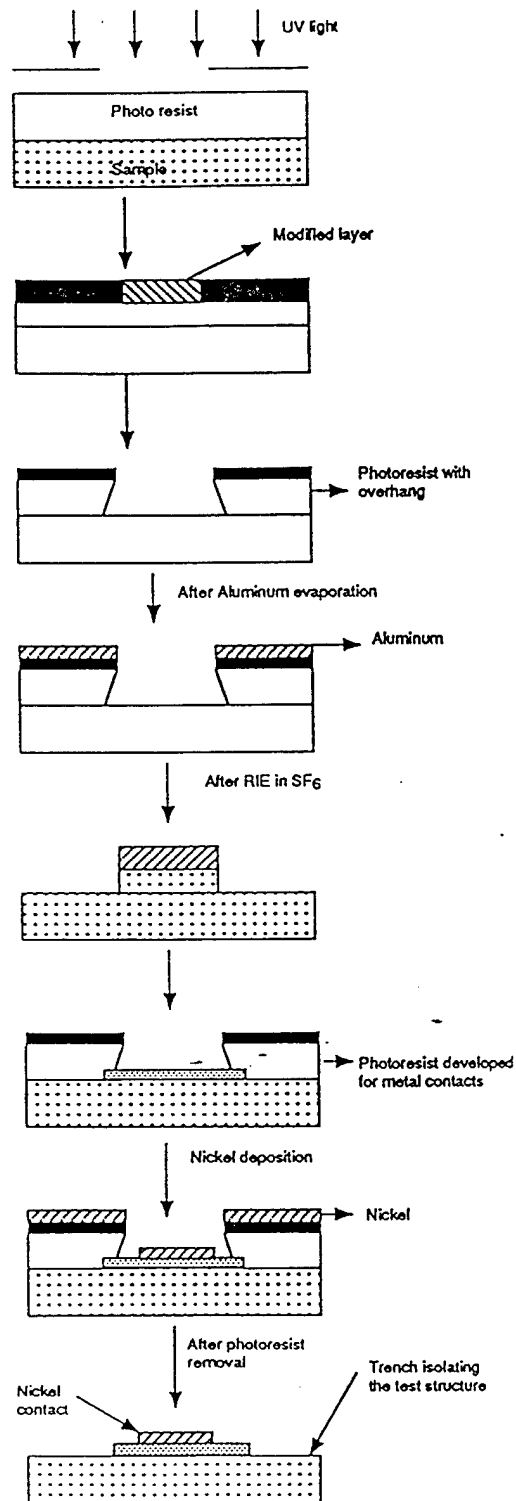


Fig.2.4 Highlights of the processing steps involved in fabricating the test structures.

### 3. MEASUREMENT SETUP

In this chapter the method of measurement will be thoroughly described. The electrical setup required to perform the measurement is also discussed. The description will illustrate how from current-voltage measurements the velocity of the carriers is extracted. TLM measurements and its data interpretation will be described. Finally, the chapter will end with the presentation of the Hall data.

#### 3.1 Measurement Technique

For accurate determination of the field and current through the channel, ohmic contacts are needed. The resistance of an ohmic contact can be measured. This can be taken into account when determining the field over the channel. However, for the doping levels of  $1 \times 10^{17} / \text{cm}^3$  it was not completely clear whether ohmic contacts would be formed. This was taken into account when designing the mask set for this experiment, with the result that two extra contacts were fabricated closest to the channel. This way there are four contacts to perform velocity - field measurement per channel. Of these four contacts, the two inner contacts are used to measure the voltage and consequently the field across the channel, while the outer two contacts independently allow for the passage of current through the channel. The experiment simply consists of applying a voltage to the channel and then measuring the current through the channel. If ohmic contacts are not formed, then using a voltmeter the voltage drop on the channel can be determined by using the inner two contacts. This would work because the very high impedance of the voltmeter only requires negligible amount of current into the voltmeter.

The principal setup for the experiment is shown in Fig. 3.1. In this setup, high voltage pulses are applied to the outer contacts. Pulses are used instead of a constant high voltage to avoid heating of the channel and the subsequent heating of the test structure. In this experiment, the carrier drift velocity is being studied at room temperature. Hence, it is crucial to minimize transient heating of the test structures. Since the experiment was to be carried over a wide range of voltage values, accumulative heating of the test structure was avoided by giving large intervals of time ( $>4\text{secs}$ ) between pulses. The current through the channel is monitored on the oscilloscope. Internal to the oscilloscope there is a  $50\Omega$  termination. Current through the channel consequently produces a voltage drop over the  $50\Omega$  resistor. The oscilloscope displays this voltage waveform on the scope screen, and scaling the waveform down by fifty gives the instantaneous current through the channel.

The voltage at each of the inner contacts is also observed on the oscilloscope with two independent channels A and B of the scope. The voltage drop across the channel is obtained by subtracting the voltages of the two channels. To accomplish this task, the oscilloscope was programmed to subtract the waveform of channel B from A and display the resulting waveform as the voltage across the channel.

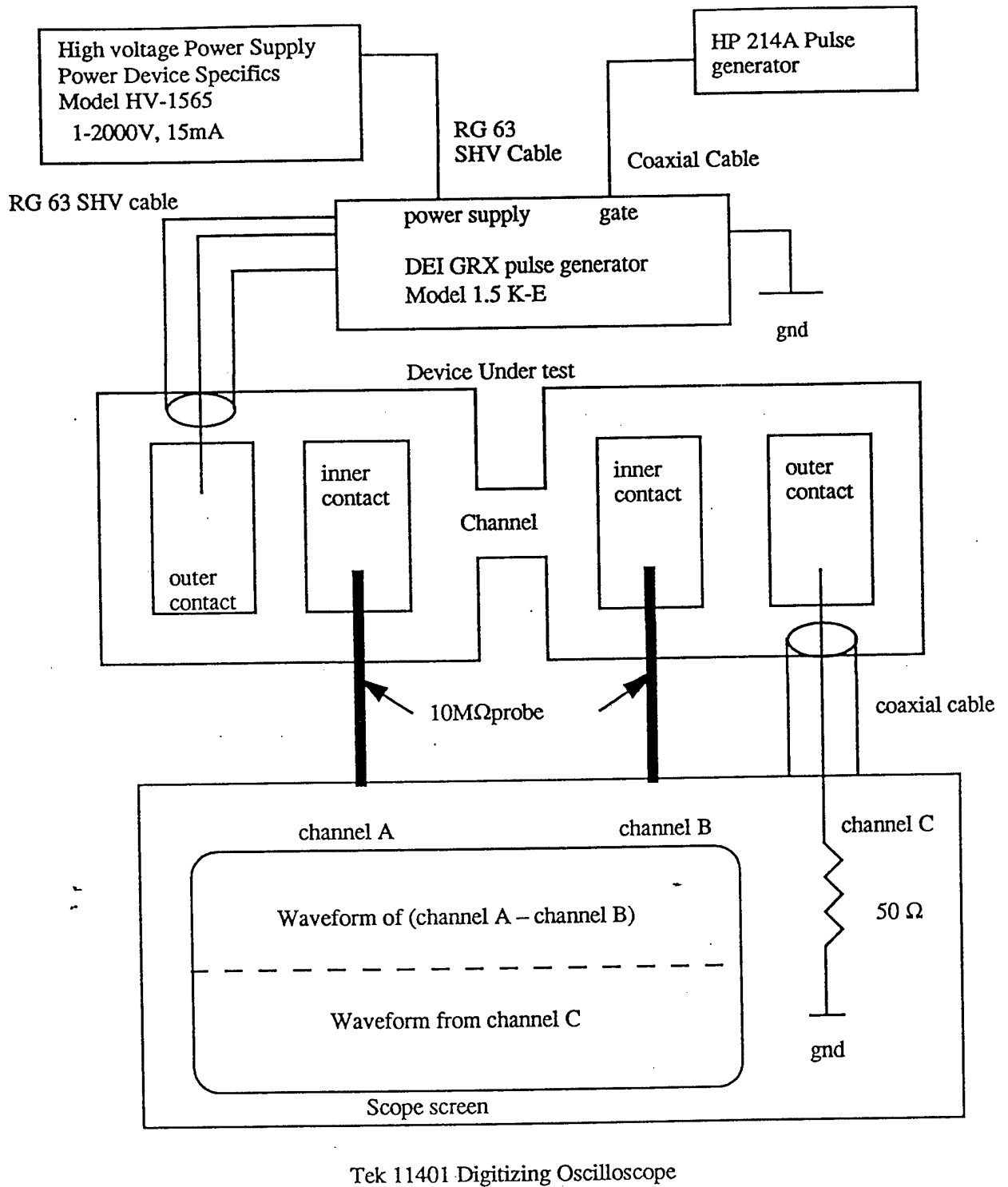


Fig. 3.1. Experimental setup used in performing the conductivity measurement on 4H and 6H SiC .



High speed pulse generators available in the lab produced voltage swings of 100V at most, producing a field of  $1e5$  V/cm and  $2e5$  V/cm over channels of length  $10\mu\text{m}$  and  $5\mu\text{m}$  respectively. Clearly this is insufficient to observe saturated drift velocity in the  $10\mu\text{m}$  channel. Furthermore, we would like to stress the devices as much as we can. A special high voltage and high speed pulse generator was bought from Directed Energy Inc.(DEI). The specs of this pulse generator are as follows

Output voltage to +/- 1500V  
Rise Time and Fall time <30ns  
Pulse width <75ns to DC

This pulse generator produces waveforms based on the input from a trigger source. Square pulses were used in this experiment, therefore the trigger source was set to produce square waves. An HP 214A pulse generator was used as the trigger source. The HP 214A has a separate button to produce single shot square waveforms. This capability was used to keep the repetition rate of the pulses below 0.25Hz, by manually depressing the button when the waveform was required. To keep the heating transient effect to a minimum, the pulse duration was kept below 0.4 to 0.5  $\mu\text{s}$ . The rise times of these pulses were between 20 to 50 ns. Theoretically, a reasonable square pulse could be obtained with pulse width of 200 ns. SHV (super high voltage) cables were provided with the pulse generator. These cables have a characteristic impedance of  $93\Omega$ . The pulse generator is also internally terminated with a  $93\Omega$  terminator. The internal termination prevents reflections from the pulse generator. These reflections, as will be discussed below, originate primarily from the probe-sample interface.

The probes available in the lab are configured for cables with a characteristic impedance of  $50\Omega$ . Furthermore, the probes have voltage rating of 500V. A special probe had to be made with a higher voltage rating, and with a characteristic impedance of  $93\Omega$ . In the construction of the probe, it was of paramount importance to retain the characteristic impedance as close as possible, all the way, to the point of contact. To achieve this goal, the SHV cable itself was used to make the probe. This way both the criteria for higher voltage rating and the characteristic impedance are met. Essentially, a probe tip was soldered to the middle conductor of the SHV cable. The cable with the probe tip was then mounted on to an unused probe arm for support. Figure 3.2 shows the fully constructed probe.

Measurements were performed with the device on the probe station. The probe station was enclosed in a black box to avoid changes in carrier concentration due to the effect of light. To prevent arcing between the closest probes due to breakdown of air, the test structure was covered in fluroinert.

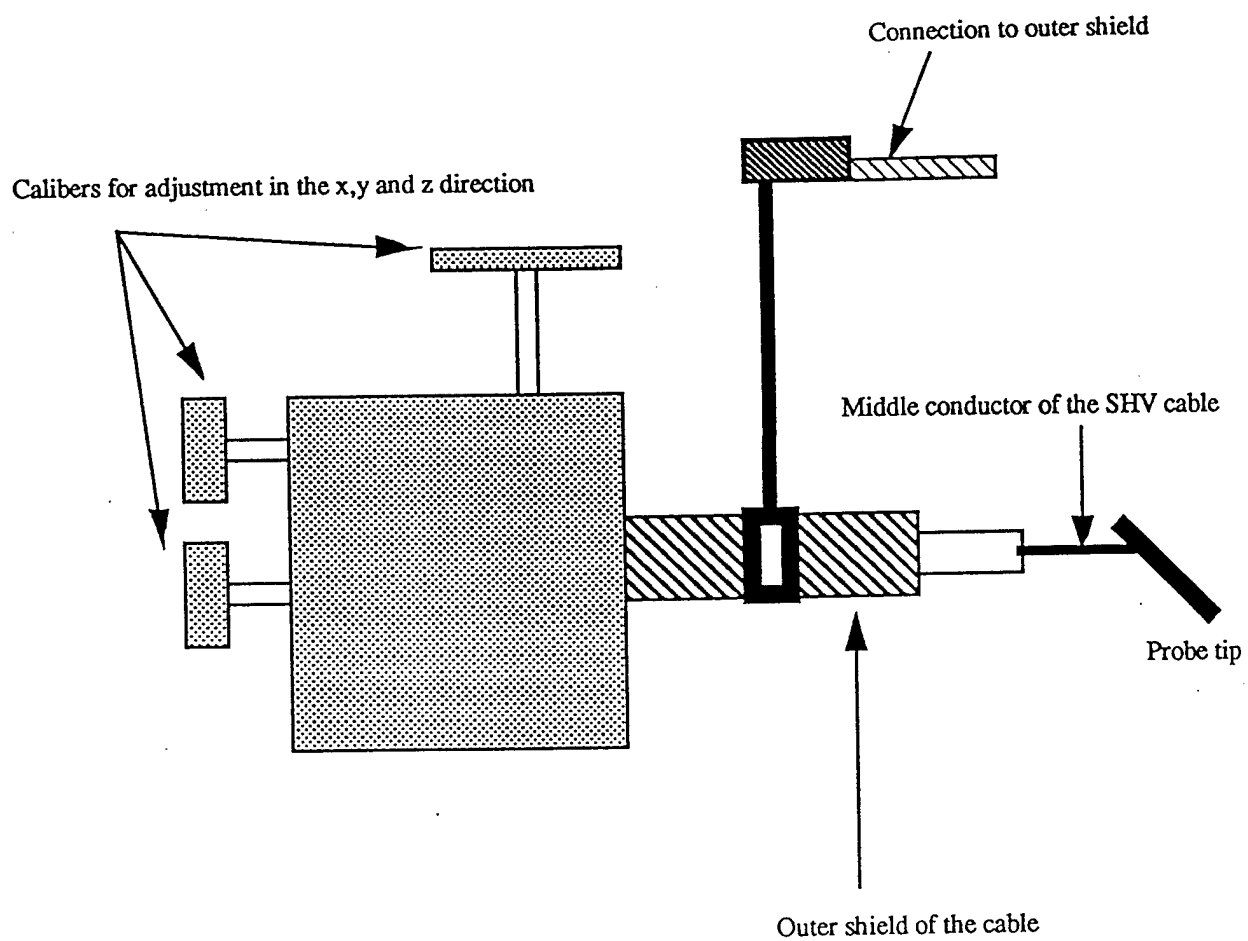


Fig.3.2. Construction of the custom probe used in the conductivity measurement.

### 3.2 TLM Measurement

Transfer length measurements were first proposed by Shockley[14]. The TLM technique enables the measurement of the contact resistance and the sheet resistance of the material. The technique is based on measuring total resistance between contacts of different spacing. From a plot of the total resistance against the contact spacing, three parameters can be extracted, the sheet resistance, the contact resistance, and the transfer length. The specific contact resistance can be computed from the transfer length. The transfer length can be thought of as the length where the voltage due to the current transferring from the metal to the semiconductor, or from the semiconductor to the metal, drops to 1/e value of its initial maximum value [15]. A typical TLM structure is shown in Fig. 3.3. For contacts with spacing greater than the transfer length, the total resistance between any two contacts is given by

$$R_T = \rho_s d/Z + 2R_C = \rho_s d/Z + 2\rho_s L_T/Z$$

where  $R_T$  is the total resistance,  $\rho_s$  is the sheet resistance of the semiconductor,  $d$  is the spacing between the contacts,  $Z$  is the width of the contact, and finally  $L_T$  is the transfer length. The above formula also assumes that the sheet resistance of the semiconductor is not changed under the contacts. This change can result from the contact formation process. Taking the derivative of the above equation with respect to the spacing 'd' yields

$$\Delta R_T / \Delta d = \rho_s / Z$$

The derivative corresponds to the slope on the plot shown in Fig. 3.4. From the slope, the sheet resistance of the semiconductor can be deduced. The intercept corresponding to  $d = 0$  gives twice the contact resistance  $R_C$ , since two contacts are being used for the measurement. Likewise, the intercept on the x-axis gives us twice the transfer length.

The transfer length method was used to characterize the contacts and obtain the sheet resistance of the n-epilayer, using the HP4145 semiconductor parameter analyzer. Non ohmic contact characteristics were obtained on the I-V curves. To effectively utilize the TLM technique, the most linear part of the I-V curves was used to obtain the total resistance. Thus the TLM structures were swept to high voltages. Our interest in TLM measurement was essentially to obtain the sheet resistance from which the carrier concentration will be extracted. In conjunction with the Hall measurement data, the carrier concentration would be verified. The sheet resistance of the n-epilayer is given as

$$\rho_s = 1/n\mu_{et}$$

where  $n$  is the carrier concentration,  $\mu$  is the mobility,  $e$  is the electronic charge, and  $t$  is the thickness of the epilayer. If the mobility is known, then the carrier concentration can be computed as below

$$n = 1/\mu\rho_s e t$$

The I-V curve for a 4H sample is shown in Fig. 3.5. The corresponding total resistance versus contact spacing is shown in Fig. 3.6. From the data analysis, a specific contact resistance of  $2.55\text{m}\Omega/\text{cm}^2$ , and a sheet resistance of  $2857\Omega$  was obtained for 4H. If a mobility of  $400\text{ cm}^2/\text{Vs}$  is used, then this yields a carrier density of about  $0.55\text{e}17/\text{cm}^3$ . CV measurement done by Cree Research revealed a concentration of  $1.0\text{e}17/\text{cm}^3$  for the 4H sample. Further CV measurements done at Purdue indicated that the carrier concentration in the 4H wafer was in the range of  $1\text{-}1.5\text{e}17/\text{cm}^3$ . This suggests that the carrier concentration obtained from the TLM measurement is not accurate. One possibility for the error could be the heating of the TLM structures at the high voltages needed to get into the quasi-linear position of the I-V curves, resulting in mobility degradation. By utilizing mobility values higher than the true value, lower carrier concentration will result. The structures were swept from 0 to 50V with peak current densities of  $12.95\text{kA}/\text{cm}^2$ . This was necessary, as pointed out earlier, to obtain the most linear part of the I-V curve. At these high voltages and current levels, appreciable transient and accumulative heating of the structures can result. To minimize the mobility degradation, the HP 4145 was replaced with the pulsed system. The pulsed system rendered the ability to use high voltages for short time intervals thus reducing the heating problem. The results obtained from this measurement technique tallied better with the CV measurements.

Table 3.1  
Carrier concentrations obtained from TLM measurement using the pulsed system.

	Carrier concentration / $\text{cm}^3$
4H	$1.34\text{e}17$
6H	$1.1\text{e}17$

Mobilities of  $400\text{ cm}^2/\text{vs}$  and  $200\text{ cm}^2/\text{vs}$  were used for 4H and 6H SiC respectively. In the next section, Hall measurements will be described. This will seek to verify the values obtained from the TLM measurements.

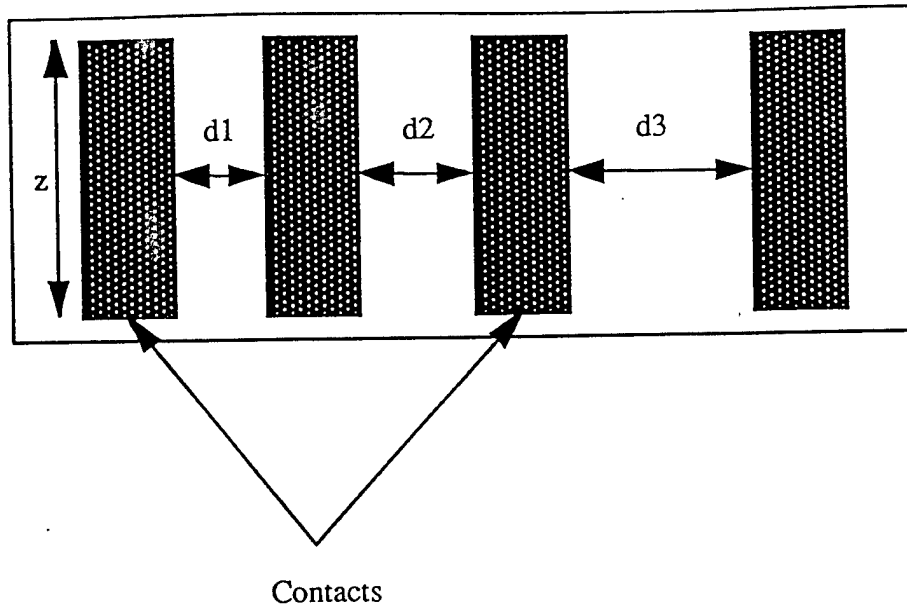


Fig. 3.3. TLM structure used to deduce sheet resistance in the conductivity experiment.

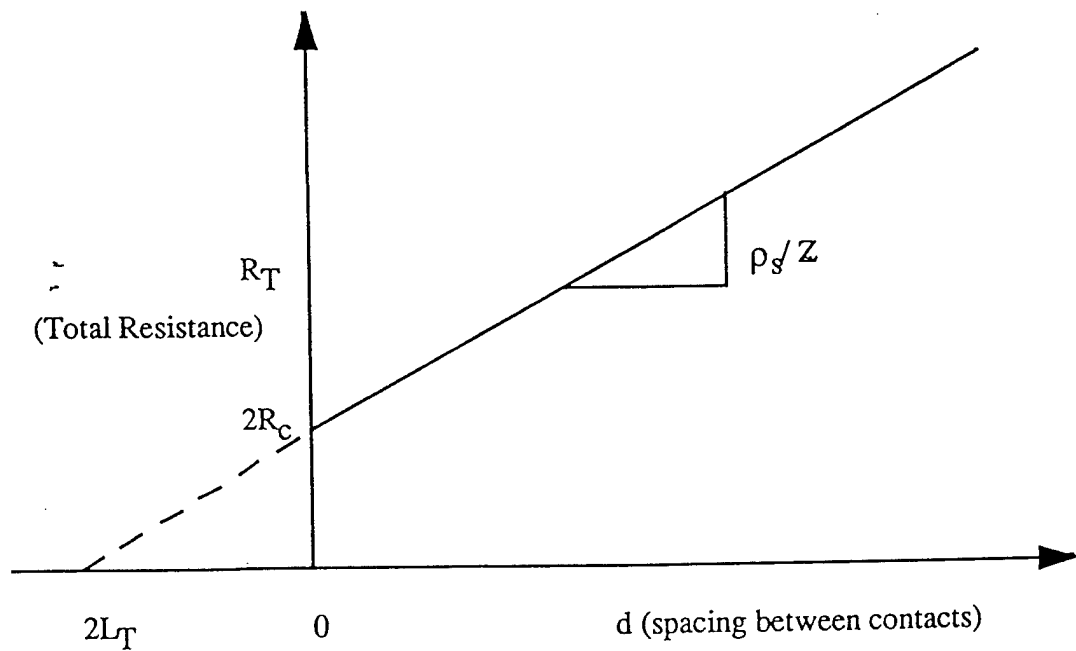


Fig. 3.4. The above figure illustrates how to extract the sheet resistance and contact resistance resistance versus spacing plot.

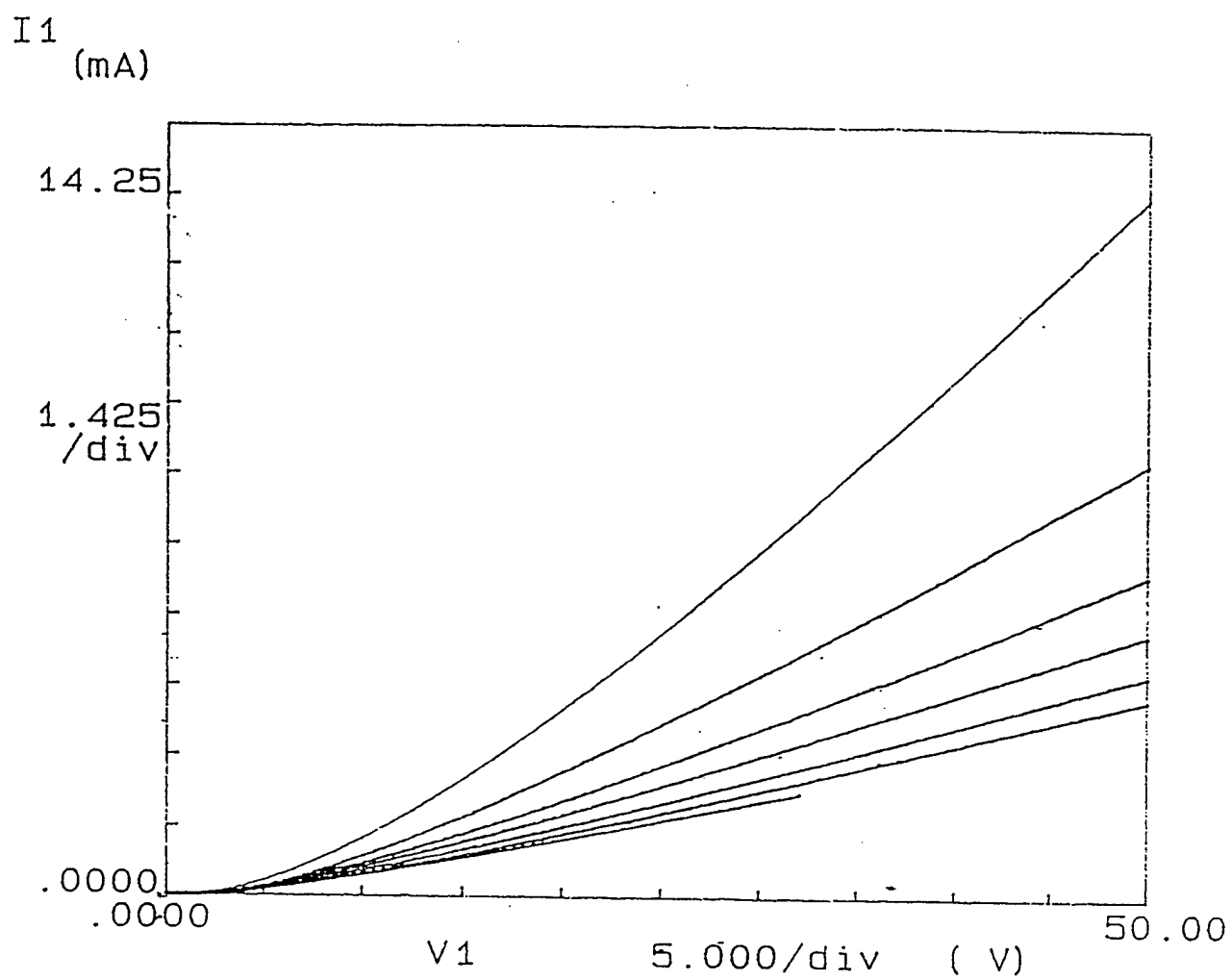


Fig. 3.5. The I-V curve obtained for 4H TLM structure using the HP 4145. Each curve corresponds to a certain contact spacing.

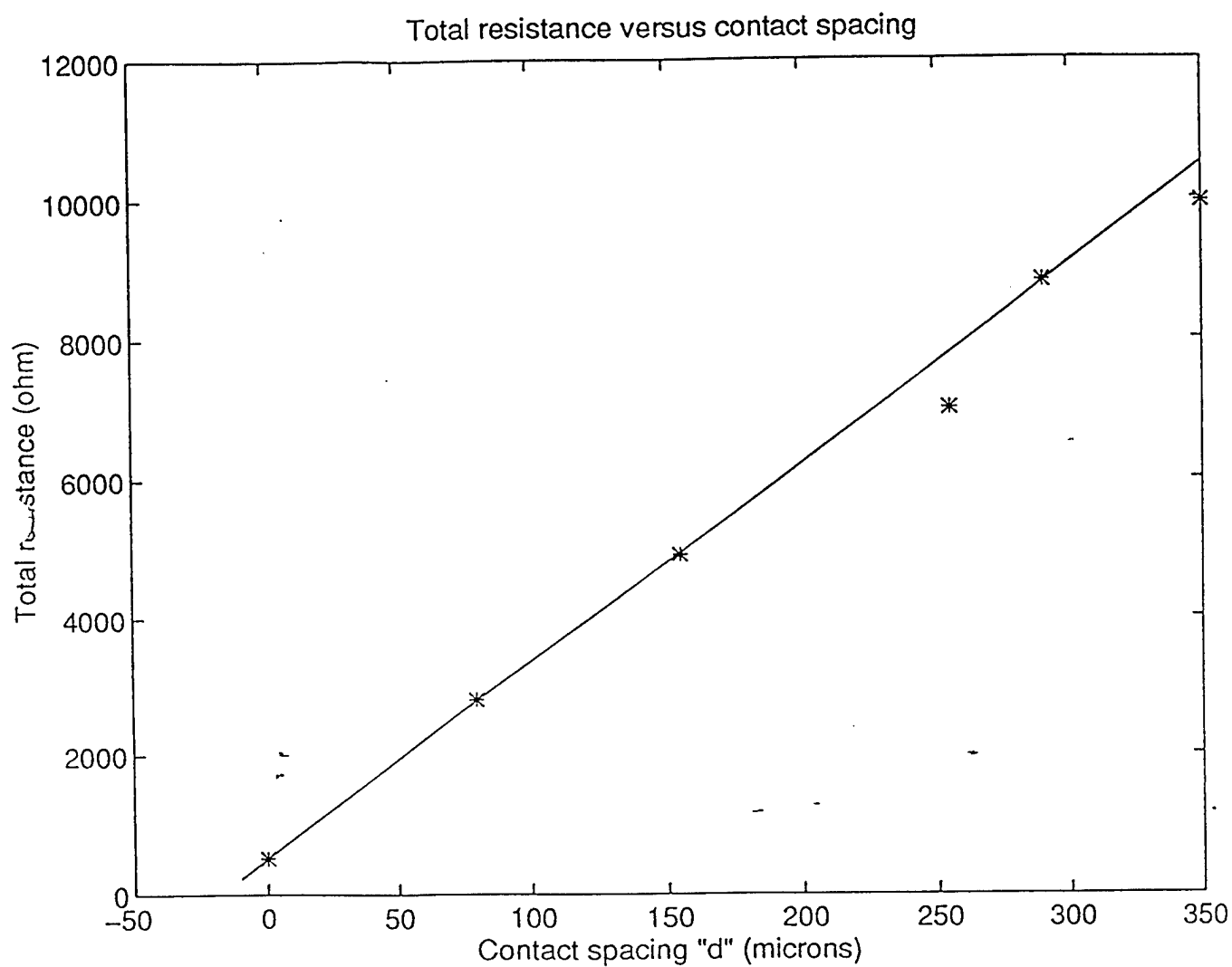


Fig. 3.6. Total resistance versus contact spacing. The sheet resistance was  $2857\Omega$  (corresponding to slope of  $28.57\Omega/\text{m}$ ). And contact resistance of  $255\Omega$  (intercept at  $d=0$  of  $510\Omega$ ).

### 3.3 Hall Measurement

The Hall effect was discovered by Hall in 1879. A comprehensive treatment of the subject is given by Putley[16]. By measuring the Hall effect, the carrier concentration can be determined. Magnetic field applied perpendicular to the current flow direction produces an electric field perpendicular to both the current flow and the applied magnetic field. Consider an n type semiconductor as shown in Fig. 3.7. The current  $I$  flows in the x-direction, indicated by the electrons flowing in the opposite direction, and a magnetic field  $\vec{B}$  is applied in the z-direction. The magnetic field coupled with the electric current causes the electrons to deflect to the bottom of the semiconductor block as shown in Fig. 3.7. The accumulation of charge on one side of the block causes a voltage to build between the two sides. The current through the block of semiconductor is given by

$$I = qwt nv_x$$

where  $q$  is the charge of the carrier,  $w$  is the width of the sample,  $t$  is the thickness,  $n$  is the carrier concentration, and  $v_x$  is the velocity of the carriers in the x-direction. The Lorentz force experienced by the electrons is given by

$$\vec{F} = q(\vec{E} - \vec{v} \times \vec{B})$$

There is no current flow in the y-direction hence there is no net force in the y-direction. This implies that

$$\begin{aligned} F_y = 0 &= q(E_y - v_x B) \\ E_y &= B v_x = BI/qwt n \end{aligned}$$

The Hall voltage can be obtained by integrating the electric field in the y direction, hence

$$V_H = BI/qtn$$

The Hall coefficient is defined as

$$R_H = t V_H / BI \text{ (m}^3/\text{C)}$$

In more practical units

$$R_H = 10^8 t V_H / BI \text{ (cm}^3/\text{C)}$$

where  $R_H$  is in units of  $\text{cm}^3/\text{C}$ ,  $V_H$  is in units of volts,  $I$  is units of amperes,  $B$  is in gauss, and  $t$  is in cm.



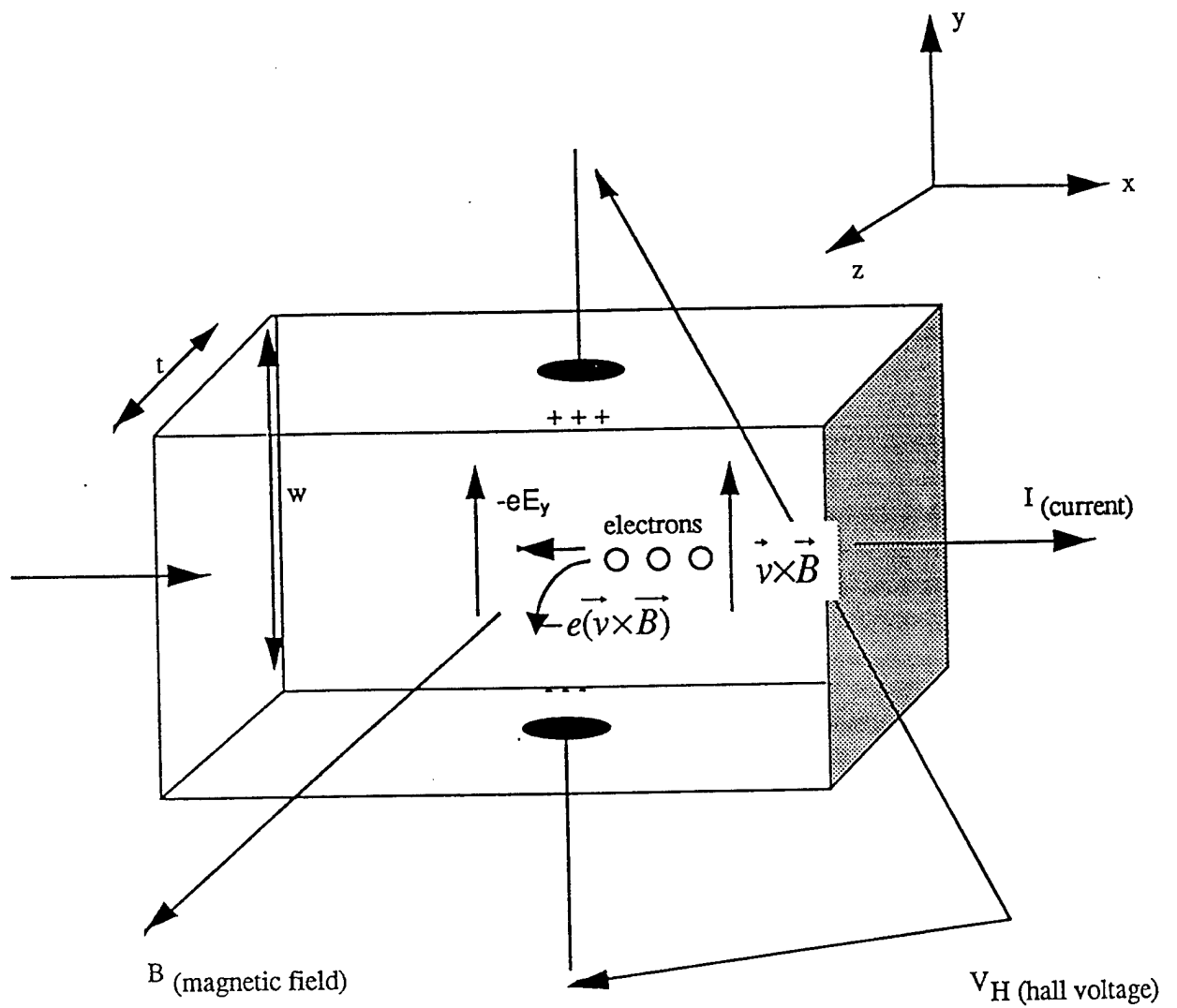


Fig. 3.7. Demonstrating the Hall effect in n-type material.

The carrier concentration ( $/\text{cm}^3$ ) is then given by

$$n = 1/qR_H$$

where  $q = -e$ . The above derivation assumes that the carriers have a uniform velocity. However, in a real semiconductor the carriers have a distribution of velocities. This comes about from the collision scattering and the distribution of energies of the carriers. Thus averages which account for the energy distribution and collision scattering have to be taken into account. Incorporating these averages results in a modified equation as shown below

$$n = r/qR_H$$

where  $r$  is the Hall scattering factor. The Hall scattering factor lies between 1 and 2 [17]. In this thesis the Hall scattering factor is neglected or it is equivalently set to 1. This is supported by the prevailing literature available on SiC, where Hall mobilities are quoted and not conductivity mobilities. Conductivity mobility is Hall mobility times the Hall scattering factor.

Non uniformity of the carrier velocities is not the only effect that needs precaution in the Hall analysis. There are thermal effects associated during the measurement process and asymmetry of the structure that can affect the Hall analysis. Most of these effects can be eliminated by averaging a series of four readings at the polarity combinations of sample current and magnetic field [18]. The table below shows the four combinations that were used during the Hall analysis.

Table 3.2  
Combinations of magnetic fields and voltages used in the Hall analysis.

Combination	Polarity of Magnetic field	Polarity of current
1	+	+
2	-	+
3	+	-
4	-	-

The following relation then gives the Hall voltage

$$(c1 - c2 - c3 + c4)/4 = V_H$$

As shown in Fig. 2.3, a cloverleaf geometry was used for Hall measurement. The main advantage of this structure is that the non ideal contact effects are reduced by removing the contacts away from the active region [19]. Before the Hall analysis could be performed, the samples had to be packaged. Initially, bonding to the small nickel contacts was unsuccessful. After depositing 500 angstroms of gold, bonding to the contacts on the Hall structures was achieved. The Hall setup available in the lab was used, the schematic is

shown in Fig. 3.8. The maximum magnetic field produced from the system was 5kG. Moderate currents were passed through the sample to reduce heating and its associated thermal effects. Typical voltages of 10mV were applied, with a 100Ω resistor in series for current monitoring, producing μA range current. The Hall analysis was repeated a number of times for both the 4H and 6H samples and was found to give identical numbers. The profile obtained from CV measurements were limited by the breakdown voltage of the Schottky barrier. For the present doping range, 0.5μm deep profile was measured. Figures 3.9 and 3.10 show the CV profiles from Cree Research. The table below summarizes the results from the Hall measurements and the CV measurements.

**Table 3.3**  
Carrier concentrations obtained using different measurement techniques.

	6H	4H
Hall	$1.2e17/cm^3$	$1.4e17/cm^3$
TLM	$1.1e17/cm^3$	$1.34e17/cm^3$
CV (Cree)	$1.4-1.5e17/cm^3$	$1.0-1.4e17/cm^3$
CV (Purdue)	$1.4-2.0e17/cm^3$	$1.0-1.5e17/cm^3$

The thickness of the epilayer was verified from the SIMS measurement performed by Cree Research. The uncalibrated SIMS plots are shown in Fig. 3.11 and Fig. 3.12 for 4H and 6H respectively. Carrier concentrations obtained from Hall measurement were deemed most accurate based on their repeatability.

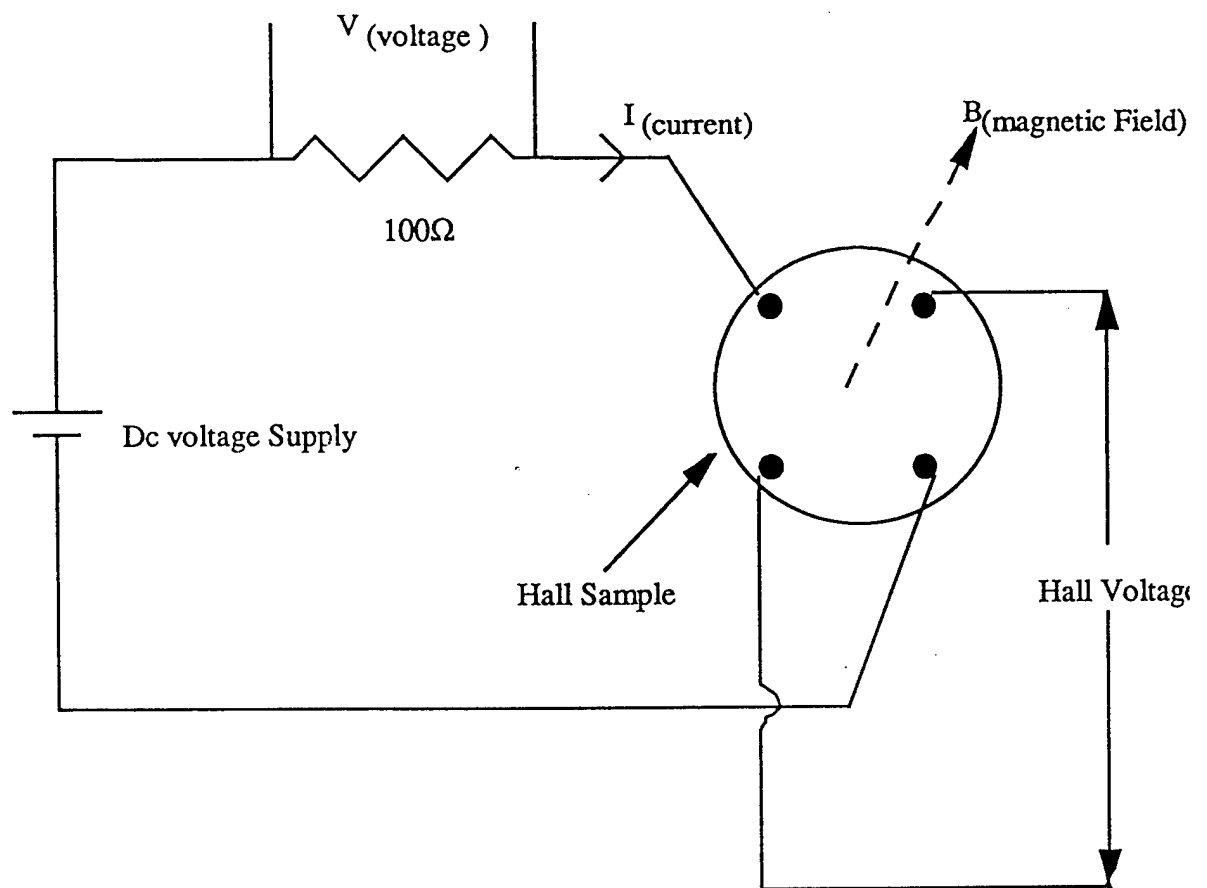


Fig. 3.8. Circuit used in measuring the Hall voltage. Carrier concentration of the n-epilayer will be determined from this measurement.



Diam: 785  $\mu$   
 Area:  $4.84E-03 \text{ cm}^2$   
 Cs: 8 pF  
 Esi: 18.83  
 Freq:  $1.8E+06 \text{ Hz}$   
 Type: N

$U_{min}$ : 0 V  
 $U_{max}$ : -48 V  
 $R_s$ : 1  $\Omega$   
 $N$ : 2  
 $\Phi I$ : -1.814 V

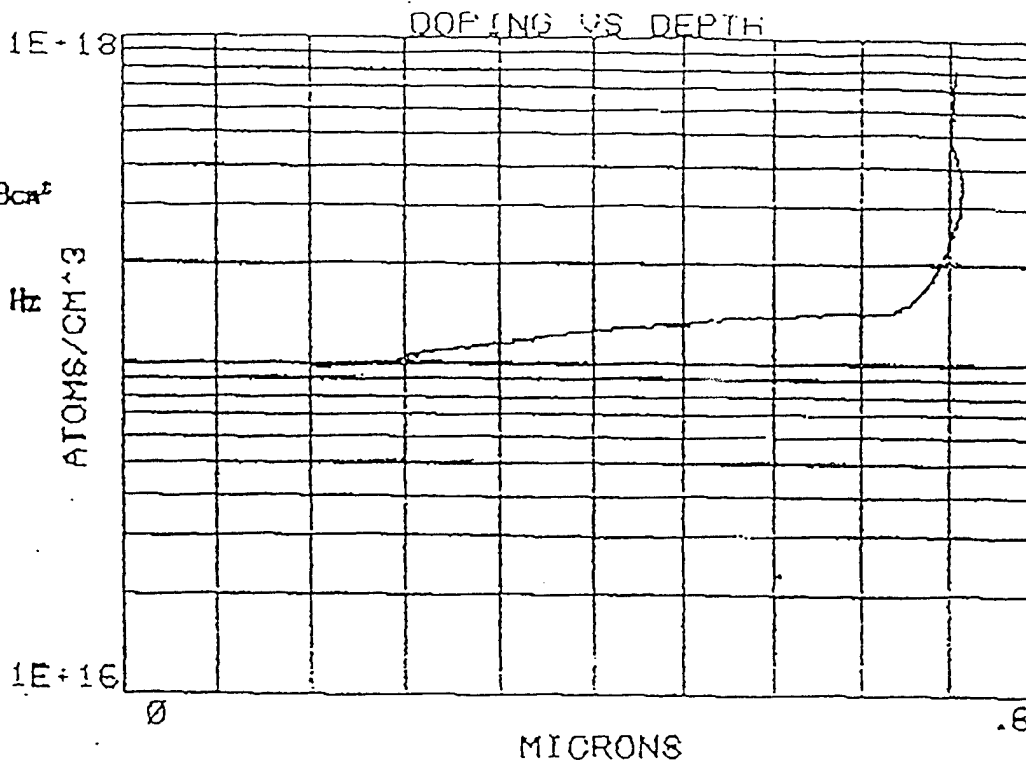


Fig. 3.9 CV profile for 4H.



Diam: 785  $\mu$   
 Area:  $4.84E-03 \text{ cm}^2$   
 Cs: 8 pF  
 Esi: 18.83  
 Freq:  $1.8E+06 \text{ Hz}$   
 Type: N

$U_{min}$ : 0 V  
 $U_{max}$ : -48 V  
 $R_s$ : 1  $\Omega$   
 $N$ : 2  
 $\Phi I$ : -1.632 V

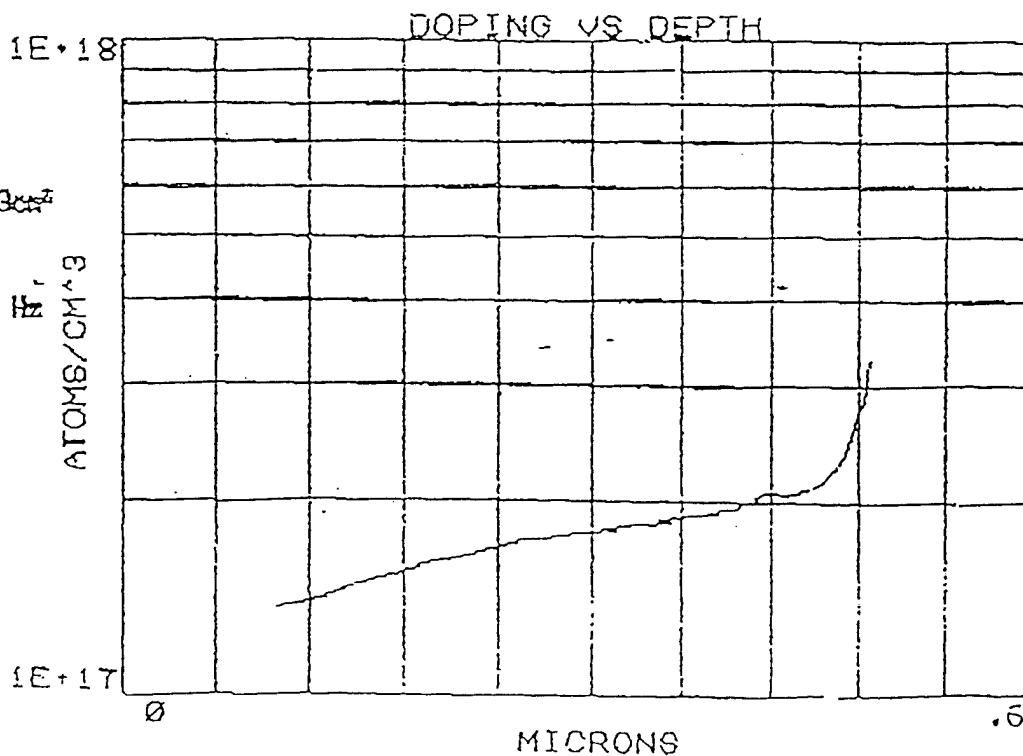
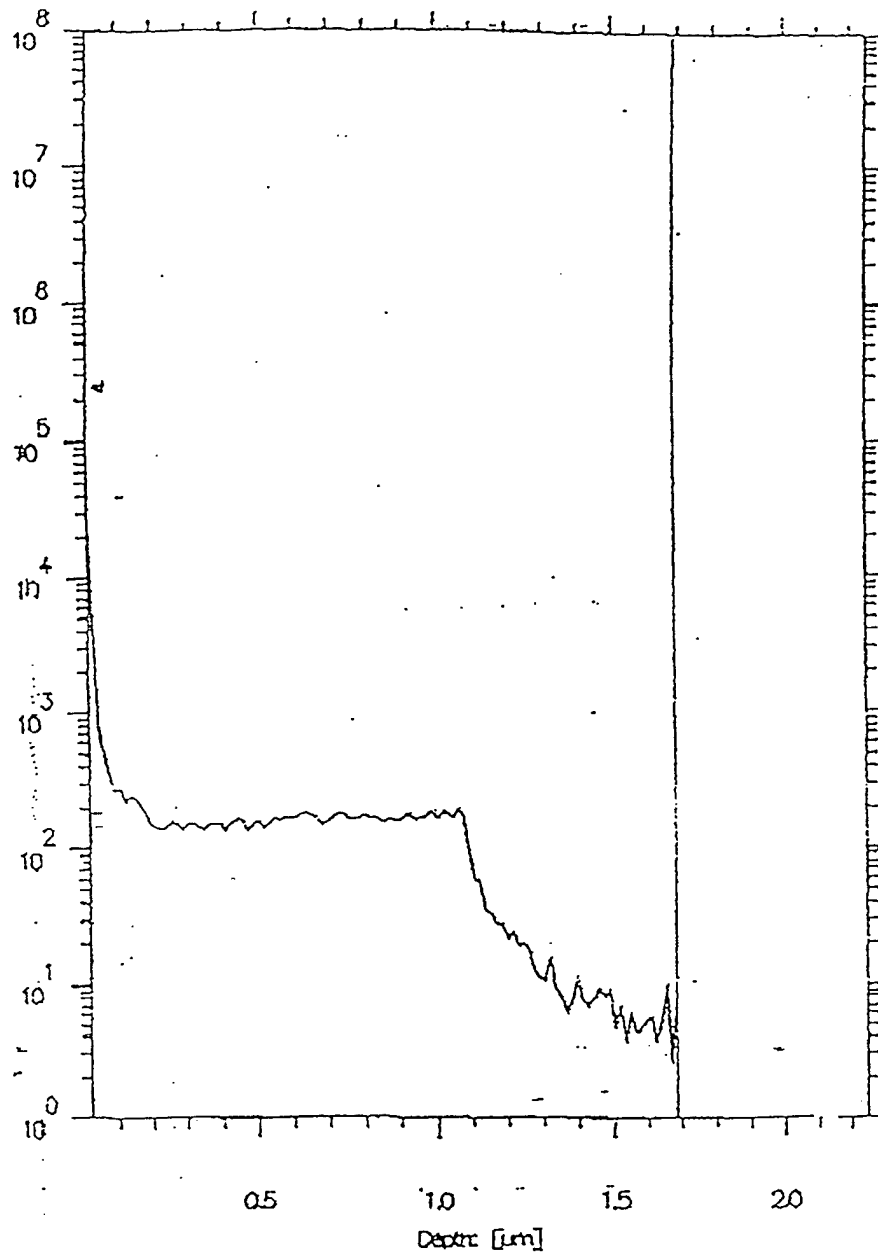
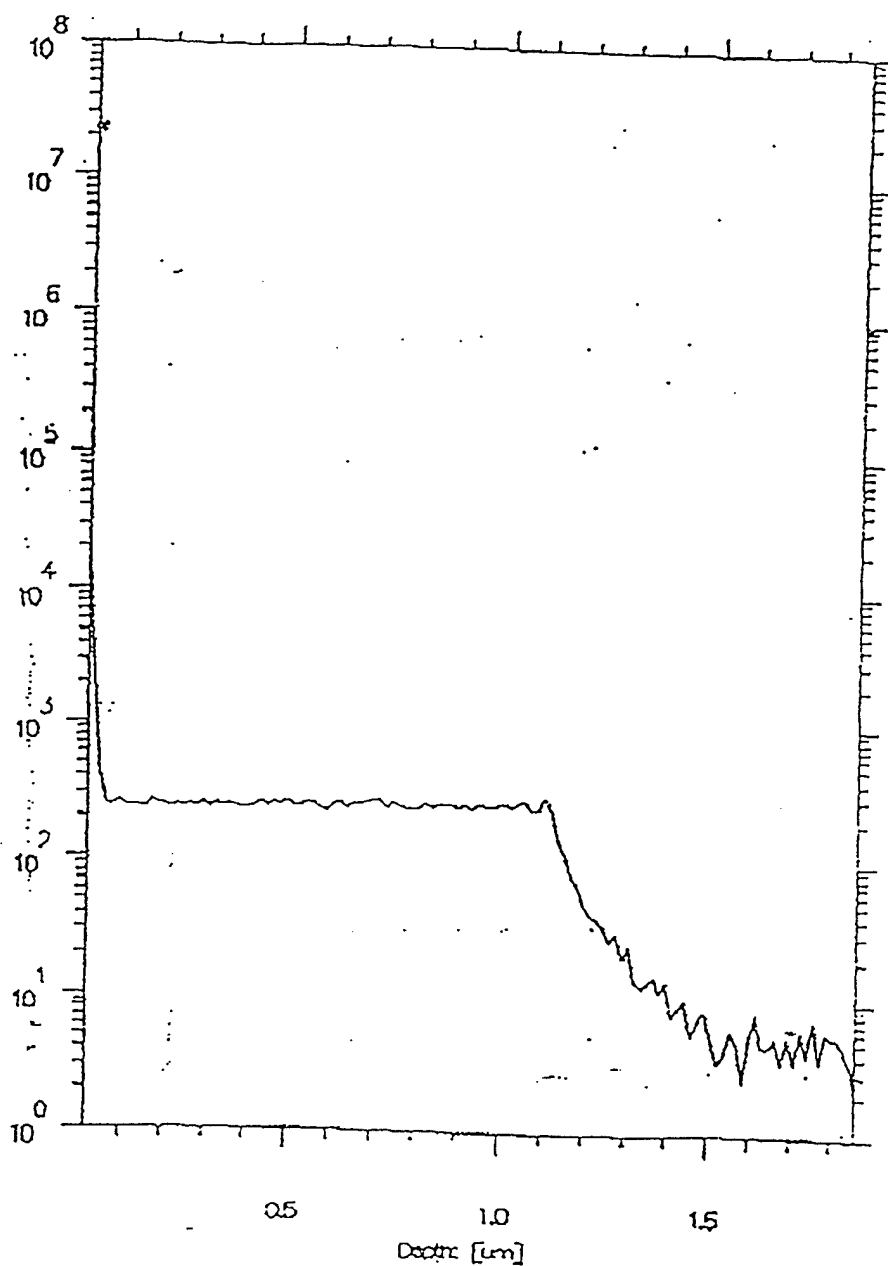


Fig. 3.10 CV profile for 6H.



$\frac{1.9}{1.5} = 1.7 \pm 12\%$

Fig. 3.11. Uncalibrated SIMS data for 4H.



2.3 ± 0.2

Fig. 3.12. Uncalibrated SIMS data for 6H.

## 4. VELOCITY FIELD DATA

Chapter 4 will present the data taken from the electrical setup described in the previous chapter. This will be followed by a discussion of the data. Adjustments to the measuring technique will be discussed next. The chapter will finally conclude with the errors associated with the measurement process and a method developed to determine the validity of the velocity field data.

### 4.1 Initial Velocity Field Data

The procedure for measurement has already been described in Chapter 3, Section 3.1. Essential points will be restated here again. Firstly, note that the inner two probes of the scope measure the voltage across the channel. The field is then simply obtained by dividing the voltage with the channel length. Secondly, the current through the channel is monitored through one of the probes of the oscilloscope (see Fig. 3.1). Figure 4.1 is the plot of the current through the channel as a function of time and the field across the channel. As can be seen from the plot, the current through the channel increases linearly up to a certain value of the field, indicating linear ohmic characteristics. After a certain field the increase in the current level is not linear with the increase in voltage. Non-ohmic characteristics of the channel implies that the velocity of the carriers (electrons) is not linearly related to the applied electric field. Note that at these high fields there is no increase in the current level with time. An increase in current with time was experienced by Bray during his conductivity experiment on germanium [20]. The effect was erroneously interpreted as negative temperature dependence of resistivity. After careful investigations by Ryder and Shockley, they explained the increase in current due to excess injection of holes from the contact [21]. Conductivity modulation can occur if the metal contacts are in close proximity of high fields. By physically placing the ohmic contacts further from regions of high field, in this case being the channel, conductivity modulation can be avoided.

From Fig. 4.1, at higher fields the current begins to fall as a function of time. Current degradation due to heating of the channel at these high fields and current levels is a probable explanation. For extracting the velocity of the carriers, the magnitude of the current is required. For low fields, the current is constant as a function of the time, but at high fields the current is not a constant function of time. At these high fields the current



value corresponding to the earlier part of the pulse is considered, since this is the least affected by the heating transients. Once the value of the current is known, extracting the carrier velocity is accomplished by using the following relation

$$v = I/qntw$$

where  $I$  is current measured from the scope,  $q$  is the electronic charge,  $n$  is the carrier density obtained from the Hall analysis,  $t$  and  $w$  are the thickness and the width of the channel.

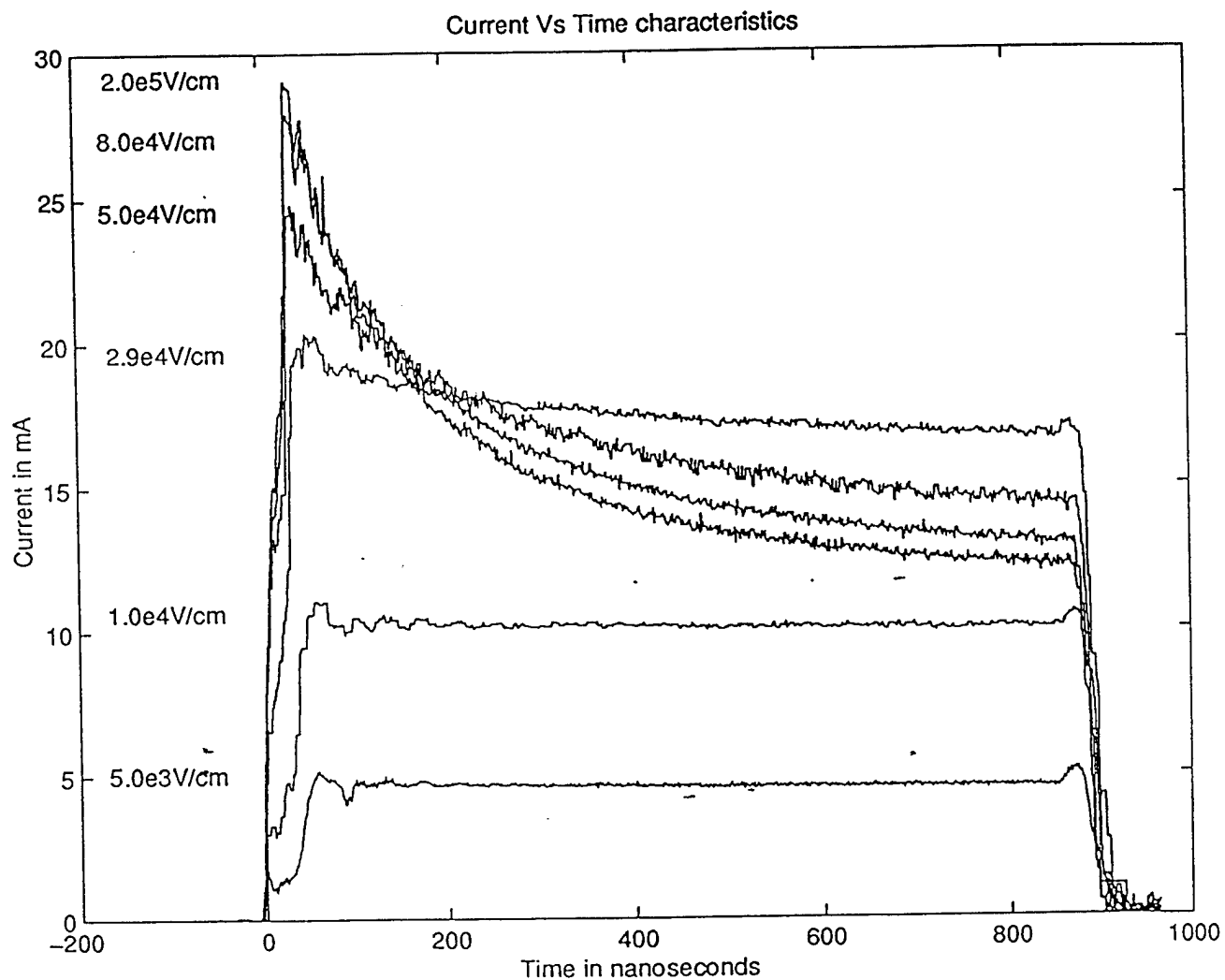


Fig. 4.1. Degradation of current through the channel (6H, 10x10 constriction) in the time domain for different voltages applied over the channel.

It is worth mentioning that the thickness of the channel corresponds to the thickness of the epilayer, and was verified with SIMS measurement. The width of the channel was verified with SEM pictures of the test structure. SEM pictures for each test structure were not taken, rather a number of measurements were taken on the same wafer and the average was computed. SEM pictures of the 5x5 and 10x10 channels are shown in Fig. 4.2. The table below contains the average values for the width and the length of the channels.

**Table 4.0**  
Average length and width of the channels.

Type of channel	Dimensions	6H	4H
5x5	length	4.69microns	4.37microns
	width	4.84microns	5.00microns
10x10	length	9.85microns	9.85microns
	width	9.38microns	9.38microns

Knowing all the parameters, the velocity of the electrons as a function of the applied field can now be obtained. Such a plot is shown in Fig. 4.3. Looking at the resulting plot the following observations can be made.

- At high fields there appears to be a negative differential mobility, as in gallium arsenide.
- The saturated drift velocity is not just dependent on the polytypes, but also on the channel dimensions. 5x5 and the 10x10 channels of the same polytype differ in their saturated drift velocities.

The mere discrepancy of data due to channel dimensions suggests that there is an error in the measurement procedure. Detailed investigations reveal the following errors.

- The effect of the voltage drop between the channel and the inner contact on the applied field is not negligible. The resistance between the channel and the inner contact is quite significant and is referred to as the "end resistance".
- At high fields, the heating transients are much larger, hence the current drops much quicker as a function of time. It will be shown in Section 4.3 that the present measurement setup was unable to monitor these quickly changing current levels.

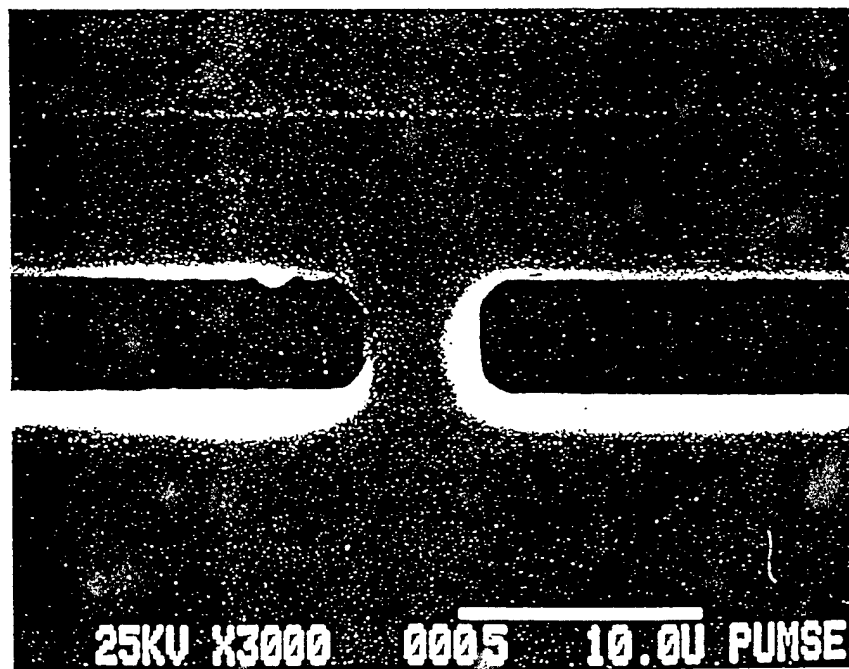
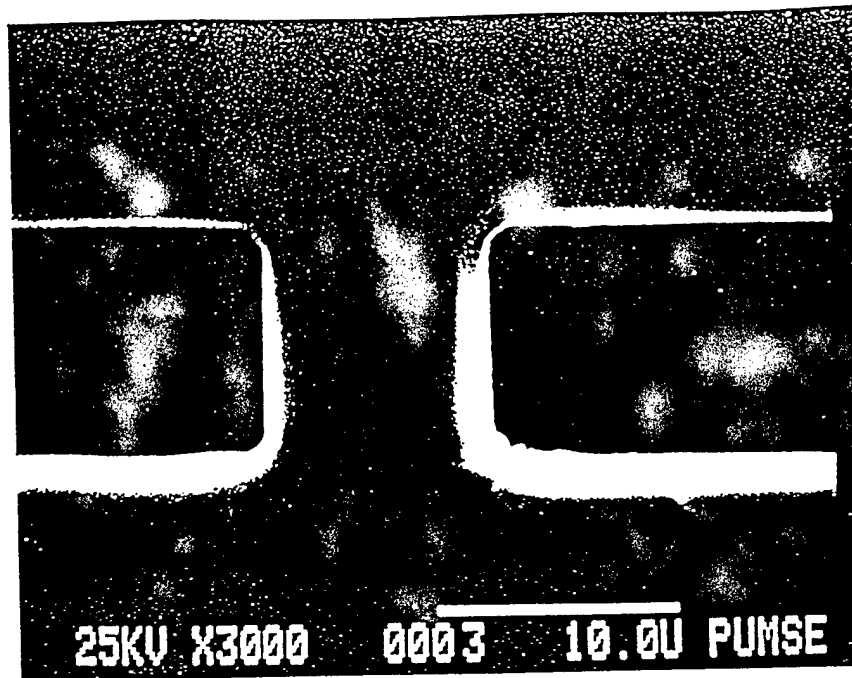


Fig. 4.2. SEM pictures of the 10x10 and 5x5 channels.

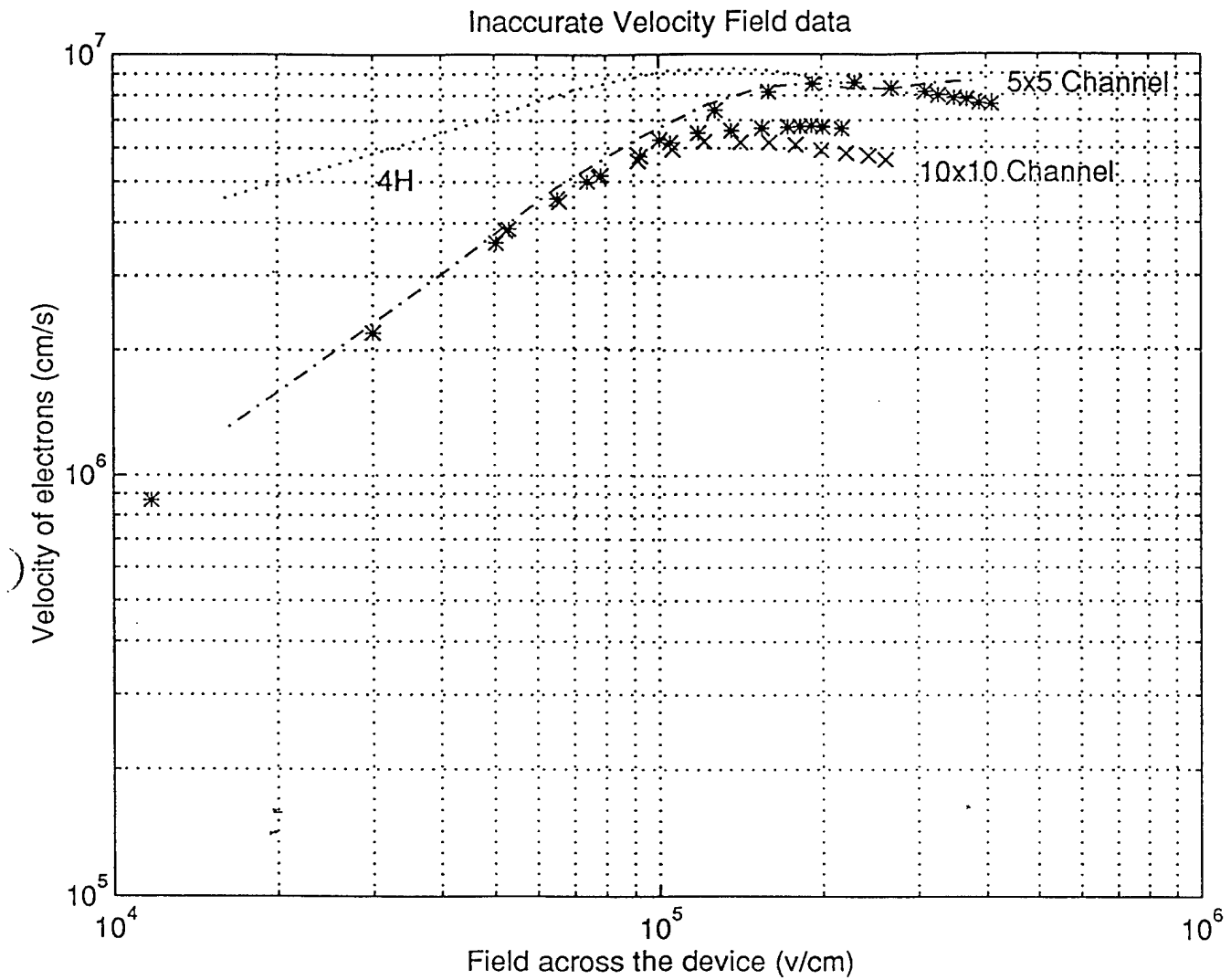


Fig. 4.3. Inaccurate Velocity-Field relationship for electrons in both 6H(\*) and 4H(all other symbols) SiC.

## 4.2 End Resistance

The end resistance correction will play a big factor in accurately determining the mobilities, the low field, and the high field velocity data for both the polytypes. End resistance originates from the current paths that exist as the electrons enter and exit the channel. Under the assumption that the bulk mobility of the electrons is isotropic, the current paths can be approximated by a trapezoid as shown in Fig. 4.4. The problem reduces to evaluating the resistance of this trapezoidal piece of semiconductor.

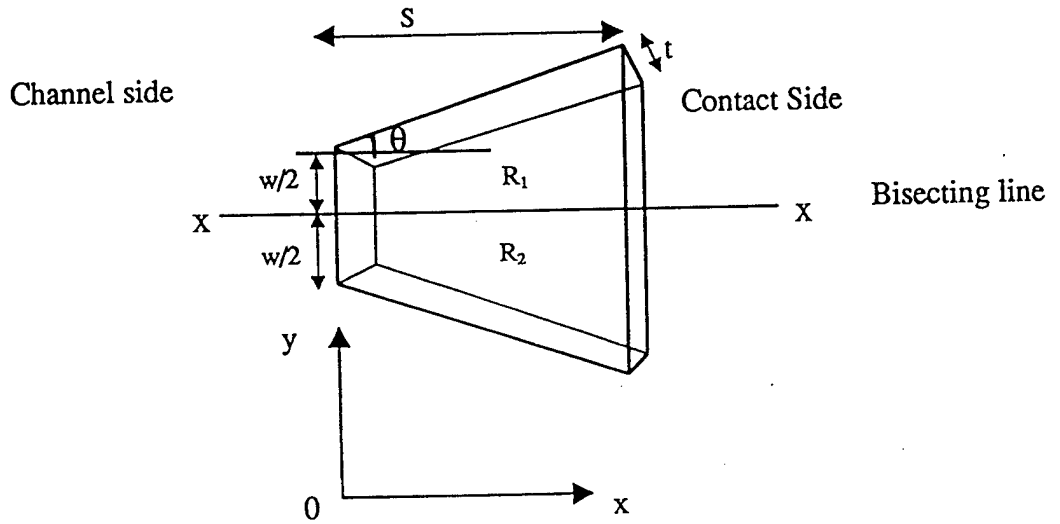


Fig. 4.4. Model used to compute the magnitude of the end resistance

Consider the block of semiconductor between the inner contact and channel, as shown above. Current flow is in the xy-plane. The resistance of half of the block is obtained by using the basic relationship for the resistor

$$dR_1 = \{\rho/t\} \{dx/(w/2 + \alpha x)\}$$

where  $R_1$  is the resistance of half of the block as shown above,  $t$  is the thickness of the block,  $w$  is the width of the block,  $S$  is the length,  $\theta$  is the spreading angle, and  $\alpha = \tan\theta$ . By integrating the right side from 0 to  $S$  we obtain the resistance.

$$R_1 = (\rho/t\alpha)\ln(1 + 2\alpha S/w) = R_2$$

Total resistance of the block is given by

$$1/R_E = 1/R_1 + 1/R_2$$

Hence the following relation gives  $R_E$  the end resistance

$$R_E = (\rho/2t\alpha)\ln(1 + 2\alpha S/w)$$

With isotropic mobilities, the angle  $\theta$  is  $45^\circ$  hence  $\alpha = 1$ . The width of the block corresponds to the width of the channel. SEM pictures were used to measure the spacing between the channel and the metal contact. The average measured values are presented below.

**Table 4.1**  
List of the average spacing between the inner contact and the constriction

Channel type	6H	4H
10x10 Spacing	10.00 microns	10.00 microns
5x5 Spacing	13.12 microns	10.31 microns

The total resistance between the inner two contacts is the sum of the resistance due to the channel and the two end resistances (see Fig.4.5). The resistance of the channel is always greater than the end resistance. At high fields the resistance of the channel becomes non ohmic. The end resistance, in this development, is assumed to approach non ohmic characteristics in the same manner. If  $V_m$  is the voltage measured between the contacts, then the field on the channel is given by

$$E = \{V_m/L\} \{R/(R+2R_E)\}$$

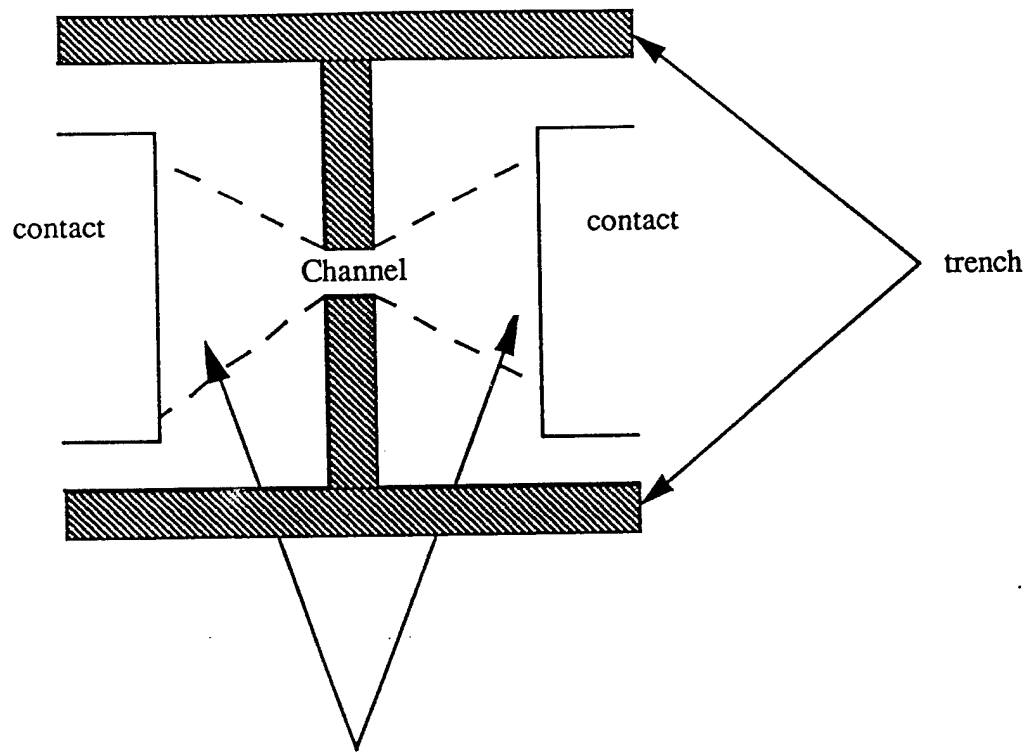
It is easy to see that the end resistance provides a correction factor for the measured field over the channel.

$$R/(R+2R_E) = 1/\{1+(w/l)\ln(1+2S/w)\} \quad (4)$$

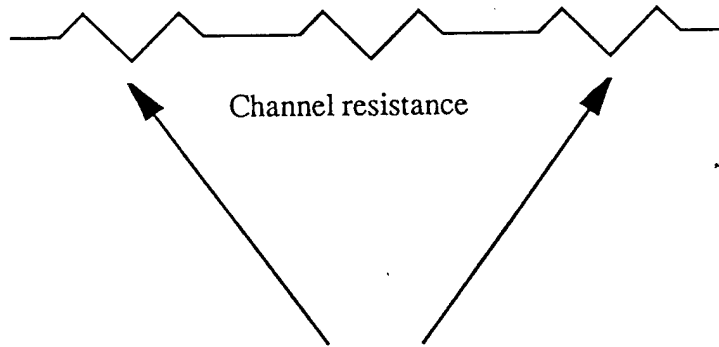
The table below shows the computed correction factors.

**Table 4.2**  
Computed correction factors for the two polytypes.

Channel type	6H	4H
5x5	0.392	0.412
10x10	0.486	0.486



Current Spreading



End Resistance due to current spreading

Fig. 4.5. Shows the current spreading around the channel and subsequently the end resistance correction required to account for this voltage drop.



### 4.3 Measurement Setup Revisited

The errors resulting from the pulsed four-probe method were subtler. As pointed out earlier, the high field data showed dependence on the channel dimensions. Greater heating transients caused the current and hence the velocity of the electrons to go down sharply with time. With the four probe measurement, there is probe-to-probe, and intrinsic probe capacitance. This capacitive network serves as a low pass filter. The filter dampens the magnitude of the high frequency components of the current pulse. The sharply decaying current level, often appearing as a current spike, primarily consists of very high frequency components. Thus the low pass filter prevents the scope from detecting the earlier part of the current pulse. By removing the two inner probes this problem was minimized. However, due to their removal the voltage over the channel cannot be monitored. The problem is further compounded by the non-ohmic contacts. The knowledge of the contact resistance can enable the determination of voltage drops adjacent to the channel. It is important to note that the four-probe measurement can be done at low fields. The heating transients are much less, hence the current level doesn't fall sharply in the time domain. This fact is highly useful, since it allows for the voltage-current characterization of the regions containing the non-ohmic contacts at low fields. This voltage drop versus current information, at low fields, can then be extrapolated to higher fields. Figures 4.6 and 4.7 help in illustrating the process. Specifically, the current-voltage characteristics between I1-I2, and I3-I4 are obtained at low fields. At higher fields the probes on I2 and I3 have to be removed. To obtain the voltage drop between I1-I2 and I3-I4, the voltage data obtained from lower currents is extrapolated to higher current levels. In essence, a lookup table is established for each test structure. This enables the determination of the voltage drops adjacent to the channels for a given value of the current. By subtracting these voltage drops from the total voltage, and multiplying the result by the correction factor, the field over the channel is obtained.

Four-probe measurement could be used for fields up to  $3 \times 10^4$  V/cm. Beyond this field two-probe measurement was used. After these adjustments, the velocity field data of the electrons did not manifest variations due to the difference in the dimensions of the channel.

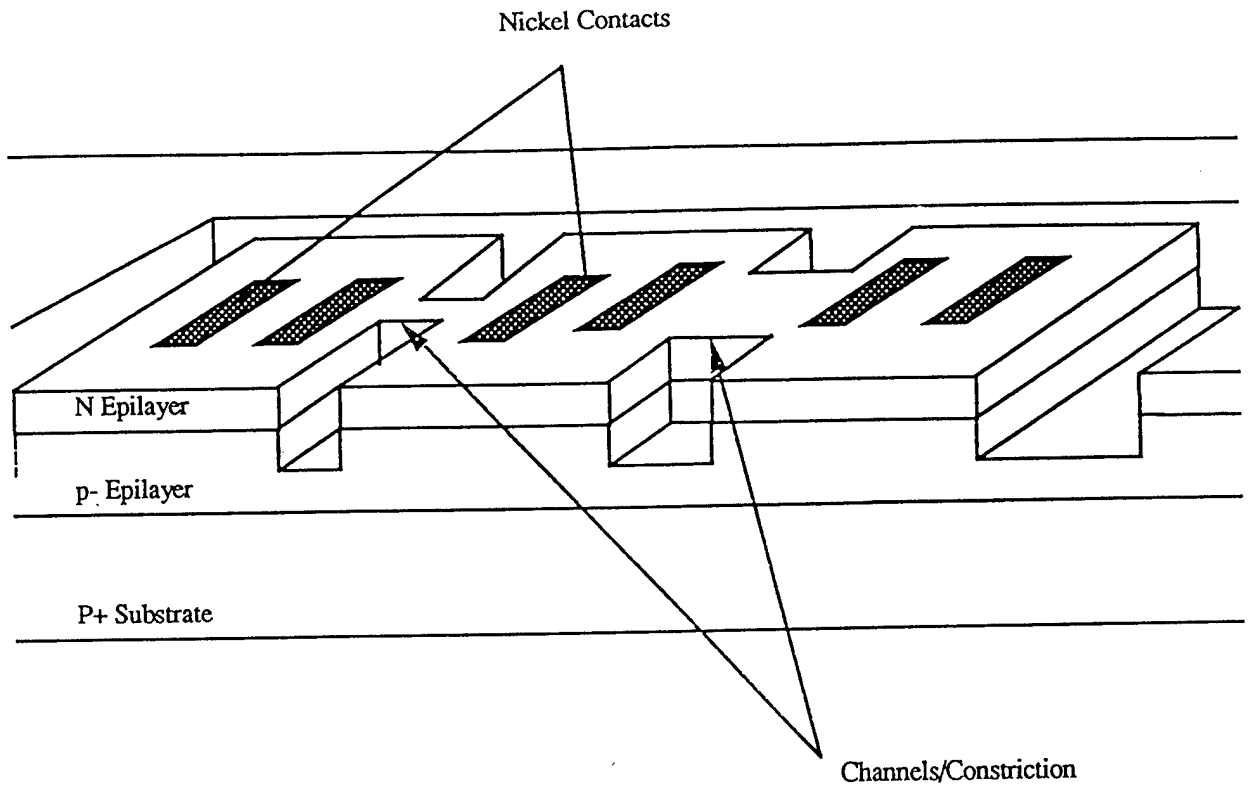


Fig. 4.6 Isometric view of the test structure

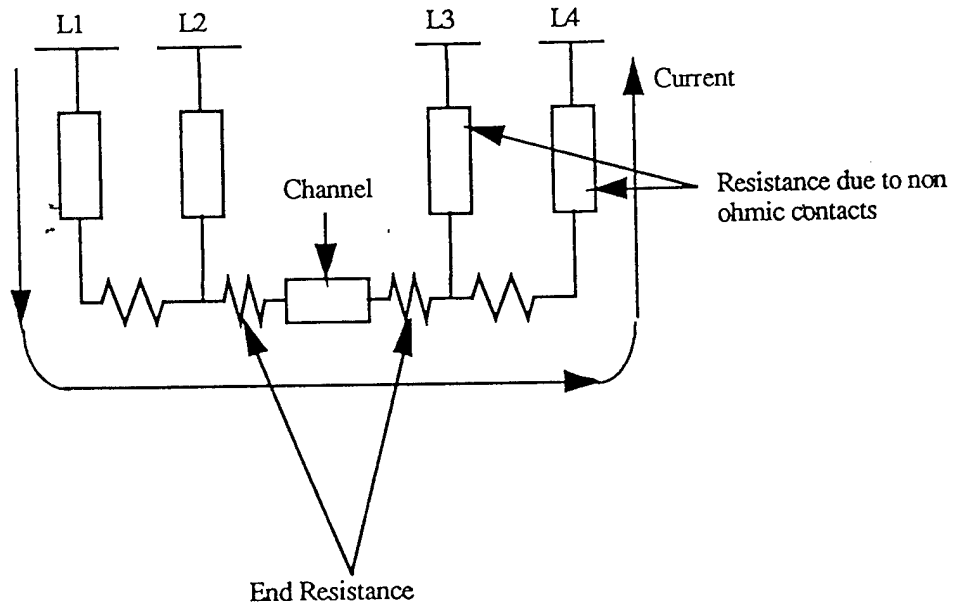


Fig.4.7. The various components over which the voltage drop needs to be subtracted from the applied voltage in order to determine the field over the channel.

#### 4.4 Depletion Region

Depletion of the channel reduces the total number of carriers in the channel. This depletion region results from the reverse bias of the pn junction, as explained in Section 2.0. To obtain the change in the carrier concentration, numerical calculations were done. The abrupt pn junction model was used to obtain the spreading of the depletion region into the channel for a given applied voltage. The depletion region at the ground end was assumed to be negligible (see Fig. 2.1). Linear voltage drop over the channel is assumed

$$\psi = Ex \quad (5)$$

where  $\psi$  is the voltage,  $E$  is the field over the channel, and  $x$  is the distance from the ground (Fig. 2.1). From (3), the depletion region into the n-channel is given by

$$w = [2\epsilon_s \psi N_a / e N_d (N_d + N_a)]^{1/2} \quad (6)$$

Substituting (5) into (6), and integrating from 0 to  $l$  gives

$$a = [2\epsilon_s E N_a / e N_d (N_d + N_a)]^{1/2} (2/3) l^{3/2} \quad (7)$$

where  $a$  is the area of the depletion region in the channel, and  $l$  is the length of the channel. The new carrier density of the channel is

$$n_d = (1-r)N_d \quad (8)$$

where

$$r = \frac{a}{l * t} \quad (9)$$

and  $t$  is the thickness of the channel. From (2), the correct drift velocity of the electrons is then

$$v = \frac{1}{1-r} v \quad (10)$$

#### 4.5 Velocity Field Data

The experimental velocity field data, adjusted for end resistance and the depletion region, is shown in Fig. 4.8 for 4H SiC, and Fig. 4.9 for 6H SiC. The linear plots are shown in Figs. 4.10 and 4.11 for 4H and 6H respectively. Figs. 4.12 and 4.13 illustrate the change in the velocity of the electrons when the depletion correction is made, while Fig 4.14 plot the values for  $r$  as function of field for 4H and 6H respectively. The highest saturated drift velocity of the electrons measured in 6H was about  $1.8 \times 10^7$  cm/s and about  $1.7 \times 10^7$  cm/s in 4H SiC. The highest fields observed before the channel breakdown were about

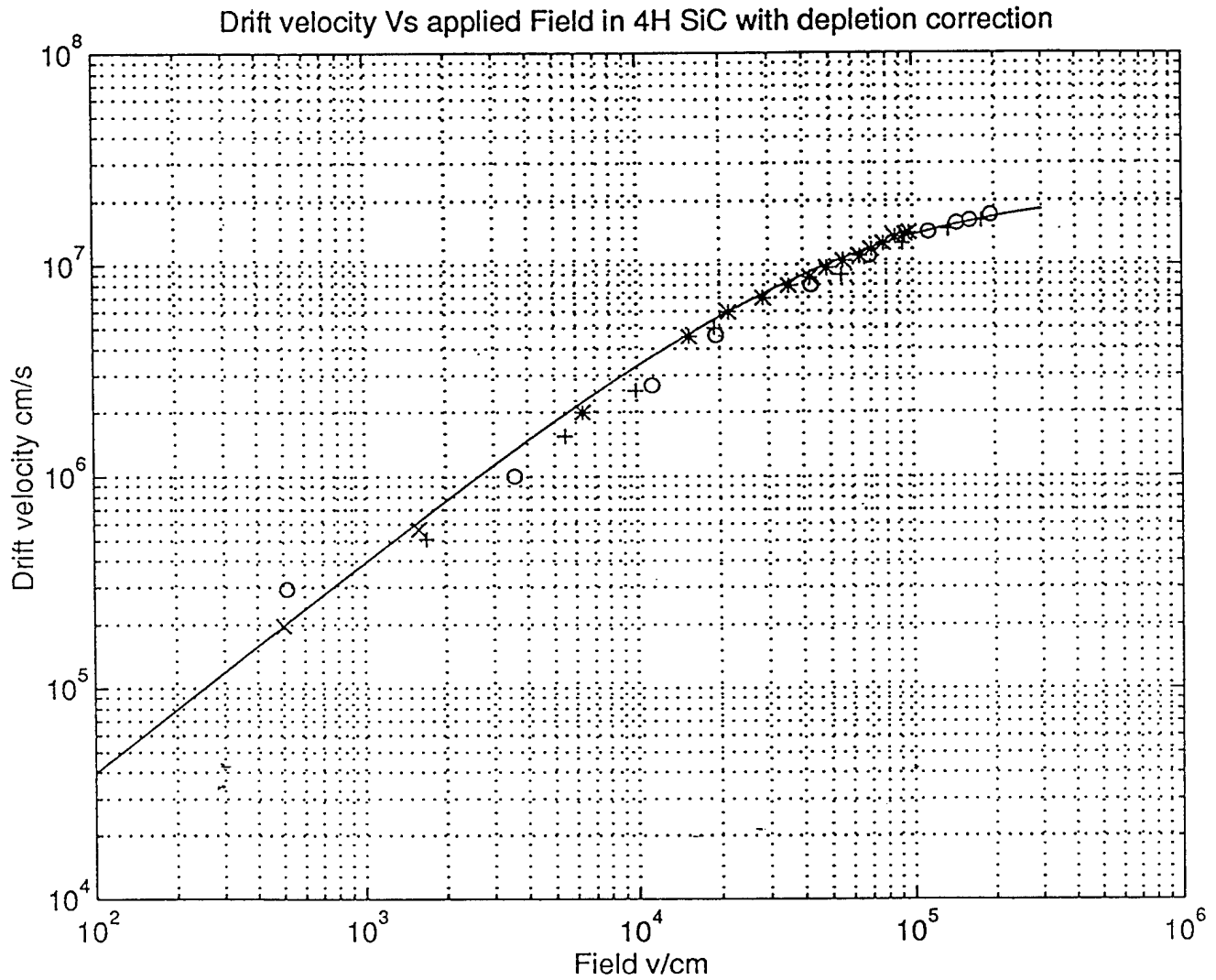


Fig. 4.8. Velocity Field relationship in 4H SiC. Solid line, best fit to data using equation (11). Circles represent data from 5x5 channels the rest from 10x10 channels.

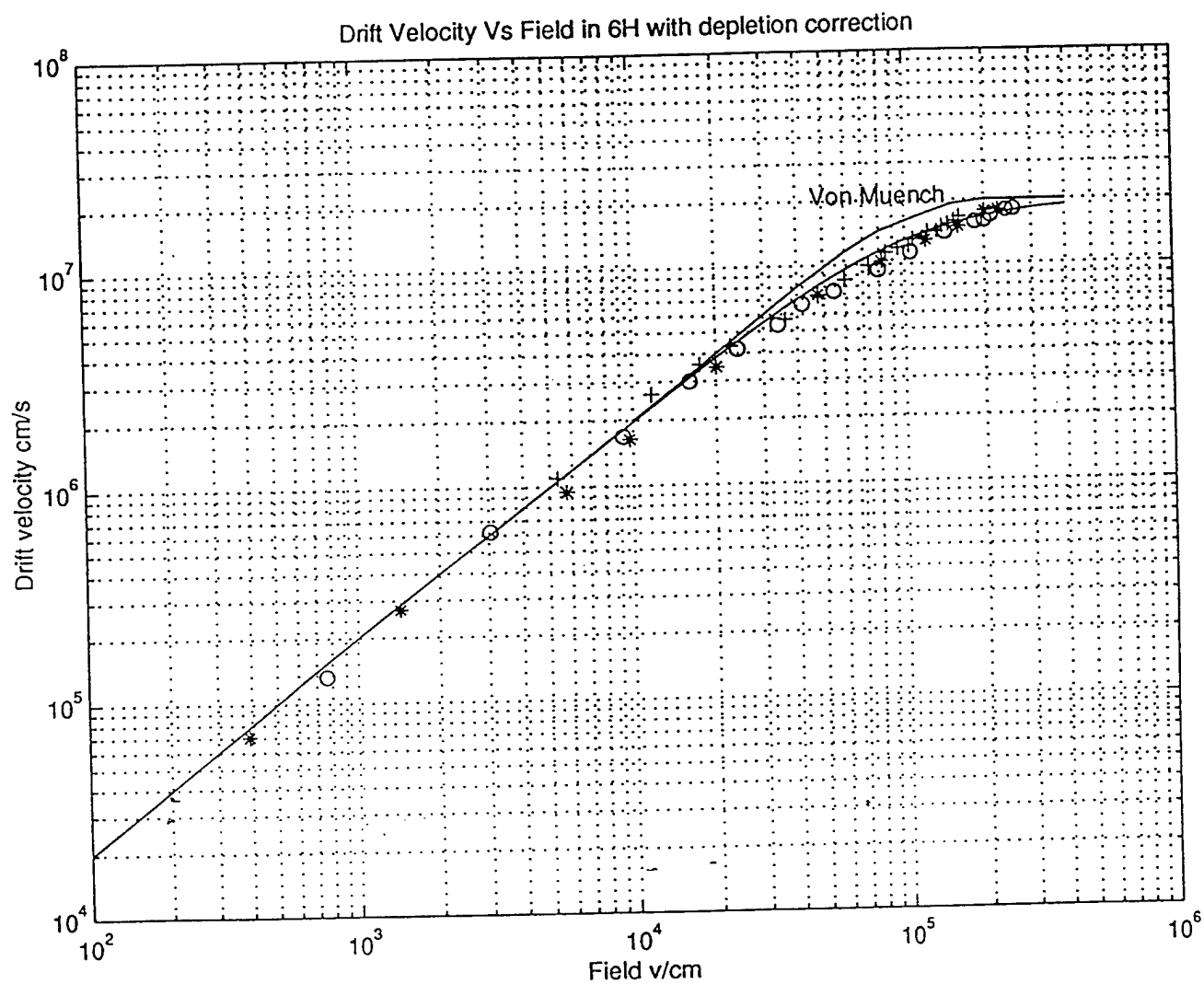


Fig. 4.9. Velocity Field relationship in 6H SiC. Solid line, best fit to data using equation (11). Circles represent data from 5x5 channels and the rest from 10x10 channels.

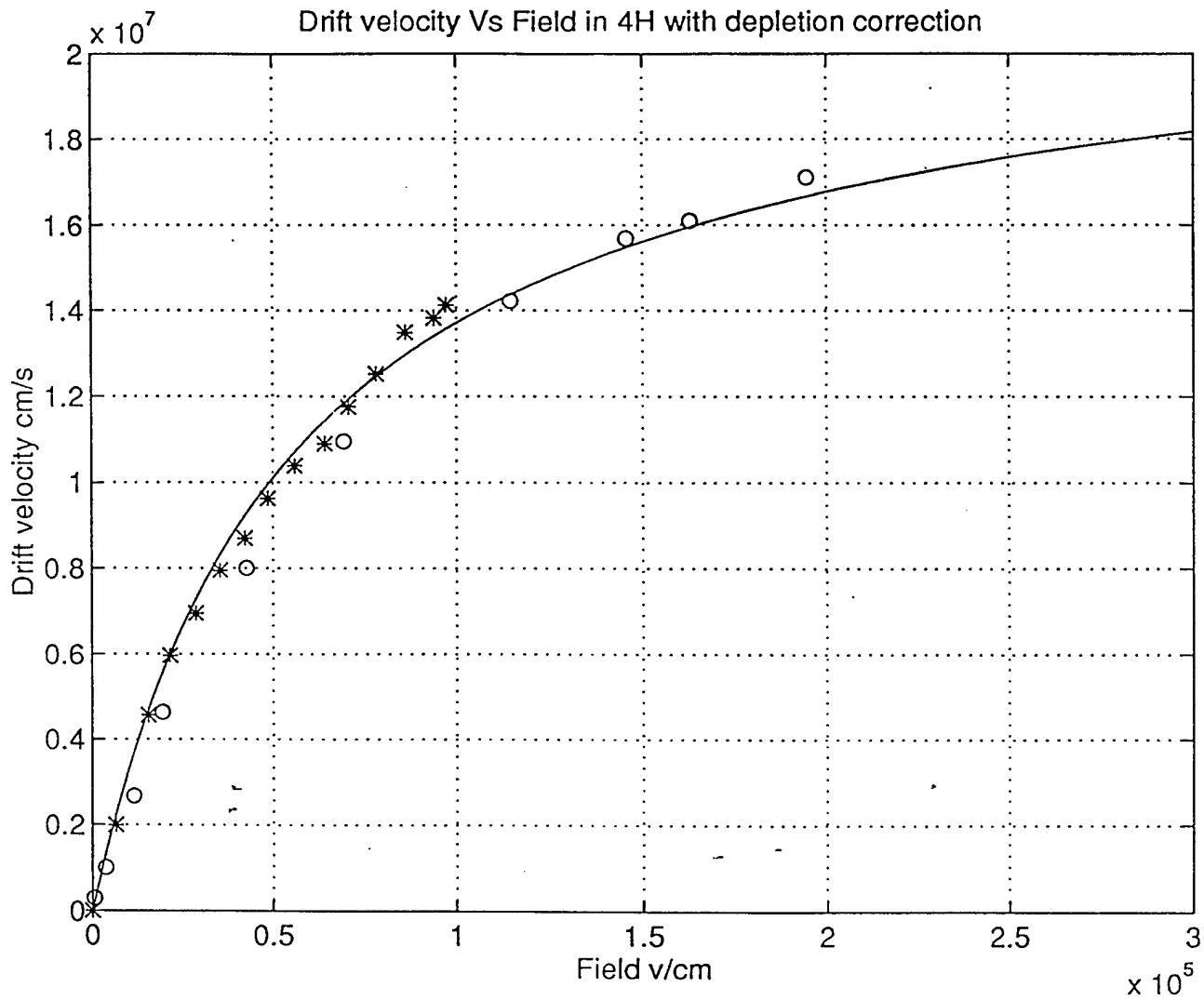


Fig. 4.10. Velocity Field relationship in 4H SiC. Solid line, best fit to data using equation (11). Circles represent data from 5x5 channels the rest from 10x10 channels.

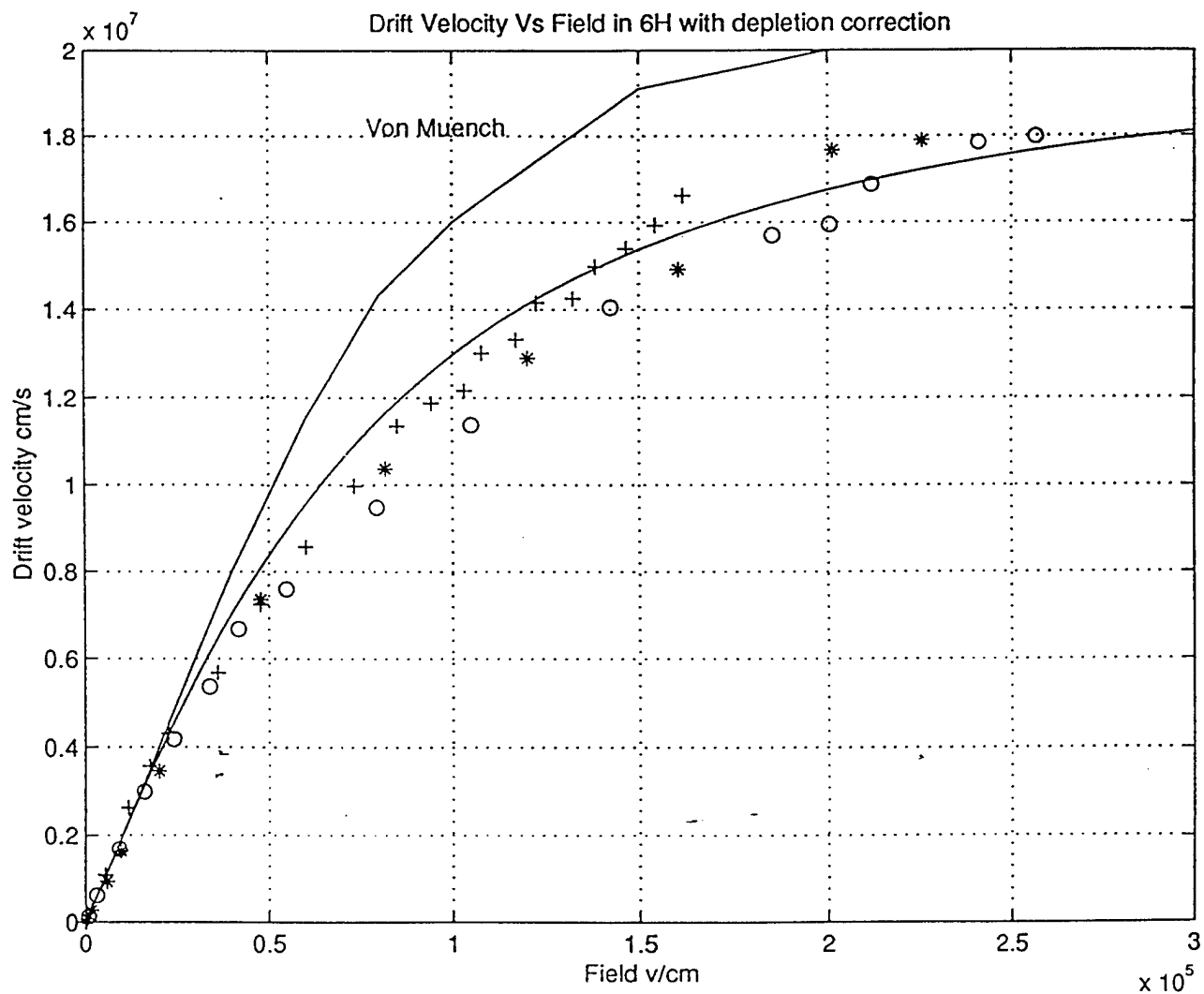


Fig. 4.11. Velocity Field relationship in 6H SiC. Solid line, best fit to data using equation (11). Circles represent data from 5x5 channels and the rest from 10x10 channels.

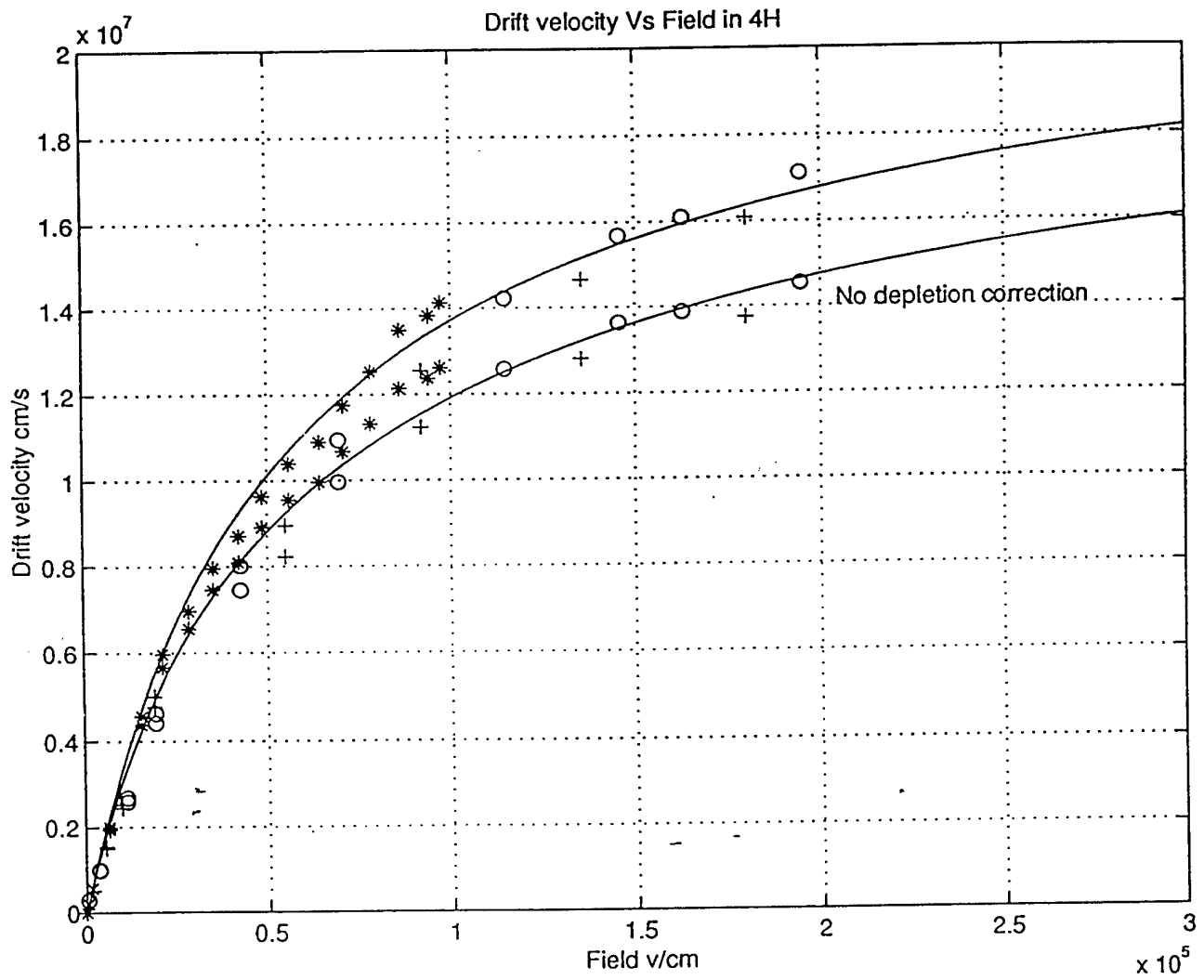


Fig. 4.12. Velocity Field relationship in 4H SiC with no depletion correction. Solid line, best fit to data using equation (11). Circles represent data from 5x5 channels the rest from 10x10 channels.



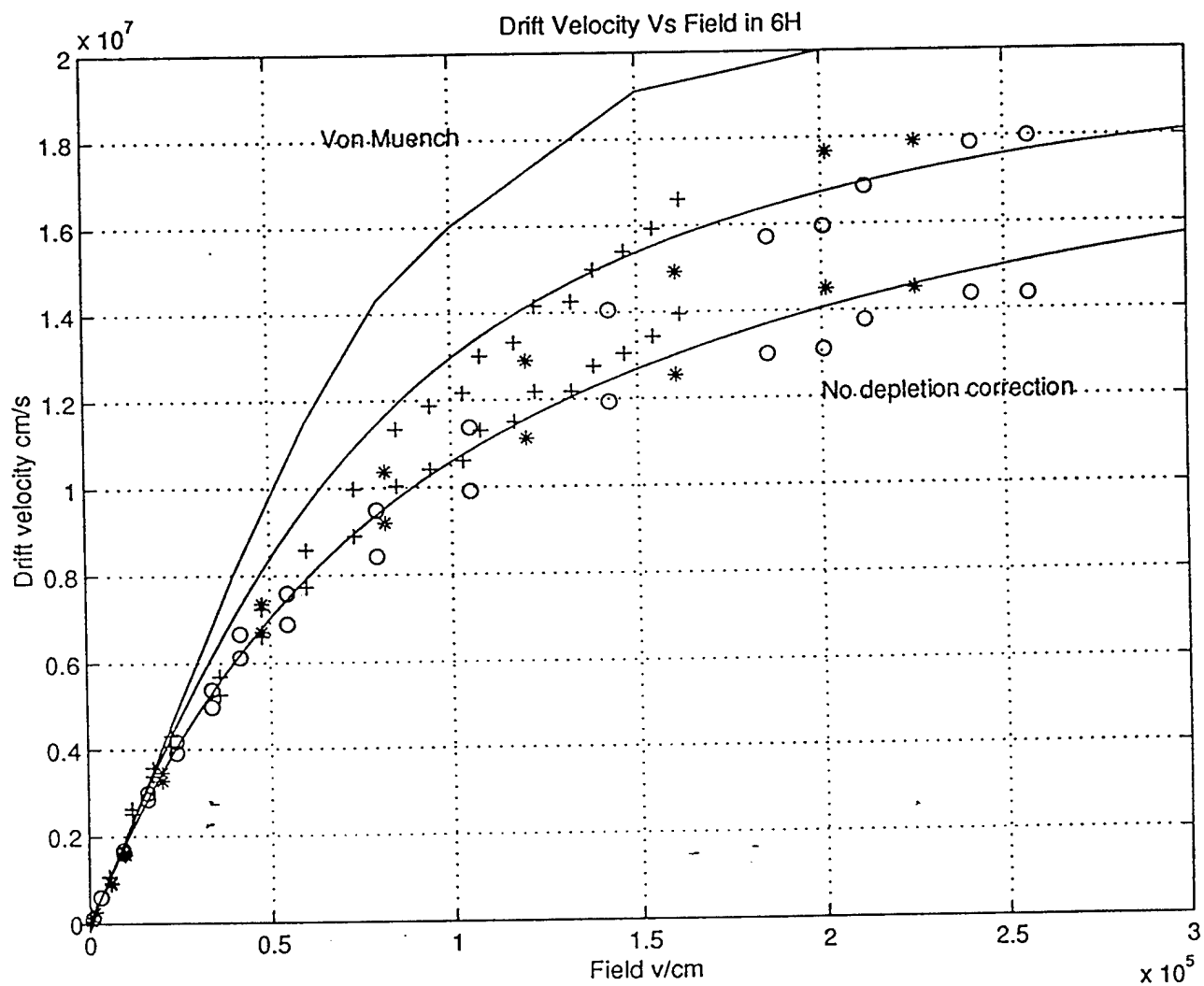


Fig. 4.13. Velocity Field relationship in 6H SiC with no depletion correction. Solid line, best fit to data using equation (11). Circles represent data from 5x5 channels and the rest from 10x10 channels.

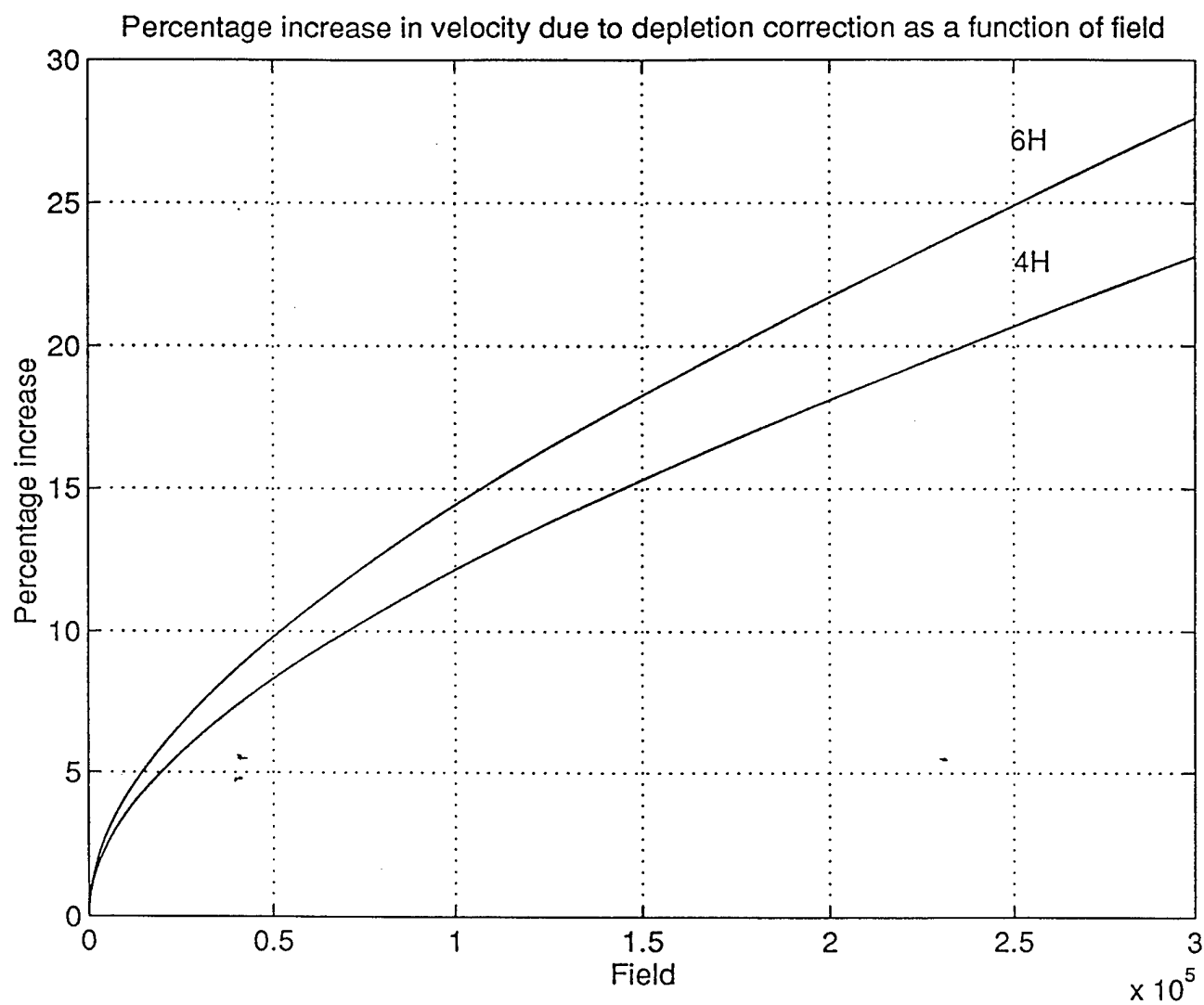


Fig. 4.14. Plot of the percentage increase in velocity ( $100 \cdot r / (1-r)$  of (9)) as a function of applied field.

of electrons measured in 6H(4H) was about  $1.8 \times 10^7$  cm/s ( $1.7 \times 10^7$  cm/s). The highest fields observed before channel breakdown were about  $2.6 \times 10^5$  V/cm. At these high fields, sharp increases in the current level sporadically located through the pulse were observed on the oscilloscope. These sharp increases in the current level are primarily due to breakdown of the channel. Fluorinert was used to cover the structure and the probe tips. It has a breakdown field of  $1.7 \times 10^5$  V/cm, much higher than air[22]. With further pulsing the channel, at these high fields, the spikes begin to dominate the current pulse. Upon examination of the channel, a burnt track usually in the middle of the channel is observed. Impact ionization, resulting in increase in the number of carriers, can probably explain the increase in current[23]. Due to the large power densities, overheating of the channel can cause it to burn. Similar burnt tracks were also observed by Gunn during his conductivity experiment on germanium[11]. He explained the breakdown mechanism due to material thermal instability.

The experimental velocity-field data were fit with the following empirical relation

$$v(E) = \mu E / \{1 + (\mu E / v_s)^\alpha\}^{1/\alpha} \quad (11)$$

where  $v$  is the velocity of the carrier,  $E$  the electric field,  $\mu$  is the mobility,  $v_s$  is the saturated drift velocity of the carriers and  $\alpha$  is the dimensionless fitting parameter. Table 4.3 below shows the best fitting parameters for Figs. 4.8 and 4.9. Table 4.4 shows the fitting parameters for Figs. 4.12 and 4.13 (no depletion correction).

**Table 4.3**  
List of parameters used in the empirical relation for Figs. 4.8 and 4.9.

	4H	6H
$\alpha$	0.95	1.6
$\mu$	400 cm <sup>2</sup> /vs	200 cm <sup>2</sup> /vs
$v_s$	$2.2 \times 10^7$ cm/s	$2.3 \times 10^7$ cm/s

**Table 4.4**  
List of parameters used in the empirical relation for Figs. 4.12 and 4.13.

	4H	6H
$\alpha$	0.825	1.09
$\mu$	400 cm <sup>2</sup> /vs	200 cm <sup>2</sup> /vs
$v_s$	$2.08 \times 10^7$ cm/s	$2 \times 10^7$ cm/s

The only other determination of the saturated electron drift velocity was done by von Muench and Pettenpaul in 1977. Figure 4.9 shows their data superimposed on our present velocity field data. They utilized the same conductivity technique, and obtained a saturated drift velocity of  $2 \times 10^7$  cm/s on 6H epilayers. This is slightly higher than the present measurements. The mobilities measured on these epi layers are slightly lower than those reported by Cree for similar dopings.

## 5. CONCLUSION AND RECOMMENDATIONS FOR FUTURE WORK

### 5.1 Conclusion

The final velocity field data for electrons, in the basal plane perpendicular to the c-axis, in both 4H and 6H SiC is presented. Essentially, the experiment conducted by von Muench and Pettenpaul on the velocity field relation of electrons in 6H SiC is repeated on epilayers grown over substrates grown by the modified sublimation process. New data has been measured on the velocity field relationship for electrons in 4H SiC. In performing these experiments, various pitfalls and non-ideal effects were discovered.

The major subtle pitfall encountered, in these experiments, were the heating transients. Eradication of this problem, as outlined in Section 4.3, utilized a combination of short high voltage pulses and probing techniques. Non ohmic contacts required careful extrapolation of the current voltage data to subtract the contact resistance.

The end resistance correction, as outlined in Section 4.2, was of great importance in determining accurately the field over the channel. The metallurgical junction between the n epilayer and the p epilayer creates a depletion region in the channel when high positive voltages are applied to the n epilayer. A simple mathematical method is used, as presented in Section 4.4, to incorporate the reduction of the number of free carriers when extracting the value of the velocity of electrons from the current flowing through the channel.

### 5.2 Future Recommendations

The corrections and extrapolations mentioned above do however introduce some errors in the data and furthermore, the difference between v. Muench and Pettenpaul data and the present results suggests that further studies on the velocity field relationship are required. A different approach, preferably time of flight technique, could be used to study the high field electron transport in silicon carbide. Accurate determination of the carrier concentration and end resistance effects are eliminated in the time of flight technique when compared to the conductivity measurement.

Within the domain of conductivity measurement, a uniform slab of semiconductor with contacts at both ends can be used in the future instead of the dumb bell structures used in this experiment. With such a structure the uncertainties in the voltage drop due to the

spreading resistance is avoided. Gunn used a similar structure in his conductivity experiment on germanium. Fabricating such a uniform piece of semiconductor from epilayers with sizable contacts might present other challenges. For instances, channels with bigger cross sectional area will require bigger systems to provide higher instantaneous power. Furthermore, the heating transient effects will be more prominent at these higher power levels.

Improvements can be made to the present measurement technique. The itemized list below highlights the various points.

- (i) The correction factor (4), due to the end resistance, can be brought closer to unity by reducing the spacing  $S$  and the width  $W$ , while increasing the length of the channel. Figure 5.1 shows the plot of (4) for varying length and width dimensions. The effect of these variations on the correction factor is shown in Fig. 5.2.
- (ii) Thicker epilayers can ensure that the fractional effect (10) of the depletion extension into the channel, resulting in the change in the carrier concentration, is to a minimum. Performing the conductivity experiment on  $n$  epilayers that are grown on fully insulating material will eradicate the depletion region from the channel.
- (iii) Errors due to the non ohmic contacts can be eliminated by incorporating a high dose implantation step.

There is no data on the velocity field relation of holes in both 4H and 6H SiC. Similar experiments, as outlined in this thesis, can be done on  $p$  epilayers. An added complexity with these experiments, will be the low activation rate of holes and its sensitivity to temperature. Due to the heating transients, there can be a substantial change in the number of free carriers.

Finally, particularly important to devices that utilize vertical FETs, there is no experimental data available on the velocity field relationship of electrons and holes in 4H and 6H SiC parallel to the  $c$ -axis. Conductivity experiments can be done to determine the velocity field relationship of electrons and holes parallel to the  $c$ -axis.

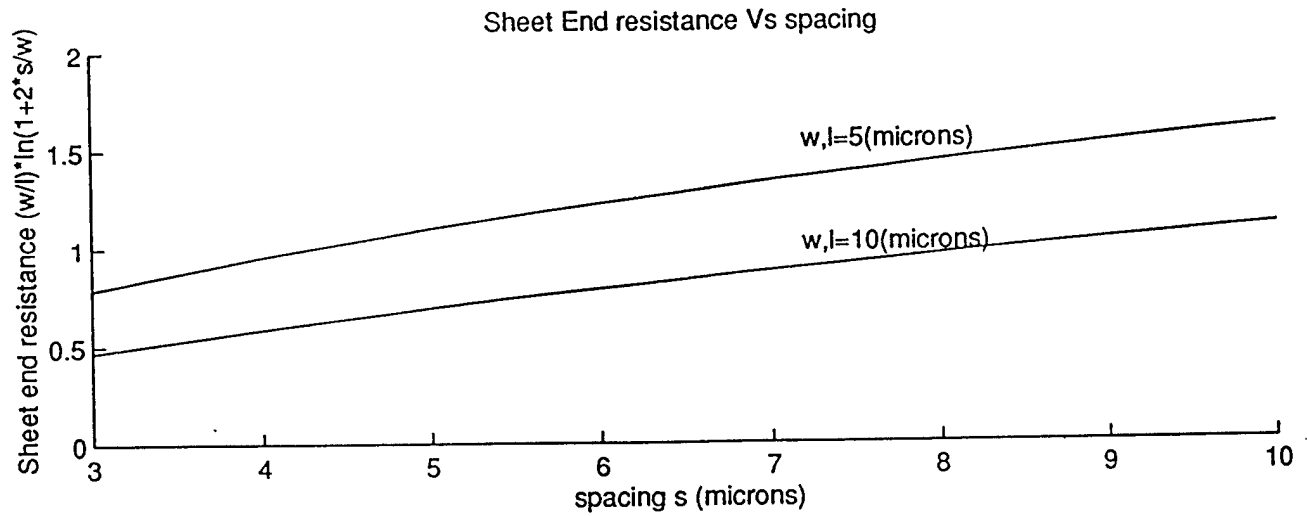


Fig. 5.1. Variation of end resistance with width and length of the channel for a given spacing.

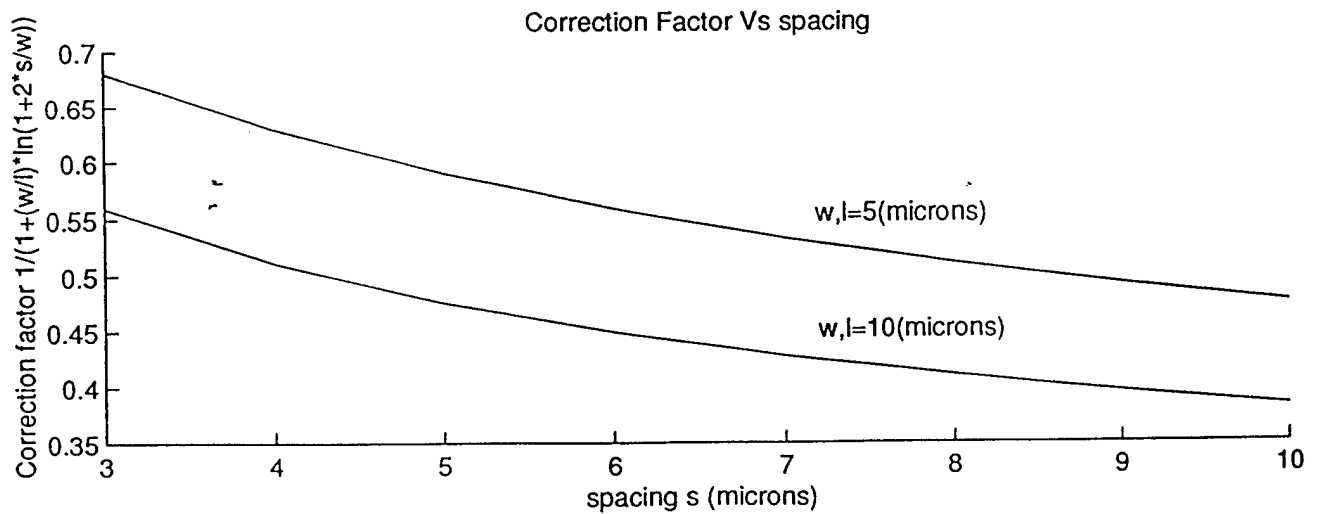


Fig. 5.2. Variation of correction factor with width and length of the channel for a given spacing.

## REFERENCES

- [1] E.O. Johnson, "Physical limitation on frequency and power parameters of transistors" RCA Rev. No. 26, 1965, Pg.163.
- [2] D. K. Ferry, "Figure of Merit for Semiconductors for High-Speed Switches," Rev. no. 312, 1975, Pg.2361.
- [3] W. v. Munech and E. Pettenpaul, "Saturated electron drift velocity in 6H SiC," J. Appl. Phys, Vol. 48, No.11, Nov 1977, Pg. 4823.
- [4] R. F. Pierret G. W. Nuedeck, "Semiconductors Fundamentals," Vol 1, *Solid State Series* 2nd Ed, Addison-Wesley, 1989,Pg.64.
- [5] D. K. Schroder, *Semiconductor Material and Device Characterization*, John Wiley & Sons, 1990, Pg. 223-224.
- [6] C. Jacoboni, C. Canali, G. O. Hanain, and A. A. Quaranta, "A review of some charge transport properties in Si," *Solid State Electron*, No.20, 1977, Pg. 77.
- [7] W. Heinle, "Determination of current waveform and efficiency of Gunn diodes," *Electron. Lett.*, vol 3, 1967, Pg.25.
- [8] M. Martin, J. W. Mayer and K. R. Ziano, *Applied Solid State Science*, (edited by R. Wolfe) Vol 3, Academic, New York, 1972.
- [9] W. Shockley, "Hot electrons in Germanium and ohms laws," *Bell System Tech J.* 30, 1951, Pg. 990.
- [10] E. J. Ryder, "Mobility of Holes and Electrons in High Electric Fields," *Physical Review*, Vol. 90, No. 5, 1953, Pg. 766.
- [11] J. B. Gunn, "The field dependence of Electron Mobility in Germanium," *J. Electronics*, No.2, 1956, Pg.87.
- [12] G. W. Neudeck, "The PN Junction" *Solid State Series* Vol 2, 2nd Ed, Addison-Wesley, 1989, Pg. 34.
- [13] M. Hatzakis, B. J. Cassavello, J. M. Shaw, "Single-step Optical Lift-off Process," *IBM J. Res. Develop.*, Vol 24, No.4, July 1980.
- [14] W. Shockley, A. Goextxberger, and R. M. Scarlett, "Research and Investigation of Inverse Epitaxial UHF Power Transistors," Rep No. AFAL-TDR-64-207, Air Force Avionics Lab., Wright-Patterson Air Force Base, OH, Sept. 1964.



- [15] D. K. Schroder, *Semiconductor Material and Device Characterization*, John Wiley & Sons, 1990, Pg. 116-117.
- [16] E. H. Putley, "The Hall Effect and Related Phenomena," Butterworths, London, 1960; "The Hall Effect and its application," *Contemp Phys.*, No.16, March 1975, Pg.101-126.
- [17] D. K. Schroder, *Semiconductor Material and Device Characterization*, John Wiley & Sons, 1990, Pg. 199-200.
- [18] Runyan, W.R. *Semiconductor Measurements and Instrumentation*, McGraw-Hill; NY, NY 1975.
- [19] D. K. Schroder, *Semiconductor Material and Device Characterization*, John Wiley & Sons, 1990, Pg. 210-211.
- [20] Ralph Bray, K. Lark-Horowitz and R. N. Smith, "Spreading Resistance Discrepancies and Field Effects in Germanium," *Phys. Rev.*, 72, Pg.530, 1947.
- [21] Ryder and W. Shockley, "Interpretation of dependence of resistivity of germanium on electric field," *Phys. Rev.*, No.75, Pg. 310, 1949.
- [22] Private communication with Jan Spitz.
- [23] S. M. Sze, *Physics of Semiconductor devices*, 2nd Ed, , John Wiley & Sons, -1981, Pg. 45.

**PART III. PAPER ON THE FINAL RESULTS OF THE EXPERIMENT**  
**(TO APPEAR IN THE FEBRUARY 2000 ISSUE OF *IEEE TRANSACTIONS***  
***ON ELECTRON DEVICES*)**

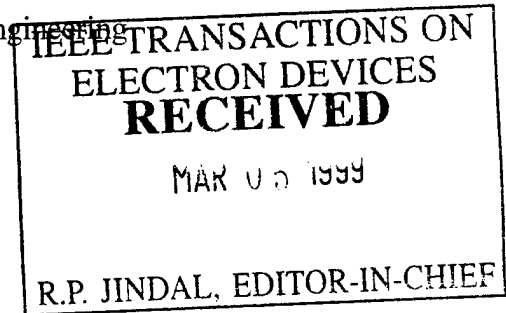
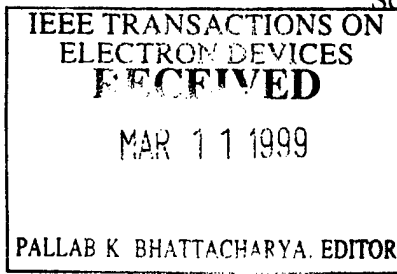
(5 pages)  
MS# 4326R

# Measurement of High-Field Electron Transport in Silicon Carbide

I. A. Khan and J. A. Cooper, Jr.

School of Electrical and Computer Engineering

Purdue University  
West Lafayette, IN



## Abstract

We report recent measurements of the drift velocity of electrons parallel to the basal plane in 6H and 4H silicon carbide (SiC) as a function of applied electric field. The dependence of the low field mobility and saturated drift velocity on temperature are also reported. The highest measured drift velocities at room temperature are  $1.8 \times 10^7$  cm/s in 6H-SiC and  $2.1 \times 10^7$  cm/s in 4H-SiC.

**Key words :** Drift velocity, saturation velocity, nonlinear transport.

## Introduction

Single crystal wafers of SiC grown by the modified sublimation process have only been commercially available since about 1990, and many of the fundamental electrical properties of SiC have not been fully characterized. This presents serious problems to device engineers, since it is difficult to predict the performance of device structures without knowledge of the basic electrical parameters.

One of the most important parameters is the relationship between the drift velocity of electrons and the applied electric field. At low fields, velocity increases linearly with field,  $v = \mu E$ , where  $\mu$  is the electron mobility. At higher fields the velocity increases

sublinearly with field, and at sufficiently high fields the velocity saturates. The first measurements of the high-field drift velocity of electrons in SiC were performed by v. Muench and Pettenpaul [1] in 1977 on Lely crystals of 6H-SiC. They reported an electron saturation velocity of  $2 \times 10^7$  cm/s parallel to the basal plane at room temperature. In this paper we present new measurements of the drift velocity of electrons in 6H-SiC and the first measurements of electron velocity in 4H-SiC, with data at both room temperature and elevated temperatures.

There are two general techniques of determining the drift velocity as a function of electric field: the conductance technique and the time-of-flight technique. The conductance technique is used by v. Muench and Pettenpaul [1], and is also employed in the experiments reported here. In this technique, the drift velocity of electrons is inferred from measurements of the conductivity of an n-type neutral region at high fields. The electron drift velocity is given by

$$v = \frac{I}{q w n t} \quad (1)$$

where  $I$  is the current through a region of width  $w$  and thickness  $t$ ,  $n$  is the electron density, and  $q$  is the electronic charge. Accurate determination of the drift velocity requires precise knowledge of the physical dimensions  $w$  and  $t$ , and the carrier density  $n$ .

### Device Fabrication

Test structures are fabricated on the (0001) face of 4H and 6H-SiC wafers obtained from Cree Research, Durham, NC. Starting substrates are 35 mm diameter, heavily-doped p-type (aluminum). The 6H substrates are oriented  $3.5^\circ$  off-axis and the 4H substrates are oriented  $8^\circ$  off-axis. Two epilayers are grown on these substrates. The first epilayer is 8  $\mu\text{m}$  thick, doped p-type  $5 \times 10^{15} \text{ cm}^{-3}$  with aluminum. The second epilayer is n-type, doped  $1 \times 10^{17} \text{ cm}^{-3}$  with nitrogen. On some wafers, the n-type epilayer is 1  $\mu\text{m}$  thick and on other wafers it is 4  $\mu\text{m}$  thick. Isolation trenches 1.5 (5)  $\mu\text{m}$  deep are

formed by reactive ion etching in SF<sub>6</sub> with an Al (Ni) etch mask. The resulting sidewalls are clean and vertical. The trench defines constrictions in the n-type epilayer, as illustrated in Fig. 1. Constrictions of dimensions (width x length) = 5x5, 5x10, 5x15, 10x10, and 10x15  $\mu\text{m}$  are included on the die. Ni ohmic contacts are deposited by E-beam evaporation, patterned by lift-off, and annealed in argon at 900 °C for 2 minutes. Ohmic contacts on the 1  $\mu\text{m}$  thick epilayer samples were found to be slightly non-ohmic, so a high dose ( $1 \times 10^{19} \text{ cm}^{-3}$ ) nitrogen implant is performed in the contact regions on the 4  $\mu\text{m}$  thick epilayer wafers before Ni deposition. This implant is annealed at 1400 °C for 18 minutes in argon. Doping-thickness ( $n \cdot t$ ) products are obtained on each sample from Hall measurements, and are listed in Table 1. In these calculations, the Hall scattering factor  $r_H$  is taken to be unity [2]. The ( $n \cdot t$ ) values in Table 1 agree well with TLM measurements. The lateral dimensions of the constrictions are determined within an accuracy of  $\pm 10\%$  from SEM photographs of the completed structures. Epilayer thickness and the uniformity of doping with depth are verified by SIMS analysis. The nitrogen concentration in the n-type epilayer is uniform within about  $\pm 10\%$  as a function of depth from the surface to the bottom of the n-type epilayer.

	1 $\mu\text{m}$ epilayer wafer ( $nt$ ) $\text{cm}^{-2}$	4 $\mu\text{m}$ epilayer wafer ( $nt$ ) $\text{cm}^{-2}$
6H	$1.2 \times 10^{13}$	$3.6 \times 10^{13}$
4H	$1.4 \times 10^{13}$	$2.4 \times 10^{13}$

Table 1. Electron density  $\cdot$  thickness product obtained from Hall analysis for four wafers at room temperature.

### Measurement Procedure and Data Reduction

The experimental devices are tested in wafer form by probing in a shielded, light-tight probe station. To prevent arcing at high fields, the samples are probed while immersed in Flourinert. The measurement apparatus is shown in Fig. 2. To minimize

transient heating, bias pulses are applied across the outer contacts  $L_1$  and  $L_4$  using a Directed Energy GRX 1.5 K-E high-voltage pulse generator, driven by a Power Device Specifics HV-1565 high-voltage DC power supply and triggered by a Hewlett-Packard HP-214A pulse generator. Bias pulses of 10 - 40  $\mu$ s duration are applied in the low field regime ( $<10^4$  V/cm), while shorter pulses in the range 75 – 200 ns are used at higher fields ( $>10^4$  V/cm). The voltage drop across the constriction is monitored by the 1 M $\Omega$  inputs of a Tektronix 11401 digitizing oscilloscope connected to inner contacts  $L_2$  and  $L_3$ , and the current through the constriction is calculated from the voltage drop across the 50  $\Omega$  oscilloscope input connecting  $L_4$  to ground. To conduct measurements at elevated temperatures, the sample is mounted on a heated chuck. The temperature at the top surface of the heated chuck is monitored using a thermocouple. The drift velocity is then obtained from (1).

The electric field in the constriction is calculated from the voltage drop across the inner contacts, with correction for the end resistance  $R_2$  and  $R_3$  between the inner contacts and the channel. Figure 3 illustrates how the end resistance is calculated. Assuming that current flow is confined to the dashed region in Fig. 3, the end resistance can be expressed as

$$R_{END} = \frac{\rho}{2 t \tan(\theta)} \ln \left( 1 + \frac{2 s \tan(\theta)}{w} \right) \quad (2)$$

where  $\rho$  is the sheet resistance of the n-type epilayer,  $t$  is the thickness of the epilayer,  $s$  is the spacing between the inner contact and the constriction,  $w$  is the width of the constriction, and  $\theta$  is the current spreading angle. In this calculation,  $\theta$  is calculated from the dimensions  $h$ ,  $s$ , and  $w$ , with the assumption that electron mobility is isotropic in the basal plane of both 6H and 4H SiC.

At high fields, sample heating causes the current (and hence the inferred electron velocity) to decrease with time during the bias pulse, as shown in Fig. 4. To minimize the effects of transient heating, measurements must be made very early in the pulse.

With the four-probe configuration, parasitic probe-to-probe capacitance limits the rise time of the bias pulse, making it difficult to obtain data early enough in the bias pulse. For this reason, measurements at high fields ( $>3 \times 10^4$  V/cm) are performed with the two inner probes  $L_2$  and  $L_3$  removed. In this configuration, the voltage across the constriction cannot be monitored directly. In this case, we use knowledge of the contact and parasitic series resistances to calculate the voltage drop across the constriction. These resistances are directly measured on the experimental device using the four-probe configuration at low fields. Figure 5 illustrates the process. First, the impedances ( $R_{C1} + R_1$ ) and ( $R_{C4} + R_4$ ) are obtained from four-probe measurements at low fields (no current flows through  $R_{C2}$  and  $R_{C3}$  due to the high impedance probes on  $L_2$  and  $L_3$ ). At higher fields, the probes on  $L_2$  and  $L_3$  are removed and the voltage drops across ( $R_{C1} + R_1$ ) and ( $R_{C4} + R_4$ ) are calculated from the measured current and known impedances. These voltage drops are then subtracted from the measured voltage between probes  $L_1$  and  $L_4$  to obtain the equivalent inner probe voltage drop.

During the experiment, high positive voltages are applied to the n-type epilayer to create high fields. These voltages reverse-bias the pn junction and create a depletion region in the n-type epilayer. Depletion of the channel reduces the total number of electrons in the channel, and this must be accounted for in calculating the velocity using (1). A first-order estimate of the electron density in the n-type channel is given by

$$n^* = (1 - r) n \quad (3)$$

where  $n^*$  is the revised carrier density,  $n$  is the original carrier density, and  $r$  is the ratio between the depleted cross section and the  $l \cdot t$  product, given by

$$r = \frac{2}{3t} \sqrt{\frac{2 \epsilon_s E N_A l}{q N_D (N_D + N_A)}} \quad (4)$$

Here  $t$  is the thickness of the n-type epilayer,  $l$  is the length of the constriction,  $\epsilon_s$  is the permittivity of SiC,  $E$  is the electric field in the constriction,  $N_D$  is the doping of the n-type

epilayer, and  $N_A$  is the doping of the underlying p-type epilayer. From (1), the corrected drift velocity for electrons is then

$$v^* = \frac{I}{I - r} v \quad (5)$$

This correction is important for samples with 1  $\mu\text{m}$  thick n-type epilayers, but is much less significant for samples with 4  $\mu\text{m}$  thick n-type epilayers. As will be shown, comparison of data from both types of samples indicates that the above correction procedure is valid.

### Experimental Results

The highest fields reached in this experiment are approximately  $3.5 \times 10^5$  V/cm. Above this field, sharp transients in the current are observed during the bias pulse. With continued pulsing, a burned track is often observed running down the middle of the constriction. This effect limits the maximum fields in this experiment, both at room and elevated temperatures.

The experimental drift velocities obtained from several constriction geometries and from two epilayer thicknesses (1 and 4  $\mu\text{m}$ ) are shown in Figs. 6 and 7 for 6H and 4H-SiC respectively. The solid curves represent empirical fits using the equation

$$v(E) = \frac{\mu E}{\left[ 1 + \left( \frac{\mu E}{v_s} \right)^\alpha \right]^{\frac{1}{\alpha}}} \quad (6)$$

where  $v$  is the electron velocity,  $E$  the electric field,  $\mu$  the mobility,  $v_s$  the saturated drift velocity, and  $\alpha$  is a dimensionless fitting parameter. Table 2 lists the fit parameters for the solid curves in Figs. 6 and 7.



Temperature	Parameter	6H	4H
23 °C	$\mu$	215 cm <sup>2</sup> /Vs	450 cm <sup>2</sup> /Vs
	$v_s$	1.9 x10 <sup>7</sup> cm/s	2.2 x10 <sup>7</sup> cm/s
	$\alpha$	1.7	1.2
135 °C	$\mu$	120 cm <sup>2</sup> /Vs	-
	$v_s$	1.4 x10 <sup>7</sup> cm/s	-
	$\alpha$	2.5	-
320 °C	$\mu$	56 cm <sup>2</sup> /Vs	130 cm <sup>2</sup> /Vs
	$v_s$	1.0 x10 <sup>7</sup> cm/s	1.6 x10 <sup>7</sup> cm/s
	$\alpha$	4.0	2.2

Table 2. Parameters used in (6) to fit the experimental velocity-field data.

The highest velocities actually measured at 23 °C are 1.8x10<sup>7</sup> cm/s for 6H-SiC and 2.1x10<sup>7</sup> cm/s for 4H-SiC. Fitting to the empirical equation (6) yields estimated saturation velocities of 1.9x10<sup>7</sup> cm/s for 6H-SiC and 2.2x10<sup>7</sup> for 4H-SiC, respectively. At higher temperatures the saturation velocities are not well determined by our measurements because data could not be obtained at sufficiently high fields. The solid curves in Figs. 6 and 7 were not obtained by a least-squares fit, but rather by manual variation of the fitting parameters. No claims are made as to the physical significance of the fitting parameters, and equation (6) is regarded only as a useful mathematical representation of the measured data.

The mobility values at 23 °C in Table 2 are about 25% lower than Hall mobilities reported for n-type epilayers of the same doping by Schaffer, et al. [3]. The reason for this discrepancy is not known, but it is not thought to be due to sample heating, since at these low fields (< 10 kV/cm) the measured current does not decrease with time during the bias pulse, as shown in Fig. 4.

## **Conclusions**

In summary, we report new measurements of electron drift velocity in 6H-SiC and the first measurements of electron velocity in 4H-SiC. The electron saturation drift velocity at room temperature is  $1.9 (2.2) \times 10^7$  cm/s in 6H (4H) SiC. At 320 °C the electron saturation velocity is  $1.0 (1.6) \times 10^7$  cm/s in 6H (4H) SiC.

## **Acknowledgements**

This work is supported by a grant from the Air Force Research Laboratories through the SiC Consortium, managed by the Auburn Space Power Institute, and by the Office of Naval Research under MURI grant No. N00014-95-1-1302. Experimental wafers are donated by Cree Research, Inc.

## References

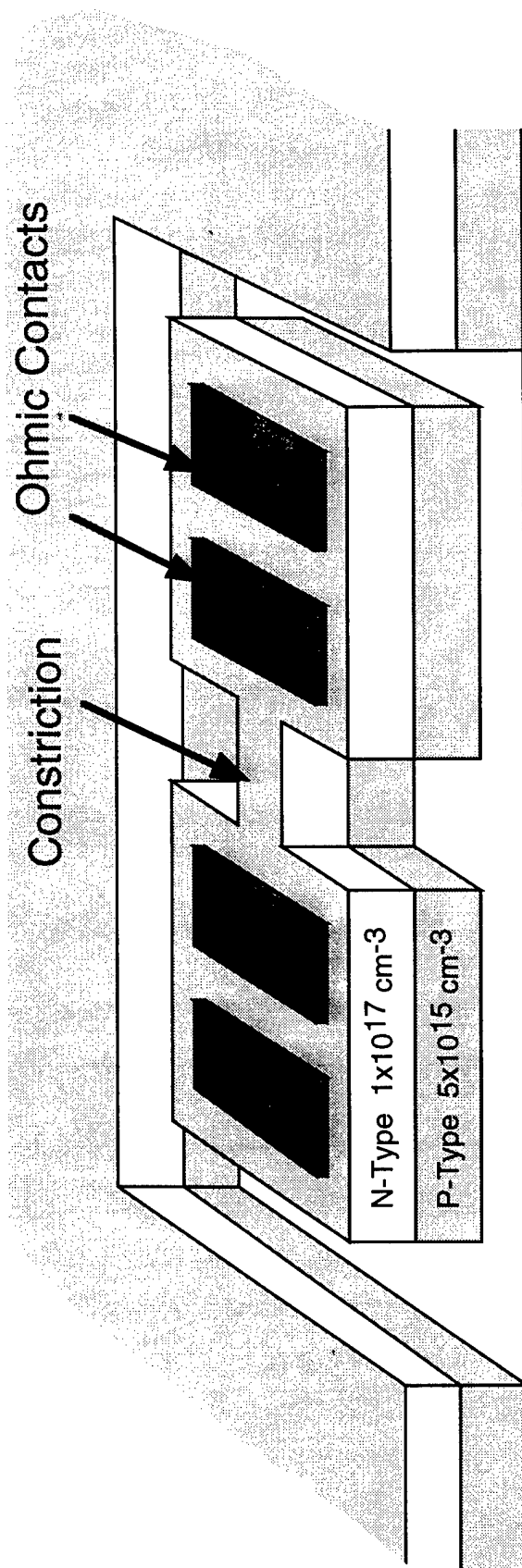
- [1] W. v. Muench and E. Pettenpaul, "Saturated Electron Drift Velocity in 6H SiC," *J. Appl. Phys.*, **48**, 4823 (1977).
- [2] G. Rutsch, R. P. Devaty, D. W. Langer, L. B. Rowland, and W. J. Choyke, "Measurement of the Hall Scattering Factor in 4H-SiC Epilayers from 40 K to 290 K and up to Magnetic Fields of Nine Tesla," *Mat'ls. Sci. Forum*, **264-268**, 517 (1998).
- [3] W. J. Schaffer, G. L. Negley, K. G. Irvine, and J. W. Palmour, "Conductivity Anisotropy in Epitaxial 6H and 4H SiC," in "Diamond, SiC, and Nitride Wide-Bandgap Semiconductors", C. H. Carter, Jr., G. Gildenblatt, S. Nakamura, and R. J. Nemanich, Eds., *Mat. Res. Soc. Proc.*, **339**, 596 (1994).

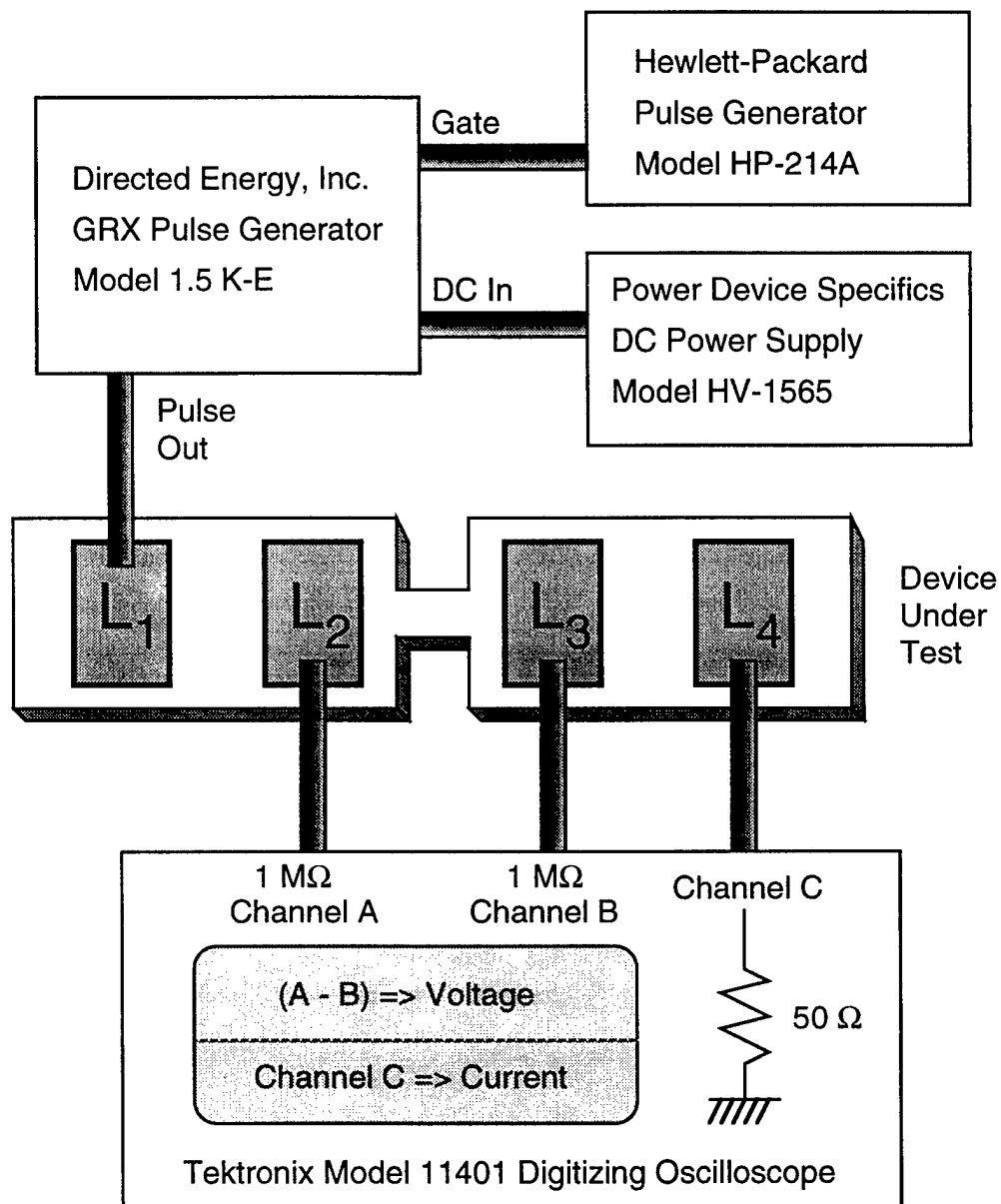
## Figure Captions

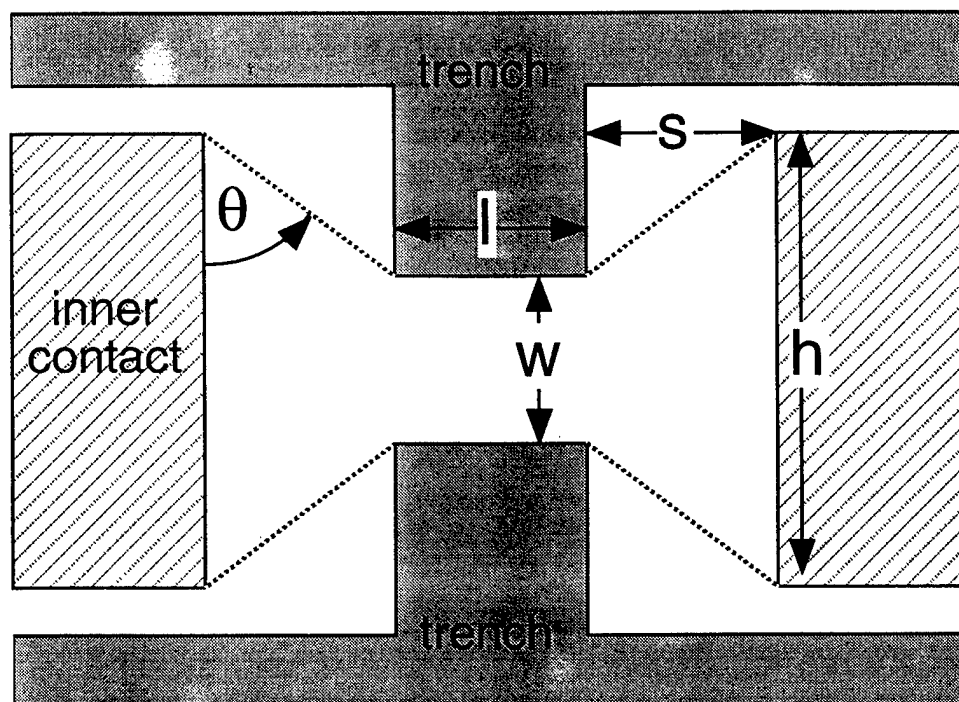
- Figure 1. Isometric representation of the test structure.
- Figure 2. Schematic of the measurement circuit. Bias pulses are applied across the outer contacts of the n-type epilayer. The voltage drop across the constriction is monitored using high impedance oscilloscope inputs connected to the inner contacts, and the current is obtained from the voltage drop across the  $50\ \Omega$  oscilloscope probe connected to contact  $L_4$ .
- Figure 3. Top view of the region between the inner contacts, including the constriction. The spreading end resistances  $R_2$  and  $R_3$  between the inner contacts and the constriction are calculated using eqn. (2).
- Figure 4. Transient current waveforms for several bias pulse voltages for the  $10 \times 10$  constriction on the  $1\ \mu\text{m}$  thick 4H-SiC sample at room temperature. Notice the rapid decrease in current with time at the highest fields. In these cases, the current reading is taken at the earliest possible point in the bias pulse.
- Figure 5. Equivalent circuit illustrating the measurement of electric field within the constriction.  $R_{C1} - R_{C4}$  represent impedances of the ohmic contacts to the n-type epilayer, and are slightly nonlinear on the  $1\ \mu\text{m}$  epilayer samples. Resistances  $R_1$  and  $R_4$  are spreading resistances between the outer and inner contacts on each side of the constriction, and resistances  $R_2$  and  $R_3$  are spreading resistances between the inner contacts and the constriction.  $L_2$  and  $L_3$  are connected to  $1\ \text{M}\Omega$  inputs to the oscilloscope, and negligible current flows through impedances  $R_{C2}$  and  $R_{C3}$ .
- Figure 6. Drift velocity of electrons parallel to the basal plane in (0001) 6H-SiC. At  $23^\circ\text{C}$ , gray circles are constrictions with (width x length x thickness) =  $(10 \times 10 \times 1\ \mu\text{m})$ , open circles are  $(10 \times 10 \times 4\ \mu\text{m})$ , triangles are  $(5 \times 15 \times 4\ \mu\text{m})$ ,

squares are  $(5 \times 5 \times 4 \text{ }\mu\text{m})$ , and diamonds are  $(5 \times 10 \times 4 \text{ }\mu\text{m})$ . At  $135 \text{ }^{\circ}\text{C}$ , closed circles are  $(10 \times 10 \times 4 \text{ }\mu\text{m})$ . At  $320 \text{ }^{\circ}\text{C}$ , open circles are  $(10 \times 10 \times 4 \text{ }\mu\text{m})$ . Solid lines are fits to the data at each temperature using empirical eqn. (6) and the fitting parameters in Table 2.

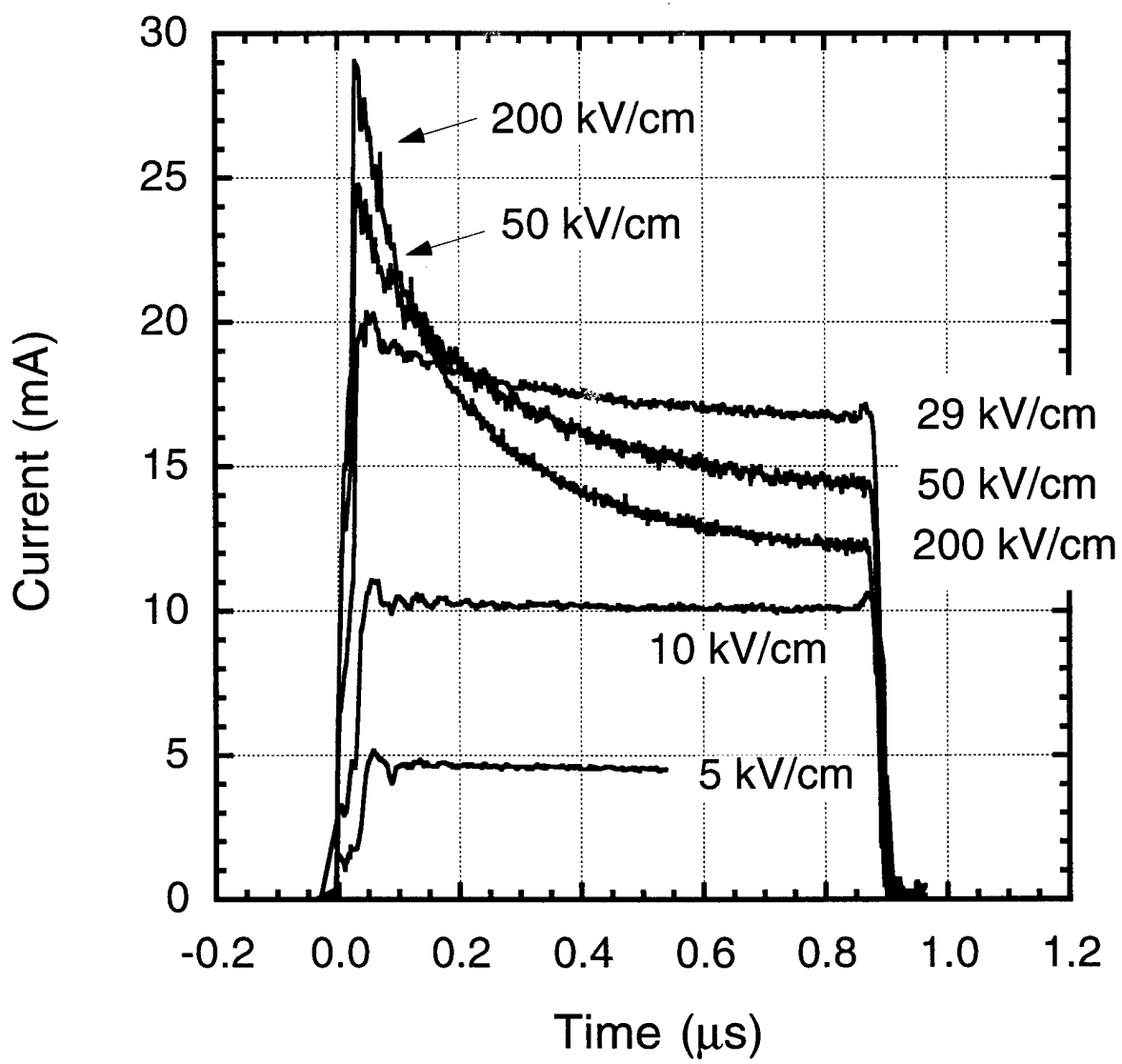
Figure 7. Drift velocity of electrons parallel to the basal plane in (0001) 4H-SiC. At  $23 \text{ }^{\circ}\text{C}$ , open circles are constrictions with (width x length x thickness) =  $(10 \times 10 \times 4 \text{ }\mu\text{m})$ , and triangles are  $(5 \times 15 \times 4 \text{ }\mu\text{m})$ . At  $320 \text{ }^{\circ}\text{C}$ , closed circles are  $(10 \times 10 \times 4 \text{ }\mu\text{m})$ . Solid lines are fits to the data at each temperature using empirical eqn. (6) and the fitting parameters in Table 2.

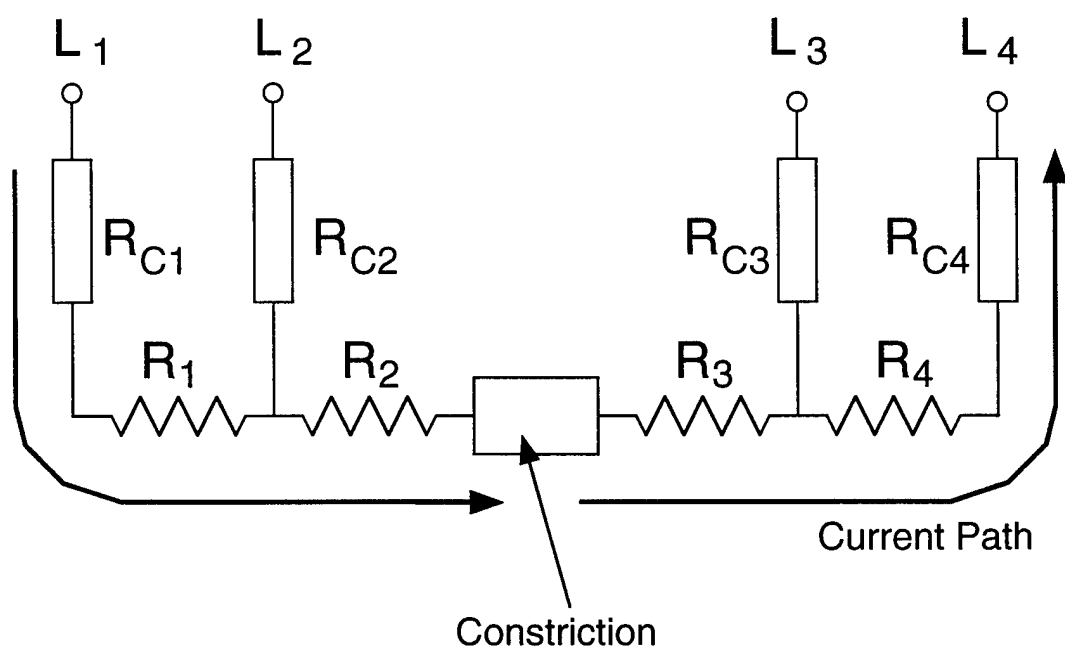


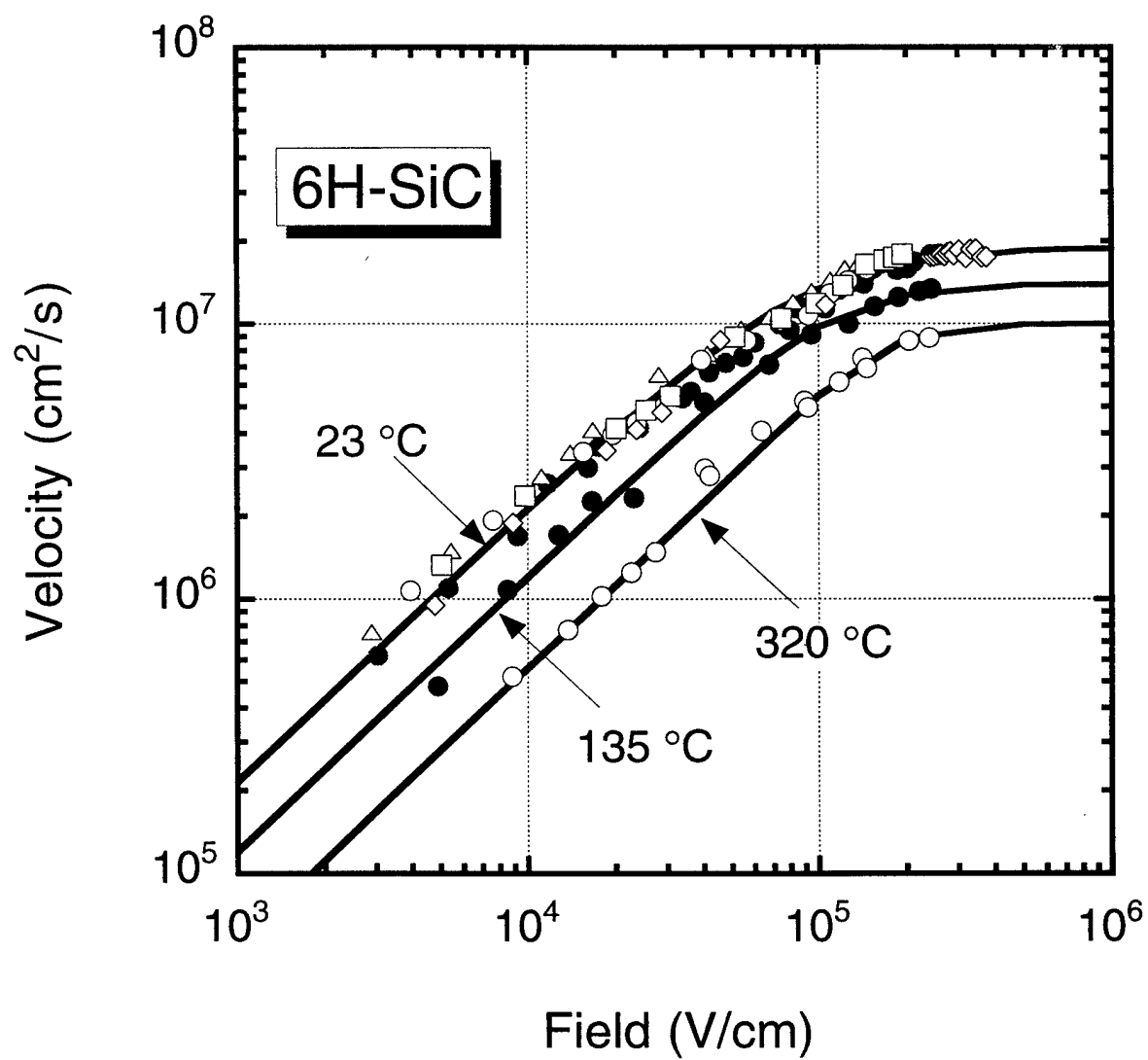


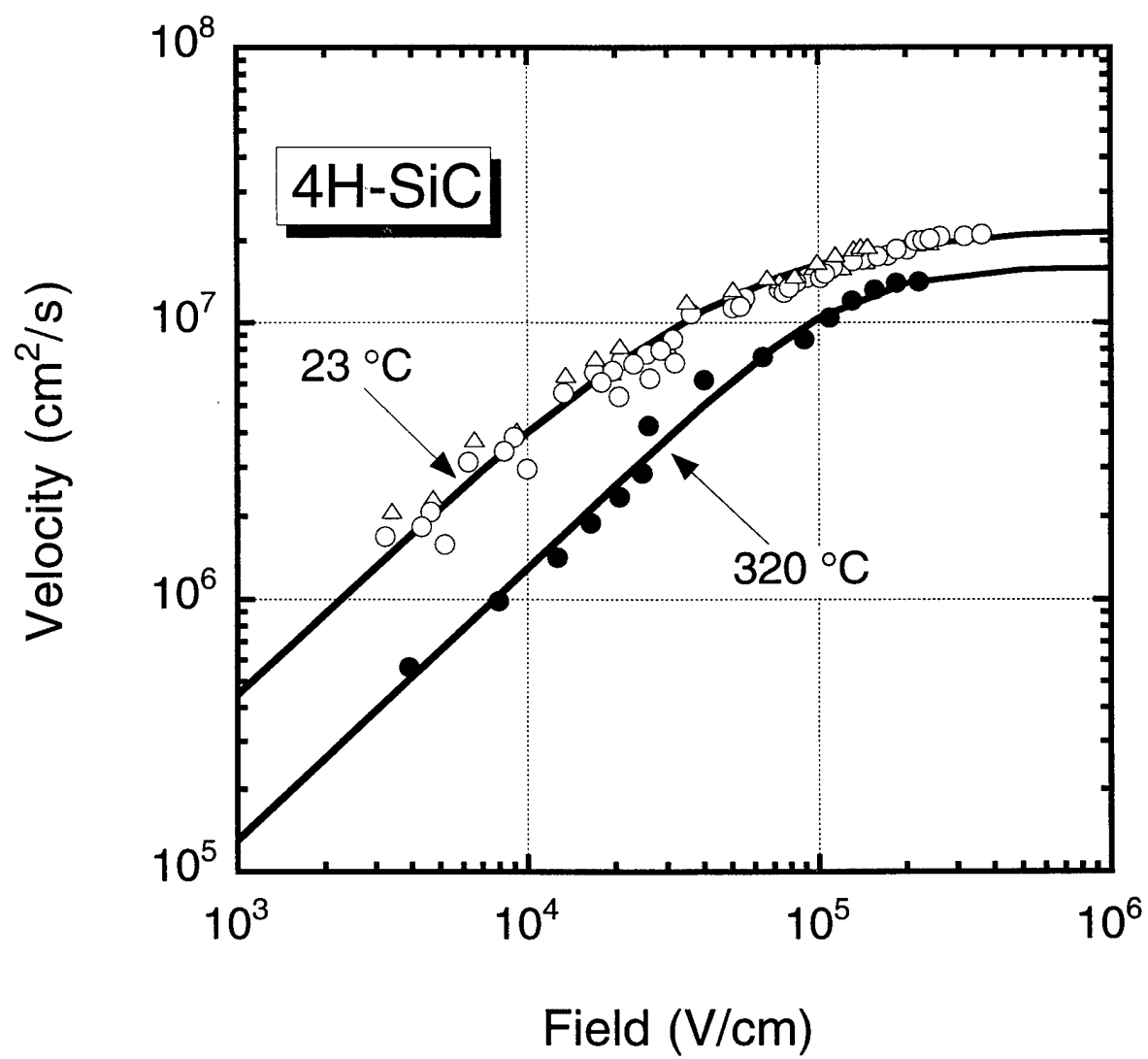












**CHARACTERIZATION OF DEFECTS AND MINORITY  
CARRIER LIFETIME IN SILICON CARBIDE MATERIALS**

**A. ROHATGI, A. DOOLITTLE**

**FINAL TECHNICAL REPORT  
OCTOBER 1995 - SEPTEMBER 1998**

**CONTRACT #95-SPI-420757-GTRC  
SILICON CARBIDE - AUBURN**

## Electron Beam Induced Current Investigations of Epitaxial 4H Silicon Carbide

EBIC was used to quantify the diffusion length variations in epitaxial 4H SiC. This technique is ideally suited for epitaxial material, due to its spatial sensitivity and near surface sensitivity. This implies that diffusion lengths determined by EBIC will accurately reflect such effects as epitaxial minority carrier lifetimes in the epitaxial films, recombination at surfaces, and at the epi/substrate interface. This is important for device modeling, so that these effects, present in actual devices, are not overlooked.

Compared to other techniques used for minority carrier lifetime determination, such as time resolved photoluminescence, infrared pump-probe and contactless photoconductive decay, EBIC-DLM gives a better understanding of the variation of lifetime with position on the wafer. EBIC-DLM is not limited to observation of either long lifetime components due to saturation of a recombination mechanism at high injection, or increased sensitivity of the technique to longer lifetime components.

The results of some of the EBIC measurements on 4H epitaxial silicon carbide performed during this program are summarized in figures 1-8. Figures 1 and 2 are EBIC images at 100 and 200 x magnification, while figures 3 and 4 are the corresponding diffusion length maps. The diffusion length maps were developed as described in a previous quarterly report for this project. Note in all images the banded regions of different quality. This non-uniformity highlights one of the EBIC techniques advantages. Specifically, its spatial resolution is excellent. Note that the diffusion length maps indicate an average diffusion length of ~1 micron, with significant variation in the lower magnification image. Indeed values as high as 4 microns are observed. Figure 4 shows that even within the narrow region observed at 200 x magnification, full width at

half maximum (FWHM) variations are on the order of 50% of the mean value. This implies significant local variation in impurity concentrations.

A second 4H epitaxial silicon carbide sample of better quality was also examined. This sample indicates higher average diffusion lengths on the order of  $\sim 2$  microns. However, within this sample, the variation in diffusion length is approximately  $\pm 25\%$  of the FWHM (see histogram in figure 7). Note also that the predominate defect in these images are linear arrays of "spots" these may be dislocations, or defects that decorate the step edges during epitaxial growth. This particular sample was grown on a misoriented substrate. Thus, step edges are present in the direction toward the miscut. Figures 6 and 8 are images at higher magnification (2000 x). These indicate a clear spotty behavior. We have observed such behavior in edge film grown silicon and have attributed it to individual dislocation activity based on etch pit studies. Thus, the nature of the defect remains unclear.

In this program, we have shown that EBIC can successfully and quantitatively distinguish between good and bad material and provide information on the structure of device limiting defects. Significant variation in the epitaxial material investigated was observed, both on the microscopic scale and the macroscopic scale. The spatial resolution of EBIC-DLM has been used to image individual defects presumed to be dislocations or decorated growth step edges. In future work, it is possible that the electrical activity of these defects could be examined at each step of the device process sequence, revealing the electrical activity of the defects as a function of processing.

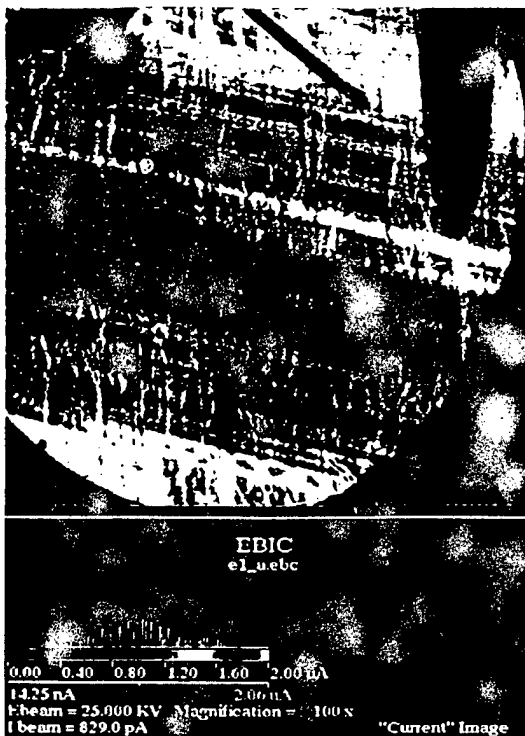


Figure 1 EBIC image of Sample E1 at 100X magnification.

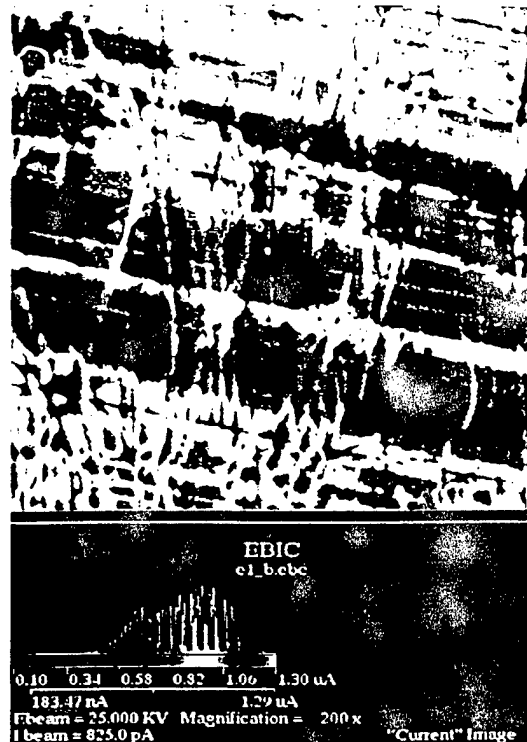


Figure 2 EBIC image of Sample E1 at 200X magnification.

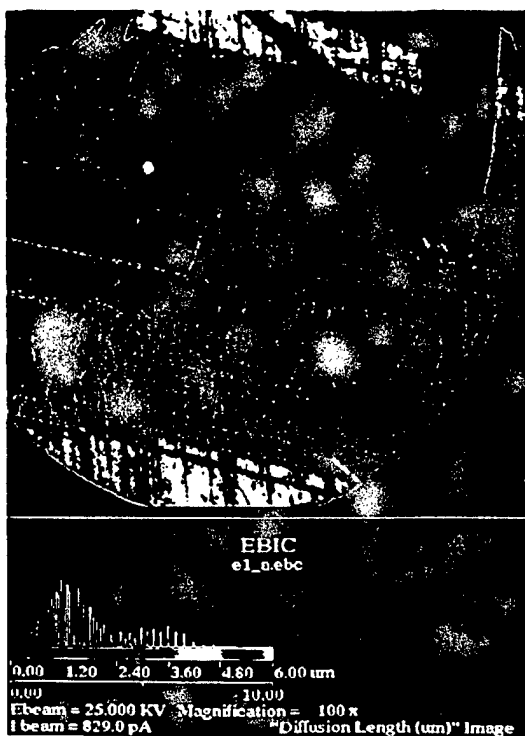


Figure 3 Diffusion Length image of Sample E1 at 100X magnification.

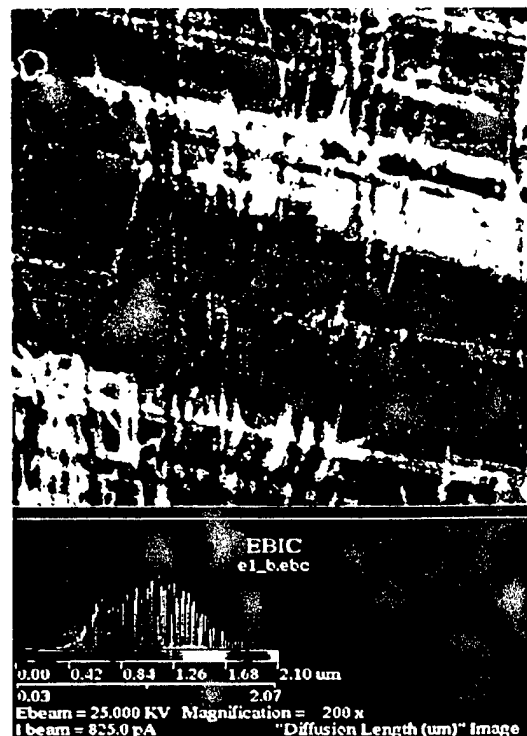


Figure 4 Diffusion Length image of Sample E1 at 200X magnification.



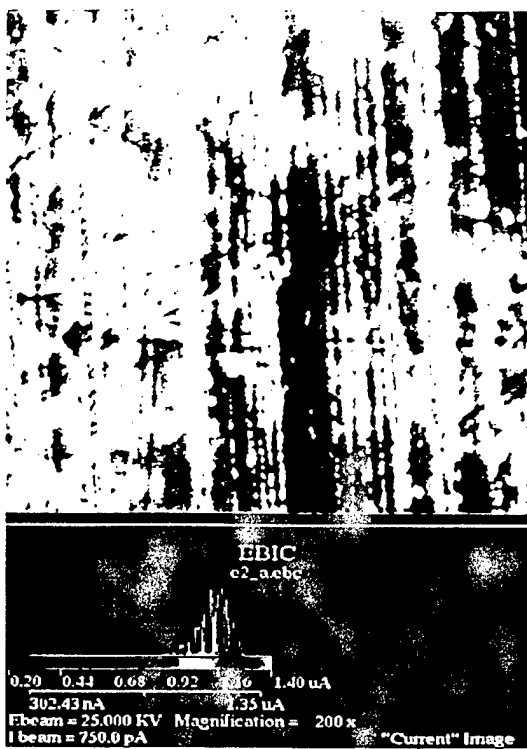


Figure 5 EBIC image of epitaxial 4H SiC at 200 x magnification.

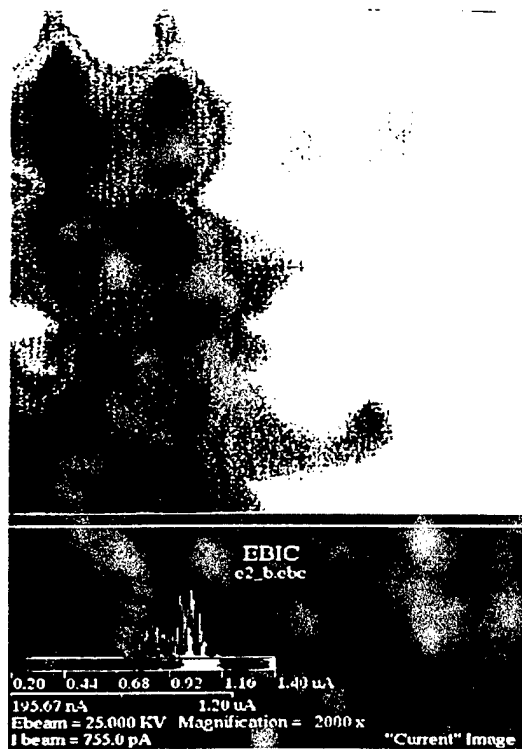


Figure 6 EBIC image of epitaxial 4H SiC at 2000 x magnification.

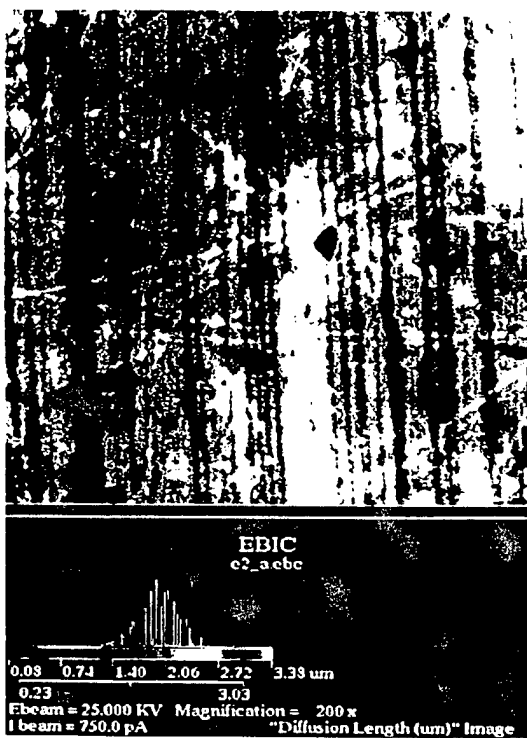


Figure 7 Diffusion length image of epitaxial 4H SiC at 200 x magnification.

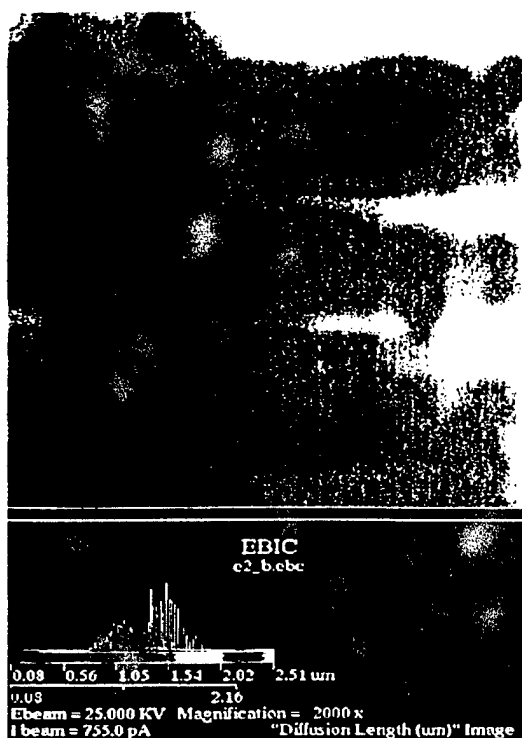


Figure 8 Diffusion length image of epitaxial 4H SiC at 2000 x magnification.

## Electron Beam Induced Current Investigations of Bulk 4H Silicon Carbide

EBIC was used to quantify the diffusion length variations in bulk 4H SiC. This technique is ideally suited for examining bulk material, due to its spatial sensitivity and near surface sensitivity. The technique is especially sensitive to degradation in electrical quality due to surface polish damage. This implies that diffusion lengths determined by EBIC will accurately reflect such effects as surface recombination at such surfaces. This is important for device modeling, so that these effects, present in actual devices, are not overlooked.

The results of some of the EBIC measurements on 4H epitaxial silicon carbide are summarized in figures 9-20. Figures 9 and 10 are EBIC and diffusion length images at 2520 x magnification, while figures 11 and 12 are EBIC and diffusion length maps at 252 x magnification. Note in all images the scratches from polish damage resulting in different quality. This non-uniformity highlights one of the EBIC technique's advantages. Specifically, its spatial resolution is excellent. Note that the diffusion length maps indicate an average diffusion length of 0.05 to 0.06 microns, with significant variation in the higher magnification image. EBIC is one of the only techniques capable of measuring such short diffusion lengths. Note also, the variation is scratch size of the individual scratch lines. This indicates that EBIC should be able to quantify the effectiveness of the polishing process at each successive polishing step. For example, when stepping down from a larger grit to a smaller grit, the size of the scratches could be monitored to determine the optimal polish time for which the larger scratches from the previous polish step have been adequately removed. Since EBIC is a subsurface technique, it is unaffected by the filling in of deep scratches by SiC amorphous polish residue. This process leads to a very good atomic force microscopy roughness, but results in poor crystal

quality for subsequent epitaxy. Upon growth of the epitaxial layers, the underlying scratch damage of the substrate is propagated into the epitaxial layer (see the figures 5-8 in the previous section for examples of the remaining scratch damage in the epitaxial layer).

Another 4H bulk silicon carbide sample showed even poorer quality (see figures 13 & 14). This sample indicates lower EBIC response with significant variation across the region examined. The current response on this sample is too low to accurately compute a diffusion length map as indicated by a constant "0" background in figure 14. The SEM image in figure 15 shows a relatively smooth surface with only a couple of micropipes observed.

One of the micropipes seen in figure 15 (upper left corner) is imaged at higher magnification (2620 X) in figures 16-18. Here we see a halo of higher current response (see figure 16) around the micropipe. This may be the result of a strain field, denuded zone or a local depleted region due to charge present at the micropipe. Figure 17 indicates that diffusion length variations on the order of 400% occur locally around the micropipe. Figure 18 indicates that the core of the micropipe contains a particle of unknown composition.

To examine the stability of the defects limiting the diffusion length, we focused the electron beam on the surface of an epitaxially grown 4H SiC layer for ~1 minute. Figure 19 shows two regions of higher current response resulting from this focused energy. Figure 20 shows a third region created by the same process. This indicates that the limiting defect in SiC may be a complex that can be disassociated by electron beam annealing. Since the contact was already annealed, we do not believe this to be a contact annealing phenomena.

In this project, we have shown that EBIC can successfully distinguish between good and bad material and provide information on the structure of device limiting defects. EBIC is particularly helpful in quantifying polish damage. Electron beam annealing also improves the

observed current response, presumably due to the disassociation of weakly bound impurities.

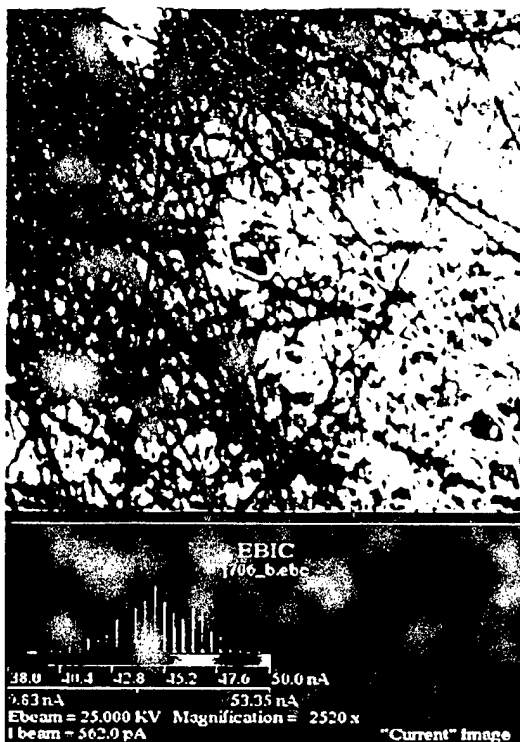


Figure 9 EBIC image of bulk 4H SiC at high magnification (2520 X).

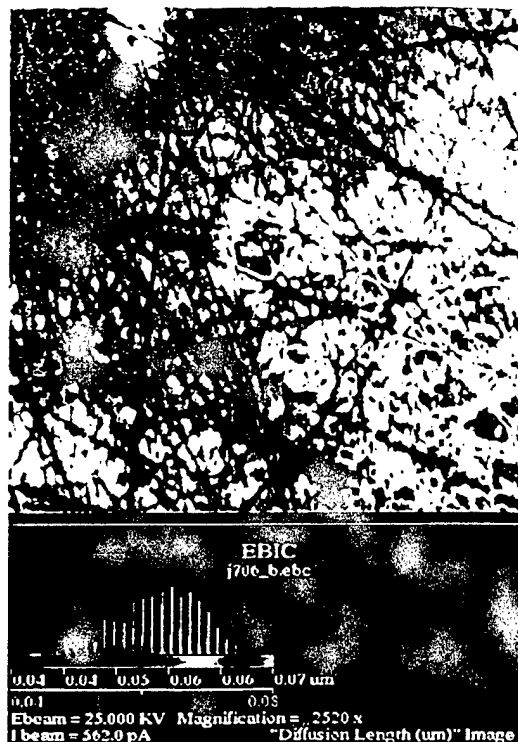


Figure 10 Diffusion length image of bulk 4H SiC at high magnification (2520 X).

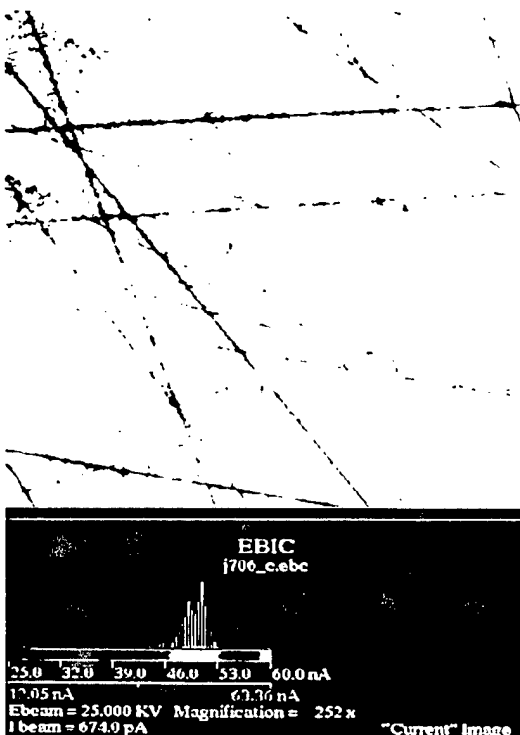


Figure 11 EBIC image of bulk 4H SiC at low magnification (252 X).

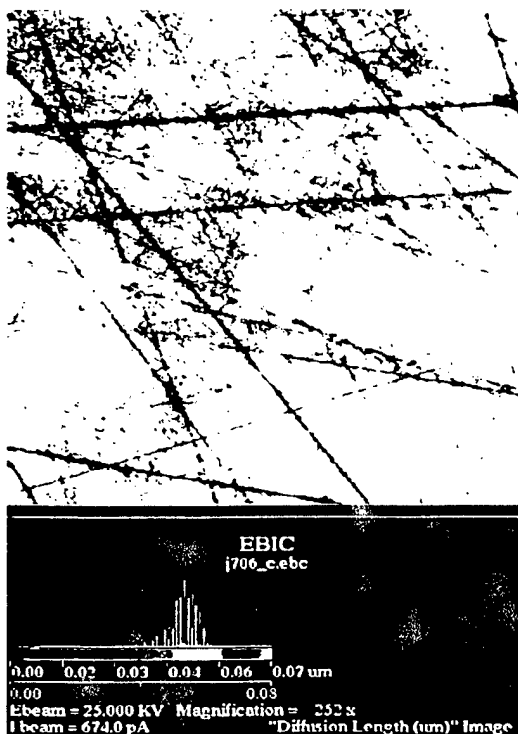


Figure 12 Diffusion Length image of bulk 4H SiC at low magnification (252 X).



Figure 13 EBIC image of "bad" bulk 4H SiC sample at low magnification (252 X).

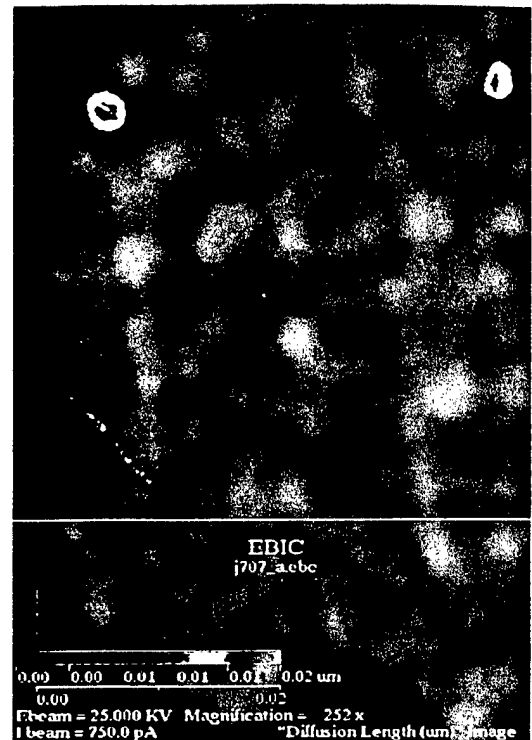


Figure 14 Diffusion length image of "bad" bulk 4H SiC sample at low magnification (252 X).

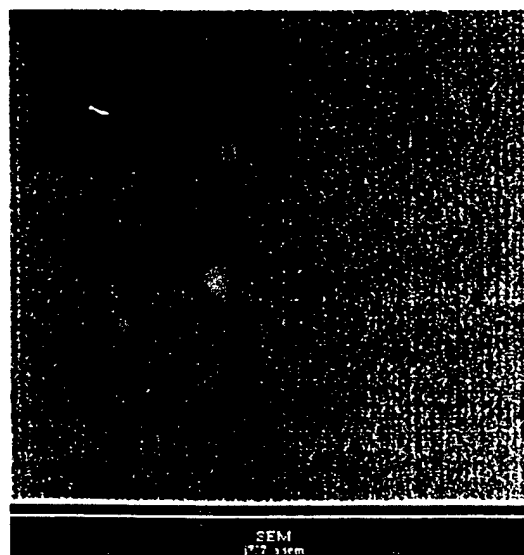


Figure 15 SEM image of region imaged in figures 5 and 6. Note relatively smooth surface.

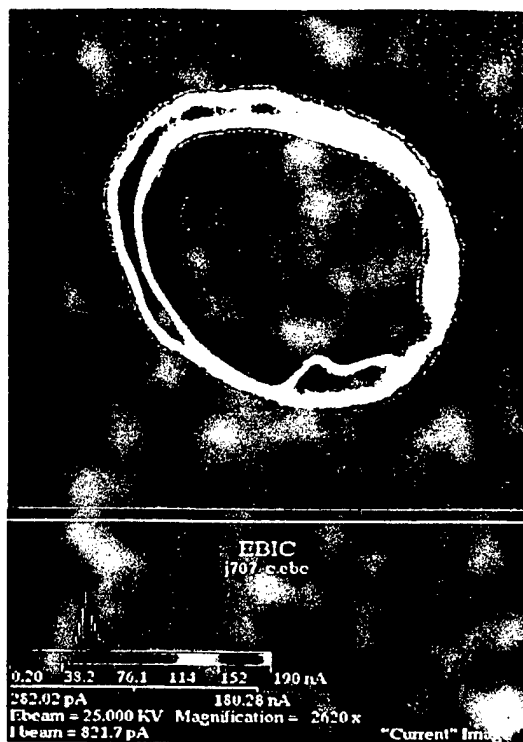


Figure 16 EBIC image of micropipe.

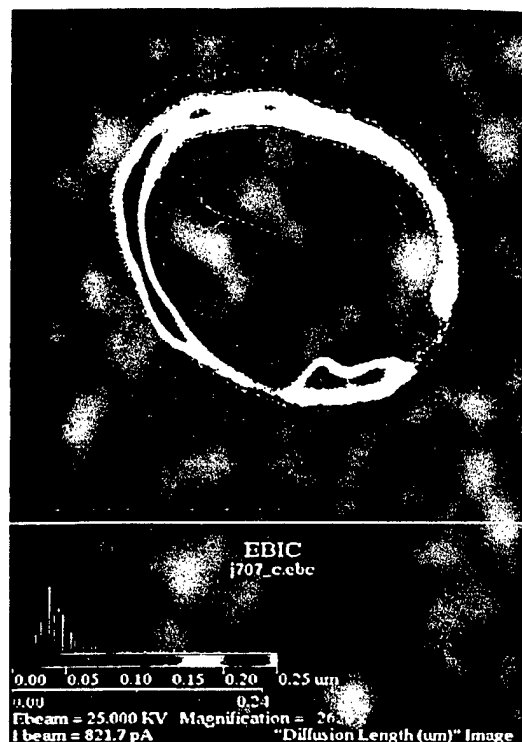


Figure 17 Diffusion length image of micropipe.

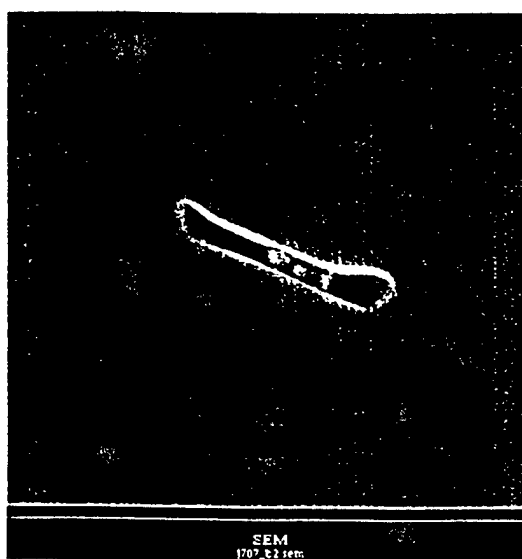


Figure 18 SEM image of micropipe imaged in figures 8 and 9.

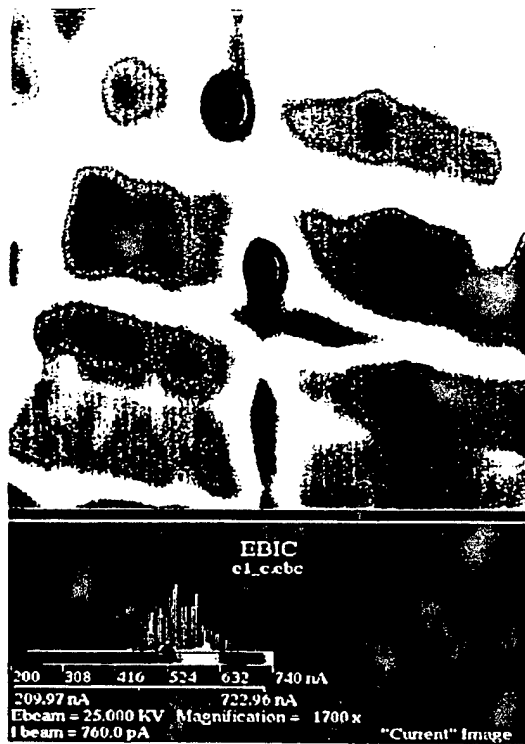


Figure 19 EBIC Image of Epitaxial 4H SiC at 1700X magnification before electron beam anneal.

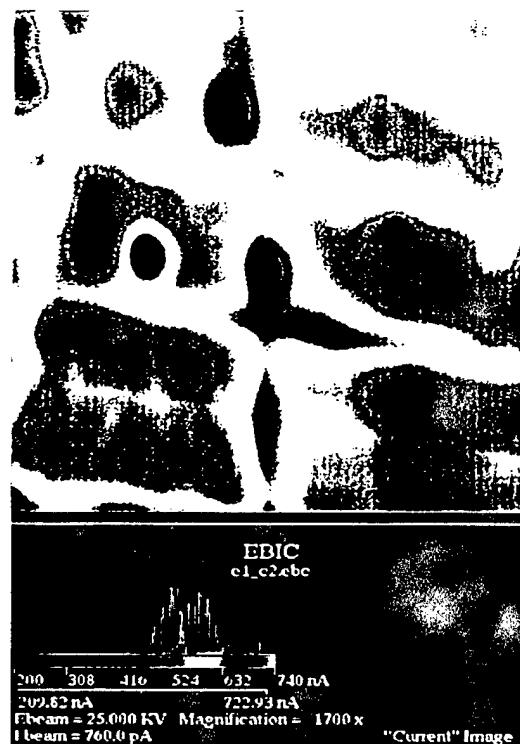


Figure 20 EBIC Image of Epitaxial 4H SiC at 1700X magnification after electron beam anneal.



low  $Q$  will provide adequate coupling and broader range of conductance. Thus, twelve different circuits were tested and finally a circuit of adequate quality factor was implemented.

The second issue to be overcome is the need for conductance versus voltage calibrations. These calibrations are critical to overcome non-linear effects in the circuit, especially those spanning many decades of conductance. Additionally, this calibration allows lifetime to be related to injection level. This provides feedback for device modeling where it is important to know what your lifetime is at a particular injection level. To achieve this voltage versus conductance calibration, the system in figure 23 was built. In this system, a high resistivity, thin, oxidized wafer was loaded onto the sample coil. A calibrated solar cell was used to determine light intensity of a variable DC light source. By scanning the DC light intensity and recording the PCD voltage and short circuit current of the solar cell, the conductance versus voltage curve was determined to within a linear factor. This linear factor accounts for differences in light impinging on the solar cell versus the PCD sample. By placing doped wafers of known conductivity on the PCD coil and recording the output voltage, this geometry factor was easily determined. Thus, the conductance versus voltage curve was determined for a vast and continuous range of conductances. All voltage signals can then be converted to conductance signals by simple point by point interpolation. The conductance versus voltage calibration curve is shown in figure 24. The possible differences in conductivity versus voltage transients are shown in figure 25.

We have measured PCD minority carrier lifetimes and have found many interesting details. These details will be outlined in a future report. However, figures 26 and 27 show the voltage versus time, conductance versus time and lifetime versus injection level plot of one 4H SiC wafer. This will be discussed in more detail in the following section.

# RF PCD System

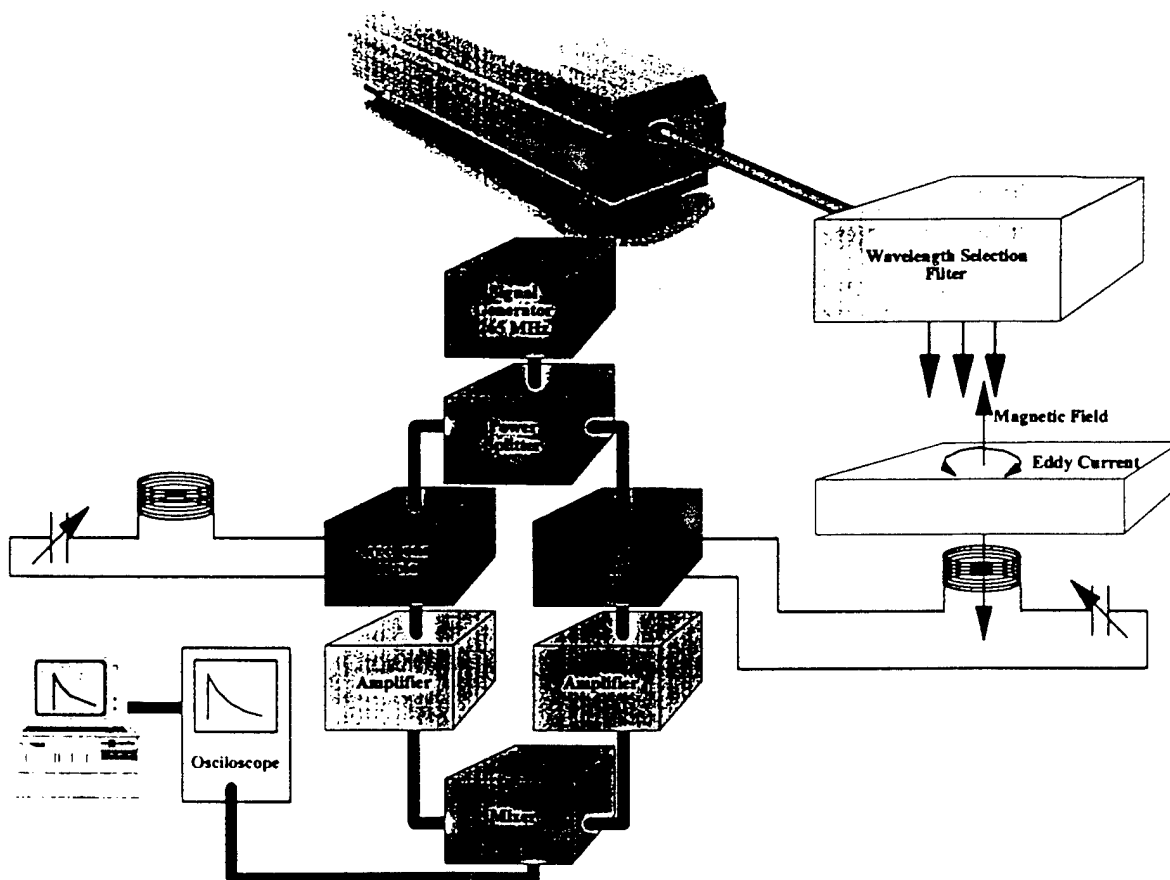
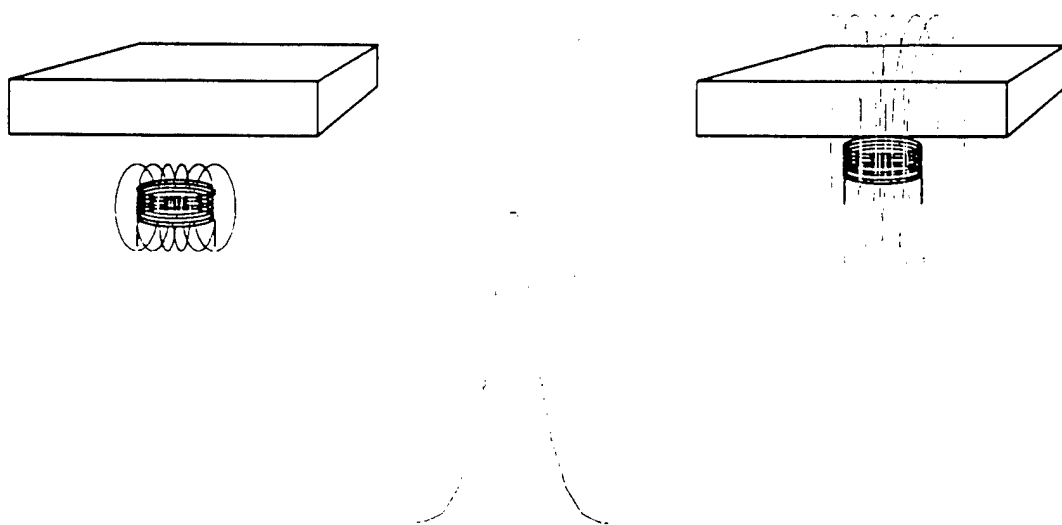


Figure 21 Schematic representation of the PCD circuit operating at Georgia Tech for SiC.

# RF PCD System Design Constraints

- High enough "Q" to ensure resonance and provide adequate sensitivity
- Low enough "Q" to couple power into sample and to allow decades of dynamic range.



**Figure 22** Differences in the coupling efficiency of high and low quality factor circuits.

# Importance of PCD Calibration

- Correct for Circuit Non-linearities
  - SiC Dynamic range:  $>100,000 \Omega/\square$  to  $\sim 1 \Omega/\square$
- Provide Lifetime verses Injection Level Capability

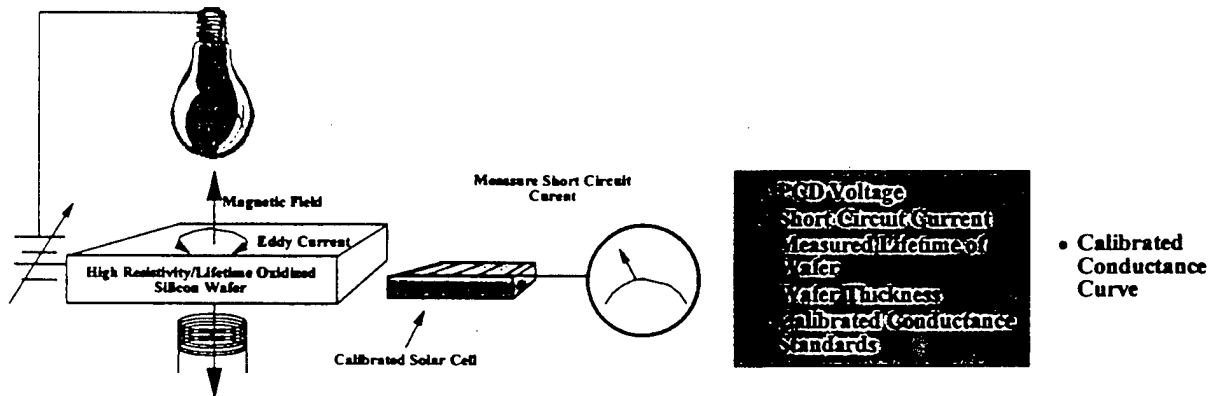


Figure 23 Calibration configuration for voltage to conductance conversion.

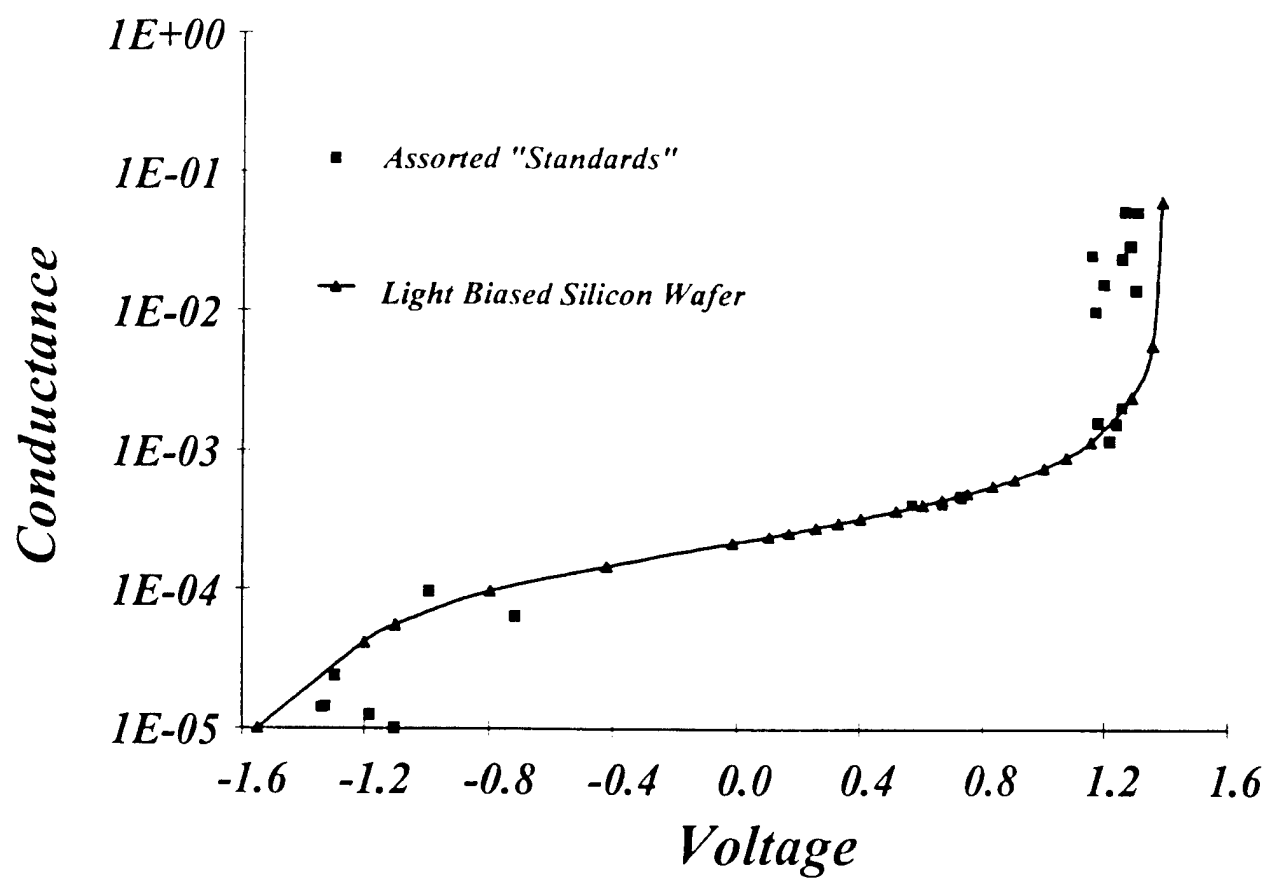


Figure 24 Conductance verses voltage calibration curve.

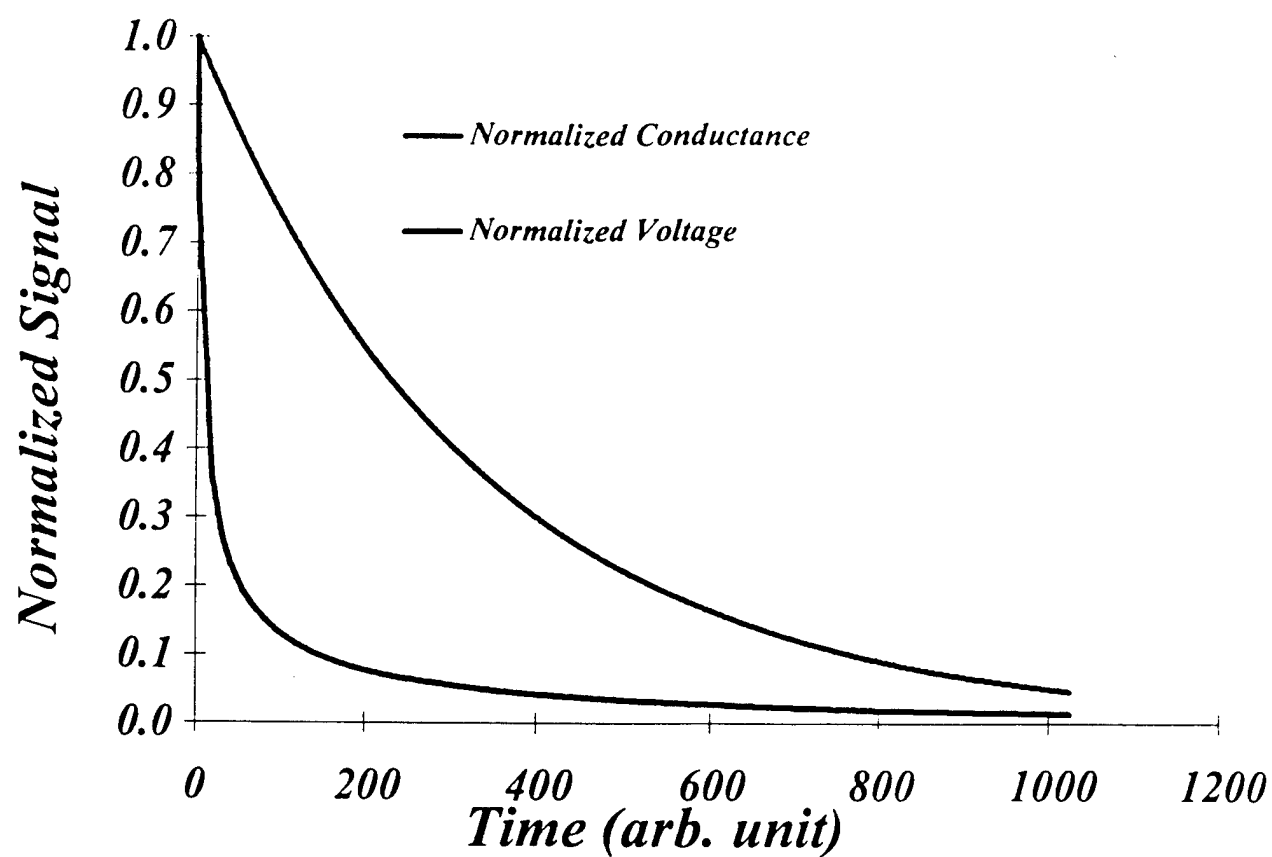


Figure 25 Possible errors due to uncorrected non-linearities in other circuits.

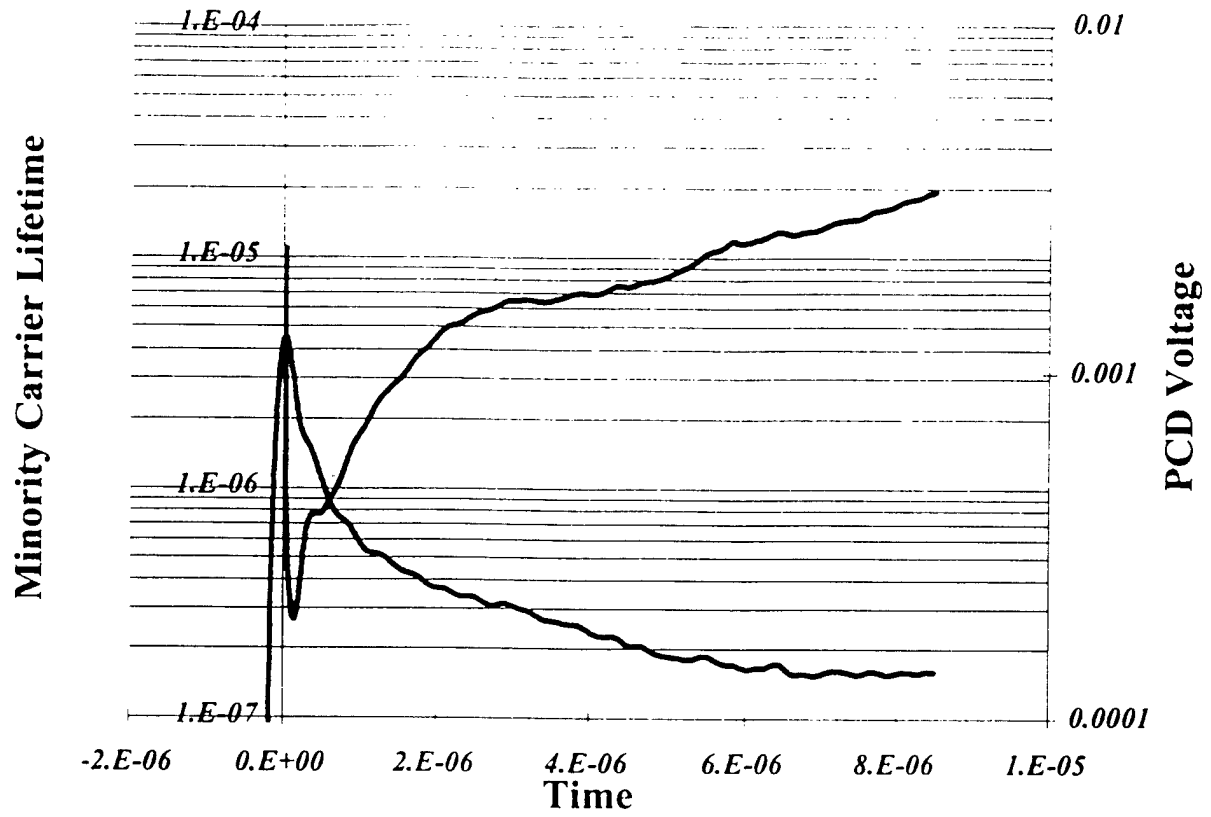


Figure 26 PCD voltage and lifetime verses time signals.

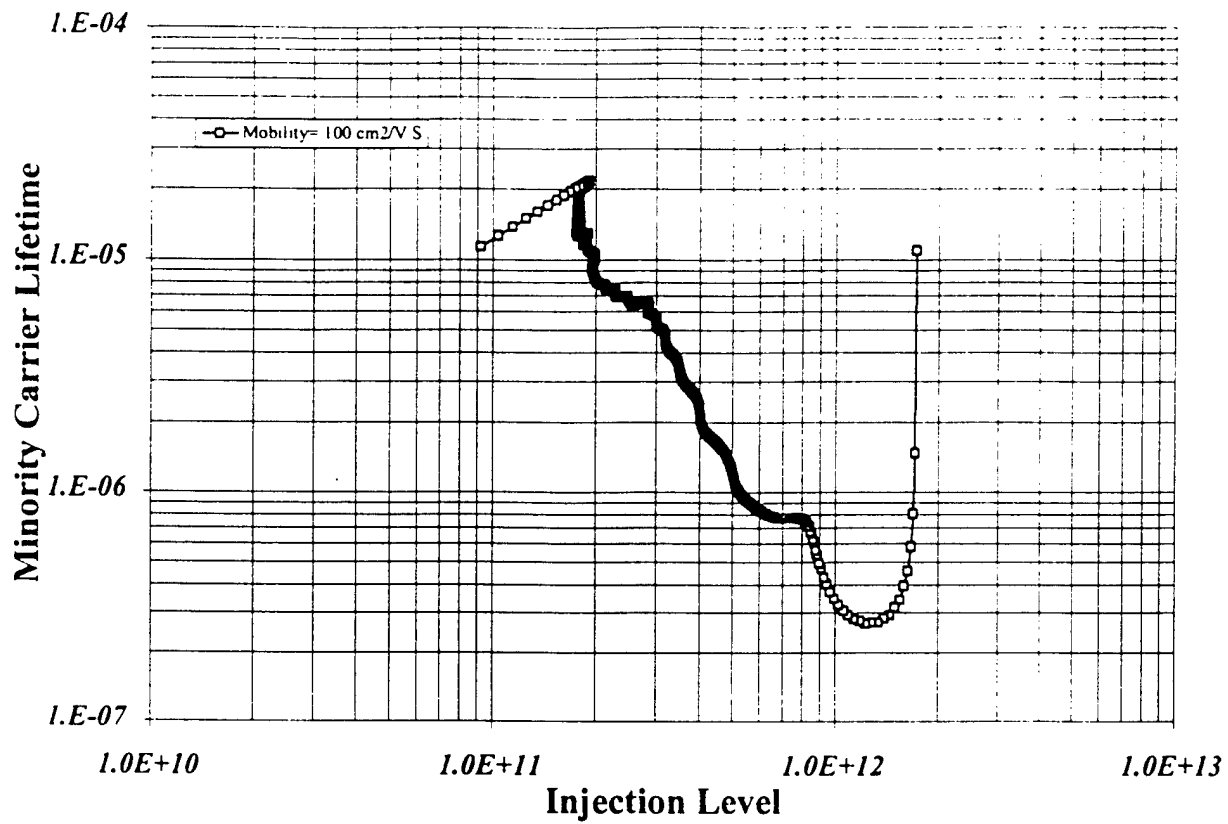


Figure 27 Lifetime verses injection level for the sample shown in figure 6.



Having developed the high frequency photoconductive decay system (PCD) and developed a calibration allowing conversion from a voltage transient to minority carrier lifetime verses injection level, we focused our efforts on examining the effects of injection level and doping on lifetime in SiC.

Before examining some experimental data, it is wise to summarize the effects of lifetime verses injection level for various types of defects present. Specifically, figure 28 shows a plot of minority carrier lifetime verses injection level for SiC. One sees that until the Auger limit, material with shallow traps present show a variation in lifetime with injection level, where as material with deep traps have lifetimes that are constant with injection level. This type of behavior, whether or not the lifetime has an injection level dependance, can be used to infer the deep level that controls the minority carrier lifetime.

The effect of doping can be seen in figure 29. As depicted in the upper part of figure 29, for a heavily doped material, the fermi level is positioned so that defects below it are filled with majority carriers (electrons in this example). As light is shown on the sample, the "traps" are depopulated, and are detected by the PCD system as a change in conductance. Note that in this case, there has been no minority carrier generation, so no minority carrier recombination can occur. However, a conductance decay can occur due to the "retrapping" of majority carriers. The time constant associated with this photoconductive decay is related entirely to the capture characteristics of the trap. Our DLTS measurements (see figure 30) have indicated the presence of deep states in high concentration, capable of fast, majority carrier capture.

On the other hand, for a low doped material (see lower part of figure 29), the fermi level is positioned such that majority carriers are not trapped by deep states. In this case, there is no depopulation of deep states by the light pulse and thus, no conductance transient. We will see

shortly, that this doping dependence is observed in bulk SiC wafers.

Figures 31-40 are pairs of plots of PCD voltage transients, minority carrier lifetime verses time (even numbered figures), and minority carrier lifetime verses injected carrier concentration (odd numbered figures) for various sheet resistance material. Sample J87-10 (figures 31 and 32) was very high resistivity and showed a very low lifetime ( $\sim 10$  nS) with no injection level dependence. This was explained above in terms of the fermi level position relative to the deep states. In this doping range, the deep states act as recombination centers in this sample.

Figures 33 and 34 represent the results from measurements on sample B73-10, a slightly higher doped sample. In this case, there is a slight injection level dependence in the range of  $2 \times 10^{12}$  to  $2 \times 10^{13} \text{ cm}^{-3}$ . Consistent with the proposed theory, not only is there an injection level dependence (due to the presence of shallow traps) but the minority carrier lifetime is larger,  $\sim 40$  to  $100$  nS.

Figures 35 and 36 represent a still higher doped sample, J54-15. This sample shows still more injection level dependence, ranging from  $10 \text{ } \mu\text{S}$  at  $2 \times 10^{11}$  to  $\sim 300$  nS at  $1.5 \times 10^{12} \text{ cm}^{-3}$ . Note that the injection level dependence of the heavier doped sample is stronger than either lighter doped sample, and the magnitude of the lifetime is higher as well.

Clearly this trend in lifetime verses injection level and magnitude of lifetime favors our theory of the fermi level covering up deep states as the doping is increased. This leaves higher lifetimes and a stronger injection level dependence for the heavier doped samples.

Finally, figures 37-40 show some aspects of anomalous behavior in these measurements due to slow retrapping of detrapped majority carriers. This sample, R21-12, shows a strong injection level dependence, that increases with injected carrier concentration from  $1 \times 10^{10}$  to  $1 \times 10^{12}$

then strongly decreases from  $1 \times 10^{13}$  to  $4 \times 10^{13}$ . The magnitude of the time constants is on the order of 10 mS. Since this high of a lifetime is comparable to very high quality, high resistivity silicon, this can not be a "minority" carrier lifetime. It clearly results from the slow recapture of majority carriers into deep states. Assuming the concentration of the defect is on the order of the injection level where a strong decrease in lifetime is observed,  $\sim 1 \times 10^{13} \text{ cm}^{-3}$ , the capture cross section would have to be on the order of  $1 \times 10^{-18} \text{ cm}^2$ . These trap parameters are extremely reasonable and probably describe very well this particular sample.

We have successfully constructed and measured PCD minority carrier lifetimes in bulk SiC. We have identified injection level and doping dependancies that infer a competition between deep and shallow defects. Short lifetimes with little injection level dependance was observed for high resistivity samples, where as long lifetimes with strong injection level dependancies was observed for heavier doped samples. Future work will attempt to relate DLTS measurements, EBIC and PCD to further identify the mechanisms of recombination.

## Effect of Defects on Minority Carrier Lifetime

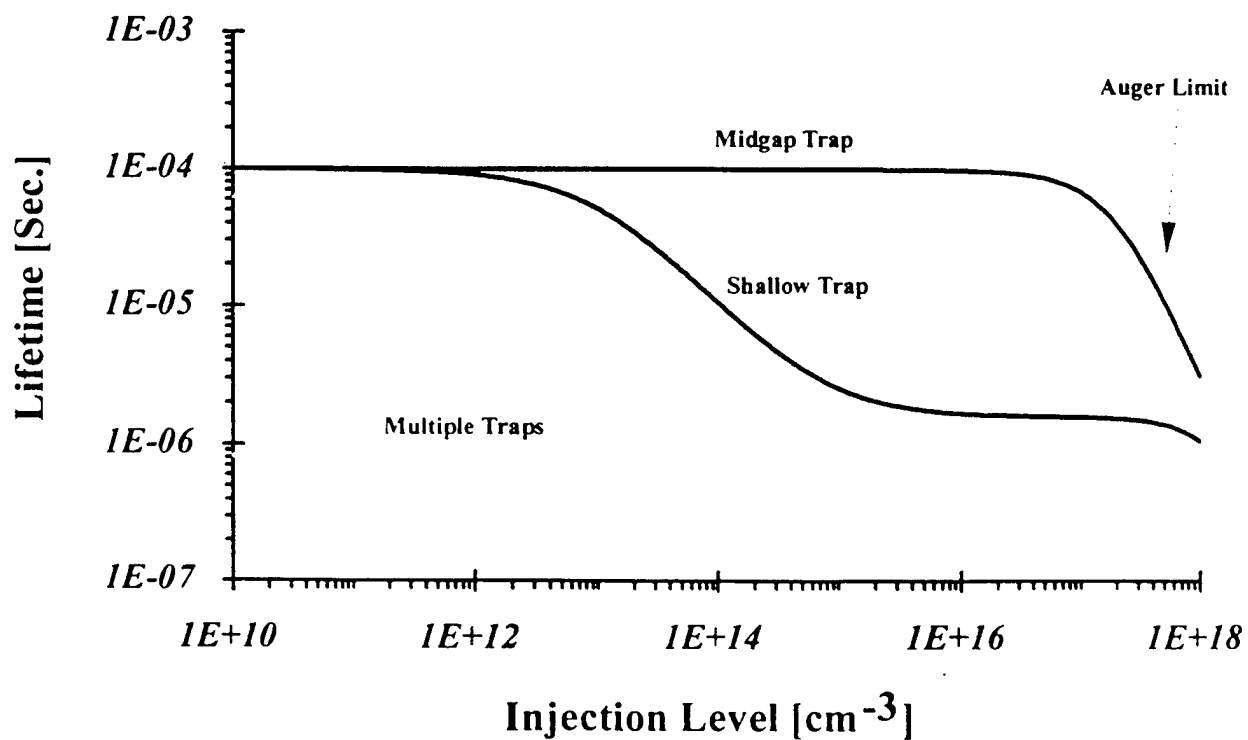
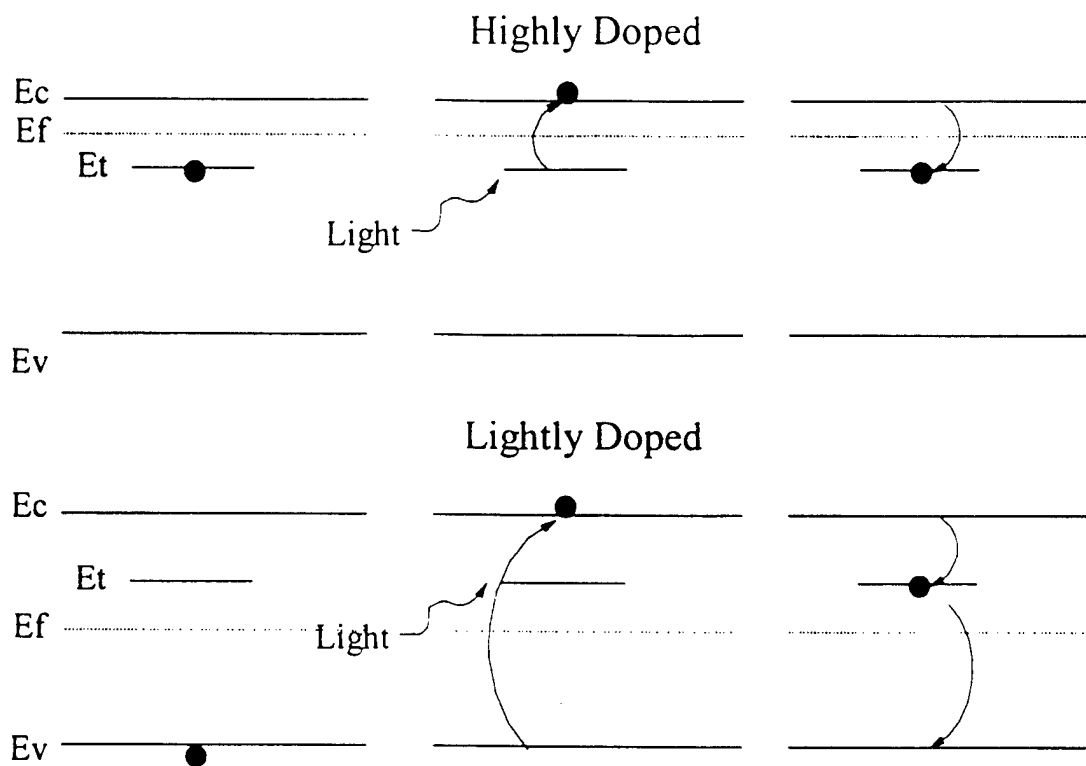


Figure 28 Injection level dependence versus trap depth in SiC.

# Role of Doping in Controlling Photoconductive Decay



**Figure 29** Schematic representation of fermi level verses doping and trap position.

## DLTS Spectra of Sample J40-9: 4H-SiC

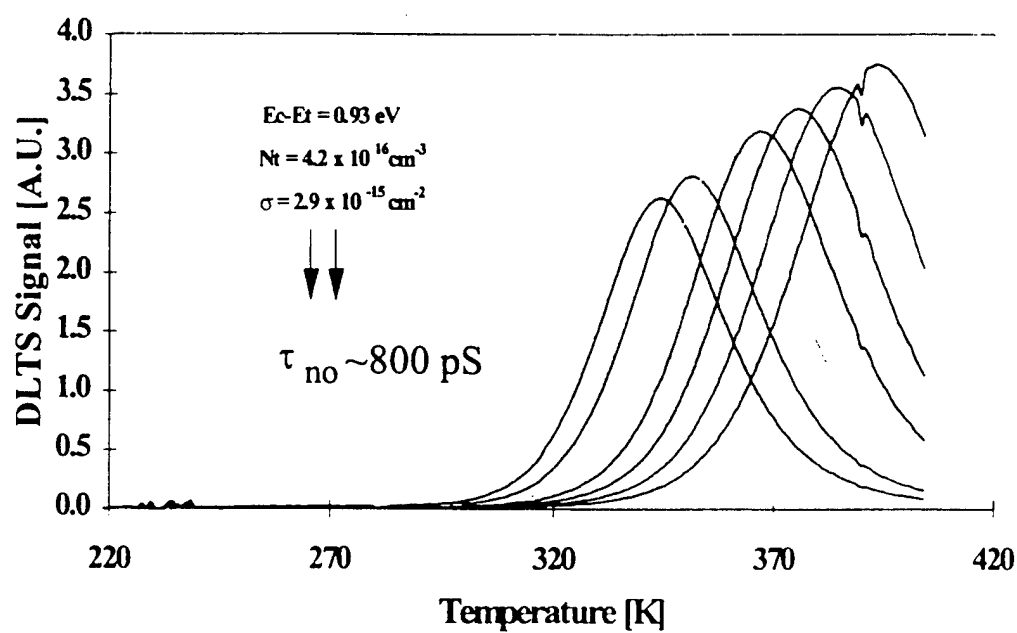


Figure 30 Deep defect detected in bulk SiC via DLTS.

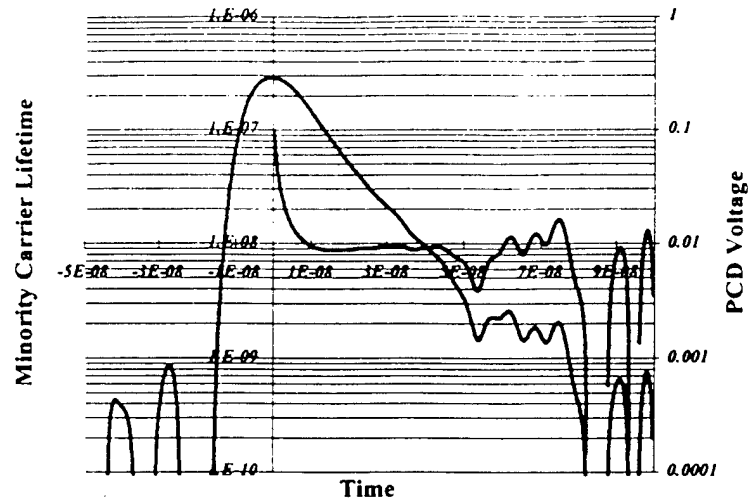


Figure 31 PCD voltage and lifetime verse time.

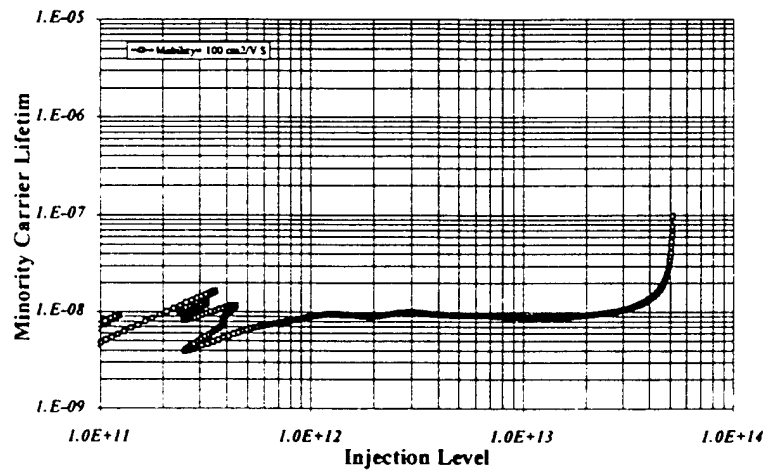


Figure 32 Minority carrier lifetime verses injected carrier concentration.

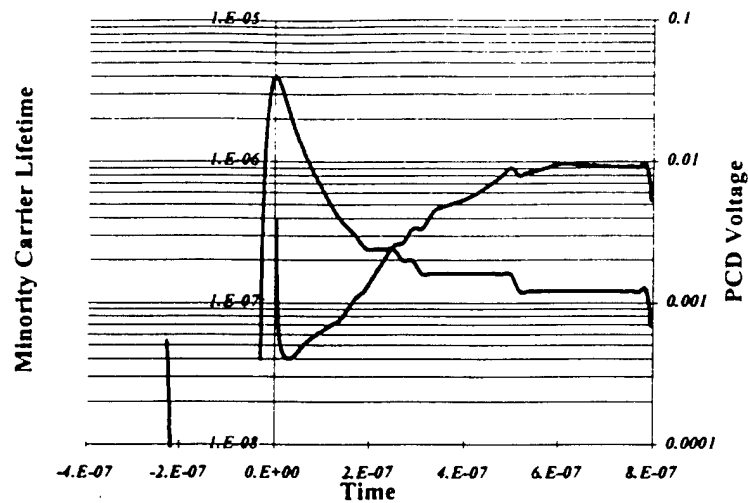


Figure 33 PCD voltage and lifetime verses time.

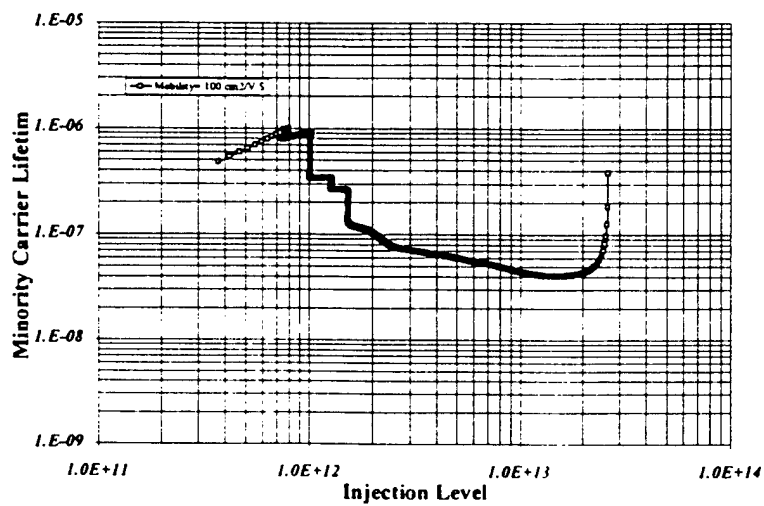


Figure 34 Lifetime verses injected carrier concentraion.



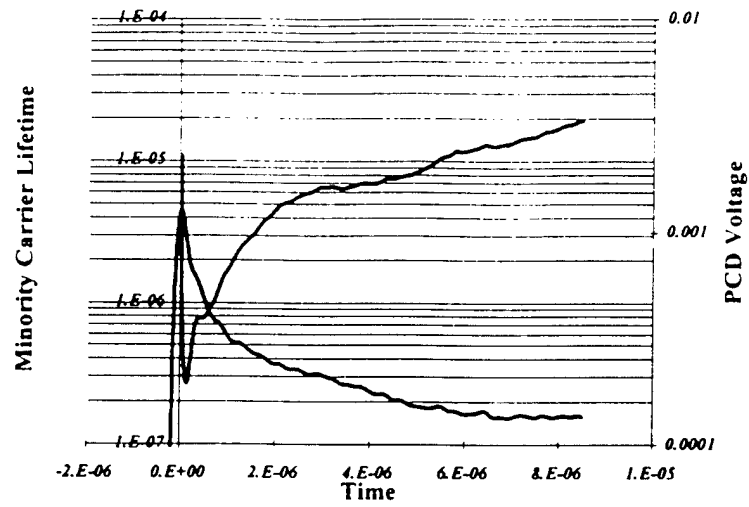


Figure 35 PCD voltage and lifetime verses time.

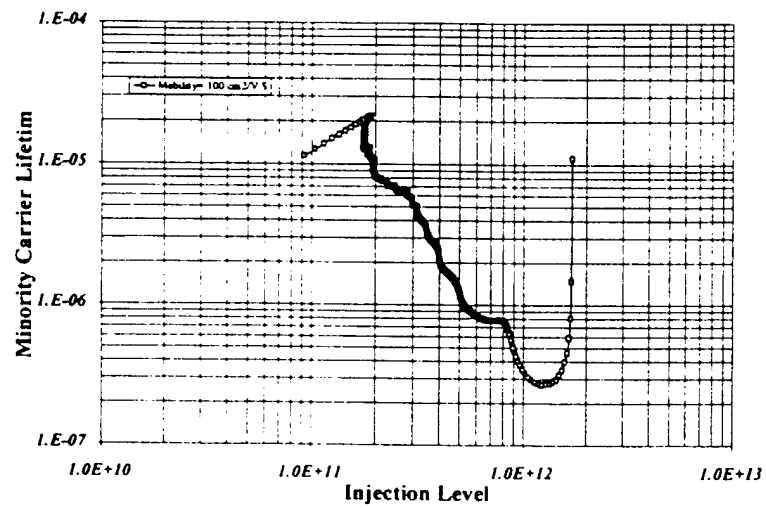


Figure 36 Lifetime verses injected carrier concentration

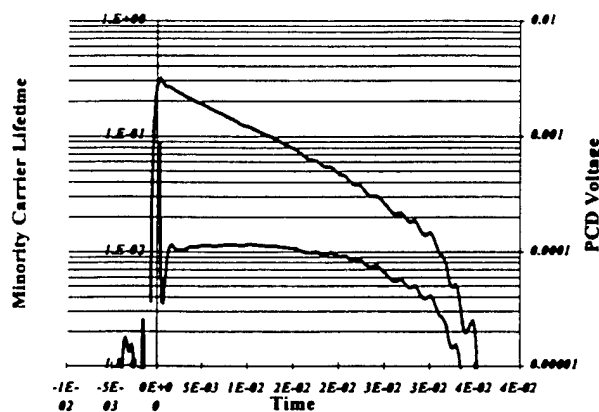


Figure 37 PCD voltage and lifetime verses time.

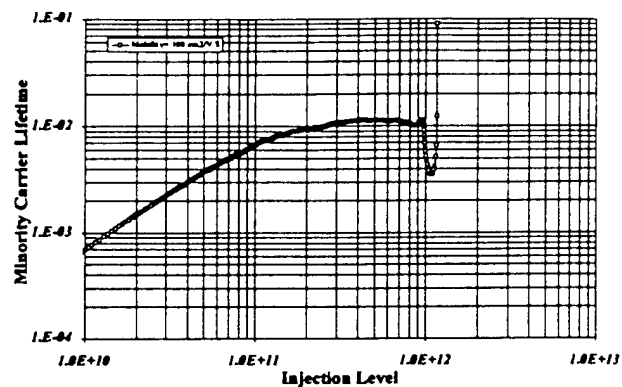


Figure 38 Lifetime verses injected carrier concentration.

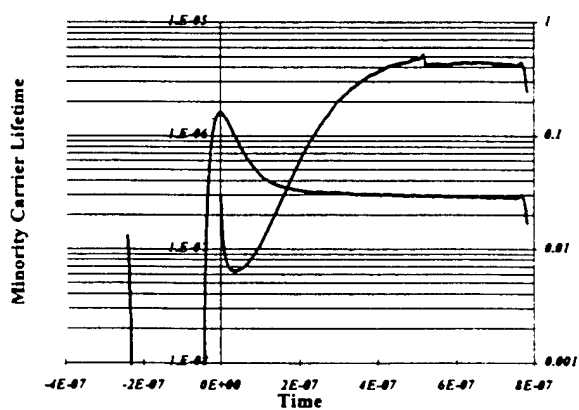


Figure 39 PCD voltage and lifetime verses time.

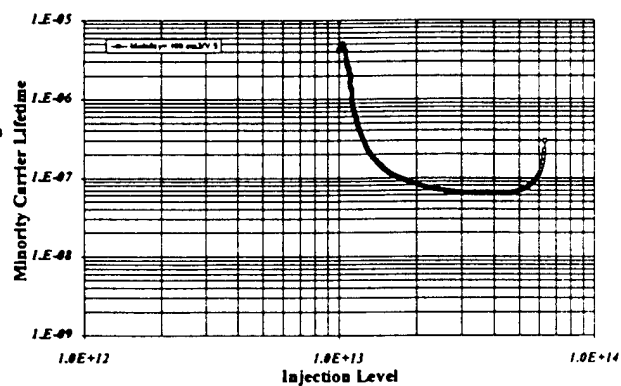


Figure 40 Lifetime verse injected carrier concentration.

## TRANSITION TEMPERATURES IN PLASTIC YIELDING AND FRACTURE OF SEMICONDUCTORS

P. PIROUZ<sup>1</sup>, L. P. KUBIN<sup>2</sup>, J. L. DEMENET<sup>3</sup>, M. H. HONG<sup>1</sup>, A. V. SAMANT<sup>1</sup>

<sup>1</sup>Department of Materials Science and Engineering, Case Western Reserve University,  
Cleveland, OH, 44106-7204, U.S.A..

<sup>2</sup>LEM, CNRS-ONERA, B.P. 72, Av. de la Division Leclerc, 92322 Châtillon Cedex, France.

<sup>3</sup>LMP, CNRS, SP2MI, Bd 3, Teleport 2, BP 179, 86960 Futuroscope Cedex, France

### ABSTRACT

Recent experiments on deformation of semiconductors show an abrupt change in the variation of the critical resolved shear stress,  $\tau_y$ , with temperature,  $T$ . This implies a change in the deformation mechanism at a critical temperature  $T_c$ . In the cases examined so far in our laboratory and elsewhere, this critical temperature appears to coincide approximately with the brittle-ductile transition temperature,  $T_{BDT}$ . In this paper, the deformation experiments performed on the wide bandgap semiconductor, 4H-SiC, over a range of temperatures and strain rates are described together with the characterization of induced dislocations below and above  $T_c$  by transmission electron microscopy. Based on these results, and those of Suzuki and coworkers on other compound semiconductors, some understanding of the different mechanisms operating at low and high temperatures in tetrahedrally coordinated materials has been gained, and a new model for their brittle-ductile transition has been proposed.

### INTRODUCTION

Recently, it has been possible to perform deformation experiments on a few (six) different compound semiconductors extending the deformation temperature to regions in which they are brittle. Specifically, Suzuki and coworkers have deformed InP, InSb, GaAs, and GaP using compression tests under hydrostatic pressure in order to prevent fracture of the deformation samples before they plastically yield [1-4]. Some low-temperature tests on GaAs under roughly the same conditions were actually performed some years ago by Rabier and coworkers [5,6]. In our deformation tests, Samant [7] investigated the plastic behavior of two wide bandgap semiconductors, 4H-SiC and 6H-SiC, by compression over a wide range of temperatures and strain rates. It should be mentioned that because single crystals of these two semiconductors were not available until recently, prior to the work of Samant, there were only a few reports of deformation tests on single crystal 6H-SiC and practically none on 4H-SiC. Some significant works that existed were reports by Fujita *et al.* [8] on compression experiments on Acheson-grown crystals over the temperature range 1300-1600°C, and creep tests on Cree-grown 6H-SiC by Corman [9]. In Samant's experiments, the rather high initial density of dislocations in the samples ( $\sim 10^3$ - $10^4$   $cm^{-2}$ ), careful alignment of the sample in the deformation jig, together with the use of very low strain rates, made it possible to deform the materials at temperatures hundreds of degrees below their usual range of BDT. The results of these experiments have been reported in Refs. [7,10,11]. More recently, Demenet repeated Samant's experiments on 4H-SiC (grown at Cree Research, Inc.) obtaining much more data in the temperature range 900-1360°C [12].

### EXPERIMENTAL PROCEDURES

The details of the experimental procedure for deforming the SiC crystals are given elsewhere (see Ref. [7]). Briefly, a single crystal ingot of 4H-SiC grown at the Cree Research, Inc. was oriented for single glide using X-ray diffraction. From the ingot,  $2.2 \times 2.2 \times 4.7$  mm<sup>3</sup> samples were cut and carefully polished on all faces. The compression tests were made over the temperature

range 900-1360°C at a strain rate of  $3.6 \times 10^{-5} \text{ s}^{-1}$ . Following the mechanical tests, thin foils parallel to the (0001) slip plane were prepared from the samples deformed at temperatures above and below the transition temperature  $T_c \approx 1100^\circ\text{C}$ . In addition to strain contrast experiments to characterize the Burgers vector of the dislocations, the large-angle convergent-beam electron diffraction (LACBED) technique was used to identify the nature of dislocation cores [13].

## RESULTS

Some of Demenet's results are shown in Fig. 1 in the form of a plot of  $\ln(\tau_y)$  vs.  $1/T$ .

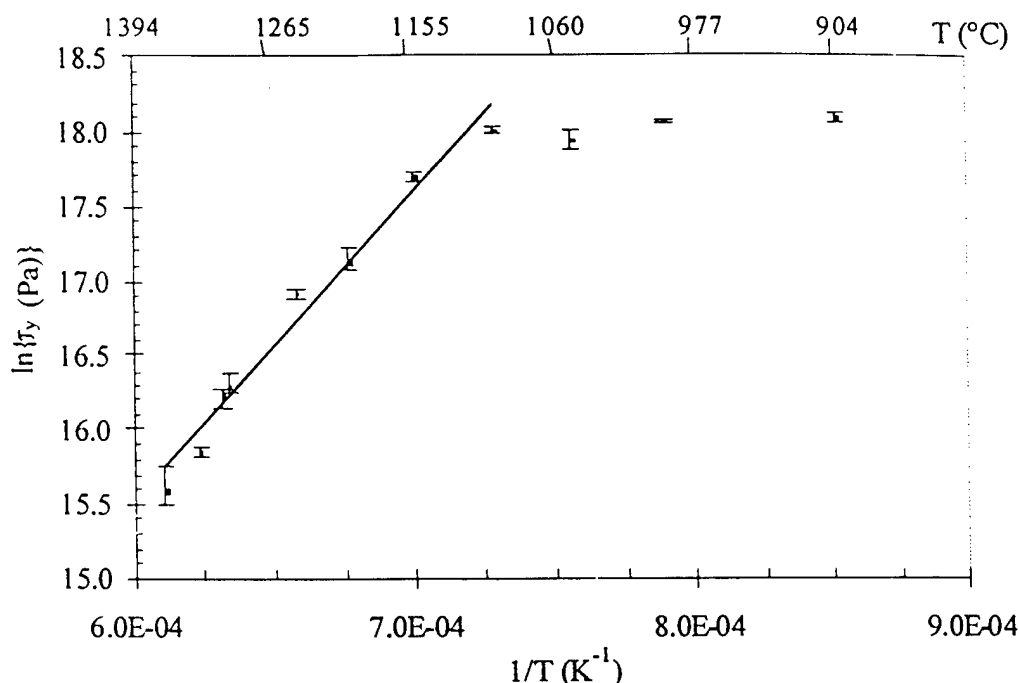


Fig. 1. Plot of  $\ln(\tau_y)$  vs.  $1/T$  for 4H-SiC deformed at a strain rate of  $3.6 \times 10^{-5} \text{ s}^{-1}$ .

As in previous experiments of Samant [7,10,11] on 4H- and 6H-SiC, there is a sharp transition at  $T_c \approx 1100^\circ\text{C}$ . It should be noted that while macroscopic plastic deformation of both 4H- and 6H-SiC polytypes is relatively easy at  $T > 1100^\circ\text{C}$ , it becomes very limited at  $T < 1100^\circ\text{C}$  and, when the samples have not failed catastrophically, deformation is very often accompanied by appearance of extensive microcracking. These observations indicate that the BDT temperature of both polytypes is  $\sim 1100^\circ\text{C}$ , consistent with experiments of Maeda and coworkers who concluded that the BDT temperature of 6H-SiC is above  $800\text{--}1000^\circ\text{C}$  [8,14]. Following the compression experiments [12], TEM of the deformed samples revealed that a very low density of dislocations was generated by deformation at  $T < T_c$  and these were predominantly single leading partials all with the same Burgers vector  $\mathbf{b}_l = 1/3[1\bar{1}00]$ . An example is shown in Figs. 2(a-c). The cores of five single partial dislocations produced by deformation at temperatures below  $T_c$  showed them to be silicon in every case. On the other hand, the samples deformed at  $T > T_c$  contained a high density of total dislocations all dissociated, i.e. they were in the form of leading/trailing pairs bounding a ribbon of stacking fault. The dislocations were predominantly screw type with a Burgers vector of  $\mathbf{b} = 1/3[\bar{2}110]$ ; an example of these dislocations is shown in Fig. 2(d).

## DISCUSSION

Similar to Fig. 1, plots of the critical yield stress versus temperature for all the six compound semiconductors mentioned previously show an abrupt transition at a critical temperature  $T_c$  [2,4,10]. It is possible that this transition exists in all the tetrahedrally coordinated materials and signifies a change of the deformation mode in the material. Also, intriguingly, in every case the transition temperature in the  $\tau_y(T)$  plot appears to coincide approximately with the brittle-to-ductile transition temperature,  $T_{BDT}$ , of that material, taking due account of the strain rate. In the following, we present a model to describe this transition in the yield stress and try to relate it to the BDT [15].

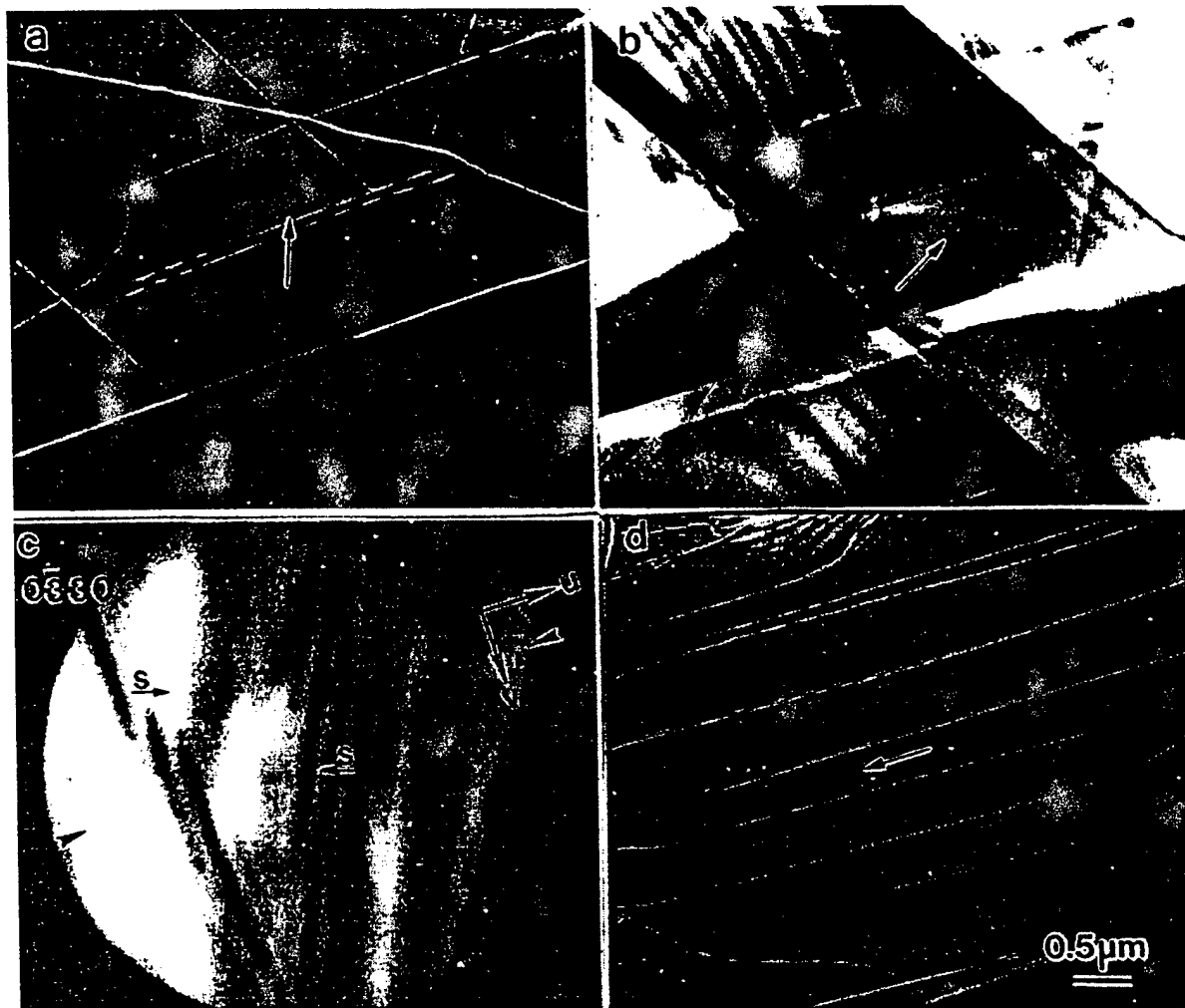


Fig. 2. (a) BF micrograph of dislocations in 4H-SiC deformed at 900°C showing single leading partial dislocations; (b) same region as (a) showing overlapping stacking faults; (c) a LACBED pattern of a single leading partial in (a). (d) BF micrograph of dislocations in 4H-SiC deformed at 1300°C showing dissociated (leading/trailing) total dislocations.

Dislocations in tetrahedrally-coordinated materials glide on the  $\{111\}$  slip plane in cubic crystals and  $(0001)$  slip plane in hexagonal materials and have Burgers vectors,  $\mathbf{b} = 1/2\langle 1\bar{1}0 \rangle$  in the former and  $\mathbf{b} = 1/3\langle 11\bar{2}0 \rangle$  in the latter. Because of the high Peierls potential in such crystals, the dislocations lie in the Peierls valleys that are parallel to  $\langle 1\bar{1}0 \rangle$  in cubic crystals and  $\langle 11\bar{2}0 \rangle$  in hexagonal crystals. As a result an ideal dislocation loop has a hexagonal shape with the segments parallel to the Peierls valleys, i.e. all the segments are  $60^\circ$  or screw dislocations. In all the

tetrahedrally coordinated materials that have been studied to date, the dislocations are dissociated according to the following reactions:

$$\frac{1}{2}\langle 1\bar{1}0 \rangle \rightarrow \frac{1}{6}\langle 1\bar{2}1 \rangle + \frac{1}{6}\langle 2\bar{1}\bar{1} \rangle$$

$$\frac{1}{3}\langle 2\bar{1}\bar{1}0 \rangle \rightarrow \frac{1}{3}\langle 1\bar{1}00 \rangle + \frac{1}{3}\langle 10\bar{1}0 \rangle$$

i.e. the partials are either  $90^\circ$  or  $30^\circ$  dislocations. The separation of the partials is of course determined by the stacking fault energy,  $\gamma$ , of the material. The latter ranges from  $\sim 2.5 \text{ mJ/m}^2$  in SiC to  $\sim 280 \text{ mJ/m}^2$  in diamond [16-18]. In addition, in the case of compound semiconductors, the core of all the dislocations (dissociated or non-dissociated) consists of only one atom species. Thus, an idealized dissociated dislocation loop, of say hexagonal SiC, will have the configuration shown in Fig. 3; depending on expansion or contraction, the inner and outer loops correspond to the leading and trailing partials, respectively. Notice that a  $60^\circ$  dislocation dissociates into a  $90^\circ$  and a  $30^\circ$  partial where both of the partials have the *same* core (either both Si(g) or both C(g)). On the other hand, a screw dislocation dissociates into two  $30^\circ$  partials that have *different* core structures (e.g. one is Si(g) while the other is C(g)). Also note that half the segments in both the inner and outer loops have a silicon core while the segments in the other half have a carbon core. We shall later argue that the core nature of the different partials in such dislocation loops plays a significant role in the mode of deformation that occurs in tetrahedrally-coordinated materials.

As can be seen in Figs. 2, our TEM results show that the microstructure of the SiC samples that were deformed below  $T_c$  consisted predominantly of only Si(g) leading partials while the microstructure of samples deformed above  $T_c$  consisted predominantly of dissociated screw dislocations (leading/trailing pairs). Let us now consider the production of dislocations during deformation of such a tetrahedrally-coordinated crystal. In general, the easiest way to produce dislocations in a crystal that contains appropriate sources is by the Frank-Read mechanism. However, if, as argued in this paper, only partial Frank-Read sources are activated (by the operation of the leading partial dislocations only) at low temperatures, then such a source will not be a multiplication site for dislocations but can operate only once. Subsequently, nucleation of dislocations will occur in the bulk or from the sample surfaces.

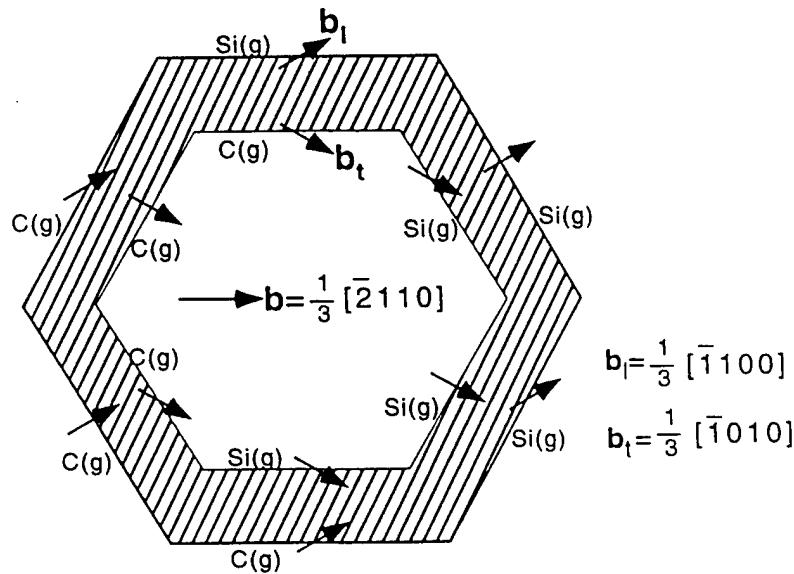


Fig. 3. A dissociated hexagonal loop on the (0001) slip plane in SiC.

In the energetics of dislocation nucleation, thermal activation is often thought to play a negligible role. The reason for this is thought to be that the available thermal energy,  $kT$ , at a temperature  $T$  is too small compared to the large energy barrier,  $\Delta H_n$ , required for dislocation nucleation. In terms of the reaction rate theory, thermally activated processes are statistical

phenomena whereby atoms that vibrate with a frequency  $\nu_0$  ( $\sim 10^{13} \text{ s}^{-1}$ ) have a Boltzmann probability  $\exp(-\Delta H_n/kT)$  of overcoming the energy barrier. Accordingly, the frequency,  $\nu$ , with which such an activation will occur is given by  $\nu = \nu_0 \exp(-\Delta H_n/kT)$ , i.e. the mean time,  $t$ , during which a successful activation occurs is  $t = 1/\nu = (1/\nu_0) \exp(\Delta H_n/kT)$ . For dislocation nucleation, the energy barrier,  $\Delta H_n$ , is thought to be so large ( $\geq 100kT$ ) that the time  $t$  for a successful operation becomes unreasonably large (e.g.,  $t \approx 2.7 \times 10^{30} \text{ s}$  for an activation enthalpy of  $100kT$ ). However, when a shear stress,  $\tau$ , is applied to the crystal, the energy barrier to overcome decreases by an amount  $\alpha\tau V^*$ , where  $V^*$  is the activation volume  $[= -(\partial H/\partial \tau)_T]$  and  $\alpha\tau$  is the stress concentration at a heterogeneity (e.g. scratch at the surface), to become  $\sim (\Delta H_n - \alpha\tau V^*)$ . Thus, the probability of overcoming it becomes  $\exp[-(\Delta H_n - \alpha\tau V^*)/kT]$  and the frequency of successful dislocation nucleation events will be:

$$\nu = \nu_0 \exp\left[-(\Delta H_n - \alpha\tau V^*)/kT\right] \quad \dots(1)$$

Based on the experimental results, we shall assume that, in the above equation, the leading and trailing partials have different activation enthalpies for dislocation nucleation,  $\Delta H_n^l$  and  $\Delta H_n^t$ , respectively, and  $\Delta H_n^l < \Delta H_n^t$ . In addition, the resolved shear stress on the leading and trailing partial dislocations will be different in Eq. (1) because they have different Burgers vectors.

Since our experiments were performed on hexagonal SiC, we shall use this material as an example, but the arguments are essentially general and can be applied to other semiconductors. Fig. 4(a) shows schematically the orientation of the parallelepiped sample used in our compression experiments. The sample is oriented for single glide, i.e. an orientation in which the  $(0001)\langle\bar{2}110\rangle$  system is primarily activated. The dislocations most probably nucleate heterogeneously as half-loops from the crystal surface; an example of one (denoted as A) on a particular  $(0001)$  slip plane is shown in Fig. 4(a). For comparison, the nucleation of a dislocation (full-)loop (denoted as A') on the same  $(0001)$  slip plane within the sample is also shown. In fact, nucleation of four types of loops on a  $(0001)$  slip plane may be envisaged as illustrated in Fig. 4(b). In cases A and A', only the leading partial has nucleated while in cases B and B', nucleation of the leading partial has been followed by that of the trailing partial.

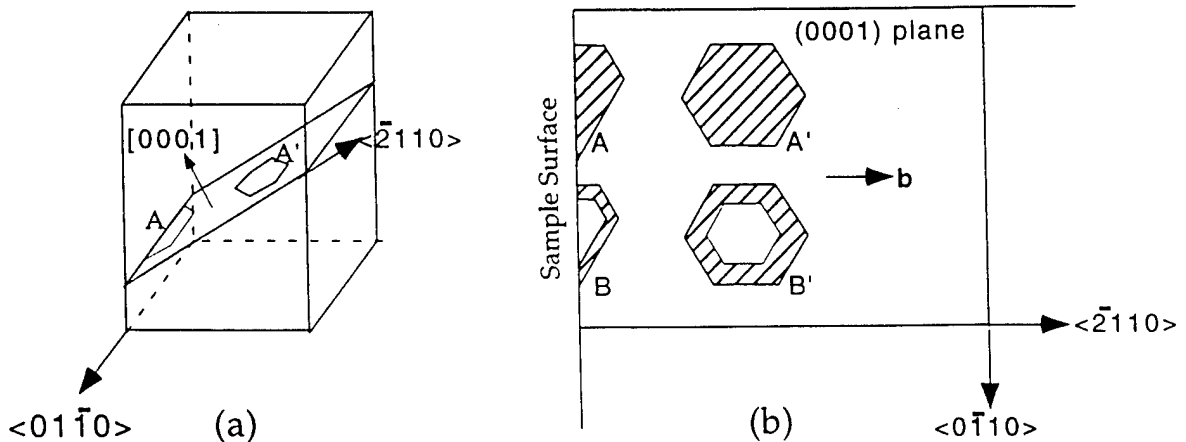


Fig. 4. (a) The geometry of a deformation sample oriented for single glide; (b) four possible ways of dislocation nucleation on the slip plane.

The formation of a dislocation loop presumably takes place by, first, the nucleation of the leading partial followed by the nucleation of the trailing partial. Assuming that intrinsic faults are favored over extrinsic ones, then the order of nucleation of the two partials can be determined from the Thomson tetrahedron [19]. It is important to note that once the leading partial forms, it creates a stacking fault behind it that changes the state of the lattice for nucleation of the trailing partial. The stacking fault of course adds an extra stress term,  $\gamma/b$ , to the external applied stress that should make it simpler for the trailing partial to nucleate. As we said, it will be assumed that  $\Delta H_n^l$  and  $\Delta H_n^t$  are different and that  $\Delta H_n^l < \Delta H_n^t$ . In fact, as shown in Ref. [20], there is some independent evidence for this hypothesis. There is, however, even more evidence for a related property of the leading and trailing partials in tetrahedrally coordinated crystals: the difference in their mobilities (for the case of Si and Ge, see, e.g., [21,22]). It appears that this difference increases as the temperature decreases. Of particular importance is the mobility difference between the two  $30^\circ$  partials of a dissociated screw dislocation where it is found that, even in elemental semiconductors, Si and Ge, the leading  $30^\circ$  partial has a higher mobility than the trailing  $30^\circ$  partial. This implies that the activation enthalpies for glide of partial dislocations,  $\Delta H_g^l$  and  $\Delta H_g^t$ , are also different and that  $\Delta H_g^l < \Delta H_g^t$ . The reasons for the differences in mobility and nucleation of the two partials are not really clear, but they probably have a similar origin. One obvious difference is the presence of a stacking fault after the formation of the leading partial that provides a different local environment for nucleation of the trailing partial. However, it is unlikely that the nucleation of a dislocation in a faulted region of the crystal will be significantly different from nucleation in a perfect crystal. Moreover, as was mentioned before, the presence of a stacking fault provides an extra stress term that should actually help the nucleation of the trailing partial. Another possibility is that the formation (and glide) of the leading partial may result in the creation of point defects in its wake (i.e. in the faulted region) which would have a much more significant effect on the local environment in which the trailing partial is nucleated. These point defects need not of course be extrinsic but can be intrinsic ones such as jogs or anti-phase defects (APDs) [23,24]. It should be mentioned that the interaction of point defects with dislocations and its effect on dislocation mobility goes back to the early works of Celli *et al.* [25] or Rybin and Orlov [26] on materials with a high Peierls barrier. Also, in the late seventies and eighties, the Soviet scientists performed many experiments on Si and Ge showing that the region of a crystal swept by a moving dislocation is significantly different from a virgin material, thus affecting the motion of subsequent dislocations (see, e.g., [27]). Some important evidence comes from Kisielowski's electron spin resonance (ESR) experiments that revealed the generation of point defects by screw dislocations in silicon [28]. In fact, in his classic review of dislocations in semiconductors, Alexander emphasizes that a consideration of the dislocation/point defect interactions is essential to an understanding of the physics of dislocations in these materials [29]. It is also important to realize that the point defects usually annihilate (or anneal out) at higher temperatures and their interaction with dislocations becomes less effective.

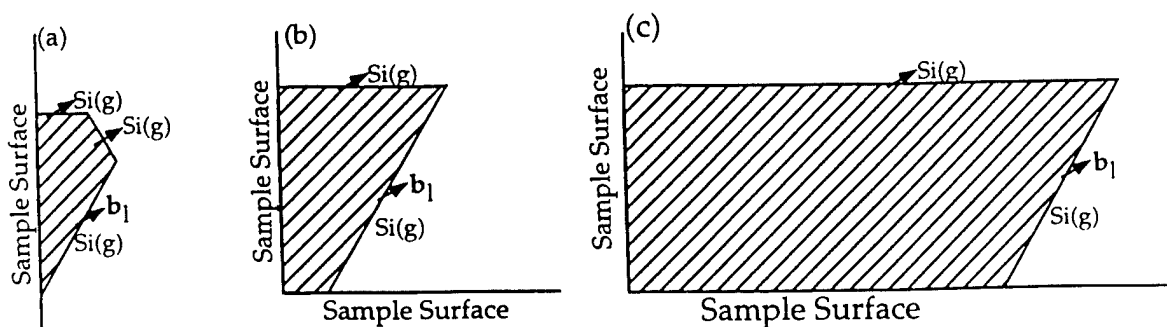


Fig. 5. Nucleation and expansion of a leading partial dislocation half-loop from the surface of the crystal at  $T < T_c$ .



In the case of compound semiconductors, where the atomistic core of the leading and trailing partials may be different, the core nature is another factor that must be taken into account in considering dislocation nucleation. Thus, in the case of SiC, the partial with the silicon core may have a smaller activation energy than the partial with the carbon core. As was mentioned before, half of a partial loop (with any Burgers vector) has a silicon core while the other half has a carbon core (Fig. 3). We suggest that, in the case of SiC, the Si(g) half loop of the leading partial (whose Burgers vector is determined from the Thomson tetrahedron) is preferentially nucleated as compared to a completely C(g) or a mixed Si(g)/C(g) half-loop (see Fig. 5(a)).

Assuming that at  $T < T_c$ , only the leading Si(g) partial (Burgers vector  $b_l$ ) is nucleated, then the sequence of events is illustrated in Fig. 5. After its nucleation from the sample surface (Fig. 5(a)), the half-loop expands and, because of the different mobilities of the segments, the semi-hexagonal shape of the half-loop is distorted. Assuming that the  $90^\circ$  Si(g) partial has a higher mobility than the two adjoining  $30^\circ$  partials, the configuration of the half loop at a later stage becomes something like that shown in Fig. 5(b). In Fig. 5(c), the  $90^\circ$  partial has moved out of the specimen and the lower  $30^\circ$  segment - that has been assumed to be more mobile than the upper  $30^\circ$  segment - is in the process of moving out. The final outcome will be a preponderance of  $30^\circ$  Si(g) dislocations left on different (and parallel) (0001) planes. Note that only a few partials can exist on each particular (0001) plane (Fig. 4(a)) because each partial drags a stacking fault behind it and the initial source (AD in Fig. 5(a)) is de-activated as a dislocation source.

Now consider the nucleation of a full half-loop from the sample surface (B in Fig. 4(b)) at  $T > T_c$ . The atomistic detail of the half-loop B in Fig. 4(b) is shown in Fig. 6 where the core of all the half-loop segments are shown reconstructed.

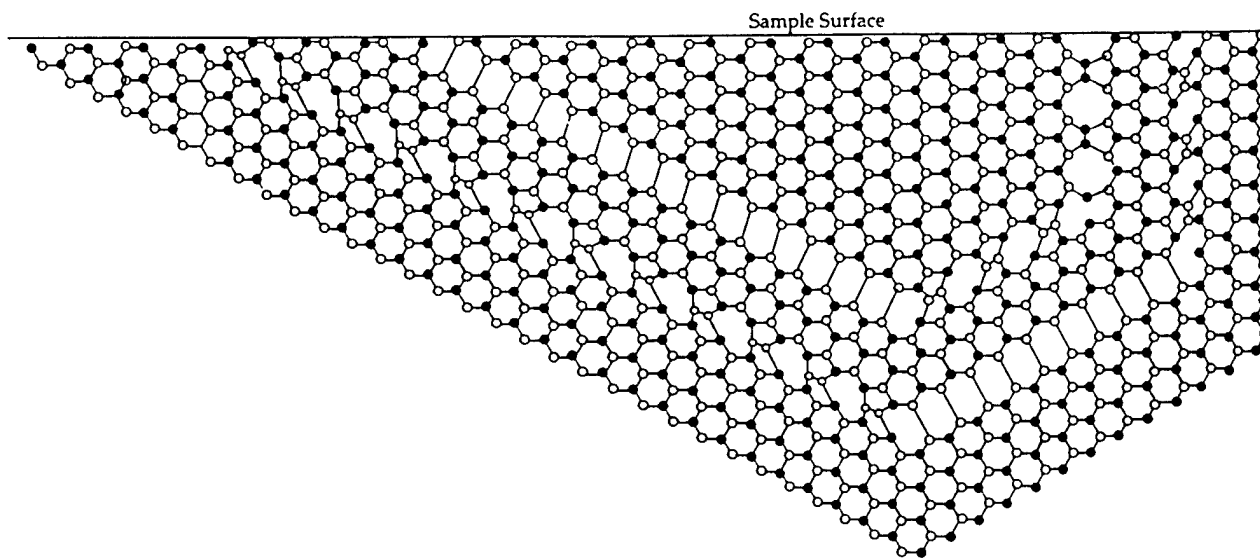


Fig. 6. Schematic illustration of the atomistic detail of a dissociated (leading/trailing) dislocation half-loop nucleated from the surface of the crystal at  $T > T_c$ .

The expansion of the perfect dislocation half-loop on the (0001) slip plane is shown in Fig. 7. Here, a dissociated dislocation half loop, ABCD, nucleates from the surface (7(a)) and expands (7(b)) until the mobile segments run out of the sample (Fig. 7(c)) leaving only the slow dissociated screw dislocation on the (0001) slip planes. In this figure, additional assumptions have been made that mobility of the upper  $90^\circ$ Si(g)/ $30^\circ$ Si(g) segment is higher than that of the lower  $30^\circ$ Si(g)/ $90^\circ$ Si(g) segment which in turn is higher than the topmost  $30^\circ$ Si(g)/ $30^\circ$ C(g) screw segment. The final configuration will be a preponderance of  $30^\circ$ Si(g)/ $30^\circ$ C(g) screw dislocations parallel to the  $[\bar{2}110]$  direction in the deformed crystal. Clearly, a better knowledge of the partial mobilities is essential to draw clearer conclusions.

The next problem to consider is the possible relation between the transition in the  $\tau_y(T)$  plot and the BDT temperature. When a load is applied to a crystal, it is initially deformed elastically whereby elastic energy is stored in the crystal. This stored elastic energy is released if the load is taken off to let the crystal relax. If, however, loading is continued, at a rate  $\dot{\tau}$ , and the stored energy continuously increases, there are two main competing ways for the crystal to relax and decrease its overall energy. One way is by brittle fracture of the crystal whereby the energy is consumed in creating two new surfaces as a crack forms and propagates.

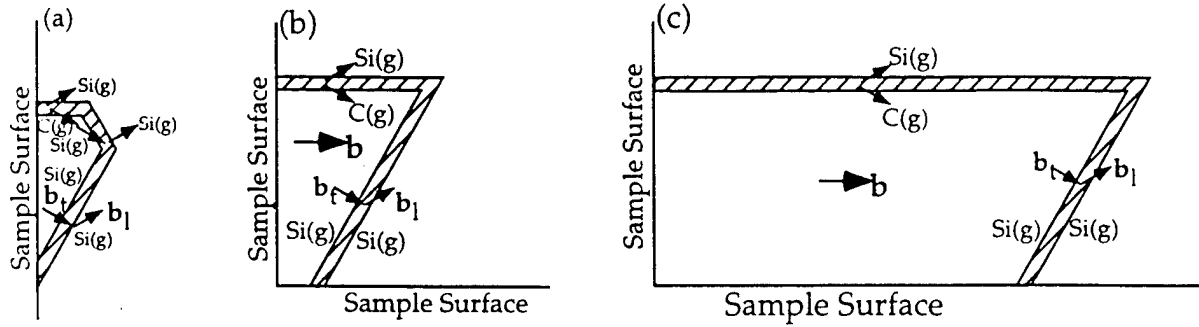


Fig. 7. Nucleation and expansion of a dissociated (leading/trailing) dislocation half-loop from the surface of the crystal at  $T > T_c$ .

The second way for the release of the stored elastic energy is to move pre-existing dislocations or nucleate and move fresh (as well as pre-existing) dislocations. The occurrence of brittle fracture versus plastic yielding of a crystal is determined by a competition between these two ways of releasing the stored elastic energy. In the case of crack propagation, the Griffith criterion can be written in the form:

$$\frac{(1 - \nu^2) K_{eff}^2}{E} \geq 2\gamma_s \quad \dots(2)$$

where  $\nu$  is the Poisson's ratio,  $E$  is the elastic modulus,  $\gamma_s$  is the surface energy and  $K_{eff}$  is the effective stress intensity factor given by [30]:

$$K_{eff} = K_{app} - K_d \quad \dots(3)$$

with:

$$K_{app} = \sqrt{\pi a} \sigma_{app} \quad \dots(4)$$

$\sigma_{app}$  being the applied tensile stress and  $a$  the crack half-length.  $K_d$  in Eq. (3) is shielding of the crack tip introduced by the compressive stress of the dislocations around it and results in a reduction of the applied tensile stress on the crack tip.

In the above conventional picture, brittleness versus ductility of a loaded crystal is considered as a competition between shearing of the crystal by dislocation motion and rupture of the bonds at the tip of a microcrack within the crystal. The general view is that the stress needed for plastic yielding (i.e., the yield stress  $\tau_y$ ) is strongly temperature dependent and decreases rapidly with increasing temperature while the (tensile) stress required for fracturing the bonds,  $\sigma_F$  (and the corresponding shear stress  $\tau_F$ ), has a much weaker temperature dependence. As a result,  $\tau_F(T)$  and  $\tau_y(T)$  intersect at a critical temperature  $T_{BDT}$ , usually known as the brittle-to-ductile transition (BDT) temperature where  $\tau_F < \tau_y$  at  $T < T_{BDT}$  (the brittle regime) and  $\tau_y < \tau_F$  at  $T > T_{BDT}$  (the ductile regime). In the model described in this paper (as illustrated in Fig. 8) the BDT, at least in tetrahedrally-coordinated materials, is determined by a competition between nucleation and propagation of leading partial dislocations versus the nucleation and propagation of perfect

(total) dislocations (i.e. that of the trailing partial). As shown by Eq. (1), such a nucleation and propagation of dislocations (partial or perfect) is temperature and stress dependent. Thus, the rupture of atomic bonds enters the picture only indirectly. It is argued that, in a constant strain rate experiment, if the temperature and stress are not sufficient to nucleate the trailing partial (and thus the perfect) dislocations, then the increasing stress will eventually reach a sufficient value ( $\sigma_F$ ) to rupture the bonds at the crack tip leading to its propagation. In such a regime, leading partial dislocations may well nucleate at the crack tip (as well as in other favorable sites), but if, at any particular site, the leading partial is not followed by nucleation of the trailing partial, then the source will shut off and stop operating. The consequence is that dislocation nucleation will soon stop and plastic deformation is limited to the strain produced by the few partial dislocations generated before the sources stopped operating. Meanwhile, the work done on the crystal by the external load continues to increase the elastic strain energy in the crystal until the critical strain energy release rate is reached and the crystal gives in and fractures. In this way, the details of bond rupture at the crack tip or temperature dependence of  $\sigma_F$  (or  $\tau_F$ ) are irrelevant to the problem of brittle-to-ductile transition.

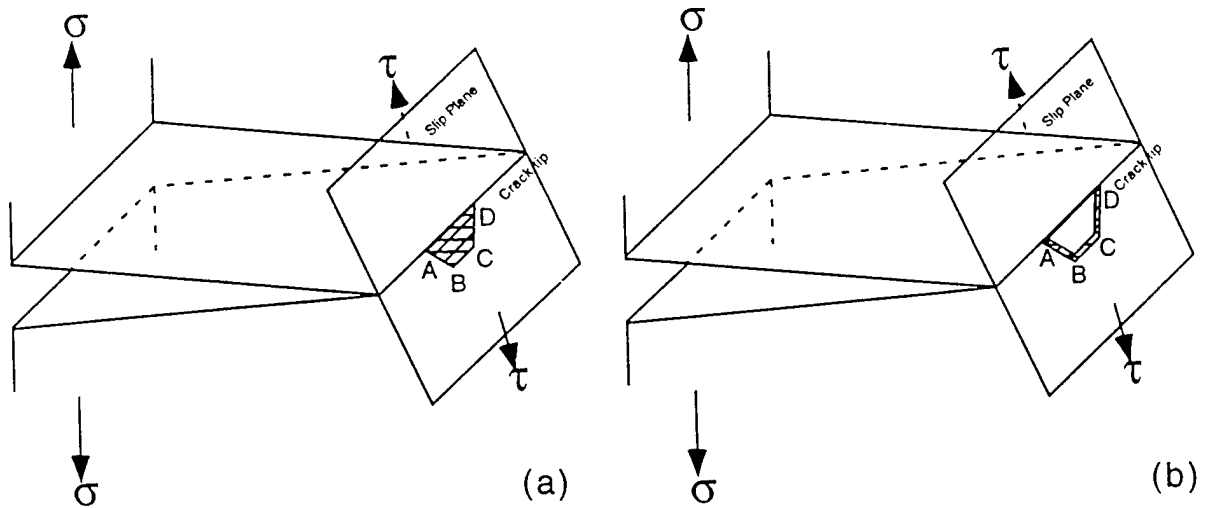


Fig. 8. Schematic illustration of dislocation nucleation at a crack tip under mode I loading: (a) at  $T < T_c$ , (b) at  $T > T_c$ .

What is of primary importance is the temperature dependence of  $\tau_n^l$  and  $\tau_n^t$ , where  $\tau_n^l$  and  $\tau_n^t$  are the minimum shear stresses required to nucleate the leading and the trailing (i.e., the total) dislocation, respectively. The BDT temperature is given by the intersection of  $\tau_n^l(T)$  and  $\tau_n^t(T)$  plots. Now, when an increasing  $K$  (related to the shear stress,  $\tau$ , by  $K = \beta^{-1}\tau$ , where  $\beta$  is a geometrical factor) is applied at a rate of  $\dot{K}$ , the question to be asked is whether a successful (dislocation) nucleation event will occur during the time period in which  $K$  increases from its initial value  $K_o$  to the stress intensity factor  $K_{lc}$  at which the crystal fails (see, Fig. 9). Note that as  $K$  (i.e.,  $\tau$ ) increases, the effective activation enthalpy for dislocation nucleation decreases. Thus, the BDT is determined by a competition between the first occurrence of two events: either (1)  $K$  reaches  $K_{lc}$  first and catastrophic failure occurs, or (2)  $(\Delta H_n^t - \alpha\beta KV^*)$  decreases sufficiently to result in the nucleation of the (trailing partial) dislocation (at a stress intensity factor  $K = K_\gamma$ ). The time taken for  $K$  to reach  $K_{lc}$  is  $(K_{lc} - K_o)/\dot{K}$  (Fig. 9). Thus, the condition for BDT is that:

$$t \leq \frac{(K_{lc} - K_o)}{\dot{K}}$$

At  $T_{BDT}$ , the stress intensity factor reaches the value  $K=K_Y$  to nucleate dislocations and thus  $t = (K_Y - K_o)/\dot{K}$  giving:

$$\frac{1}{v_o} \exp\left(\frac{\Delta H_n^i - \alpha \tau_Y V^*}{kT_{BDT}}\right) = \frac{(K_Y - K_o)}{\dot{K}}$$

i.e.:

$$\dot{K} = v_o (K_Y - K_o) \exp\left(-\frac{\Delta H_n^i - \delta K_Y}{kT_{BDT}}\right) \quad \dots(5)$$

where  $\delta = \alpha \beta V^*$  is a constant. Thus, a plot of  $\ln(\dot{K})$  versus  $1/T_{BDT}$  should be a straight line with a slope  $\left[\frac{(\Delta H_n^i - \delta K_Y)}{k}\right]$ , and an intercept  $\ln[v_o (K_Y - K_o)]$ . Since experiments show that a plot of  $\ln(\dot{K})$  versus  $1/T_{BDT}$  has a slope equal to that of (total) dislocation glide (see, e.g., [31]), then Eq. (5) would imply that the activation enthalpy for trailing partial nucleation,  $\Delta H_n^{eff} = (\Delta H_n^i - \delta K_Y)$ , is approximately the same as that for dislocation glide.

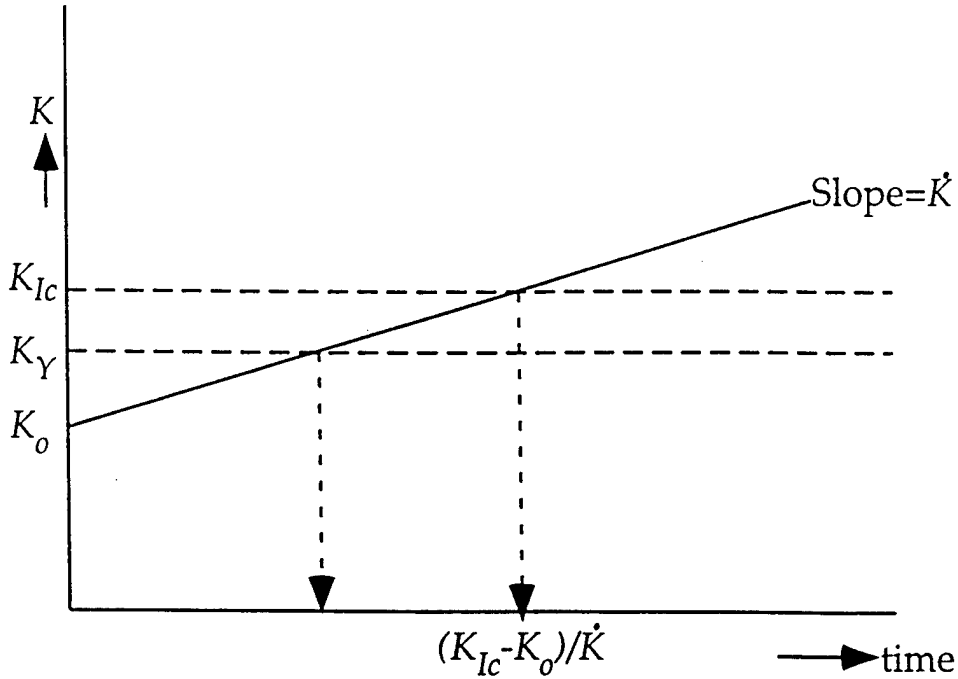


Fig. 9. Schematic plot of  $K$  versus time in a constant  $\dot{K}$  experiment.

A number of experiments have shown that when high quality (very low dislocation density) semiconducting crystals are deformed under hydrostatic pressure, there is a range of temperatures,  $T_{BDT} > T > T_H$ , over which the crystal is extremely brittle [3,4]. This is so much that if the crystals have not already fractured during the deformation test, then they usually shatter into small pieces during decompression of the sample cell. An example is GaAs that was found to be extremely brittle between 300 to 400 K even when the confining pressure was increased up to 1.2 GPa; consequently, it has been very difficult to prepare thin foils and perform TEM experiments on the samples deformed in this range [3]. However, interestingly, below this range, i.e. at temperatures less than  $T_H$ , it again becomes possible to deform the crystal, albeit it at very high stresses and under hydrostatic pressure. Thus, Suzuki *et al.* [3] could deform GaAs at 300 K under a confining pressure of 400 MPa! TEM of samples deformed at these very low temperatures show a microstructure consisting of predominantly *perfect* screw dislocations. At first sight, this appears to be contrary to the argument put forward in this paper that only leading

partial dislocations may be nucleated at  $T < T_{BDT}$ . However, according to Eq. (1), the effective activation enthalpy for dislocation nucleation,  $\Delta H_n^{eff} = \Delta H_n - \alpha \tau V^*$ , is lowered by the applied resolved shear stress  $\tau$ . Thus, it may be that at the very high stresses (over 0.5 GPa) applied at temperatures below  $T_H$ , the effective activation energy,  $\Delta H_n^{eff}$ , is sufficiently lowered to make nucleation of the trailing partial dislocation possible, resulting in leading/trailing pairs of partials, i.e. perfect dislocation half-loops. This is also supported by theoretical calculations of Brochard *et al.* [32] who have shown that the nucleation of dislocations is stress-dependent, and at a high enough applied stresses, both partials can nucleate from a surface source. The screw nature of the dislocations is probably due to the much higher velocity of non-screw segments of a half-loop that, under the very high stresses, rapidly move out of the crystal and leave the much slower screw segments in the sample (as in Fig. 7).

## CONCLUSION

New deformation experiments on 4H-SiC confirm the existence of a transition in the variations of the critical yield stress with temperature at approximately 1100°C at a low strain rate of  $3.6 \times 10^{-5} \text{ s}^{-1}$ . This transition temperature is close to the BDT of 4H-SiC. TEM experiments have verified that the low density of dislocations produced in the samples deformed below  $T_c$  are predominantly single leading partials with a silicon core, while a high density of Si(g)/C(g) dissociated screw dislocations are produced in the samples deformed above  $T_c$ . A model has been presented that associates the transition temperature  $T_c$  with a change in the mode of deformation. In this model, only leading partial dislocations are nucleated at  $T < T_c$  that glide on the slip plane but contribute to a very limited extent to the straining of the crystal, specially since the sources that produced them become inoperative after they emit only one partial dislocation. On the other hand, at  $T > T_c$ , full dislocations can be nucleated repeatedly from sources in the crystal and their glide produces large strains and causes macroscopic yielding of the crystal. Additionally, the model relates the transition temperature  $T_c$  in the yielding of the crystal to the temperature at which the brittle-to-ductile transition in the fracture of the crystal occurs.

## ACKNOWLEDGEMENTS

This work was supported by grant number FG02-93ER45496 from the Basic Energy Sciences Division of the Department of Energy. Collaboration between CWRU and LMP was initiated by the NATO grant number CRG940295. Thanks are due to Dr. Calvin Carter, Jr. of Cree Research, Inc. for providing a single crystal ingot of 4H-SiC. The authors would like to thank Drs. Christian Kisielowski and Boris Farber for useful discussions.

## REFERENCES

- [1] T. Suzuki, T. Nishisako, T. Taru and T. Yasutomi, *Plastic deformation of InP at temperatures between 77 and 500 K*, Phil. Mag. Lett. **77**(4), 173-180, (1998).
- [2] T. Suzuki, T. Yasutomi, T. Tokuoka and I. Yonenaga, *Plasticity of III-V Compounds at Low Temperatures*, phys. stat. sol. (a) **171**, 47-52, (1999).
- [3] T. Suzuki, T. Yasutomi, T. Tokuoka and I. Yonenaga, *Plastic deformation of GaAs at low temperatures*, Phil. Mag. A **79**(11), 2637-2654, (1999).
- [4] K. Edagawa, H. Koizumi, Y. Kamimura and T. Suzuki, *Temperature Dependence of the Flow Stress of III-V Compounds*. Submitted to Phil. Mag. A (1999).
- [5] P. Boivin, J. Rabier and H. Garem, *Plastic deformation of GaAs single crystals as a function of electronic doping. I: Medium temperatures (150-650°C)*, Phil. Mag. A **61**(4), 619-645, (1990).
- [6] P. Boivin, J. Rabier and H. Garem, *Plastic deformation of GaAs single crystals as a function of electronic doping. II: Low temperatures (20-300°C)*, Phil. Mag. A **61**(4), 647-672, (1990).

- [7] A. V. Samant, *Effect of Test Temperature and Strain-Rate on the Critical Resolved Shear Stress of Monocrystalline Alpha-SiC*, Ph.D. thesis, Case Western Reserve University, (1999).
- [8] S. Fujita, K. Maeda and S. Hyodo, *Dislocation glide motion in 6H SiC single crystals subjected to high-temperature deformation*, Phil. Mag. A **55**(2), 203-215, (1987).
- [9] G. S. Corman, *Creep of 6H  $\alpha$ -Silicon Carbide Single Crystals*, J. Am. Ceram. Soc. **75**(12), 3421-3424, (1992).
- [10] A. V. Samant and P. Pirouz, *Activation parameters for dislocation glide in  $\alpha$ -SiC*, Int. J. Refractory Metals and Hard Materials **16**(4-6), 277-289, (1998).
- [11] A. V. Samant, W. L. Zhou and P. Pirouz, *Effect of Temperature and Strain Rate on the Yield Stress of Monocrystalline 6H-SiC*, phys. stat. sol. (a) **166**, 155-169, (1998).
- [12] J. L. Demenet, M. H. Hong and P. Pirouz, *Deformation tests on 4H-SiC single crystals between 900°C and 1360°C and the microstructure of the deformed samples*, in "ICSCRM '99", ed. R. Devaty and G. Rohrer, (Trans Tech Publications Ltd., Switzerland: 1999). In press.
- [13] X. J. Ning and P. Pirouz, *A large angle convergent beam electron diffraction study of the core nature of dislocations in 3C-SiC*, J. Mater. Res. **11**(4), 884-894, (1996).
- [14] K. Maeda and S. Fujita, *Microscopic Mechanism of Brittle-to-Ductile Transition in Covalent Ceramics*, in "Lattice Defects in Ceramics", ed. by S. Takeuchi and T. Suzuki, pp. 25-31, (Jap. J. Appl. Phys. - Series 2, Tokyo, 1989).
- [15] P. Pirouz, A. V. Samant, M. H. Hong, A. Moulin and L. P. Kubin, *On temperature-dependence of deformation mechanism and the brittle-ductile transition in semiconductors*, J. Mater. Res. **14**(7), 2783-2793, (1999).
- [16] H. Gottschalk, G. Patzer and H. Alexander, *Stacking Fault Energy and Ionicity of Cubic III-V Compounds*, phys. stat. sol. (a) **45**, 207-217, (1978).
- [17] S. Takeuchi, K. Suzuki, K. Maeda and H. Iwanaga, *Stacking-Fault Energy of II-VI Compounds*, Phil. Mag. A **50**(2), 171-178, (1984).
- [18] S. Takeuchi and K. Suzuki, *Stacking Fault Energies of Tetrahedrally Coordinated Crystals*, phys. stat. sol. (a) **171**, 99-103, (1999).
- [19] J. P. Hirth and J. Lothe, *Theory of Dislocations*, (McGraw-Hill, New York, 1968).
- [20] X. J. Ning, T. Perez and P. Pirouz, *Indentation-induced dislocations and microtwins in GaSb and GaAs*, Phil. Mag. A **72**(4), 837-859, (1995).
- [21] K. Wessel and H. Alexander, *On the mobility of partial dislocations in silicon*, Phil. Mag. **35**(6), 1523-1536, (1977).
- [22] H. Alexander, H. Eppenstein, H. Gottschalk and S. Wendler, *TEM of dislocations under high stress in germanium and doped silicon*, Journal of Microscopy **118**(1), 13-21, (1980).
- [23] P. B. Hirsch, *The structure and electrical properties of dislocations in semiconductors*, J. Microscopy **118**(1), 3-12, (1980).
- [24] M. Heggie and R. Jones, *Solitons and the electrical and mobility properties of dislocations in silicon*, Phil. Mag. B **48**(4), 365-377, (1983).
- [25] V. Celli, M. Kabler, T. Ninomiya and R. Thomson, *Theory of Dislocation Mobility in Semiconductors*, Phys. Rev. **131**(1), 58-72, (1963).
- [26] V. V. Rybin and A. N. Orlov, *Dislocation Mobility in Crystals with a High Peierls Barrier*, Sov. Phys. - Solid State **11**(12), 2635-3024, (1970).
- [27] I. E. Bondarenko, V. G. Eremenko, B. Y. Farber, V. I. Nikitenko and E. B. Yakimov, *On the Real Structure of Monocrystalline Silicon near Dislocation Slip Planes*, phys. stat. sol. (a) **68**, 53-60, (1981).
- [28] C. Kisielowski-Kemmerich, *Vacancies and Their Complexes in the Core of Screw Dislocations: Models Which Account for ESR Investigations of Deformed Silicon*, phys. stat. sol. (b) **161**, 111 -132, (1990).
- [29] H. Alexander, *Dislocations in Covalent Crystals*, in "Dislocations in Solids", ed. by F. R. N. Nabarro, pp. 114-234, (Elsevier Science Publishers B. BV, Amsterdam, 1986).
- [30] R. Thomson, *Physics of Fracture*, in "Solid State Physics", ed. by H. Ehrenreich and D. Turnbull, pp. 1-129, (Academic Press, New York, 1986).
- [31] P. B. Hirsch and S. G. Roberts, *The brittle-ductile transition in silicon*, Phil. Mag. A **64**(1), 55-80, (1991).
- [32] S. Brochard, J. Rabier and J. Grilhé, *Nucleation of partial dislocations from a surface-step in semiconductors: a first approach of the mobility effect*, Eur. Phys. J. - AP **2**, 99-105, (1998).

In the Proceedings of the Acta Mater. Workshop on  
*Ceramic and Bimaterial Interfaces: Designing for Properties*  
Sept. 20-23, Seville, Spain. Ed. by A. P. Tomsia, and J. Moya  
To be published in Acta Mater. (2000).

## Defect Distribution in 3C-SiC Grown on Rigid versus Compliant Substrates

M. H. HONG\*, J. CHUNG\*, F. NAMAVAR\*, and P. PIROUZ\*†

*Department of Materials Science and Engineering, Case western Reserve University,  
Cleveland, OH 44106*

*\*Optoelectronic Division, Spire Corporation, One Patriots Park, Bedford, MA 01730*

### ABSTRACT

Cubic 3C-SiC films have been grown heteroepitaxially on rigid and compliant silicon substrates and the nature and density of lattice defects in them are compared. For this purpose, SiC has been chemically vapor deposited on bulk silicon and two different types of SIMOX. In one of the SIMOX samples (referred to as the "thick SIMOX"), the topmost silicon and SiO<sub>2</sub> layers are relatively thick (>200 nm) while in the other one (the "thin SIMOX"), the topmost silicon and SiO<sub>2</sub> layers are much thinner (~35 nm). The microstructure of the three films have been compared by X-ray diffractometry as well as by cross-sectional and plan-view transmission electron microscopy. The defects in all three films are predominantly planar in nature with a significantly lower density in the SiC epilayer deposited on the thin SIMOX. The defect density in the films grown on bulk silicon and the thick SIMOX are not significantly different. The difference in the defect content of the film grown on the thin SIMOX relative to the film grown on bulk silicon or the thick SIMOX is tentatively attributed to the difference in compliance of the different substrates.

## 1. INTRODUCTION

Based on the pioneering work of Tairov and Tsvetkov [1], two monocrystalline polytypes of SiC, 6H and 4H, are now being grown as ingots by the technique of sublimation growth and 2" wafers of these two polytypes are commercially available for the fabrication of SiC devices, as well as for substrates to grow GaN thin films. On the other hand, the cubic polytype, 3C, is not yet available in a bulk form and can presently be grown in a monocrystalline form only as a thin film deposited on a substrate. The successful growth of large-area monocrystalline 3C-SiC on Si was first reported by Nishino and coworkers [2, 3] using the technique of chemical vapor deposition (CVD). Despite the availability of 4H- and 6H-SiC and the lack of 3C-SiC wafers, there are numerous advantages in growing 3C-SiC thin films on Si, not the least of which is the potential integration of SiC with the silicon technology. On the other hand, because of the large lattice and thermal mismatch between Si ( $a=0.357$  nm), and 3C-SiC ( $a=0.357$  nm), heteroepitaxial 3C-SiC films generally contain a high density of lattice defects (see, e.g., [4-8]). These defects can be very detrimental to SiC electronic devices, and their density must be minimized for optimum performance and high efficiency of the devices. A rather novel class of substrates for growth of semiconductors, including SiC [9], is silicon-on-insulator (SOI) where the SiC film is grown on the top Si layer of the SOI multilayer. The advantages of such systems are the potential of achieving dielectric isolation as well the possibility that they pave the way for monolithic integration of SiC electronic devices with advanced Si technology.

In general, in CVD deposition of SiC on silicon, the SiC film forms in its cubic 3C polytype with a parallel epitaxial orientation relationship (OR) with respect to the silicon substrate, i.e.:

$$\begin{array}{l} (001)_{\text{SiC}} \parallel (001)_{\text{Si}} \\ [1\bar{1}0]_{\text{SiC}} \parallel [1\bar{1}0]_{\text{Si}} \end{array} \quad \dots(1)$$

It is also well established that, because of the large lattice (~20%) and thermal (8%) mismatches between the Si substrate and the SiC film, the 3C-SiC epilayer is heavily faulted; the defects in the film are predominantly planar stacking faults and microtwins [4-7]. This paper deals with an attempt to grow improved quality 3C-SiC on silicon by depositing the film on a compliant substrate. The compliant substrate used in this study is in the form of SIMOX (separation by implantation of oxygen) that is a type of SOI. We shall start with a brief explanation of the stresses in a film deposited on a mismatching substrate, the concept of critical thickness and film relaxation through the formation of misfit dislocations, introduce the concept of a compliant substrate and the one used in this study (SIMOX), and finally an X-ray and transmission electron microscopy (TEM) investigation of the microstructure of 3C-SiC films grown on three different types of substrates: (a) bulk silicon, (b) the relatively thick silicon layer of standard SIMOX (hereto referred to as "thick SIMOX"), and (c) the thin silicon layer of a newly-developed SIMOX (hereto referred to as "thin SIMOX"). As will be shown, a pronounced difference in the defect density of the different films is found; the SiC film deposited on the thin SIMOX has a much lower defect content than the SiC deposited on the thick SIMOX or on the bulk Si substrate. The possible reasons for the decrease in the defect density is briefly discussed in terms of misfit accommodation by compliant substrates.



## 1. Stresses in a Film Deposited on a Mismatching Substrate

### 1.1. The Case of a Rigid Substrate

Deposition of thin films on a substrate has been studied since the early part of this century. A fundamental insight into this work was the concept of "misfit dislocations" as introduced by Frank and van der Merwe [10-12] who considered the deposition of a monolayer on a crystalline substrate allowing for the difference in natural lattice-spacing between the surface layer and the substrate. This was later developed, predominantly, by van der Merwe (e.g., [13-16]) and by Matthews (e.g., [17-23]) for the general case of crystalline overgrowths and epitaxial growth of a thin film on a rigid substrate. Basically, according to this concept, when a film is deposited on a rigid substrate, and provided that the film/substrate adhesion is sufficiently strong, the film becomes coherent with the substrate, i.e. the lattice of the film strains to attain the same in-plane lattice constants as those of the substrate lattice. Under this condition, the film will be under a biaxial strain,  $\epsilon_{//}^f$ , and is said to be pseudomorphic with respect to the substrate. Initially, this biaxial strain is equal to the mismatch,  $f$ , between the in-plane interplanar spacings of the film,  $d_{//}^f$ , and the substrate,  $d_{//}^s$ . Since we will be dealing with the deposition of cubic SiC (with a zincblende structure) on the (001) face of silicon (with a diamond cubic structure), and the OR is, according to Eq. (1), parallel epitaxial, we shall henceforth deal with the lattice parameters of the film and substrate,  $a_f$  and  $a_s$ , rather than the in-plane interplanar spacings,  $d_{//}^f$  and  $d_{//}^s$ . Thus, the "lattice mismatch", or "misfit parameter", is:

$$f = \frac{d_{//}^f - d_{//}^s}{d_{//}^f} = \frac{a_f - a_s}{a_f} \quad \dots (2)$$

The strained film has a higher energy than its relaxed state proportional to  $(\epsilon_{//}^f)^2$  and the bielastic modulus of the film,  $B_f$ . This is for a unit volume of the film and if we take a unit area of the film with a thickness  $h_f$ , then the strain energy  $E_e$ , is given by:

$$E_e = h_f B_f (\epsilon_{//}^f)^2 \quad \dots (3)$$

In general, for an anisotropically elastic film, the bielastic modulus depends on the particular surface,  $(hkl)$ , on which the film is grown and is a complicated function of the film elastic constants,  $C_{ij}$  [24]. For an isotropic film:

$$B_f = 2\mu_f \frac{(1+\nu)}{(1-\nu)} \quad \dots (4)$$

where  $\mu_f$  and  $\nu$  are, respectively, the shear modulus and Poisson's ratio of the film. Although not strictly true, we shall assume henceforth that all the materials in the system under consideration (Si, SiC and SiO<sub>2</sub>) are isotropic. From equation (3), the strain energy of the film is linearly proportional to its thickness,  $h_f$ , and thus as the film grows thicker, its strain energy increases. This situation of increasing strain energy because of the growing volume of the strained film can obviously not continue as the film thickness increases. In fact, at a critical film thickness,  $h_c^f$ , it becomes energetically favorable for the film to relax (i.e. become unstrained) by some mechanism. Among the more important relaxation mechanisms are cracking of the film, and generation of non-screw dislocations at the film/substrate interface. In the latter case, the strain in the film is accommodated by an array of interfacial misfit dislocations that are usually generated at the film surface and

glide on their slip planes to deposit at the interface. Each misfit dislocation with a Burger vector  $\mathbf{b}$  relaxes the biaxial strain by an amount  $b_{//}$  - where  $b_{//}$  is the in-plane (parallel to the interface) component of  $\mathbf{b}$  - and decreases the instantaneous strain in the film to  $\epsilon_{//}^f (= f - b_{//})$ . Note, however, that a misfit dislocation has energy  $E_d$  that, like a lattice dislocation [25], is proportional to  $b^2$  and also to the logarithm of the film thickness. In fact, for a dislocation lying along the z-axis at the film/substrate interface that is normal to the y-axis, we have that :

$$E_d = \frac{\mu_f [b_x^2 + b_y^2 + (1-\nu)b_z^2]}{4\pi(1-\nu_f)} \left[ \ln \left( \frac{\beta h_f}{r_o} \right) \right] \quad \dots (5)$$

where  $b_x$ ,  $b_y$ , and  $b_z$  are the components of the Burgers vector  $\mathbf{b}$  along the x-, y-, and z-axis, respectively [19]. In the above approximate equation, the inner and outer core radii of the dislocation (used in evaluating the energy integral) have been taken as  $r_o$  and  $h_i$ , respectively. Thus, a decrease in the total film energy by a reduction of its bielastic strain is compensated by an increase due to the presence of misfit dislocations. To obtain the critical thickness, van der Merwe [16] and also Matthews [19, 20, 22] considered a film that is partially relaxed, i.e. contains some misfit dislocations (see also Refs. [26] and [27]). Assuming that, at a certain instant (i.e., film thickness), a periodic array of misfit dislocations with a spacing  $S$  has been generated, then there will be  $n=1/S$  dislocations per unit length of the interface and the residual biaxial strain in the film will be  $\epsilon_{//}^{res} (= f - \frac{b_{//}}{S})$ .

In this case, the total energy of the film,  $E_{tot}$ , consists of two terms, (i) strain energy of the partially relaxed film,  $E_\epsilon = h_f B_f (\epsilon_{//}^{res})^2$ , and (ii) energy of the misfit dislocations,  $E_d/S$ . There will be a critical strain,  $\epsilon_{//}^*$ , at which the total energy of the film is a minimum (obtained by setting  $dE_{tot}/d\epsilon_{//}^f = 0$ ) and this gives the critical thickness when  $\epsilon_{//}^*$  equals the misfit parameter  $f$ . Thus, at the thickness  $h_c^f$ , given by:

$$h_c^f = \frac{[b_x^2 + b_y^2 + (1-\nu)b_z^2]}{8\pi(1+\nu_f)b_x} \frac{1}{f} \left[ \ln \left( \frac{h_c^f}{r_o} \right) \right] \quad \dots (6)$$

generation of the first misfit dislocation becomes energetically favorable

## 1.2. The Case of Non-Rigid (Compliant) Substrate

The van der Merwe/Matthews treatment assumes an infinitely thick and rigid substrate that basically remains strain-free during film deposition. However, in general, the substrate is not completely rigid and deposition of the film sets up opposite biaxial strains in the film and the substrate. In fact, for a thin and non-rigid (compliant) substrate, the distribution of the elastic energy between the film and the substrate is comparable. Based on these concepts, Lo [28, 29] concluded that for a substrate less than the critical film thickness, the overall strain energy would never be large enough to create misfit dislocations in the film. To appreciate Lo's suggestion, consider a thin film deposited on a comparably thin substrate. In this case, the total strain,  $\epsilon_m$ , is partitioned between the substrate and the epilayer as  $-\epsilon_s$  and  $\epsilon_f$ , respectively (remembering that the biaxial strains in the substrate and the epilayer are in opposite directions, i.e. compressive (tensile) versus tensile (compressive)). Now, in general, the rigidity of the film and the

substrate is proportional to their respective elastic moduli  $B_x$  and  $B_s$ , and their thicknesses,  $h_f$  and  $h_s$ . Thus, if the film and the substrate have the same elastic modulus, then the thinner each one is, the more strain can it accommodate. Assuming that the deformations in epilayer and substrate are compatible (i.e.,  $\epsilon_s = \epsilon_m - \epsilon_f$ ), and the net force on them exactly balance (i.e.,  $B_f \epsilon_f h_f = -B_s \epsilon_s h_s$ ), Freund and Nix [30], obtained the following equations for  $\epsilon_s$  and  $\epsilon_f$ :

$$\epsilon_s = -\epsilon_m \frac{h_f}{h_s + h_f} \quad \text{and} \quad \epsilon_f = \epsilon_m \frac{h_s}{h_s + h_f} \quad \dots (7)$$

Then, the critical thickness for the generation of dislocations in the film is [30]:

$$h_f = \frac{[b_x^2 + b_y^2 + (1-\nu)b_z^2]}{8\pi(1-\nu)b_x} \frac{h_s + h_f}{h_s h_f} \frac{1}{\epsilon_m} \ln \left[ \frac{h_s h_f}{r_o(h_s + h_f)} \right] \quad \dots (8)$$

This equation is symmetric in the substrate and film thickness,  $h_s$  and  $h_f$ , because their roles are now interchangeable and there is no fundamental distinction between them. Also the equation reduces to the bulk substrate case, Eq. (6), as  $h_f \rightarrow 0$  and  $h_s \rightarrow \infty$ .

The ideal compliant substrate is a "freestanding" one that is only a few monolayers thick. However, this is not technologically feasible and various configurations have been proposed for simulating a freestanding substrate. One of these is a substrate consisting of a thin layer of a single-crystal material (e.g., GaAs) wafer-bonded to a bulk substrate of the same material with a deliberate angular misorientation [31, 32]. The idea is that the thin substrate layer, that forms a twist boundary to the underlying bulk layer, closely resembles an ideal compliant substrate in its "lattice flexibility" [33].

The other configuration that has been employed is a semiconductor-on-insulator (SOI) composite [34]. The SOI composite consists of a thin single crystal of a semiconductor bonded to a thin insulating oxide layer, which in turn is bonded to a much thicker wafer. During the pseudomorphic growth of an epilayer, the thin crystal substrate layer will deform elastically together with the epilayer because the insulating oxide underneath it is a viscoelastic material that flows at growth temperatures and thus allows the thin crystal substrate to deform elastically [35] (Fig. 1). This is the configuration used in the present work.

As mentioned before, the SOI employed is actually a SIMOX sample that is fabricated by implanting a high dose of oxygen into a standard silicon substrate. The multilayer structure of SIMOX is shown schematically in Fig. 2 and consists of two monocrystalline layers of silicon separated by an amorphous  $\text{SiO}_2$  layer. The standard SIMOX sample is fabricated by a single high-dose oxygen implantation ( $1.5$  to  $1.8 \times 10^{18} \text{ O}^+ \text{ cm}^{-2}$  at  $150$  to  $200 \text{ kV}$ ) followed by annealing at or above  $\sim 1300^\circ\text{C}$  to re-grow the silicon and redistribute the oxygen [36, 37]. This process results in a SIMOX structure that has a silicon top layer, Si(II), of about  $140$  to  $240 \text{ nm}$  thick and a buried  $\text{SiO}_2$  layer of about  $350$  to  $400 \text{ nm}$  thick. On the other hand, an ultrathin SIMOX structure is produced by a lower-dose ion implantation ( $1.5 \times 10^{17} \text{ O}^+ \text{ cm}^{-2}$ ) at  $30 \text{ kV}$ , followed by high-temperature annealing using a multiple implantation process [38, 39]. Low-energy SIMOX structures with a  $35 \text{ nm}$  silicon top layer possess excellent integrity compared to thinned commercial SIMOX (e.g., one with a  $200 \text{ nm}$  Si layer and  $400 \text{ nm}$  buried  $\text{SiO}_2$  layer) because of low-dose oxygen implantation. Because of the higher compliancy of thin Si layers, it is expected that when an ultrathin SIMOX wafer is used as a substrate for 3C-SiC

epitaxy, the density of lattice defects in the SiC film would be lower as compared to that in SiC films deposited on standard SIMOX and/or bulk Si substrates.

## 2. EXPERIMENTAL PROCEDURES

The three types of samples investigated all consisted of SiC epilayers deposited at 1350 °C on (001) silicon. All the depositions were done in the same CVD reactor using the standard technique of carbonizing the silicon substrate and growing SiC from silane and propane as precursor gases [40]. In the first sample, a 20  $\mu\text{m}$  epitaxial film of 3C-SiC was deposited on a 500  $\mu\text{m}$ -thick (001) silicon wafer. In a second sample, SiC was deposited on "thick SIMOX" consisting of a  $\sim 200\text{ nm}$  Si(II) top layer lying on a  $\sim 400\text{ nm}$  SiO<sub>2</sub> layer. In a third sample, a 40  $\mu\text{m}$  epitaxial film of 3C-SiC was deposited on "thin SIMOX" consisting of a  $\sim 35\text{ nm}$  Si(II) top layer lying on a  $\sim 40\text{ nm}$  SiO<sub>2</sub> layer. The silicon substrate was cut from a commercial 4" Czochralski-grown Si wafer, the "thick SIMOX" was cut from a commercial 4" one produced by SOITEC, and the "thin SIMOX" was produced in Spire Corporation. To make the growth conditions as similar as possible, the silicon wafer and the "thin SIMOX" were loaded into the reactor at the same time and SiC deposition was carried out simultaneously for these two samples. Following growth, the full maximum at half-width (FMHW) of the 200 X-ray diffraction peak of the three films was measured by double crystal X-ray diffractometry (XRD). Subsequently, plan-view and cross-sectional TEM foils were prepared from the three samples by standard methods, including the conventional sandwich technique for cross-sectional foils with the foil surface normal to the  $[1\bar{1}0]_{\text{Si}}$  direction. The multi-layer samples were ground with emery paper to a thickness of approximately 100  $\mu\text{m}$ , dimpled to a thickness of 15  $\mu\text{m}$ , and subsequently ion-thinned to electron transparency. Due to the very different thinning rates between Si and SiC, a low angle ( $\sim 6\text{--}7^\circ$ ) was adopted for ion-beam thinning. In order to compare the defect density more accurately, plan-view TEM specimens were also prepared using one-side thinning from the back Si(I) layer. TEM observations were carried out in a Philips CM20 electron microscope operated at an accelerating voltage of 200 kV.

## 3. RESULTS

Typical X-ray rocking curves, showing the SiC 200 peak at  $\sim 40.4^\circ$ , for the three samples are shown in Fig. 3. The full-width-at-half-maximum (FWHM) of the XRD peaks was measured and is shown in Table I.

The narrowest peak of 180 arcsec corresponds to the SiC film grown on the "thin SIMOX" substrate whereas the largest value of 234 arcsec corresponds to the film deposited on the "thick SIMOX". The value of FWHM for the SiC film deposited on the (bulk) silicon wafer is less than that for growth on the "thick SIMOX". The reason for this is probably due to the fact that the initial defect density in SIMOX is usually much higher than that in a high-quality silicon wafer. Specifically, it is known that a large fraction of defects in epitaxially-deposited films originate from heterogeneities on the substrate surface, and the surface state of the SIMOX samples is usually inferior to that of high-quality silicon wafers.

The defect distribution in a SiC film grown on bulk Si typically consists of a high density of planar defects lying on the four {111} planes, as shown in cross-sectional (Fig. 4) and plan-view (Fig. 5) micrographs. These figures are from the multilayer sample consisting of a 40  $\mu\text{m}$ -thick SiC film deposited on the bulk silicon (001) wafer. The orientation relationship is parallel epitaxy as given by Eq. (1). As shown clearly in these figures, like all other epitaxial semiconductors, the defect density is highest close to the film/substrate interface but decreases rapidly in going toward the surface. In general, for the SiC/Si system, the rate of decrease is greatest in the first  $\sim 100\text{-}200\text{ nm}$  from the interface and then slows down but continues all the way to the film surface.

Overall cross-sectional views of SiC grown on (a) thick and (b) thin SIMOX are shown in figures 6. The thickness of the SiC epilayer in Fig. 6(a) is 20  $\mu\text{m}$  and that in Fig. 6(b) is 40  $\mu\text{m}$ . As mentioned before, the SiC growths on both SIMOX samples were carried out in the same reactor as for growth on the bulk silicon wafer (Figs. 4 and 5). The selected area diffraction pattern (SADP) from each region of the multilayer is inset in Fig. 6; these and convergent beam electron diffraction (CBED) patterns (not shown) confirm that, as in the case of growth on bulk Si, there is a parallel epitaxial orientation relationship (OR) between the SiC film and the underlying Si substrate (given by Eq. (1)). It is also interesting that the thin Si(II) layer in the SIMOX has a parallel epitaxial OR with respect to the thicker Si(I) layer that is separated from it by the amorphous  $\text{SiO}_2$  layer. This is well-known in the SIMOX literature and is thought to be due to the formation of Si(II) layer by a solid phase epitaxial growth (SPEG) process from the crystalline nuclei left in silicon that was damaged and had become disordered by oxygen ion-implantation. Thus, the orientation relationship in the multilayer is:

$$\begin{aligned} (001)_{\text{SiC}} // (001)_{\text{Si(II)}} // \text{Amorphous}_{\text{SiO}_2} // (001)_{\text{Si(I)}}; \\ [1\bar{1}0]_{\text{SiC}} // [1\bar{1}0]_{\text{Si(II)}} // \text{Amorphous}_{\text{SiO}_2} // [1\bar{1}0]_{\text{Si(I)}}. \end{aligned}$$

The SiC film is clearly monocrystalline but, in the case of the film grown on the thick SIMOX, the density of planar defects is sufficiently high to give rise to streaks in the SADP of the 3C-SiC film.

Fig. 7 shows a high-resolution transmission electron micrograph (HRTEM) of the sample shown in Fig. 6(b). Note the planar faults in the epilayer and also some interesting morphological defects in Si(II) probably caused by compressive stresses in the thin substrate. The interfaces between the crystalline SiC and Si(II), and also between the crystalline Si(II) and amorphous  $\text{SiO}_2$ , are sharp and appear free of contaminations.

In figures 8-11, we look in more detail at the defect distribution in the two SiC films and compare them. Fig. 8 shows cross-sectional views of the SiC film grown on the thin SIMOX. As in the other figures, (a), (b), and (c) refer to the different regions of the film: (a) near the SiC/Si interface, (b) approximately halfway between the SiC/Si interface and the SiC surface, and (c) near the SiC surface. From these and the plan-view micrographs (shown in Fig. 9), the planar defect density was evaluated to be  $\sim 40\ \mu\text{m}^{-1}$  in region (a),  $\sim 10\ \mu\text{m}^{-1}$  in region (b), and  $\sim 2.5\ \mu\text{m}^{-1}$  in region (c). The decrease of defect density with distance away from the film/substrate interface is consistent with previous results on 3C-SiC epitaxial films on bulk silicon [4-7] and, indeed, with films of other compound semiconductors grown on Si substrates [41]. Also, as reported for the SiC/Si system, the majority of the lattice defects are planar faults with most of them being stacking faults

(SFs) or microtwins; the  $\langle 110 \rangle$  trace directions of the SFs confirms that they lie on inclined  $\{111\}$  planes.

The micrographs in Fig. 8 and 9 may be compared with those in Fig. 10 and 11 that are from the different regions of the 3C-SiC film deposited on the "thick SIMOX". In the latter case, the high strain of the region close to the SiC/Si interface, resulting from the very high density of planar faults [Figs. 10(a) and 11(a)], makes an evaluation of the defect density impractical. On the other hand, in the region close to the SiC surface [Figs. 10(b) and 11(b)], the SF density is much lower and estimated to be  $\sim 27.5 \mu\text{m}^{-1}$ .

#### 4. DISCUSSION

The most interesting result obtained in the present study is that the defect density in the epitaxial 3C-SiC film deposited on the thin SIMOX is appreciably less than in the film deposited on the thick SIMOX (or on the bulk silicon wafer). By comparing the defect contents of the SiC film in Fig. 4(c), Fig. 8(c), and Fig. 10(c), it can be seen that the SF density in the region near the surface of 3C-SiC film is more than an order of magnitude smaller in the thin SIMOX than in the thick SIMOX or in bulk silicon. Here, it should be noted that the thickness of the 3C-SiC film is different in the two systems:  $\sim 20 \mu\text{m}$  in the thick SIMOX versus  $40 \mu\text{m}$  in the thin SIMOX and in bulk silicon. To obtain a more direct comparison, we have also estimated the SF density in approximately equivalent regions (equidistant, at about  $20 \mu\text{m}$ , from the SiC/Si interface) in the three systems. The film SF density in the thin SIMOX (Fig. 9(b)) is still nearly 3 times less than that in bulk silicon (Fig. 5(b)) or in the thick SIMOX (Fig. 11(b)).

A reasonable explanation for the difference in the density of planar faults in the three films is the higher compliance of the thin Si substrate in the thin SIMOX as compared to that in the thick SIMOX or in bulk silicon. In a low stacking fault energy material such as SiC ( $\gamma \approx 2.5 \text{ mJ/m}^2$ ), the film/substrate lattice and/or thermal mismatches are predominantly relaxed by nucleation of partial dislocations at the interface, and their subsequent glide on  $\{111\}$  planes that give rise to stacking faults. If the substrate is more compliant, then it will accommodate part of these interfacial stresses by itself and result in a lesser residual stress in the film [28, 29].

Figs. 12(a-c) are from the same TEM specimens as the ones in Figs. 4(a), 6(a), and 6(b), but the strain contrast has been enhanced to clearly show any defects that may have been generated in the silicon substrate underlying the SiC films. In the case of depositions on bulk Si and "thick SIMOX", the silicon substrate is effectively free of any lattice defects; the few dark fringes near the interface are caused by elastic strains. On the other hand, there is a relatively high density of lattice defects in the silicon substrate in the "thin SIMOX" sample (Fig. 12(c)). These lattice defects have most probably been generated by the mismatch stresses, thus indicating a partition of the strain between the film and the substrate. Since part of the film/substrate mismatch stress is accommodated by the production of defects in the thin substrate, the remaining stress in the film can be relaxed by nucleation and glide of a lower density of partial dislocations in SiC. For this increased compliancy of the Si substrate, it is of course essential that the underlying amorphous  $\text{SiO}_2$  layer be able to relax. In fact, the glass transition temperature,  $T_g$ , of  $\text{SiO}_2$  is (depending on the cooling rate) about  $1100^\circ\text{C}$  [42]. Since, the growth temperature used for depositing SiC on the thin Si top layer of SIMOX is  $\sim 1350^\circ\text{C}$ , stress release by structural

relaxation in  $\text{SiO}_2$  should be appreciable because this is above  $T_g$  and is able to partially relax the elastic stresses transmitted to it by the overlaying Si wafer [42].

One point that should be kept in mind is the large lattice-mismatched system that has been investigated in this work. In general, when the film/substrate misfit parameter is larger than  $\sim 5\%$ , the growth mode is practically always three-dimensional, the critical thickness is less than a monolayer, and misfit dislocations exist at the interface from the very initial stages of film deposition. The end(s) of a large fraction of these misfit dislocations are connected to threading segments that are undesirable in a heteroepitaxial film. Even though these misfit dislocations, that have a nearly equilibrium spacing, release most of the mismatch stresses, there remains appreciable residual stresses in the film (aside from thermal mismatch stresses). It is believed that it is mostly these residual stresses that are accommodated by the thin compliant substrate resulting in smaller stresses to produce defects in the film.

## 5. CONCLUSION

Cubic 3C-SiC was heteroepitaxially grown on silicon by CVD on three different substrates and its microstructure compared to see the effect of substrate rigidity on the defect microstructure of the film. One of the substrates was a  $500\text{ }\mu\text{m}$ -thick wafer of Si(001), whereas the other two were a thick SIMOX(001) and a thin SIMOX(001). The latter two substrates differed by the thickness of the top silicon/silica layers on which SiC was deposited. X-ray diffractometry characterization of the films exhibited a smaller full-maximum at half width (FWHM) of the 002 peaks of SiC for the film grown on the thin SIMOX as compared to the films grown on bulk silicon and on thick SIMOX. The best value of 180 arcsec was obtained for the SiC film grown on the "thin SIMOX", a significant improvement from 234 arcsec, the FWHM of the SiC film grown on "thick SIMOX". A plan-view and cross-sectional TEM investigation of the different films confirmed the X-ray results; the defects in the SiC film, mostly of planar nature such as stacking faults, were appreciably lower in the film grown on the "thin SIMOX". One may conclude that thin SIMOX does act as a compliant substrate for growth of heteroepitaxial films and partially accommodates the mismatch stresses. This is supported by the occurrence of a relatively high density of lattice defects in the silicon substrate that underlies the SiC film in the "thin SIMOX" sample. We also conclude that, for growth of wide lattice mismatch systems such as GaN/Si or SiC/Si, the improvement in the film quality is not dramatic by using a thin compliant silicon substrate. However, it is anticipated that the improvement in film quality will be much more significant when the film/Si lattice mismatch is small, say,  $f \leq 3\%$ .

## ACKNOWLEDGEMENT

MHH and PP would like to acknowledge partial support from the Department of Energy (grant #FG02-93ER45496) monitored by Dr. Alan Dragoo. The work at SPIRE was supported in part by NASA SBIR Phase II Contract Number NAS3-27747 and NSF Phase II grant number DMI-9710628.

## REFERENCES

- [1] Y. M. Tairov and V. F. Tsvetkov, *Investigation of Growth Processes of Ingots of Silicon Carbide Single Crystals*, J. Crystal Growth **43**(2), 209-212, (1978).
- [2] S. Nishino, J. A. Powell and H. A. Will, *Production of large-area single-crystal wafers of cubic SiC for semiconductor devices*, Appl. Phys. Lett. **44**(5), 460-462, (1983).
- [3] H. Matsunami, S. Nishino and H. Ono, *Heteroepitaxial Growth of Cubic Silicon Carbide on Foreign Substrates*, IEEE Trans. Electron Devices **ED-28**, 1235-1236, (1981).
- [4] C. M. Chorey, P. Pirouz, J. A. Powell and T. E. Mitchell, *TEM Investigation of  $\beta$ -SiC Grown Epitaxially on Si Substrate by CVD*, in "Semiconductor-Based Heterostructures: Interfacial Structure and Stability", ed. M. L. Green, J. E. E. Baglin, G. Y. Chin, H. W. Deckman, W. Mayo and D. Narasinhham, pp. 115-125, (The Metallurgical Society Publications, 1986).
- [5] S. R. Nutt, D. J. Smith, H. J. Kim and R. F. Davis, *Interface structure in beta-silicon carbide thin films*, Appl. Phys. Lett. **50**(4), 203-205, (1987).
- [6] P. Pirouz, C. M. Chorey, T. T. Cheng and J. A. Powell, *Lattice Defects in  $\beta$ -SiC Grown Epitaxially on Silicon Substrates*, in "Heteroepitaxy on Silicon II", ed. J. C. C. Fan, J. M. Phillips and B.-Y. Tsaur, Mat. Res. Soc. Symp. Proc., **91**, pp. 399-404, (Materials Research Society, Pittsburgh, PA, 1987).
- [7] P. Pirouz, C. M. Chorey, T. T. Cheng and J. A. Powell, *Microscopy of Epitaxially Grown  $\beta$ -SiC on {001} Silicon*, in "Microscopy of Semiconducting Materials, 1987", ed. A. G. Cullis and P. D. Augustus, Inst. Phys. Conf. Ser., **87**, pp. 175-180, (Institute of Physics, Bristol, England, 1987).
- [8] Y. Nakajima, *Epitaxial Growth of SiC Single Crystal Films*, in "Silicon Carbide Ceramics-1; Fundamental and Solid Reaction", ed. by S. Somiya and Y. Inomata, pp. 45-75, (Elsevier Applied Science, London and New York, 1991).
- [9] A. J. Steckl, C. Yuan, Q.-Y. Tong, U. Gösele and M. J. Loboda, *SiC Silicon-on-Insulator Structures by Direct Carbonization Conversion and Postgrowth from Silacyclobutane*, J. Electrochem. Soc. **141**(6), L66-L68, (1994).
- [10] F. C. Frank and J. H. van der Merwe, *One-Dimensional Dislocations. I. Static Theory*, Proc. R. Soc. London **A198**, 205-216, (1949).
- [11] F. C. Frank and J. H. van der Merwe, *One-Dimensional Dislocations. II. Misfitting Monolayers and Oriented Overgrowth*, Proc. R. Soc. London **A198**, 216-225, (1949).
- [12] F. C. Frank and J. H. van der Merwe, *One-dimensional dislocations. III. Influence of the second harmonic term in the potential representation on the properties of the model*, Proc. Roy. Soc. London **A200**, 125-134, (1949).
- [13] J. H. van der Merwe, *On the Stresses and Energies Associated with Inter-Crystalline Boundaries*, Proc. Phys. Soc. Lond. **A63**, 616-637, (1950).
- [14] J. H. van der Merwe, *Strains in crystalline overgrowths*, Phil. Mag. **7**, 1433-1434, (1962).
- [15] J. H. van der Merwe, *Crystal interfaces. Part I. Semi-infinite crystals*, J. Appl. Phys. **34**(1), 117-122, (1963).
- [16] J. H. van der Merwe, *Crystal interfaces. Part II. Finite overgrowths*, J. Appl. Phys. **34**(1), 123-127, (1963).
- [17] J. W. Matthews, *Accommodation of misfit across the interface between single-crystal films of various face-centered cubic metals*, Phil. Mag. **13**, 1207-1221, (1966).
- [18] J. W. Matthews, S. Mader and T. B. Light, *Accommodation of misfit across the interface between crystals of semiconducting elements or compounds*, J. Appl. Phys. **41**, 3800-3804, (1970).



pseudopotentials, the values of  $J_i$  (in eV per SiC pair) were calculated by Cheng *et al.* (1988, 1990a), and later by Karch *et al.* (1994) (as quoted by Käckell *et al.* (1988), and Käckell *et al.* (1994). Recently, Limpijumnon and Lambrecht (1998) calculated the interaction energies by means of the all-electron full-potential linear muffin-tin orbital method. The values of  $J$  as calculated by the different authors are given in Table 4.

Accordingly, from equation (3), the energies of the 4H and 6H polytypes are (per SiC pair)

$$E_{22} = E_0 + J_2, \quad (4a)$$

and

$$E_{33} = E_0 - \frac{1}{3}J_1 + \frac{1}{3}J_2 + J_3. \quad (4b)$$

#### 4.2. Estimates of the stacking fault energy of 4H and 6H polytypes

The stacking fault energy per SiC layer can be written (Käckell *et al.* 1998) as

$$\gamma = \frac{\Delta E}{A} = \frac{E(\text{faulted}) - E(\text{perfect})}{A}, \quad (5)$$

where  $A (= \sqrt{3}/2 a^2)$  is the area per atom in the (0001) plane. Gomes de Mesquita (1967) performed precision measurement of lattice parameters  $a$  and  $c$  for a 6H-SiC crystal and obtained a value of  $a = 0.3081$  nm. This gives  $A = 8.221 \times 10^{-20} \text{ m}^2$  and is the value that we use for both the 4H and 6H crystals.

It should be noted that, in calculating the energy of a faulted crystal, equation (3) cannot be used in the form given because the equation assumes that the layer sequence is periodic. However, this is not true when a stacking fault exists in the crystal because the fault does not repeat itself periodically. Thus, we calculate  $\Delta E$  from the equation:

$$\Delta E = nE(\text{faulted}) - nE(\text{perfect}), \quad (6)$$

where the energy of a crystal of  $n$  layers is calculated from

$$nE = nE_0 - \sum_{i=1}^n \sum_{j=1}^{\infty} J_j \sigma_i \sigma_{i+j}. \quad (7)$$

In this case, the energy of a 4H crystal containing  $n$  layers is

$$E_{\text{perfect}}^{4\text{H}} = nE_0 + nJ_2, \quad (8a)$$

Table 4. Parameter in the ANNNI model as calculated by different groups.<sup>a</sup>

Interaction parameter $s$	Cheng <i>et al.</i> (1988)	Cheng <i>et al.</i> (1990a)	Karch <i>et al.</i> (1994)	Käckell <i>et al.</i> (1994)	Limpijumnon and Lambrecht (1998)
$J_1$ (meV)	$4.85 \pm 1.20$	2.33	4.80	1.08	3.056
$J_2$ (meV)	$-2.56 \pm 0.32$	-3.39	-2.93	-2.45	-2.57
$J_3$ (meV)	$-0.50 \pm 0.23$	0.25	-0.45	-0.18	-0.354
$J_1/ J_2 $	$1.89 \pm 0.52$	0.668	1.638	0.44	1.19
$J_1/ J_3 $	$9.7 \pm 4.6$	9.32	10.667	6	8.63

<sup>a</sup> $J_1$  is the short-range interaction between second-nearest neighbour bonds (in the direction of the bonding chain), while  $J_2$  and  $J_3$  are longer range interactions.

while that of a 6H crystal containing  $n$  layers is given by:

$$E_{\text{perfect}}^{6\text{H}} = nE_0 - \frac{n}{3} J_1 + \frac{n}{3} J_2 + nJ_3. \quad (8b)$$

Now, a 4H polytype containing a layer of intrinsic stacking fault changes from  $\dots T_1 T_2 T_1' T_3' \dots$  (that is,  $\dots \uparrow\uparrow\downarrow\downarrow \dots$ ) (figure 2(a)) to  $\dots T_1' T_3' T_1 T_2 / T_3 T_2' T_3 T_1' T_3' T_2' \dots$  (i.e.,  $\dots \uparrow\downarrow\downarrow\downarrow \dots$ ) (figure 2(b)). Thus, according to equation (7), the energy of a faulted 4H-SiC (consisting of  $n$  layers with the  $(n+1)/2$ th layer faulted) is

$$E_{\text{faulted}}^{4\text{H}} = nE_0 + (n-4)J_2,$$

giving

$$\Delta E_{4\text{H}} = -4J_2. \quad (9a)$$

Thus, according to equation (4), the stacking fault energy of 4H-SiC is:

$$\gamma_{4\text{H}} = -\frac{4J_2}{A}. \quad (9b)$$

For the 6H-SiC polytype, the introduction of an intrinsic stacking fault would change the tetrahedral coordination from  $\dots T_1 T_2 T_3 T_2' T_1' T_3' \dots$  (that is,  $\dots \uparrow\uparrow\downarrow\downarrow \dots$ ) (figure 1(a)) to  $\dots T_1 T_2 T_3 / T_1 T_3' T_2' T_3 T_1 \dots$  (i.e.,  $\dots \uparrow\uparrow\downarrow\downarrow \dots$ ) (figure 1(b)). From equation (7) the energy of a faulted 6H crystal (consisting of  $n$  layers with the  $(n+1)/2$ th layer faulted) would be

$$E_{\text{faulted}}^{6\text{H}} = nE_0 - \frac{n}{3} J_1 + \frac{n}{3} J_2 + (n-4)J_3, \quad (10a)$$

and

$$\Delta E_{6\text{H}} = -4J_3.$$

Thus, the stacking fault energy of 6H-SiC is

$$\gamma_{6\text{H}} = -\frac{4J_3}{A}. \quad (10b)$$

The calculated values of  $\Delta E_{4\text{H}}$ ,  $\Delta E_{6\text{H}}$ ,  $\gamma_{4\text{H}}$  and  $\gamma_{6\text{H}}$  are shown in table 5.

Equations (9) and (10) indicate that  $\gamma_{4\text{H}}$  is proportional to  $J_2$ , the interaction between fourth-nearest neighbour bonds (along the bonding chain), while  $\gamma_{6\text{H}}$  is proportional to  $J_3$ , the interaction between sixth-nearest neighbour bonds (along the bonding chain). Since  $J_2$  is a shorter range interaction than  $J_3$ , the stacking fault energy of the 4H polytype is expected to be larger than that of the 6H polytype. This is consistent with the present experimental results ( $\gamma_{4\text{H}} = 14.7 \pm 2.5 \text{ mJ m}^{-2}$  versus  $\gamma_{6\text{H}} = 2.9 \pm 0.6 \text{ mJ m}^{-2}$ ). Moreover, the theoretically estimated values are in reasonable agreement with the experimental results, differing by about 5% for 6H-SiC and about 40% for 4H-SiC (assuming the latest calculated values of  $J$  by Limpijumpong and Lambrecht (1998)). In fact, comparing values of the ratio  $\gamma_{4\text{H}}/\gamma_{6\text{H}}$ , the earlier  $J$  values of Cheng *et al.* (1988) give a ratio that is closer to the experimental value than the more recent values of  $J$ !

## § 5. CONCLUSION

In conclusion, we have deformed bulk single crystalline samples of 6H-SiC and 4H-SiC oriented for easy glide at about 1300°C and measured the stacking fault

Table 5. Values of stacking fault energy of 4H-SiC and 6H-SiC calculated on the basis of the ANNNI model.<sup>a</sup>

	$J_2$ (meV)	$J_3$ (meV)	$\Delta E_{4H}$ (meV)	$\gamma_{4H}$ (mJ m <sup>-2</sup> )	$\Delta E_{6H}$ (meV)	$\gamma_{6H}$ (mJ m <sup>-2</sup> )
Cheng <i>et al.</i> (1988)	-2.56 ±0.32	-0.50 ±0.23	10.24	19.96	2.0	3.90
Cheng <i>et al.</i> (1990a)	-3.49	0.25	13.96	27.21	-1.0	-1.95
Karch <i>et al.</i>	-2.93	-0.45	11.72	22.84	1.8	3.51
Käckell <i>et al.</i> (1994)	-2.45	-0.18	9.8	19.1	0.72	1.40
1200 K	-3.42	-0.28	13.68	26.66	1.12	2.18
Bechstedt <i>et al.</i> (1997)						
Limpijumnong and Lambrecht (1988)	-2.57	-0.354	10.28	20.035	1.416	2.759

<sup>a</sup> Note that the  $J_3$  value of Cheng *et al.* (1990a) gives a negative stacking fault energy for 6H-SiC.

energy by two-beam bright-field and weak-beam techniques of TEM. The experimental stacking fault energy of 6H-SiC is determined to be  $2.9 \pm 0.6 \text{ mJ m}^{-2}$  while that of 4H-SiC is determined to be  $14.7 \pm 2.5 \text{ mJ m}^{-2}$ . Estimates based on the ANNNI model (interlayer interactions) show that the stacking fault energy of 4H-SiC depends on the fourth-nearest neighbours while that of 6H-SiC depends on the sixth-nearest-neighbour interactions. Because of this, the stacking fault energy of 4H-SiC is expected to be much larger than that of 6H-SiC. This is consistent with our experimental findings, and the theoretical values are in reasonable agreement with them.

#### ACKNOWLEDGEMENT

We would like to express our thanks to Mr. Sukit Limpijumnong and Professor Walter Lambrecht for useful discussions on the ANNNI calculations. This work was supported by Grant Number FG02-93ER45496 from the Department of Energy, and Subcontract Number 95-SPI-420757-CWRU from the Silicon Carbide consortium. Thanks are due to Dr Calvin Carter, Jr. (of Cree Research, Inc.) and Dr. Don Hobgood (previously of Northrop-Grumman) for providing single-crystal samples of 6H-SiC and 4H-SiC, respectively.

#### REFERENCES

- ALEXANDER, H., HAASEN, P., LABUSCH, R., and SCHRÖTER, W., 1979, Foreword to *J. Phys. (Paris)*, **40**, Colloque C6.
- AMELINCKX, S., 1979, *Dislocations in Particular Solids*, edited by F. R. N. Nabarro (Amsterdam: North-Holland).
- AMELINCKX, S., STRUMANE, G., and WEBB, W. W., 1960, *J. appl. Phys.*, **31**, 1359.
- BECHSTEDT *et al.* 1997.
- BROWN, L. M., and THÖLEN, A. R., 1964, *Discuss Faraday Soc.*, **38**, 35.
- CHENG, C., HEINE, V., and NEEDS, R. J., 1990a, *J. Phys.: condens. Matter*, **2**, 5115; 1990b, *Europhys. Lett.*, **12**, 69.
- CHENG, C., NEEDS, R. J., and HEINE, V., 1988, *J. Phys. C*, **21**, 1049.

- CHOYKE, W. J., MATSUNAMI, H., and PENSL, G., 1997, *Silicon Carbide, A Review of Fundamental Questions and Applications to Current Device Technology* (Berlin: Akademie Verlag).
- COCKAYNE, D. J. H., RAY, I. L. F., and WHELAN, M. J., 1969, *Phil. Mag.*, **20**, 1265.
- CORMAN, G. S., 1992, *J. Amer. Ceram. Soc.*, **75**, 3421.
- FUJITA, S., MAEDA, K., and HYODO, S., 1986, *J. Mater. Sci. Lett.*, **5**, 450; 1987, *Phil. Mag. A*, **55**, 203.
- GOMES DE MESQUITA, A. H., 1967, *Acta crystallogr.*, **23**, 610.
- GOTTSCHALK, H., PATZER, G., and ALEXANDER, H., 1978, *Physica Status Solidi (a)*, **45**, 207.
- HEINE, V., CHENG, C., ENGEL, G. E., and NEEDS, R. J., 1992, *Wide Band Gap Semiconductors*, edited by T. D. Moustakas, J. I. Pankove and Y. Hamakawa (Pittsburgh, PA: Materials Research Society), p. 507.
- [HONG, M. H., SAMANT, A. V., and PIROUZ, P., 1999,
- KÄCKELL, P., FURTHMÜLLER, J., and BECHSTEDT, F., 1998, *Phys. Rev. B*, **58**, 1326.
- KÄCKELL, P., WENZIE, B., and BECHSTEDT, F., 1994, *Phys. Rev. B*, **50**, 17037.
- KARCH, K., WELLENHOFER, G., PAVONE, P., RÖSSLER, U., and STRAUCH, D., 1994, *22nd International Conference on the Physics of Semiconductors*, edited by D. Lockwood (Singapore: World Scientific), p. 401.
- LAMBRECHT, W. R. L., SEGALL, B., METHFESSEL, M., and VAN SCHILFGAARDE, M., 1991, *Phys. Rev. B*, **44**, 3685.
- LIMPIJUMNONG, S., and LAMBRECHT, W. R. L., 1998, *Phys. Rev. B*, **57**, 12017.
- MAEDA, K., SUZUKI, K., FUJITA, S., ICHIHARA, M., and HYODO, S., 1988, *Phil. Mag. A*, **57**, 573.
- MAEDA, K., SUZUKI, K., and ICHIHARA, M., 1993, *Microsc. Microanal. Microstruct.*, **4**, 211.
- NING, X. J., HUVEY, N., and PIROUZ, P., 1997, *J. Amer. Ceram. Soc.*, **80**, 1645.
- NING, X. J., and PIROUZ, P., 1996, *J. Mater. Res.*, **11**, 884.
- PILYANKEVICH, A. N., and BRITUN, V. F., 1984, *Physica Status Solidi (a)*, **82**, 449.
- PILYANKEVICH, A. N., BRITUN, V. F., and KRAVETS, V. A., 1982, *Sov. Phys. Solid State*, **24**, 862.
- PIROUZ, P., 1997, *Solid State Phenomena*, **56**, 107.
- PIROUZ, P., and NING, X. J., 1995, *Microscopy of Semiconducting Materials*, edited by A. G. Cullis and A. Staton-Bevan (Bristol, UK: Institute of Physics), p. 69.
- PIROUZ, P., and YANG, J. W., 1993, *Ultramicroscopy*, **51**, 189.
- RAMSDELL, L. S., 1947, *Amer. Mineralogist*, **32**, 64.
- SAMANT, A. V., 1999, Ph.D. thesis, Case Western Reserve University.
- SAMANT, A. V., HONG, M., and PIROUZ, P., 1999, *Acta Mater.*, in press.
- STEEDS, J. W., 1973, *Introduction to Anisotropic Elasticity Theory of Dislocations* (Oxford: Clarendon Press).
- STEVENS, R., 1970, *J. Mater. Sci.*, **5**, 474; 1972, *J. Mater. Sci.*, **7**, 517.
- SUEMATSU, H., SUZUKI, T., ISEKI, T., and MORI, T., 1991, *J. Amer. Ceram. Soc.*, **74**, 173.
- TAIROV, Y. M., and TSVETKOV, V. F., 1978, *J. Crystal Growth*, **43**, 209.
- [TAKEUCHI, S., and SUZUKI, K., 1999, *Physica Status Solidi (a)*, in press.
- TAKEUCHI, S., SUZUKI, K., MAEDA, K., and IWANAGA, H., 1984, *Phil. Mag. A*, **50**, 171.
- YANG, J. W., 1993, Ph.D. thesis, Case Western Reserve University.
- YANG, J. W., NING, X. J., and PIROUZ, P., 1994, *Japan-US Workshop on Functional Fronts in Advanced Ceramics*, edited by K. Yanagida, and R. Newnham (Tsukuba, Japan: Ceramic Society of Japan).
- YANG, J. W., and PIROUZ, P., 1993, *J. Mater. Res.*, **8**, 2902.
- ZHDANOV, G. S., 1945, *C. R. Acad. Sci. USSR*, **48**, 39.

# Activation parameters for dislocation glide in $\alpha$ -SiC

A. V. Samant, P. Pirouz\*

*Department of Materials Science and Engineering, Case Western Reserve University, Cleveland, OH 44106, USA*

Received 9 March 1998; accepted 8 September 1998

## Abstract

The critical resolved shear stress for activating the  $\langle 2\bar{1}10 \rangle (0001)$  slip system of monocrystalline  $\alpha$ -SiC ( $6H$  and  $4H$  polytypes) has been determined as a function of test temperature and strain rate via constant-displacement compression tests. Tests were conducted at temperatures between 550 and 1300°C and strain rates between  $3.1 \times 10^{-5} \text{ s}^{-1}$  and  $6.5 \times 10^{-4} \text{ s}^{-1}$ . The current study shows that  $\alpha$ -SiC crystals can be plastically deformed via relatively modest resolved shear stresses on the basal plane at temperatures as low as 550°C. Two different methods to determine the activation parameters for dislocation glide have been examined. Transmission electron microscopy (TEM) was used to rationalize some of the results. © 1998 Elsevier Science Ltd. All rights reserved.

**Keywords:** SiC; Dislocations; Compression; Shear stress; Activation parameters

## 1. Introduction

There has been significant work published in the area of plastic deformation of both elemental semiconductors, e.g. Si [1–9], and compound semiconductors, e.g. GaAs [10–16]. However, due to lack of availability of high quality single-crystalline, single-polytype samples of wide bandgap compound semiconductors, e.g. SiC, until very recently, there has been less research on their plastic deformation (see, however [17–25]).

Fujita et al. [17] and Maeda et al. [18] studied deformation of single-crystalline  $6H$ -SiC by high temperature indentation and compression followed by transmission electron microscopy (TEM) investigation of dislocations generated. They found that the flow rate,  $\dot{\gamma}$ , in their experiments could be expressed in the form:

$$\dot{\gamma} \propto (\tau_c - \tau_i)^n \exp(-U/kT)$$

where the activation energy,  $U$ , the stress exponent,  $n$ , and the internal stress,  $\tau_i$

evaluated to be  $3.4 \pm 0.7 \text{ eV}$ ,  $3.1 \pm 0.4$  and  $3 \text{ MPa}$ , respectively [17]. In the above expression,  $\tau_c$  is the

critical resolved shear stress,  $k$  is the Boltzmann constant, and  $T$  is the absolute temperature.

Corman [20] conducted constant-load creep tests on  $6H$ -SiC for orientations parallel to and at 45°C to  $[0001]$ . Deformation of the 45° oriented crystal was dominated by basal slip. The steady-state creep rate,  $\dot{\epsilon}$ , of the crystals in this orientation in the range 800–1200°C, and at stresses,  $\sigma$ , from 50 to 200 MPa, could be described as:

$$\dot{\gamma} = A\sigma^n \exp(-U/kT)$$

where the activation energy  $U$ , and the stress exponent  $n$ , were evaluated to be  $2.87 \pm 0.25 \text{ eV}$  and  $3.32 \pm 0.41$ , respectively [20]. By analogy with the work of Fujita et al. [17], Corman [20] concluded that the controlling mechanism for basal slip in  $6H$ -SiC is thermally-assisted activation over the Peierls barrier.

The present paper deals with some recent experiments on two of the hexagonal polytypes of silicon carbide, namely  $6H$ - and  $4H$ -SiC.

## 2. Experimental procedure

The  $6H$ -SiC bulk single crystal was provided by Cree Research Inc. (Durham, North Carolina, USA) and

\*Corresponding author. E-mail: pirouz@cwmsd.mse.cwru.edu

was grown along the [0001] direction by a modified sublimation technique. The 4H-SiC bulk single crystal was obtained from Northrop Grumman Corp. (Pittsburgh, Pennsylvania, USA) and was grown along the [0001] direction by the physical vapor transport technique. Secondary Ion Mass Spectroscopy (SIMS) was used to determine the oxygen ( $<5 \times 10^{16} \text{ cm}^{-3}$  for 6H and  $<1.5 \times 10^{17} \text{ cm}^{-3}$  for 4H) and nitrogen ( $\approx 5 \times 10^{16} \text{ cm}^{-3}$  for 6H and  $\approx 1.1 \times 10^{19} \text{ cm}^{-3}$  for 4H) contents. Photographic Emission Spectroscopy [26] revealed that the concentration of each of the common impurity elements, such as titanium, iron, aluminum, nickel and manganese, was below the detection limit of 5 ppm for the 6H crystal. The 4H crystal had similar impurity element concentrations as the 6H crystal with the exception of a higher aluminum concentration of  $\approx 6$  ppm.

The orientations of the bulk crystals were determined by the X-ray Laue back-reflection technique and the samples were cut into parallelepiped-shaped specimens (with nominal dimensions  $\approx 2.0 \times 2.0 \times 4.0 \text{ mm}^3$  for the 6H samples and  $\approx 1.8 \times 1.8 \times 3.5 \text{ mm}^3$  for the 4H samples) in an orientation similar to the 45° orientation used by Corman [20], such that each sample had a pair of {1100} lateral faces, with the (0001) basal plane inclined by 45° to the compression axis (shown schematically in Fig. 1). After cutting, all the faces of each specimen were ground using a 20  $\mu\text{m}$  diamond-impregnated disc followed by a 9  $\mu\text{m}$  diamond polish. Each specimen thus had the optimal orientation for maximum resolved shear stress (i.e. Schmid factor,  $S = 0.5$ ) for one of the three independent  $\langle 2\bar{1}10 \rangle$ (0001) primary slip systems.

The samples were tested using a 1361 Instron machine equipped with an electromechanical actuator, in a specially machined polycrystalline SiC jig. The machine was fitted with a furnace with MoSi<sub>2</sub> heating elements. Tests were conducted at temperatures between 550 and 1300°C. The temperature was monitored with a Pt-30%Rh vs Pt-6%Rh thermocouple. All the tests were conducted in an inert

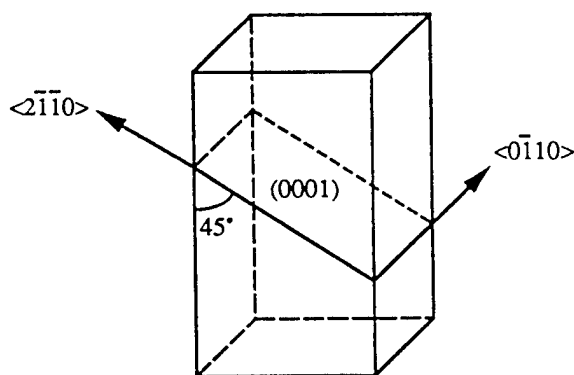


Fig. 1. Schematic of the compression specimen.

atmosphere of ultra-high purity argon gas, at three different initial strain rates of  $3.1 \times 10^{-5}$ ,  $6.3 \times 10^{-5}$  and  $1.3 \times 10^{-4} \text{ s}^{-1}$  for the 6H-SiC samples, and three different initial strain rates of  $6.3 \times 10^{-5}$ ,  $1.3 \times 10^{-4}$  and  $6.5 \times 10^{-4} \text{ s}^{-1}$  for the 4H-SiC samples.

Stress relaxation tests were carried out on some of the samples tested, wherein at some point during the experiment (either immediately after the onset of plastic flow or at some fixed value of plastic strain), the crosshead was stopped and the stress decay ( $\Delta\tau$ ) was recorded until the load versus time curve exhibited a change in curvature (discussed later). This usually required between 1 and 4 min depending on the test temperature and the flow stress value at which the crosshead had been stopped during the compression test.

For some compression tests on 4H-SiC samples, after yielding had occurred at an initial strain rate of  $1.3 \times 10^{-4} \text{ s}^{-1}$ , strain rate jump tests were conducted by suddenly increasing the crosshead speed by a factor of five to obtain a faster strain rate of  $6.5 \times 10^{-4} \text{ s}^{-1}$ . The samples were then further compressed until yielding was observed at this faster strain rate.

### 3. Experimental results

Shown in Fig. 2(a) and (b) are the engineering stress ( $s$ ) vs engineering strain ( $e$ ) curves for some of the 6H- and 4H-SiC samples, respectively, tested in uniaxial compression at various temperatures, at a strain rate of  $1.3 \times 10^{-4} \text{ s}^{-1}$ . These curves have been corrected for the machine-jig compliance. The critical resolved shear stress ( $\tau_c$ ) was assumed to be the stress value at the onset of non-linearity after the elastic region of the engineering stress-strain curve, multiplied by the Schmid factor ( $S = 0.5$ ), assuming that slip occurred on the  $\langle 2\bar{1}10 \rangle$ (0001) primary slip system of 6H- and 4H-SiC.

Figure 3(a) and (b) show the effect of test temperature on the critical resolved shear stress ( $\tau_c$ ) of 6H- and 4H-SiC, respectively, determined at the different strain rates. Each data-point in Fig. 3(a) and (b) represents one test. It is clear from these figures that the critical resolved shear stress for both 6H- and 4H-SiC increases sharply at test temperatures below 700°C and drops gradually in the temperature range 700–1300°C. Note that the critical resolved shear stress for 4H-SiC is much lower than that for 6H-SiC for temperatures below 700°C, at a given strain rate. At higher temperatures the critical resolved shear stress of 4H-SiC is only slightly lower than 6H-SiC and in some cases the difference is within the limits of experimental scatter. Thus, at a strain rate of  $6.3 \times 10^{-5} \text{ s}^{-1}$ , 4H-SiC yields at a critical resolved shear stress of  $\approx 235 \text{ MPa}$  at a temperature of 550°C and  $\approx 8 \text{ MPa}$  at a temperature of

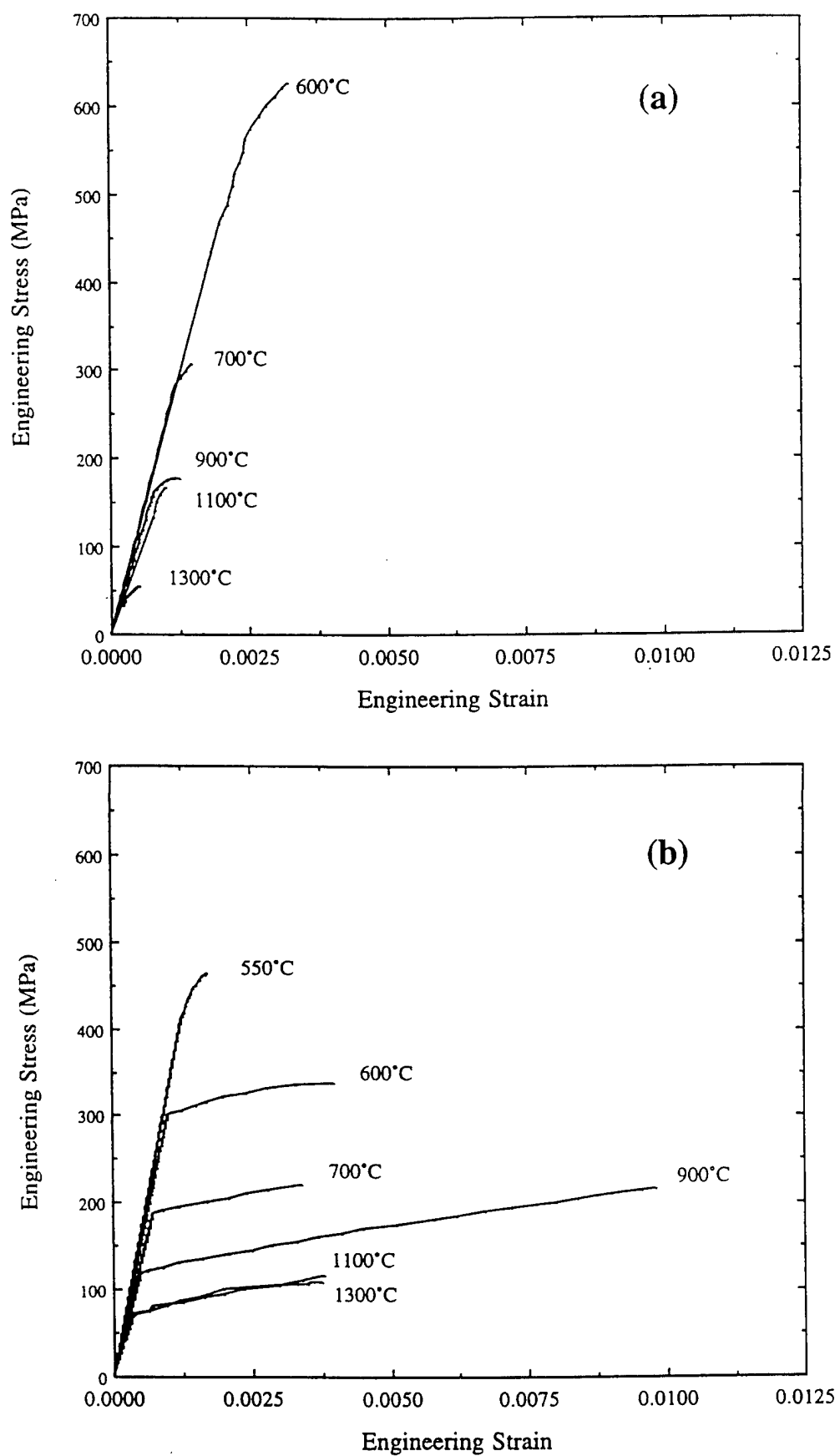


Fig. 2. Engineering stress-strain curves for the compression tests conducted on (a) 6H-SiC and (b) 4H-SiC at a strain rate of  $1.3 \times 10^{-4} \text{ s}^{-1}$ .

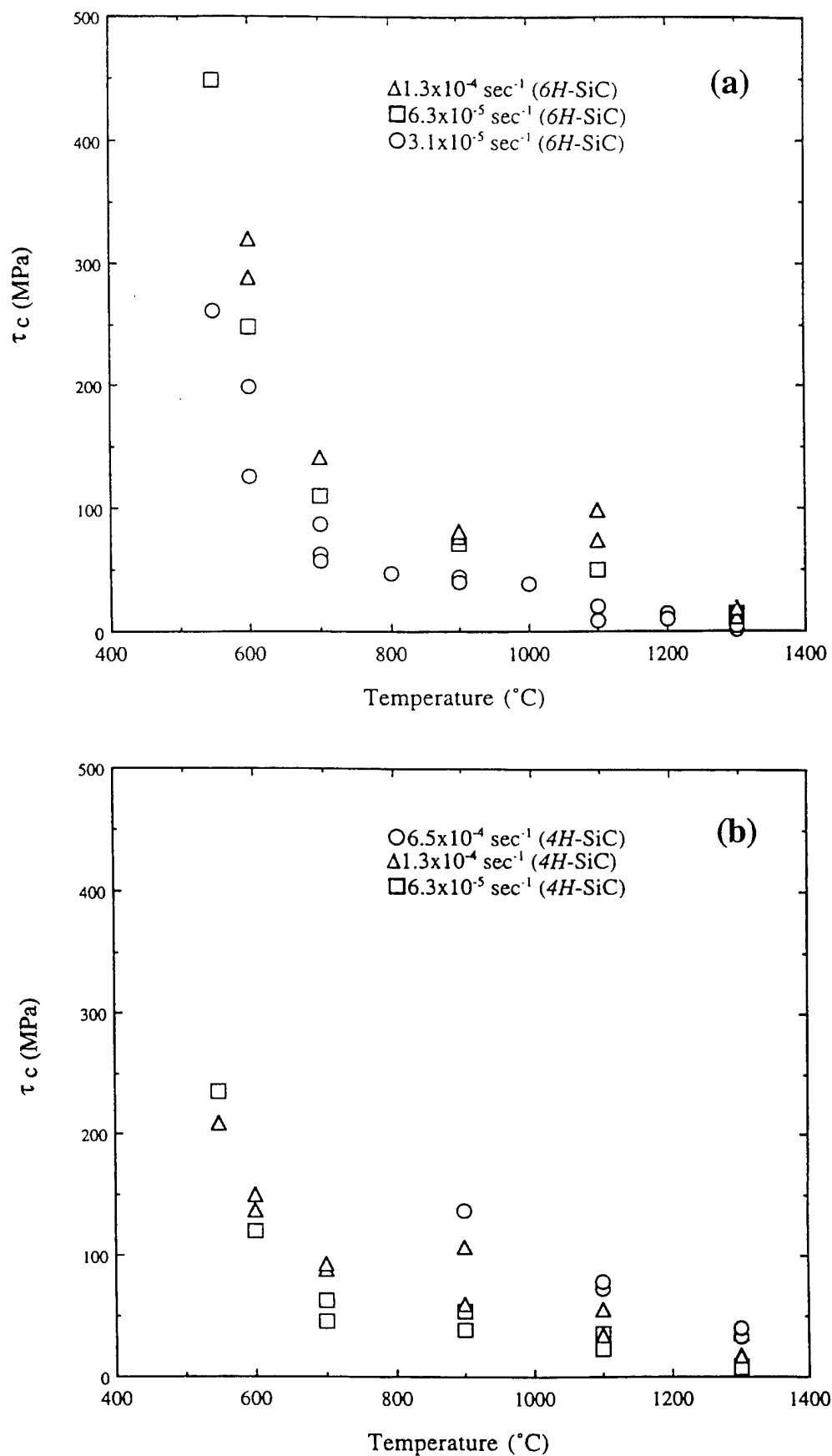


Fig. 3. Effect of test temperature and strain rate on the critical resolved shear stress,  $\tau_c$ , for the  $\langle 2\bar{1}10 \rangle (0001)$  primary slip system of (a) 6H- and (b) 4H-SiC.



1300°C, whereas 6H-SiC yields at  $\approx 450$  MPa and  $\approx 13$  MPa respectively, at the same temperatures. 4H-SiC can be plastically deformed at 550°C at a strain rate of  $1.3 \times 10^{-4} \text{ s}^{-1}$ , whereas 6H-SiC fractures catastrophically at this temperature. Note however, that we were able to plastically deform 6H-SiC at 550°C at the slower strain rate of  $3.1 \times 10^{-5} \text{ s}^{-1}$ .

To the best of our knowledge there have been no previous reports on the deformation of single-crystalline 4H-SiC. Also, we could not find any literature on plastic deformation of single-crystalline SiC at temperatures as low as 550°C, in experiments similar to the ones discussed here.

Figure 4 shows some engineering stress ( $\sigma$ ) vs engineering strain ( $\epsilon$ ) curves for the strain rate jump tests conducted on some 4H-SiC samples initially deformed at a strain rate of  $1.3 \times 10^{-4} \text{ s}^{-1}$ ; after yielding had occurred at this strain rate, the crosshead speed was suddenly increased by a factor of five to obtain a faster strain rate of  $6.5 \times 10^{-4} \text{ s}^{-1}$ . Due to the extensive cracking which accompanied plastic deformation, these tests could not be carried out at temperatures below 900°C.

## 4. Discussion

### 4.1. Calculation of activation parameters

Starting from Orowan's equation for the shear strain rate [7],

$$\dot{\gamma} = \dot{\gamma}_0 \exp\left(-\frac{\Delta H}{kT}\right) \quad (1)$$

where,  $\dot{\gamma}_0$  is the pre-exponential factor, and  $\Delta H$  is the activation enthalpy, two basic methods for the analysis of activation parameters will be examined [7,9,14–17,27]. The difference between these two methods is the way that the stress dependence of the plastic strain rate,  $\dot{\gamma}$ , is taken into account (the temperature dependence of  $\dot{\gamma}$  is exponential in both methods).

### 4.2. Stress-dependent activation enthalpy

In the first method, the activation enthalpy ( $\Delta H$ ) in eqn (1) is assumed to be stress-dependent whereas the

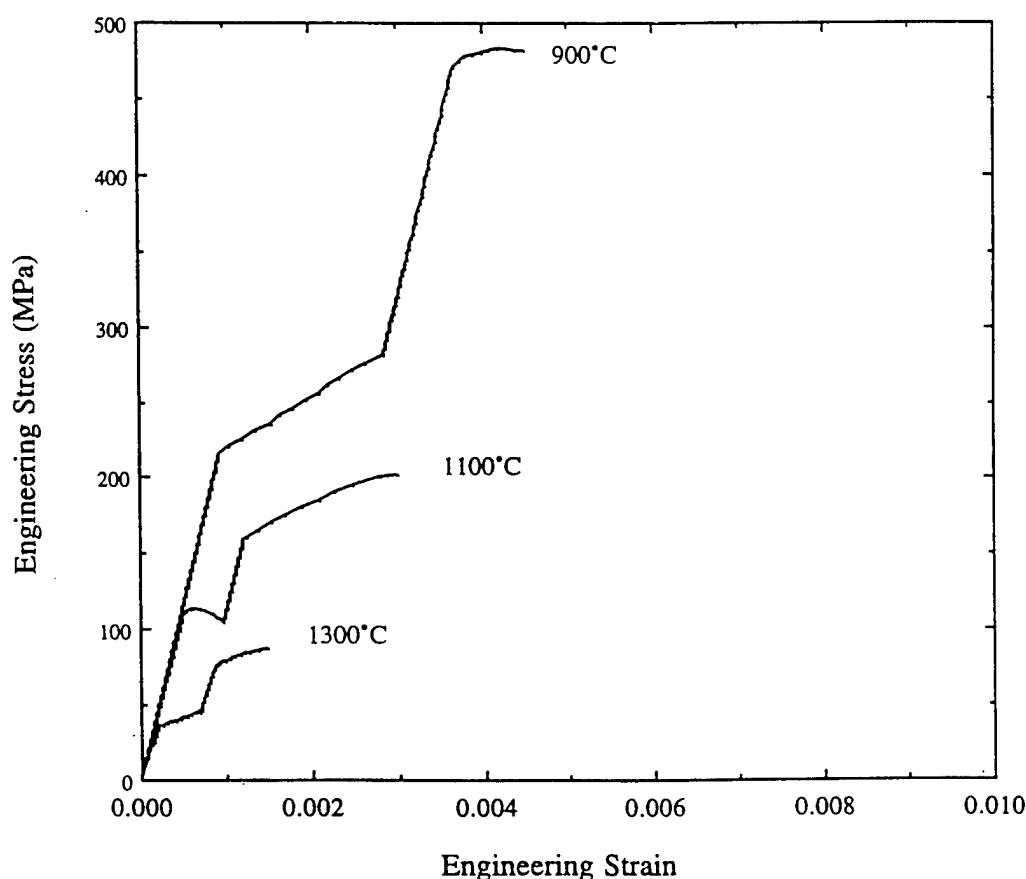


Fig. 4. Engineering stress-strain curves for the strain rate jump tests conducted on 4H-SiC from an initial strain rate of  $1.3 \times 10^{-4} \text{ s}^{-1}$  to a strain rate of  $6.5 \times 10^{-4} \text{ s}^{-1}$ .

pre-exponential factor ( $\dot{\gamma}_0$ ) is assumed to be independent of stress, i.e.:

$$\dot{\gamma} = \dot{\gamma}_0 \exp\left(-\frac{H(\tau)}{kT}\right) \quad (2)$$

where  $\dot{\gamma}_0$  is the stress-independent pre-exponential factor, and  $H(\tau)$  is the stress-dependent activation enthalpy.

Taking logarithms on both sides of eqn (2), differentiating with respect to the shear stress,  $\tau$ , and rearranging:

$$\left(\frac{\partial H(\tau)}{\partial \tau}\right)_T = -kT \left(\frac{\partial \ln \dot{\gamma}}{\partial \tau}\right)_T \quad (3)$$

The left hand side of eqn (3), i.e. the stress-dependence of the activation enthalpy is usually defined as the activation volume,  $V$ :

$$V \equiv -\left(\frac{\partial H}{\partial \tau}\right)_T \quad (4)$$

Thus,

$$V = kT \left(\frac{\partial \ln \dot{\gamma}}{\partial \tau}\right)_T \quad (5)$$

#### 4.2.1. Activation volume calculation: stress relaxation tests

One method of obtaining the activation volume,  $V$ , is from stress relaxation tests according to the Guin and Pratt analysis [28] and Omri et al. [7]. According to Omri et al. [7] and Boivin et al. [15], the recorded decay of stress ( $\Delta\tau$ ) after time,  $t$ , where the crosshead has been stopped at  $\tau = \tau_0$  and  $t = 0$ , can be written as,

$$\Delta\tau = \frac{kT}{V} \ln\left(1 + \frac{t}{c}\right) \quad (6)$$

The constant  $c$  in eqn (6) is related to the testing conditions by,

$$c = kT/MV\dot{\gamma}_0 \quad (7)$$

where  $\dot{\gamma}_0$  is the plastic strain rate at  $t = 0$  and  $M$  is the stiffness of the machine-sample assembly. Omri et al. [7] emphasized that the Guin and Pratt analysis [28] is not valid for long relaxation times because the dislocation structure could be transient during a relaxation test. In our experiments, in a manner similar to that employed by Omri et al. [7], the load decay ( $\Delta\tau$ ) was recorded until the load versus time curve exhibited a change in curvature. This usually

required between 1 and 4 min depending on the test temperature and the flow stress value at which the crosshead had been stopped during the compression test. The activation volume,  $V$ , can be determined from the slope  $\lambda$  of the semi-logarithmic plot of  $\Delta\tau$  vs  $\ln(1+t/c)$  using a value of  $c$  which linearizes the plot. Figure 5(a) and (b) show the linearized semi-logarithmic plots of  $\Delta\tau$  vs  $\ln(1+t/c)$  for 6H- and 4H-SiC, respectively, conducted at various test temperatures. Table 1 lists the values of the constant  $c$  obtained for the relaxation tests, as a function of the test temperature and the shear stress. The activation volumes at the various temperatures were calculated using the slope  $\lambda$  (also listed in Table 1) from the straight lines shown in Fig. 5(a) and (b) and eqn (6). The open symbols in Fig. 6 show these experimentally calculated activation volumes plotted as a function of the shear stress,  $\tau$ . Note the very small values of the activation volume ( $\approx 0.3 \times 10^{-27} \text{ m}^3$ ) at higher stresses ( $> 150 \text{ MPa}$ ); at very low stresses ( $< 10 \text{ MPa}$ )  $V$  increases to  $\approx 10 \times 10^{-27} \text{ m}^3$ .

#### 4.2.2. Activation volume calculations: strain rate jump tests

Another method of obtaining the activation volume,  $V$ , is to carry out strain rate jump tests where, at a certain stress,  $\tau$ , corresponding to a certain strain,  $\gamma$ , the strain rate is suddenly changed from  $\dot{\gamma}_1$  to  $\dot{\gamma}_2$  and the resulting stress change,  $\Delta\tau[(\tau_2 - \tau_1)]$ , is measured. The activation volume can then be determined from these experiments using eqn (5) in the form [17],

$$V = -kT \frac{\ln(\dot{\gamma}_1/\dot{\gamma}_2)}{\Delta\tau} \quad (8)$$

The solid square symbols in Fig. 6 show the activation volumes calculated using eqn (8) and the strain rate jump tests conducted on some 4H-SiC samples, described in Section 3, plotted as a function of the shear stress,  $\tau$ . Also shown in Fig. 6 for comparison purposes, are the activation volumes obtained by Fujita et al. [17] from strain rate jump tests on 6H-SiC.

Having determined the activation volume using either the stress relaxation tests (Section 4.2.1) or the strain rate jump tests (Section 4.2.2), the stress-dependent activation enthalpy,  $H(\tau)$ , can be estimated by the partial differentiation of eqn (2) with respect to  $T$  under a given  $\dot{\gamma}$  as:

$$H(\tau) = T \frac{\partial H}{\partial \tau} \left(\frac{\partial \tau}{\partial T}\right) - \frac{kT^2}{\rho} \left(\frac{\partial \rho}{\partial T}\right) \quad (9)$$

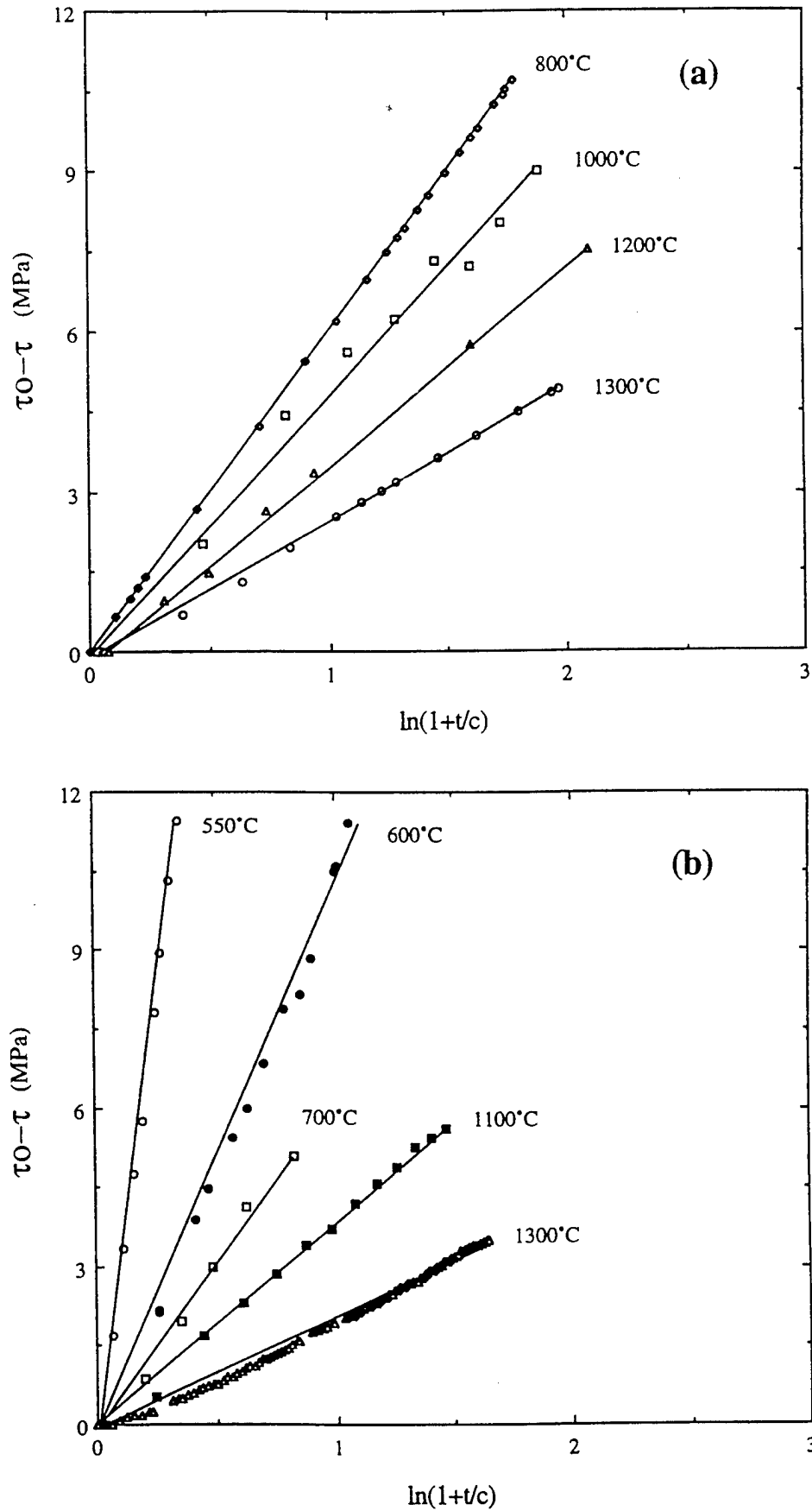


Fig. 5. Linearized semi-logarithmic plots of the stress decay  $\Delta\tau$  [i.e.  $(\tau_0 - \tau)$ ] vs  $\ln(t+c)$  from stress relaxation tests on (a) 6H- and (b) 4H-SiC.

Using eqn (5) it can be shown [17] that eqn (9) reduces to:

$$H = -VT \left( \frac{\partial \tau}{\partial T} \right) \quad (10)$$

Figure 7 shows the stress-dependent activation enthalpy, calculated using eqn (10) and data from Fig. 3 and Fig. 6, plotted as a function of the shear stress,  $\tau$ . In the present experiments the stress-

dependent activation enthalpy for 4H-SiC drops rapidly from  $\approx 7.4$  eV at a shear stress of 8 MPa to  $\approx 4.0$  eV at a shear stress of 60 MPa, and then gradually to  $\approx 2.8$  eV at shear stresses in excess of 235 MPa. For 6H-SiC the stress-dependent activation enthalpy drops rapidly from  $\approx 8.1$  eV at a shear stress of 4 MPa to  $\approx 3.0$  eV at a shear stress of 47 MPa. Fujita et al. [17] observed that the shape of their stress-dependent activation enthalpy curve (also shown in Fig. 7 for comparison purposes), which indicated an increase in the activation energy with increasing stress, was physically unacceptable, specially in light of the positive values of the activation volumes,  $V$ . They concluded that a consistent analysis is not possible if eqn (2) was used to describe the plastic strain rates. In other words, the authors concluded that the assumption of a stress-dependent activation enthalpy was not reasonable for these materials. In the present experiments however, an increase in the stress-dependent activation enthalpy after the initially high values at low stresses was not observed. Although the activation volumes obtained in the present experiments compare well with those obtained by Fujita et al. [17] (see Fig. 6), the slope of their critical resolved shear stress vs temperature

Table 1  
Tabulation of data from the relaxation tests

Material	Temperature (°C)	Shear stress ( $\tau$ ) (MPa)	$\epsilon$ (s)	Slope ( $\lambda$ ) (MPa)
6H-SiC	800	47.0	67.6	6.0
6H-SiC	1000	38.0	29.8	4.8
6H-SiC	1200	14.0	17.9	3.7
6H-SiC	1300	4.2	12.0	2.6
4H-SiC	550	235.0	40.0	47.4
4H-SiC	600	120.0	19.9	11.4
4H-SiC	700	63.7	9.9	6.7
4H-SiC	1100	23.2	14.0	3.4
4H-SiC	1300	8.0	7.4	2.3

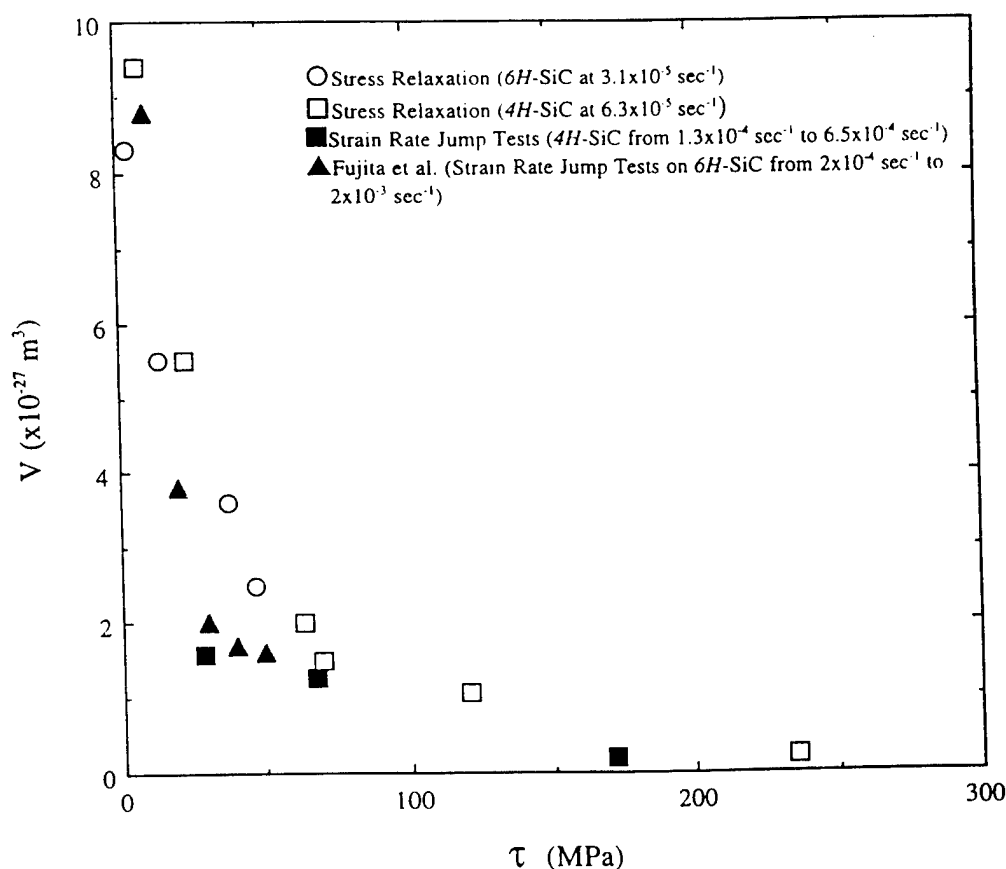


Fig. 6. Apparent activation volumes as a function of the shear stress, calculated from stress relaxation and strain rate jump tests. Also included are the data from Fujita et al. [17].

curve increased sharply in a narrow temperature range. From eqn (10) it can be seen that this rapid rise in the slope,  $(\partial\tau/\partial T)_\dot{\gamma}$ , would result in an increase in the activation enthalpy at higher shear stresses unless this was compensated by much lower activation volumes at similar shear stresses. In the present experiments since the slope,  $(\partial\tau/\partial T)_\dot{\gamma}$ , of the curves [see Fig. 3(a) and (b)], does not increase rapidly down to temperatures as low as 700°C, we do not see an increase in the stress-dependent activation enthalpy with increasing stresses since the steep rise in the slope below this temperature is compensated by the corresponding lower activation volumes.

#### 4.3. Stress-independent activation enthalpy

In the second method, the activation energy ( $\Delta H$ ) in eqn (1) is assumed to be independent of stress, and the stress-dependence of the plastic strain rate ( $\dot{\gamma}$ ) is introduced in the pre-exponential term as,

$$\dot{\gamma} = A\tau_c^n \exp[-Q/kT] \quad (11)$$

where,  $A$  is a constant,  $n$  is the stress exponent, and  $Q$  is the stress-independent activation enthalpy.

For 'constant' strain rate type tests, similar to those in the present study, eqn (11) can be rewritten as follows:

$$\ln \tau_c = \frac{Q}{nkT} + \frac{1}{n} [\ln \dot{\gamma} - \ln A] \quad (12)$$

where the second term on the right hand side of eqn (12) is a constant. Thus, according to eqn (12), a plot of  $\ln \tau_c$  vs  $1/T$  should be linear with a slope of  $Q/nk$ . The stress exponent,  $n$ , can be calculated according to the following expression which can be obtained from eqn (12):

$$n = \frac{\ln(\dot{\gamma}_1/\dot{\gamma}_2)}{\ln(\tau_{c1}/\tau_{c2})} \quad (13)$$

where  $\tau_{c1}$  and  $\tau_{c2}$  are the critical resolved shear stresses at the two independent strain rates  $\dot{\gamma}_1$  and  $\dot{\gamma}_2$  at the same test temperature,  $T$ .

Figure 8(a) and (b) are plots of the natural log of the critical resolved shear stress,  $\ln \tau_c$ , vs the reciprocal of the absolute temperature,  $1/T$ , for compression tests on 6H- and 4H-SiC, respectively. Table 2 summarizes the slopes,  $Q/n$ , and the stress-independent activation

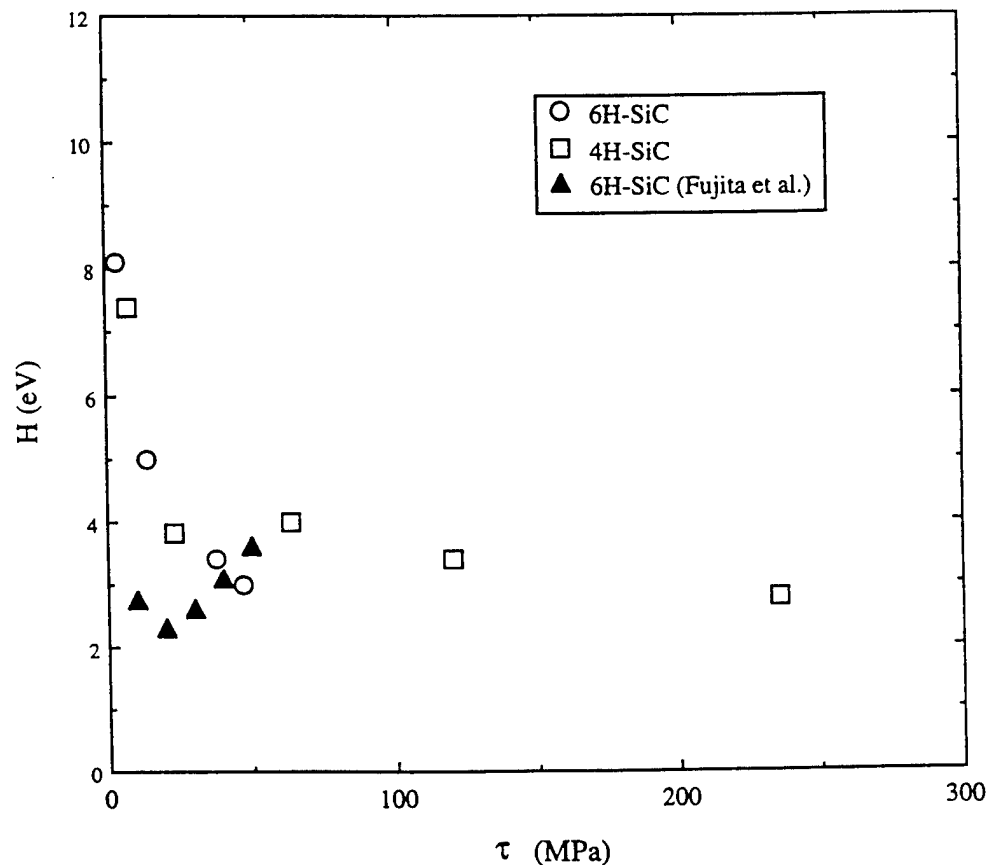


Fig. 7. Stress dependent activation enthalpy as a function of the shear stress. Also included are data from Fujita *et al.* [17].

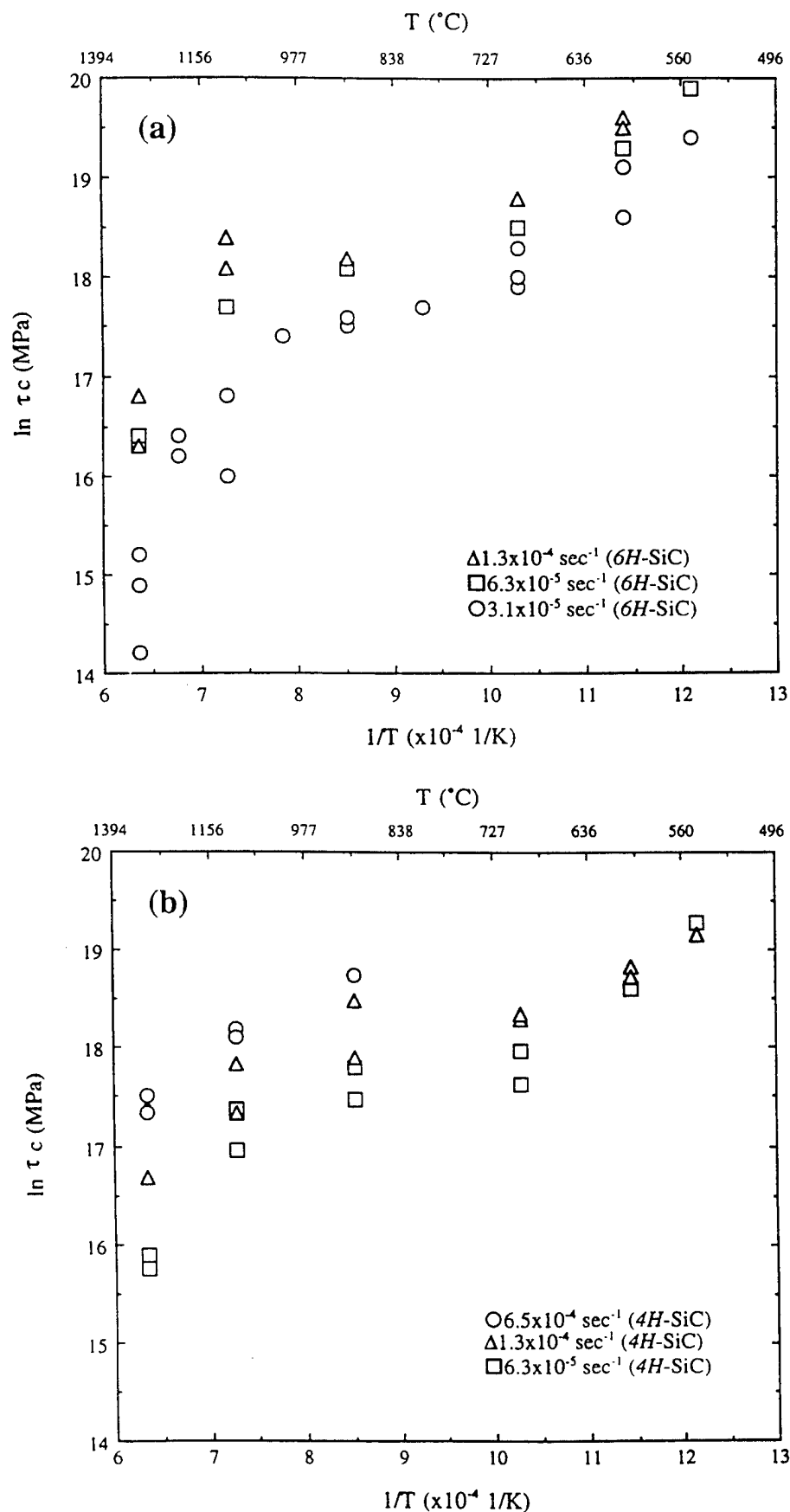
Fig. 8. Plot of  $\ln \tau_c$  vs  $1/T$  following eqn (12) for (a) 6H- and (b) 4H-SiC.

Table 2  
Tabulation of data from the stress-independent activation enthalpy ( $Q$ ) calculations

Material	Strain rate ( $s^{-1}$ )	Temperature range ( $^{\circ}C$ )	$Q/n$ (eV)	$Q^*$ (eV)
6H-SiC	$1.3 \times 10^{-4}$	550–1300	0.6	$1.8 \pm 0.7$
6H-SiC	$6.3 \times 10^{-5}$	550–1300	0.8	$2.4 \pm 0.8$
6H-SiC	$3.1 \times 10^{-5}$	550–1100	0.6	$1.8 \pm 0.7$
6H-SiC	$3.1 \times 10^{-5}$	1100–1300	1.6	$4.8 \pm 1.8$
4H-SiC	$6.5 \times 10^{-4}$	550–1300	0.6	$1.8 \pm 0.7$
4H-SiC	$1.3 \times 10^{-4}$	550–1300	0.7	$2.1 \pm 0.8$
4H-SiC	$6.3 \times 10^{-5}$	550–1100	0.7	$2.1 \pm 0.8$
4H-SiC	$6.3 \times 10^{-5}$	1100–1300	1.2	$3.6 \pm 1.2$

$n = 3.0 \pm 0.8$ .

enthalpy,  $Q$ , for the different strain rates and temperatures, for both 6H- and 4H-SiC. Using eqn (13) the average value of  $n$  was estimated to be  $3.0 \pm 0.8$  for both 6H- (from constant strain rate tests) and 4H-SiC (from constant strain rate tests as well as strain rate jump tests). It is clear from Fig. 8(a) and (b) and Table 2 that the linear relationship predicted by eqn (12) is indeed observed for the faster strain rates of  $1.3 \times 10^{-4}$  and  $6.3 \times 10^{-5} s^{-1}$  for 6H-SiC, and  $6.5 \times 10^{-4}$  and  $1.3 \times 10^{-4} s^{-1}$  for 4H-SiC, over the entire temperature range tested (550–1300 $^{\circ}C$ ). The linear relationship predicted by eqn (12) is also observed up to a temperature of  $\approx 1100^{\circ}C$  for the slower strain rate tests (i.e.  $3.1 \times 10^{-5} s^{-1}$  for 6H-SiC and  $6.3 \times 10^{-5} s^{-1}$  for 4H-SiC). However, at temperatures above  $\approx 1100^{\circ}C$ , for these slower strain rates, there is considerable deviation from linearity, indicating that a unique slope,  $Q/n$ , can no longer be used to estimate the stress-independent activation enthalpy,  $Q$ . Based on the data presented in Fig. 8(a) and (b) and Table 2, the stress-independent activation enthalpy ( $Q$ ) for the faster strain rates of  $1.3 \times 10^{-4}$  and  $6.3 \times 10^{-5} s^{-1}$  for 6H-SiC, and  $6.5 \times 10^{-4}$  and  $1.3 \times 10^{-4} s^{-1}$  for 4H-SiC, over the entire temperature range tested (550–1300 $^{\circ}C$ ), as well as for the slower strain rate tests (i.e.  $3.1 \times 10^{-5} s^{-1}$  for 6H-SiC and  $6.3 \times 10^{-5} s^{-1}$  for 4H-SiC) up to a temperature of  $\approx 1100^{\circ}C$  was evaluated to be  $2.1 \pm 0.7$  eV. The stress-independent activation enthalpy ( $Q$ ) for the slower strain rate tests at temperatures above  $\approx 1100^{\circ}C$ , was evaluated to be  $4.8 \pm 1.8$  eV for 6H-SiC and  $3.6 \pm 1.2$  eV for 4H-SiC.

#### 4.4. Possible origins of the change in the stress-independent activation enthalpy

The results of some preliminary transmission electron microscopy studies on some of the 6H-SiC samples deformed at the slow strain rate of  $3.1 \times 10^{-5} s^{-1}$ , where a change in the activation enthalpy is observed at a temperature of  $\approx 1100^{\circ}C$ ,

have been presented in Ref. [24]. 6H-SiC samples deformed at this slow strain rate and a temperature below (900 $^{\circ}C$ ) and above (1300 $^{\circ}C$ ) the critical temperature of  $\approx 1100^{\circ}C$  (described in Section 4.3) were selected for TEM examination in order to compare the dislocation structure in them.

Most of the dislocations observed in the sample deformed at 1300 $^{\circ}C$  appeared to be complete dissociated dislocations, with both the partials visible in the field of view. Analysis of the dislocations using the  $g\cdot b$  method proved the dissociation reaction to be:

$$\frac{1}{3} [2\bar{1}\bar{1}0] \rightarrow \frac{1}{3} [1\bar{1}00] + \frac{1}{3} [10\bar{1}0]$$

In contrast, most of the dislocations observed in the sample deformed at 900 $^{\circ}C$  appeared singly and not as pairs (like those seen in the sample deformed at 1300 $^{\circ}C$ ). This could either mean that such dislocations are complete and undissociated, or that they are partials and their complimentary partials are not present in the viewing area. In fact,  $g\cdot b$  analysis showed these to be single partial dislocations with a  $\frac{1}{3}\langle 10\bar{1}0 \rangle$  Burgess vector. The question that remains unanswered at the moment is whether these dislocations are one of the partials (leading or trailing) of a pair where the complimentary (trailing or leading) partials are far from them and out of the viewing area, or whether these dislocations are single leading partials that have nucleated without their complimentary trailing partials having been nucleated. However, some recent work on 4H-SiC [23] has shown that, under certain conditions of deformation, leading partial dislocations can nucleate singly without their trailing partials nucleating.

The fact that the dislocations in the 6H-SiC sample deformed at 1300 $^{\circ}C$  consisted primarily of complete (albeit dissociated) dislocations, whereas the dislocations in the sample deformed at 900 $^{\circ}C$  were primarily a single partial, may explain the change of slope at  $\approx 1100^{\circ}C$  for the tests conducted at the slowest strain rates for both 6H- and 4H-SiC, shown in Fig. 7(a) and (b). In earlier studies [23,29,30], evidence has been presented that in semiconductors, the leading partial is the one which has a lower activation enthalpy, and thus nucleates before the trailing partial dislocation, with a higher activation enthalpy. Moreover, at lower temperatures, if the applied shear stress is not sufficiently high, the trailing particles may not nucleate at all, and the leading partial may glide singly leaving a stacking fault behind it. Thus, in the present experiments it is possible that for the faster strain rate tests in test temperature range of 550–1300 $^{\circ}C$ , and also for the slowest strain rate tests at temperatures lower than  $\approx 1100^{\circ}C$ , the deformation of 6H- and 4H-SiC takes place primarily by nucleation and glide of the more

mobile leading partial dislocations alone. The change in the slope of the curve in Fig. 8(a) and (b) for the slowest strain rate tests at a temperature of  $\approx 1100^\circ\text{C}$  may then correspond to a change in the activation enthalpy from that of the activation enthalpy for the leading partial at temperatures below  $\approx 1100^\circ\text{C}$  to that of the activation enthalpy of the complete dislocation (controlled by the mobility of the slower trailing partial) at temperatures above  $\approx 1100^\circ\text{C}$ .

It was further shown in earlier studies [23,29,30] that the more mobile partial dislocations in SiC have a silicon core [Si(g)] while the less mobile partial dislocations have a carbon core [C(g)]. The fact that the activation enthalpy of  $2.1 \pm 0.7$  eV for the faster strain rates of  $1.3 \times 10^{-4}$  and  $6.3 \times 10^{-5} \text{ s}^{-1}$  for 6H-SiC, and  $6.5 \times 10^{-4}$  and  $1.3 \times 10^{-4} \text{ s}^{-1}$  for 4H-SiC, over the entire temperature range tested (550–1300°C), as well as for the slower strain rate tests (i.e.  $3.1 \times 10^{-5} \text{ s}^{-1}$  for 6H-SiC and  $6.3 \times 10^{-5} \text{ s}^{-1}$  for 4H-SiC) up to a temperature of  $\approx 1100^\circ\text{C}$ , is approximately the same as that for glide of dislocations in elemental Si [9], suggests that we might in fact be measuring the activation enthalpy of Si(g) partial dislocation in this temperature-strain rate regime, and that this partial has approximately the same activation enthalpy as that for dislocation glide in elemental Si. After all, the activation enthalpy for the glide of Si(g) dislocations in both SiC and Si is primarily determined by the strength of the Si-Si bond in the reconstructed dislocation core [31]. On the other hand, the higher activation enthalpy of  $4.8 \pm 1.8$  eV for 6H-SiC and  $3.6 \pm 1.2$  eV for 4H-SiC for the slower strain rate tests (i.e.  $3.1 \times 10^{-5} \text{ s}^{-1}$  for 6H-SiC and  $6.3 \times 10^{-5} \text{ s}^{-1}$  for 4H-SiC) at temperatures above  $\approx 1100^\circ\text{C}$  suggests that we might be measuring an activation enthalpy that is controlled by the less mobile C(g) partial dislocation in this temperature-strain rate regime, and that this activation enthalpy is significantly higher than that for the glide of Si(g) partial dislocations.

## 5. Summary and conclusions

Compression tests were conducted on 6H- (at initial strain rates of  $3.1 \times 10^{-5}$ ,  $6.3 \times 10^{-5}$  and  $1.3 \times 10^{-5} \text{ s}^{-1}$ ) and 4H-SiC (at initial strain rates of  $6.3 \times 10^{-5}$ ,  $1.3 \times 10^{-4}$  and  $6.5 \times 10^{-4} \text{ s}^{-1}$ ) samples in the temperature range 550–1300°C.

Two methods of estimating the activation enthalpy for thermally-assisted dislocation glide were examined. The first method assumes a stress-dependent activation enthalpy [ $H(\tau)$ ] which was estimated from experimentally determined (i.e. from stress relaxation tests and strain rate jump tests) activation volumes. For 4H-SiC,  $H(\tau)$  drops rapidly from  $\approx 7.4$  eV at a shear stress of 8 MPa to  $\approx 4.0$  eV at a shear stress of 60 MPa, and

then gradually to  $\approx 2.8$  eV at shear stresses in excess of 235 MPa. For 6H-SiC the stress-dependent activation enthalpy drops rapidly from  $\approx 8.1$  eV at a shear stress of 4 MPa to  $\approx 3.0$  eV at a shear stress of 47 MPa.

The second method assumes a stress-independent activation enthalpy ( $Q$ ) which was estimated from the stress exponent,  $n$ , and the slope ( $Q/n$ ) of a plot of the natural log of the critical resolved shear stress vs the inverse of the absolute temperature. Based on this method the stress-independent activation enthalpy ( $Q$ ) for the faster strain rates of  $1.3 \times 10^{-4}$  and  $6.3 \times 10^{-5} \text{ s}^{-1}$  for 6H-SiC, and  $6.5 \times 10^{-4}$  and  $1.3 \times 10^{-4} \text{ s}^{-1}$  for 4H-SiC, over the entire temperature range tested (550–1300°C), as well as for the slower strain rate tests (i.e.  $3.1 \times 10^{-5} \text{ s}^{-1}$  for 6H-SiC and  $6.3 \times 10^{-5} \text{ s}^{-1}$  for 4H-SiC) up to a temperature of  $\approx 1100^\circ\text{C}$ , was evaluated to be  $2.1 \pm 0.7$  eV. The value of  $Q$  for the slower strain rate tests (i.e.  $3.1 \times 10^{-5} \text{ s}^{-1}$  for 6H-SiC and  $6.3 \times 10^{-5} \text{ s}^{-1}$  for 4H-SiC) at temperatures above  $\approx 1100^\circ\text{C}$ , was evaluated to be  $4.8 \pm 1.8$  eV for 6H-SiC and  $3.6 \pm 1.2$  eV for 4H-SiC. The change in the slope ( $Q/n$ ) of the plot of the natural log of the critical resolved shear stress vs the inverse of the absolute temperature above a critical temperature of  $\approx 1100^\circ\text{C}$  at the slowest strain rates might imply that the activation enthalpy for dislocation glide at lower temperatures is controlled by the activation enthalpy of the more mobile Si(g) partial dislocations whereas the activation enthalpy for dislocation glide at higher temperatures is controlled by the activation enthalpy of the less mobile C(g) partial dislocations.

Additional deformation tests need to be conducted in the 1100–1300°C temperature regime at the slowest strain rates for both 6H- and 4H-SiC, in order to accurately determine the temperature at which the slope of the  $\ln \tau_c$  vs  $1/T$  curve changes to a higher value. Deformation tests could also be done on both 6H- and 4H-SiC at even slower strain rates to determine whether this change of slope in the  $\ln \tau_c$  vs  $1/T$  curve shifts to a lower ( $< 1100^\circ\text{C}$ ) critical temperature. In addition, TEM experiments are continuing to determine the nature of the dislocation cores in the samples deformed at these slowest strain rates, as well as at the faster strain rates.

## Acknowledgements

The authors wish to thank Dr Calvin Carter of Cree Research Inc. for providing the bulk 6H-SiC crystal and Dr Don Hobgood of Northrop Grumman Corp. for providing the 4H-SiC crystal used in this study. This work was supported by subcontract number 95-SPI-420757-CWRU from the Silicon Carbide Consortium and contract number DE-FG02-93ER45496 from the Department of Energy.



## References

- [1] Mil'vidskii MG, Stolyarov OG, Berkova AV. Mechanical properties of strongly doped silicon single crystals. *Sov Phys Sol St* 1965;6(10):2531–2.
- [2] Eremenko VG, Nikitenko VI. Electron microscope investigation of the microplastic deformation mechanisms of silicon by indentation. *Phys Stat Sol* 1972;14:317–30.
- [3] Siethoff H, Schroter W. Dynamical recovery and self-diffusion in silicon. *Phil Mag A* 1978;37(6):711–18.
- [4] Michel JP, Omri M, Oueldenaoua A, George A. Plastic deformation and surface investigations of  $\langle 100 \rangle$  oriented silicon single crystals. *Ser Metall* 1982;16:677–82.
- [5] Demenet JL, Desoyer JC, Rabier J, Veyssiere P. On the plasticity of silicon below 650°C. *Ser Metall* 1984;18:41–5.
- [6] Brion HG, Haasen P. Screw dislocation networks generated in Ge and Si by stage IV compression. *Phil Mag A* 1985;51(6):879–91.
- [7] Omri M, Tete C, Michel J, George A. On the yield point of floating-zone silicon single crystals I. Yield stresses and activation parameters. *Phil Mag A* 1987;55(5):601–16.
- [8] George A, Rabier J. Dislocations and plasticity in semiconductors. I. Dislocation structures and dynamics. *Rev Phys Appl* 1987;22:941–66.
- [9] Rabier J, George A. Dislocations and plasticity in semiconductors. II. The relation between dislocation dynamics and plastic deformation. *Rev Phys Appl* 1987;22:1327–51.
- [10] Sazhin NP, Mil'vidskii MG, Osvenskii VB, Stolyarov OG. Influence of doping on the plastic deformation of gallium arsenide single crystals. *Sov Phys Sol St* 1966;8(5):1223–7.
- [11] Laister D, Jenkins GM. Deformation of single crystals of gallium arsenide. *J Mat Sci* 1973;8:1218–32.
- [12] Swaminathan V, Copley SM. Temperature and orientation dependence of plastic deformation in GaAs single crystals doped with Si, Cr, or Zn. *J Am Ceram Soc* 1975;58:482–5.
- [13] Steinhardt H, Haasen P. Creep and dislocation velocities in gallium arsenide. *Phys Stat Sol (a)* 1978;49:93–101.
- [14] Astié P, Couderc JJ, Chomel P, Quelard D, Duseaux M. Thermal activation of plastic deformation of undoped GaAs between 528 and 813 K. *Phys Stat Sol (a)* 1986;96:225–42.
- [15] Boivin P, Rabier J, Garem H. Plastic deformation of GaAs single crystals as a function of electronic doping. I: medium temperature (150–650°C). *Phil Mag A* 1990;61:619–45.
- [16] Boivin P, Rabier J, Garem H. Plastic deformation of GaAs single crystals as a function of electronic doping. II: low temperature (20–300°C). *Phil Mag A* 1990;61:645–72.
- [17] Fujita S, Maeda K, Hyodo S. Dislocation glide in 6H SiC single crystals subjected to high-temperature deformation. *Phil Mag A* 1987;55:203–15.
- [18] Maeda K, Suzuki K, Fujita S, Ichihara M, Hyodo S. Defects in plastically deformed 6H SiC single crystals studied by transmission electron microscopy. *Phil Mag A* 1988;57:573–92.
- [19] Suematsu H, Suzuki T, Iseki T. Kinking and cracking caused by slip in single crystals of silicon carbide. *J Am Ceram Soc* 1991;74: 173–8.
- [20] Corman GS. Creep of 6H  $\alpha$ -silicon carbide single crystals. *J Am Ceram Soc* 1992;75(12):3421–4.
- [21] Yang J, Suzuki T, Pirouz P, Powell J, Iseki T. Stress-induced polytypic transformation in SiC. *Mater Res Soc Symp Proc* 1992;242:531–6.
- [22] Ning XJ, Pirouz P. Kink and crack interfaces in deformed 6H-SiC single crystals. *Mater Res Soc Symp Proc* 1995;357: 157–62.
- [23] Ning XJ, Huvey N, Pirouz P. Dislocation cores and hardness polarity of 4H-SiC. *J Am Ceram Soc* 1997;80(7):1645–52.
- [24] Samant AV, Zhou WL, Pirouz P. Effect of test temperature and strain rate on the yield stress of monocrystalline 6H-SiC. *Phys Stat Sol (a)* 1998;166:155–69.
- [25] Samant AV, Wei XL, Pirouz P. An optical and transmission electron microscopy study of deformation-induced defects in 6H-SiC. *Phil Mag A* 1998;78(3):737–46.
- [26] Standard Recommended Practice for Photographic Photometry in Spectrochemical Analysis. Modified ASTM Stand. E116. In: Annual book of ASTM standards. Philadelphia, PA, American Society for Testing and Materials: 1996.
- [27] Escaig B, Farvacque JL, Ferré D. On the measurement of thermally activated slip parameters in tetrahedrally coordinated semiconductors. *Phys Stat Sol (a)* 1982;71:329–4.
- [28] Guio F, Pratt PL. Stress relaxation and the plastic deformation of solids. *Phys Stat Sol* 1964;6:111–20.
- [29] Ning XJ, Perez T, Pirouz P. Indentation-induced dislocations and microtwins in GaSb and GaAs. *Phil Mag A* 1995;72(4):837–59.
- [30] Ning XJ, Pirouz P. A large angle convergent beam electron diffraction study of the core nature of dislocations in 3C-SiC. *J Mater Res* 1996;11(4): 884–94.
- [31] Pirouz P, Ning XJ. Partial dislocations in semiconductors: structure, properties and their role in strain relaxation. In: Cullis AG, Staton-Beven A, editors. *The microscopy of semiconducting materials IX*. Bristol: Inst Phys Conf Ser 146, 1995: 69–77.

phys. stat. sol. (a) **166**, 155 (1998)

Subject classification: 62.20.Fc; S6

## Effect of Test Temperature and Strain Rate on the Yield Stress of Monocrystalline 6H-SiC

A. V. SAMANT, W. L. ZHOU, and P. PIROUZ

*Department of Materials Science and Engineering, Case Western Reserve University, Cleveland, OH 44106, USA*

(Received October 29, 1997)

Dedicated to Professor Dr. MANFRED RÜHLE on the occasion of his 60th birthday

The critical resolved shear stress for activating the (0001) ( $2\bar{1}\bar{1}0$ ) slip system of monocrystalline 6H-SiC has been determined as a function of test temperature and strain rate via constant-displacement compression tests. Tests were conducted at temperatures between 550 and 1300 °C at strain rates of  $1.3 \times 10^{-4}$ ,  $6.3 \times 10^{-5}$  and  $3.1 \times 10^{-5} \text{ s}^{-1}$ . The current study shows that 6H-SiC crystals can be plastically deformed via relatively modest resolved shear stresses on the basal plane at temperatures as low as  $\approx 550$  °C. For temperatures below  $\approx 1300$  °C for the fast and intermediate strain rates, and for temperatures below  $\approx 1100$  °C for the slow strain rate, the stress exponent  $n$ , and the activation enthalpy  $H$  were estimated to be  $(3.0 \pm 0.7)$  and  $(2.1 \pm 0.7)$  eV, respectively. At higher temperatures at the slowest strain rate, the activation enthalpy was determined to be  $(4.5 \pm 1.2)$  eV. Subsequent to the deformation tests, transmission electron microscopy (TEM) was used to rationalize some of the results.

### 1. Introduction

In addition to its use as a reinforcement in metal- and ceramic-matrix composites, silicon carbide (SiC) has drawn increasing attention from researchers in recent years because of its potential as a wide bandgap semiconductor. Despite its increasing popularity as an electronic material, however, the deformation behavior of monocrystalline SiC has been studied only to a limited extent.

Fujita et al. [1] studied deformation of single-crystalline 6H-SiC by high temperature indentation and compression followed by transmission electron microscopy (TEM) investigations of dislocations generated. The  $\alpha$ -SiC bulk single crystals used in their study were grown by the Acheson technique. The two strain rates employed by these authors were approximately  $2 \times 10^{-4}$  and  $2 \times 10^{-3} \text{ s}^{-1}$ , respectively. Two orientations, one in which a basal slip system was preferentially activated, and another in which basal slip was suppressed, were chosen.

Suematsu et al. [2] compressed single crystals of 6H-SiC, grown by a Acheson technique, parallel to the basal plane (i.e. zero resolved shear stress on the (0001) easy glide plane) at various temperatures between 900 and 1500 °C. The specimens were compressed at strain rates of  $2.8 \times 10^{-5}$  to  $5.6 \times 10^{-5} \text{ s}^{-1}$  to a point where they kinked. TEM studies of the deformed specimens showed a high density of dislocations around the kinked sections. The kinking was attributed to slight misalignments in the specimen during deformation.

Yang et al. [3] conducted constant-load compression tests on 6H-SiC single crystals in the temperature range 800 to 1400 °C, in an orientation similar to that employed by Fujita et al. [1]. These crystals were also grown by the Acheson technique.

Corman [4] conducted constant-load creep tests on 6H-SiC for orientations parallel to and at  $45^\circ$  to [0001]. Tests were conducted at temperatures ranging from 800 to 1850 °C to determine the steady-state creep rates for the two different orientations. Deformation of the  $45^\circ$  oriented crystal was dominated by basal slip.

Ning and Pirouz [5] deformed 6H-SiC single crystals in compression and indentation. The orientation chosen for compression was such that easy (basal) glide was not favored and the loading axis was normal to the (2023) end surfaces. In constant-load tests similar to those conducted by Yang et al. [3], they compressed the specimens at 1380 °C under a stress of 70 MPa. Extensive transmission electron microscopy was conducted to propose mechanisms for the formation of kinks and cracks in the crystals induced by deformation.

In the current work the primary interest was to determine the compressive yield strength of monocrystalline 6H-SiC as a function of test temperature and strain rate. The orientation of the single crystals was similar to that used by Corman [4]. The aim was to obtain the maximum possible Schmid factor,  $S$  (i.e. equal to a maximum possible value of 0.5), for the (0001)  $\langle 2\bar{1}10 \rangle$  slip system as well as to have a high value of  $S$  for the (0110)  $\langle 2\bar{1}10 \rangle$  secondary slip (cross-glide) system. Subsequent transmission electron microscopy on the deformed samples enabled the rationalization of the deformation behavior of 6H-SiC.

## 2. Experimental Procedures

The 6H-SiC bulk single crystal was obtained from Cree Research Inc.<sup>1)</sup> The crystal was grown along the [0001] direction by a modified sublimation technique, and was pale green and transparent in its as-received condition. Raman spectroscopy was conducted on the as-received single crystal in an effort to identify the presence of other polytypes of SiC. Fig. 1 shows a typical spectrum obtained. According to the data reported in the literature [6 to 9] all the peaks in the figure correspond to those of single crystalline pure

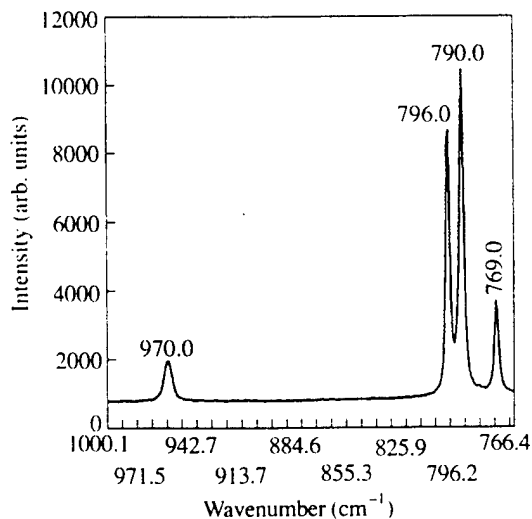


Fig. 1. Raman spectrum from the as-received 6H-SiC single crystal

<sup>1)</sup> Durham, North Carolina, USA.

- [19] J. W. Matthews and A. E. Blakeslee, *Defects in Epitaxial Multilayers: I. Misfit Dislocations*, J. Crystal Growth **27**, 118-125, (1974).
- [20] J. W. Matthews, *Defects associated with the accommodation of misfit between crystals*, J. Vac. Sci. Technol. **12**, 126-133, (1975).
- [21] J. W. Matthews, *Coherent interfaces and misfit dislocations*, in "Epitaxial Growth, Part B", ed. by J. W. Matthews, pp. 559-609, (Academic Press, New York, 1975).
- [22] J. W. Matthews and A. E. Blakeslee, *Defects in Epitaxial Multilayers: II. Dislocation Pile-Ups, Threading Dislocations, Slip Lines and Cracks*, J. Crystal Growth **29**, 273-280, (1975).
- [23] J. W. Matthews, *Misfit Dislocations*, in "Dislocations in Solids", ed. by F. R. N. Nabarro, pp. 462-545, (North-Holland Publishing Company, Amsterdam, 1979).
- [24] J. W. Cahn, *On Spinodal Decomposition in Cubic Crystals*, Acta Met. **10**(3), 179-183, (1962).
- [25] J. P. Hirth and J. Lothe, *Theory of Dislocations*, (McGraw-Hill, New York, 1968).
- [26] L. B. Freund, *The stability of a dislocation threading a strained layer on a substrate*, J. Appl. Mech. **54**, 553-557, (1987).
- [27] W. D. Nix, *Mechanical properties of thin films*, Met. Trans. **20A**, 2217-2245, (1989).
- [28] Y. H. Lo, *New approach to grow pseudomorphic structures over the critical thickness*, Appl. Phys. Lett. **59**(18), 2311-2313, (1991).
- [29] Y. H. Lo, W. J. Schaff and D. Teng, *Extended Pseudomorphic Limits Using Compliant Substrates*, in "Semiconductor Heterostructures for Photonic and Electronic Applications", ed. D. C. Houghton, C. W. Tu and R. T. Tung, Mat. Res. Soc. Symp. Proc., **281**, pp. 191-196, (Materials Research Society, Pittsburgh, PA, 1993).
- [30] L. B. Freund and W. D. Nix, *A critical thickness condition for a strained compliant substrate/epitaxial film system*, Appl. Phys. Lett. **69**(2), 173-175, (1996).
- [31] F. E. Ejeckam, Y. H. Lo, S. Subramanian, H. Q. Hou and B. E. Hammons, *Lattice engineered compliant substrate for defect-free heteroepitaxial growth*, Appl. Phys. Lett. **70**(13), 1685-1687, (1997).
- [32] F. E. Ejeckam, M. L. Seaford, Y.-H. Lo, H. Q. Hou and B. E. Hammons, *Dislocation-free InSb grown on GaAs compliant universal substrates*, Appl. Phys. Lett. **71**(6), 776-778, (1997).
- [33] W. A. Jesser, J. H. van der Merwe and P. M. Stoop, *Misfit accommodation by compliant substrates*, J. Appl. Phys. **85**(4), 2129-2139, (1999).
- [34] A. R. Powell, S. S. Iyer and F. K. LeGoues, *New approach to the growth of low dislocation relaxed SiGe material*, Appl. Phys. Lett. **64**(14), 1856-1858, (1994).
- [35] T.-Y. Zhang and Y.-J. Su, *Elasticity Studies of the Critical Thickness of an Epilayer Deposited on a Compliant Substrate*, Acta mater. **47**(4), 1289-1296, (1999).
- [36] K. Izumi, M. Doken and H. Ariyoshi, Electron. Lett. **14**(18), 593-594, (1978).
- [37] I. Hamaguchi, T. Fujita, T. Yano, S. Hayashi and K. Kajiyama, Jpn. J. Appl. Phys. **34**(6A), 2989-2993, (1995).
- [38] F. Namavar, E. Cortesi, B. Buchanan and P. Sioshansi, "Low Energy SIMOX (LES)," in "IEEE SOS/SOI Tech. Conf. Proc.", pp. 117-118, (Stateline NV, 1989).
- [39] F. Namavar, E. Cortesi, B. Buchanan, J. M. Manke and N. M. Kalkhoran, "Ultrathin SOI Structures by Low Energy Oxygen Implantation," in "Phase Formation and Modification by Beam-Solid Interactions", ed. G. S. Was, L. E. Rehn and D. Follstaedt, Mat. Res. Soc. Symp. Proc., **235**, pp. 109-105, (Materials Research Society: Pittsburgh, PA, 1992).

- [40] F. Namavar, P. Colter, A. Cremins-Costa, C.-H. Wu, E. Gagnon, D. Perry and P. Pirouz, *Growth of Crystalline Quality SiC on Thin and Thick Silicon-on-Insulator Structures*, in "II-Nitride, SiC and Diamond Materials for Electronic Devices", ed. D. K. Gaskill, C. D. Brandt and R. J. Nemanich, Mat. Res. Soc. Symp. Proc., **423**, pp. 409-414, (Materials Research Society: Pittsburgh, PA, Pittsburgh, PA, 1996).
- [41] P. Pirouz, F. Ernst and T. T. Cheng, *Heteroepitaxy on (001) Silicon: Growth Mechanisms and Defect Formation*, in "Heteroepitaxy on Silicon: Fundamentals, Structures, and Devices", ed. H. K. Choi, H. Ishiwara, R. Hull and R. J. Nemanich, Mat. Res. Soc. Symp. Proc., **116**, pp. 57-70, (Materials Research Society, Pittsburgh, PA, 1988).
- [42] W. D. Kingery, H. K. Bowen and D. R. Uhlmann, *Introduction to Ceramics*, (John Wiley & Sons, New York, 1976).

**Table I.** Average FWHM of the SiC 200 peak for the SiC films grown on the three different substrates.

Sample	Thickness of SiC film ( $\mu m$ )	Substrate	Thickness of Si/SiO <sub>2</sub> (nm / nm)	FWHM (arcsec)
1	~40	Bulk Si <001>	500,000/0	198
2	~20	Thick SIMOX <001>	200/400	234
3	~40	Thin SIMOX <001>	35/40	180

## FIGURE CAPTIONS

Fig. 1. Schematic diagram of an epilayer on a compliant substrate. In this case, the compliant substrate consists of a thin monocrystalline silicon layer sitting on an amorphous silica layer that flows at a sufficiently high temperature and allows the Si substrate to plastically deform and accommodate the elastic stresses  $B_s \epsilon_s$  in it. There is thus weak shear forces, and sufficiently strong vertical adherence, between the thin Si substrate and the silica.

Fig. 2. Schematic configuration of a SIMOX structure as a Si(II)/SiO<sub>2</sub>/Si(I) multilayer.

Fig. 3. Typical X-ray rocking curves from the 3C-SiC film deposited on (a) bulk silicon wafer, (b) thick SIMOX, (c) thin SIMOX.

Fig. 4. Cross-sectional micrographs of the defect distribution in the 40  $\mu\text{m}$ -thick SiC grown on bulk Si from the region (a) near the SiC/Si interface, (b) halfway in the film, and (c) near the surface.

Fig. 5. Plan-view micrographs of the same sample as in Fig. 1 from the region (a) near the SiC/Si interface, (b) halfway in the film, and (c) near the surface.

Fig. 6. Cross-sectional view of SiC grown on (a) thick and (b) thin SIMOX. The SiC epilayer thickness in (a) is 20  $\mu\text{m}$  while that in (b) is 40  $\mu\text{m}$ . The SADP from the different regions of the multilayer are inset.

Fig. 7. A HTREM micrograph of the SiC deposited on the thin SIMOX. Only the SiC, Si(II) and SiO<sub>2</sub> layers are shown here.

Fig. 8. Cross-sectional TEM micrographs of the 40  $\mu\text{m}$ -thick 3C-SiC film grown on thin SIMOX from a region (a) near the SiC/Si interface, (b) nearly halfway between the SiC/Si interface and the SiC surface, (c) close to the film surface.

Fig. 9. Plan-view TEM micrographs of the 40  $\mu\text{m}$ -thick 3C-SiC film grown on thin SIMOX from a region (a) near the SiC/Si interface, (b) nearly halfway between the SiC/Si interface and the SiC surface, (c) close to the film surface.

Fig. 10. Cross-sectional view of the 20  $\mu\text{m}$ -thick SiC epilayer grown on the thick SIMOX (a) near the film surface and (b) near the SiC/Si interface.

Fig. 11. Plan-view micrographs corresponding to those shown in Fig. 10.

Fig. 12. Strain contrast BF micrographs focusing on the Si layer on which SiC is deposited: (a) bulk silicon wafer, (b) "thick SIMOX", (c) "thin SIMOX", note the lattice defects that have been generated in this case.

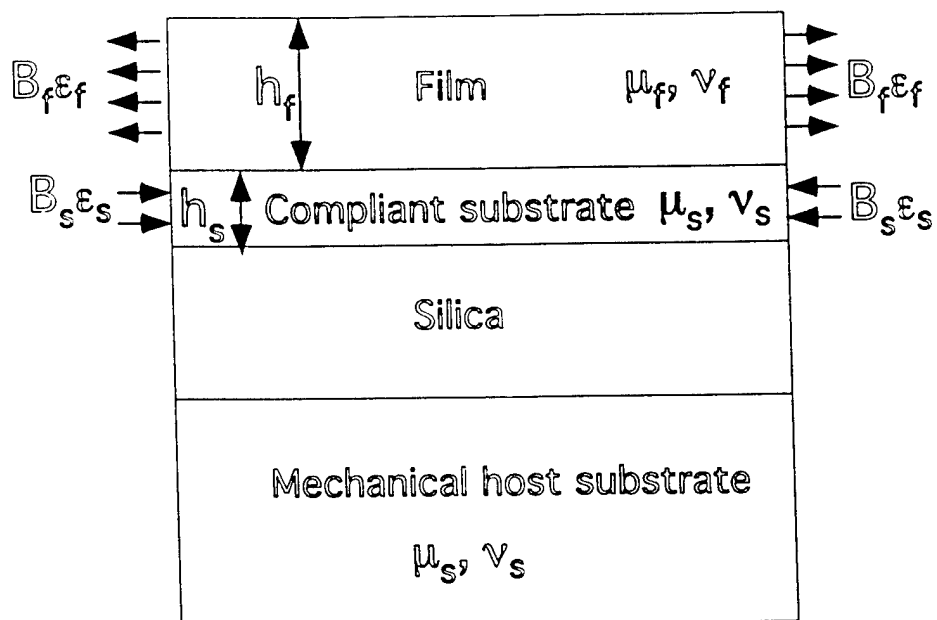
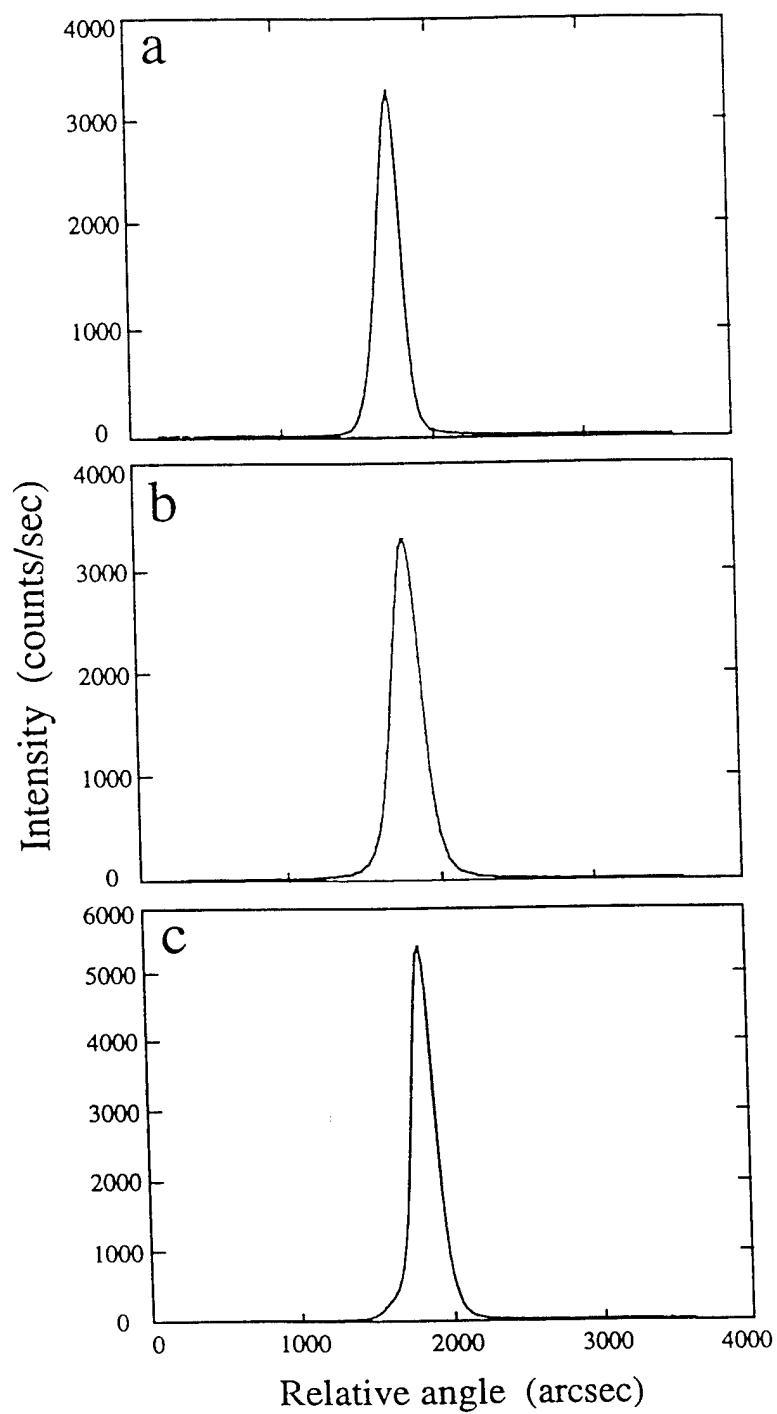
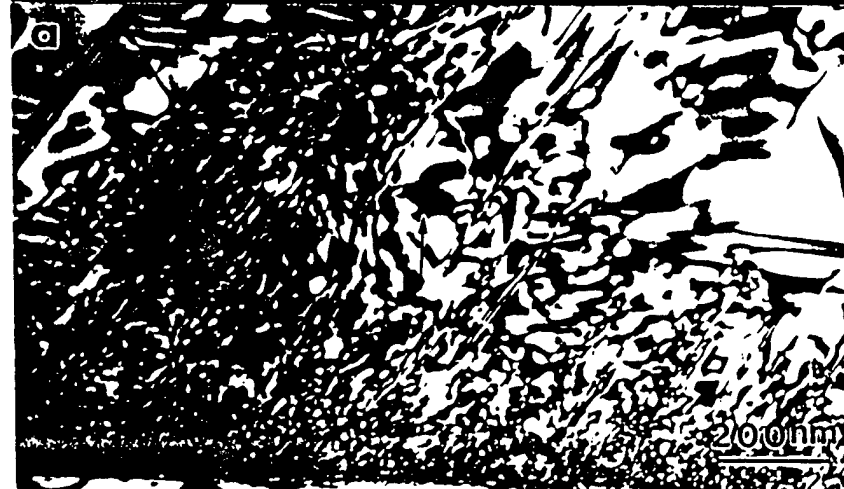
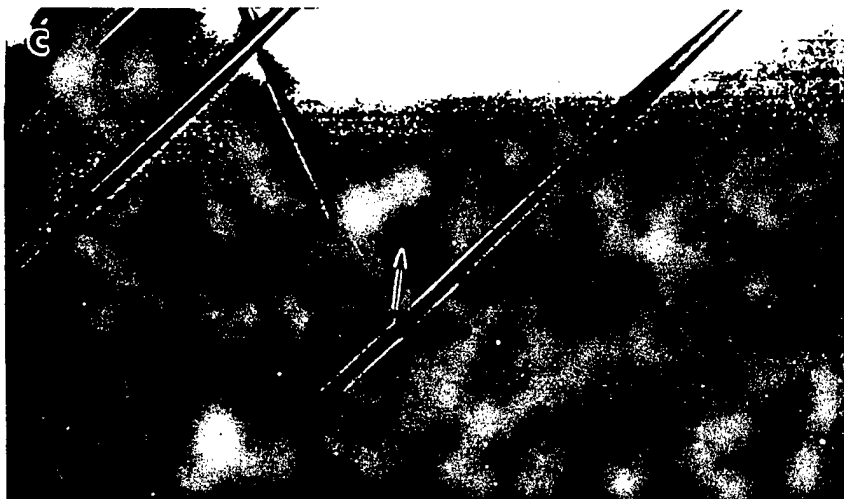


Fig. 1



Si
SiO <sub>2</sub>
Si





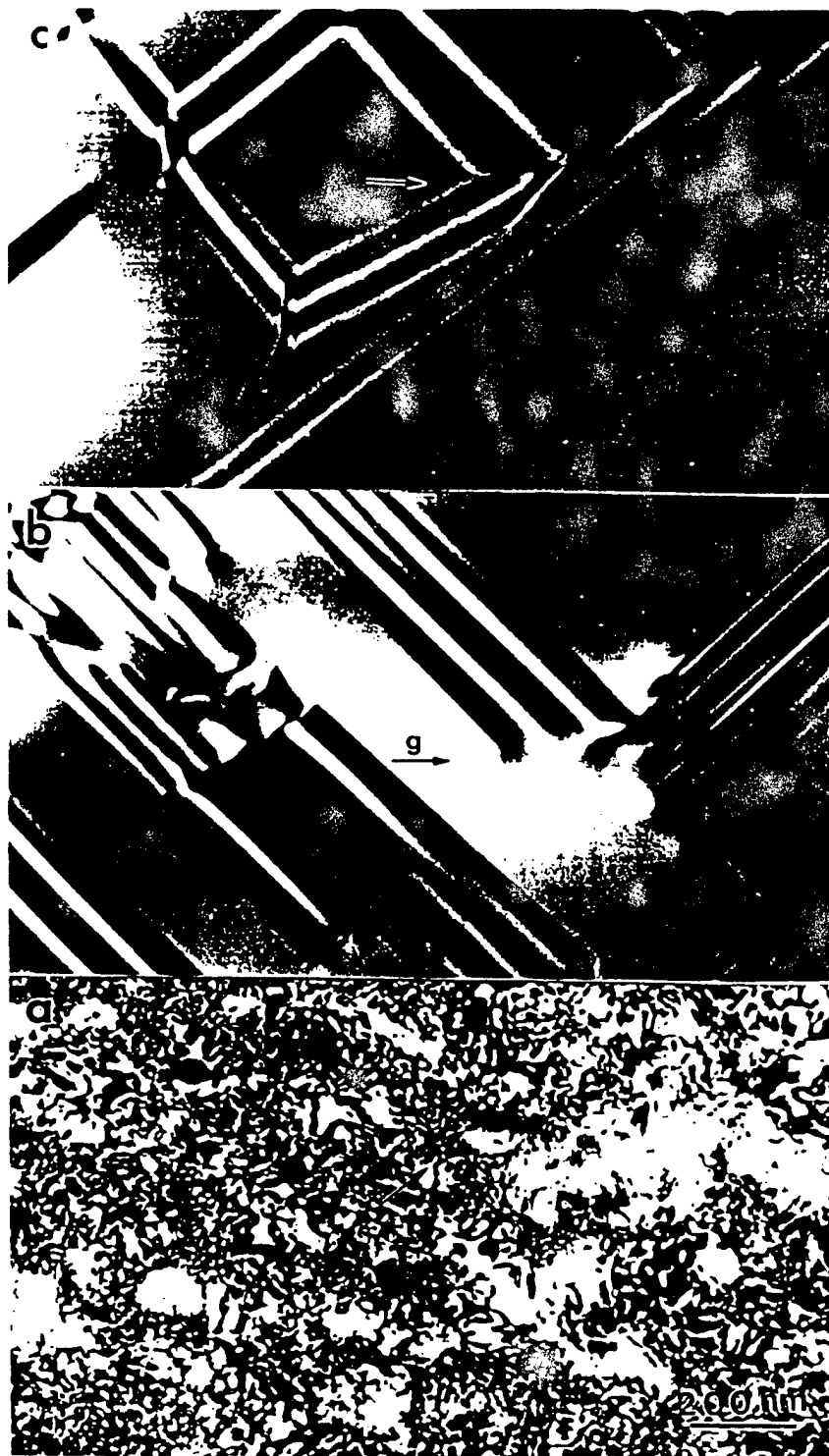
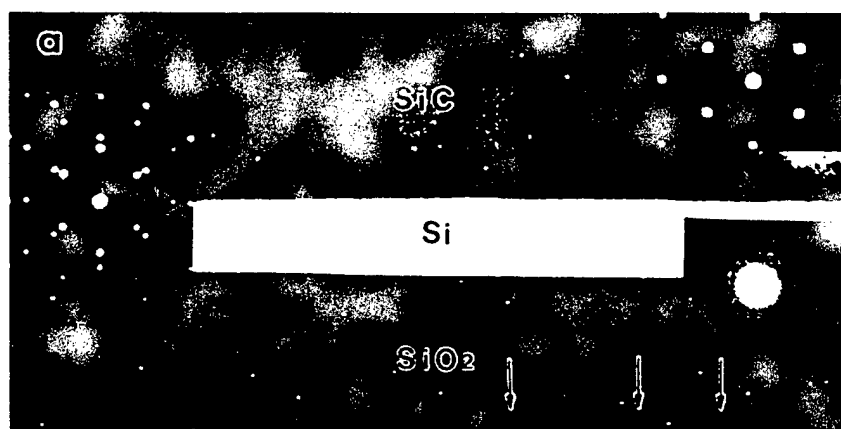
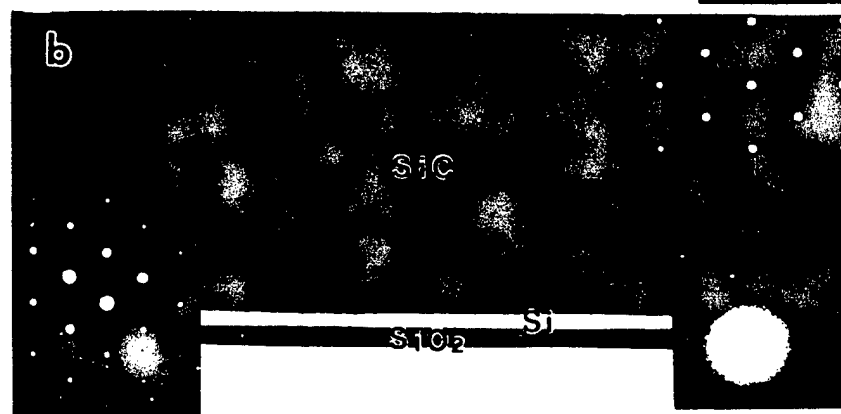


Fig 5 172



Si



Si



200 nm

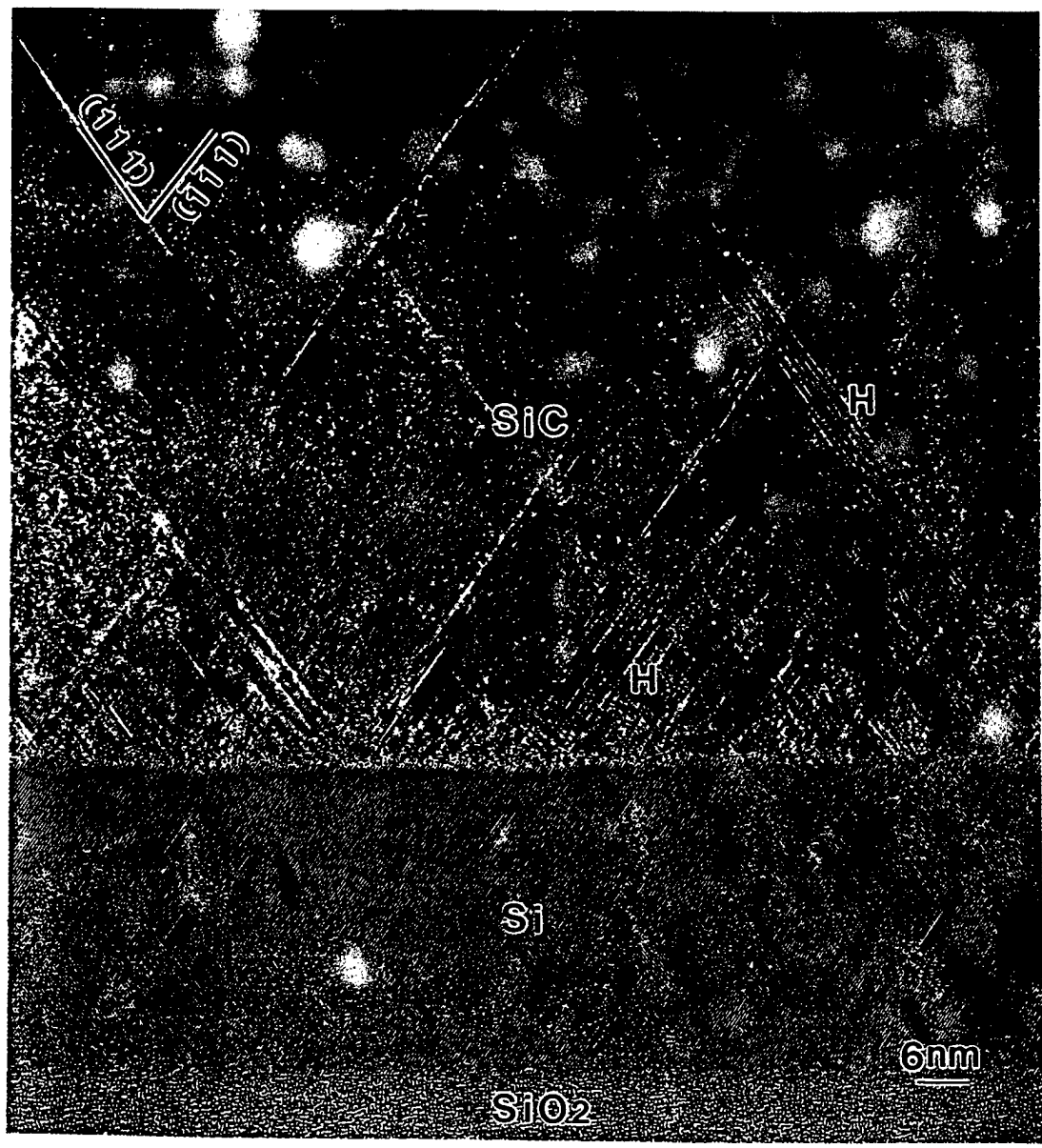


Fig. 7 174



Fig. 8 175

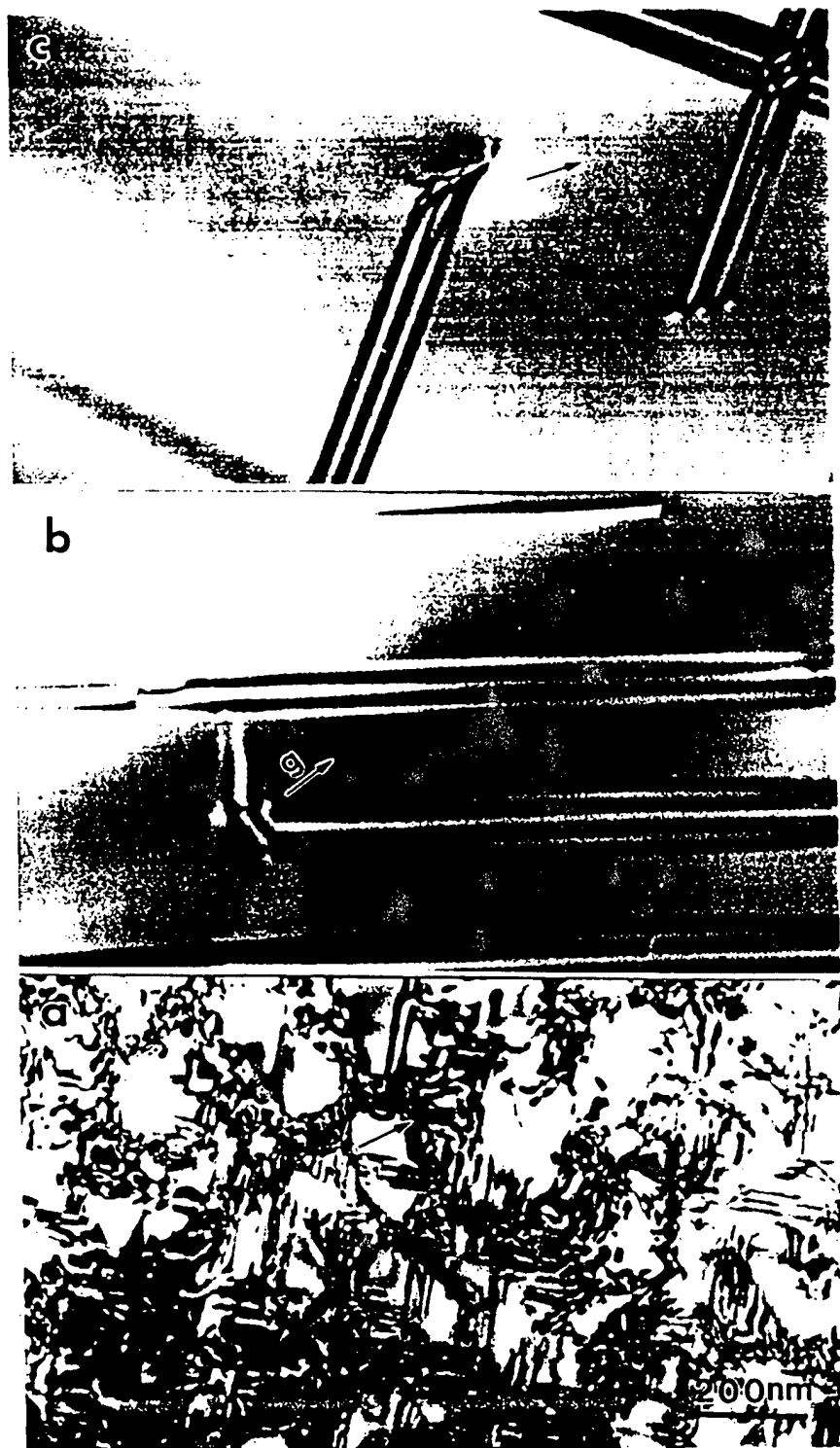


Fig. 9 176



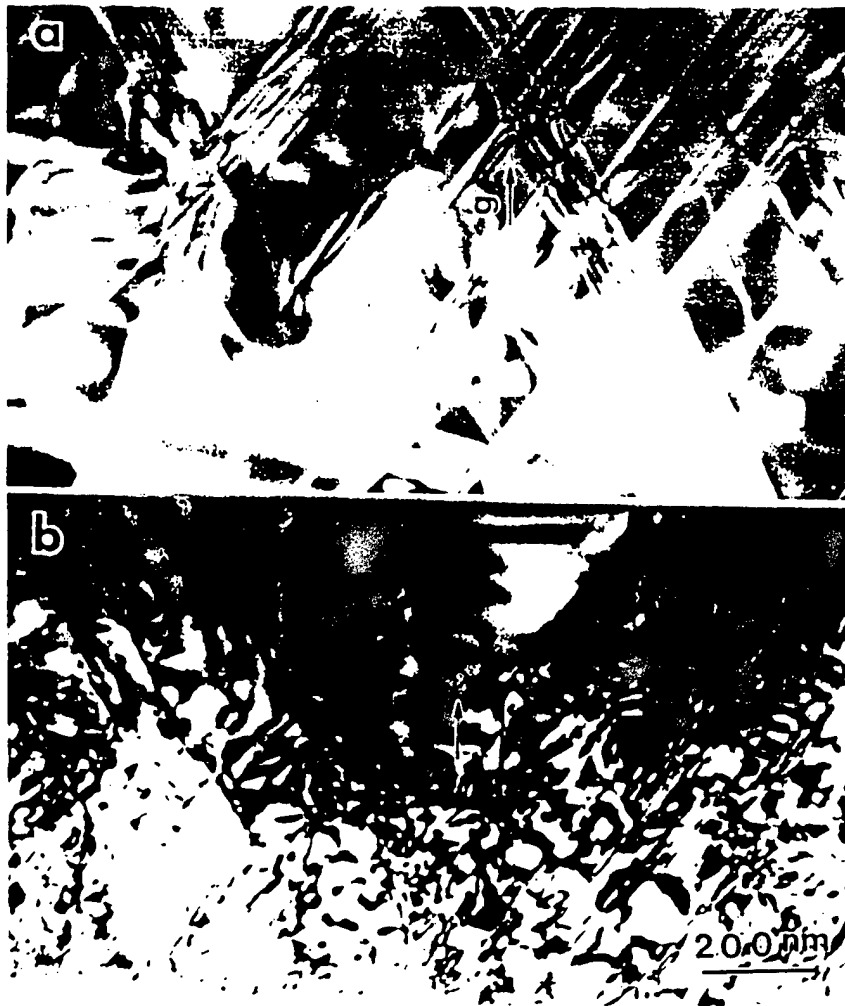


Fig. 10

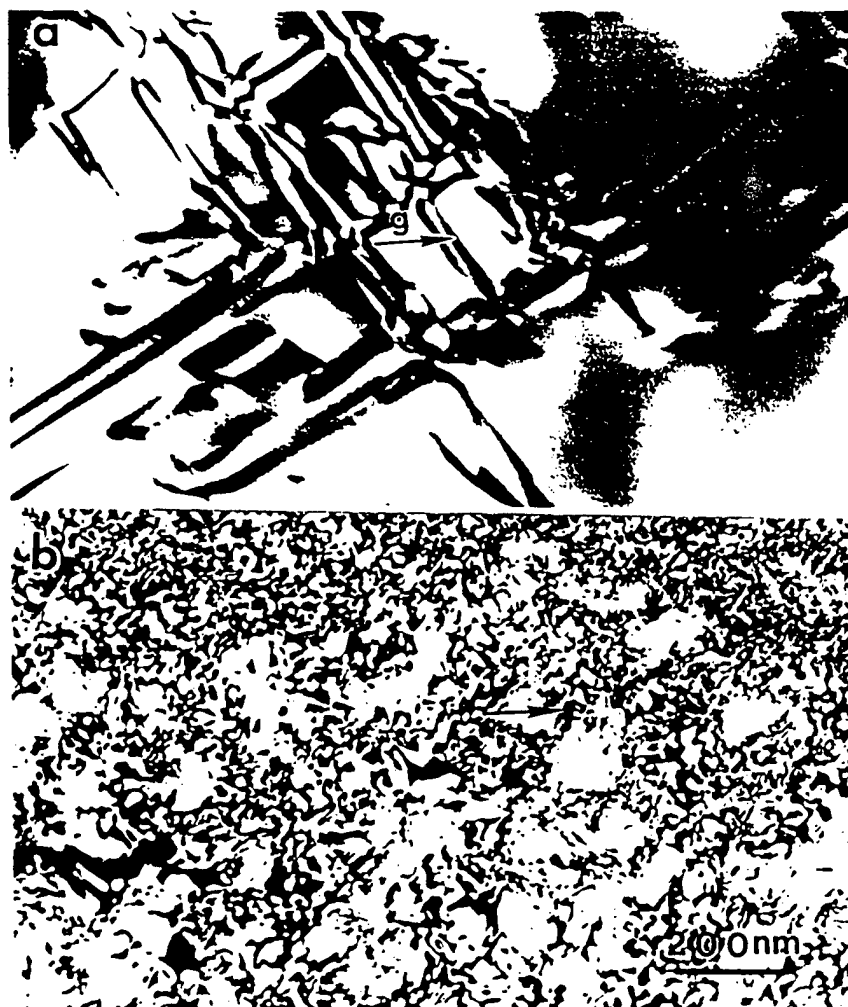


Fig. 11

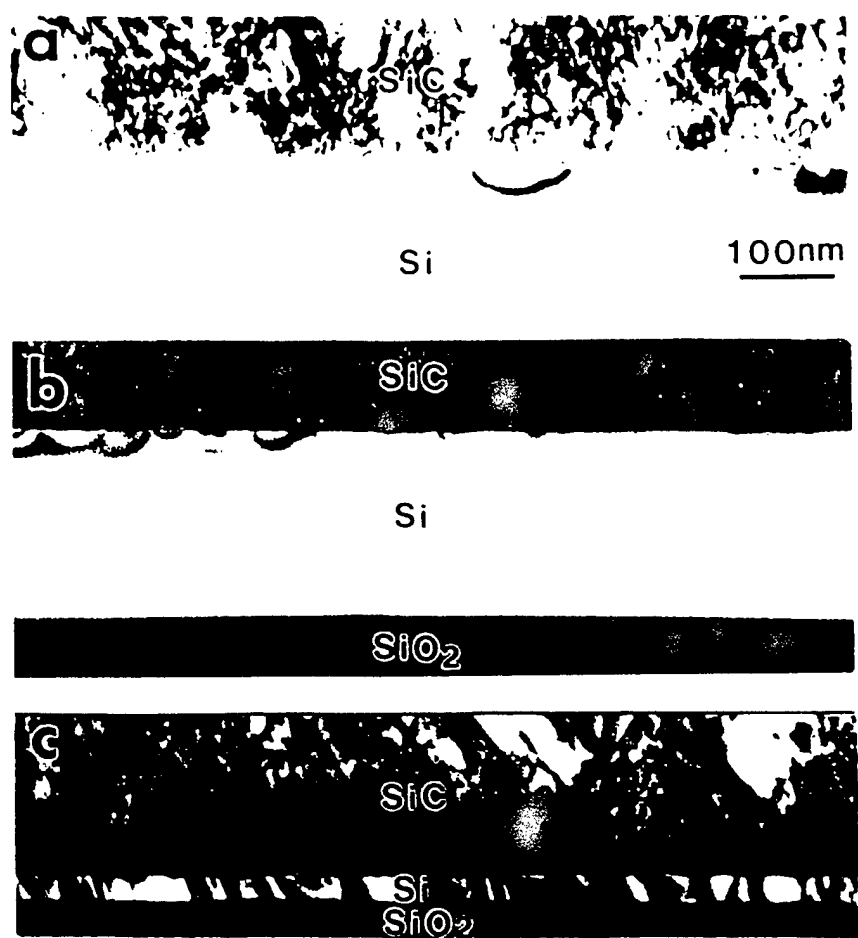


Fig. 12 179



## Stacking fault energy of 6H-SiC and 4H-SiC single crystals

M. H. HONG, A. V. SAMANT and P. PIROUZ\*

Department of Materials Science and Engineering, Case Western Reserve University, Cleveland, OH 44106-7204, USA

[Received 15 February 1999 and accepted in revised form 25 June 1999]

### ABSTRACT

Single crystal 4H and 6H polytypes of SiC have been deformed in compression at 1300°C. All the deformation-induced dislocations were found to be dissociated into two partials bounding a ribbon of intrinsic stacking fault. Using two-beam bright-field and weak-beam dark-field techniques of transmission electron microscopy, the stacking fault energy of these two SiC polytypes has been determined from the separation width of the two partials of dissociated dislocations. The stacking fault energy of 4H-SiC is determined to be  $14.7 \pm 2.5 \text{ mJ m}^{-2}$ , and that of 6H-SiC to be  $2.9 \pm 0.6 \text{ mJ m}^{-2}$ . As a verification, the stacking fault energy of 4H-SiC has been determined also from the minimum radius of curvature of extended nodes. This latter method gave a value of  $12.2 \pm 1.1 \text{ mJ m}^{-2}$  which is within the range determined from measurement of partial dislocation separations. The experimental values of stacking fault energy for 4H- and 6H-SiC have been compared with estimates obtained from a generalized axial next-nearest-neighbour Ising (ANNNI) spin model. It is found that the theoretical models predict the lower stacking fault energy of 6H-SiC compared with that of 4H-SiC, and the predicted energies are, respectively, within 5% and 40% of the experimental values.

### §1. INTRODUCTION

SiC occurs in many different phases (polytypes) mostly with hexagonal or rhombohedral structures, generally known as  $\alpha$ -SiC, and also a unique cubic phase, with the zincblende structure, known as  $\beta$ -SiC. All the different SiC polytypes are tetrahedrally bonded and can be envisaged as an assembly of corner-sharing tetrahedra. Each tetrahedron  $T$  consists of four silicon (carbon) atoms at its corners bonded to a carbon (silicon) at the centroid of the tetrahedron. In the tetrahedron, there is threefold rotational symmetry about each of the four SiC bonds any of which may be taken as the  $c$  axis. As a result, a rotation of  $180^\circ$  about such a direction breaks the threefold symmetry and produces a different ('twinned') variant  $T'$ .

The 'normal' ('twinned') tetrahedra can occupy three different spatial positions denoted as  $T_1, T_2, T_3$  ( $T'_1, T'_2$  and  $T'_3$ ). The SiC polytypes are built up from an assembly of normal ( $T_i$ ), and twinned ( $T'_i$ ),  $i = 1, 2, 3$ , variants with the restriction that any two neighbouring tetrahedra share a corner (for more details, refer to, for example, Pirouz and Yang (1993), Pirouz (1997)).

---

\*Author for correspondence. e-mail: [pirouz@cwmsd.mse.cwru.edu](mailto:pirouz@cwmsd.mse.cwru.edu)

A simple classification of the polytypes is by the Ramsdell (1947) notation where a polytype  $nL$  is characterized by a number  $n$  and a letter  $L$ . The number  $n$  gives the periodicity of the tetrahedra along the  $c$  axis and the letter  $L$  ( $= C, H$ , and  $R$  for cubic, hexagonal and rhombohedral, respectively) indicates the symmetry of the resulting structure. In general, when  $n$  ( $= 2m$ ) is an even integer consisting of an equal number of normal,  $mT_i$ , and twinned,  $mT'_i$ , tetrahedra (symmetric configuration), the resulting  $nH$  polytype has hexagonal symmetry while when  $n$  is an odd integer, or  $n$  ( $= m + m'$  with  $m \neq m'$ ) is even but consists of unequal numbers of normal,  $mT_i$ , and twinned,  $m'T'_i$ , tetrahedra (asymmetric configuration), the  $nR$  polytype has rhombohedral symmetry. For the case of  $n = 3$  a unique structure is obtained in that the resulting structure consists of only one tetrahedral variant,  $T_i$  or  $T'_i$ . This rhombohedral polytype, with a periodicity of three, has a tetrahedral sequence  $\dots T_1 T_2 T_3 \dots$  (or  $\dots T'_1 T'_2 T'_3 \dots$ ) along the  $c$  axis that gives it an additional cubic symmetry; thus it is usually known as 3C (zincblende) rather than 3R. All the other SiC polytypes consist of an assembly of the two variants  $T_i$  and  $T'_i$ . Thus, 2H is the rare wurtzite structure with a tetrahedral sequence  $\dots T_1 T'_3 \dots$  and a periodicity of two. The two most common polytypes of SiC under ambient conditions are 6H-SiC (figure 1(a)) and 4H-SiC (figure 2(a)) with tetrahedral sequences  $\dots T_1 T_2 T_3 T'_2 T'_1 T'_3 \dots$  and  $\dots T_1 T_2 T'_1 T'_3 \dots$ , respectively.

In any of the SiC polytypes, the plane normal to the  $c$  axis defines the basal plane that is parallel to a  $\{111\}$  in the cubic 3C polytype and to (0001) in hexagonal or rhombohedral polytypes. Because of the polar nature of the SiC tetrahedron, each basal plane consists of two parallel planes, one (denoted as  $\alpha, \beta, \gamma$ ) consisting of only carbon atoms and the other, (denoted as  $A, B, C$ ) consisting of only silicon atoms. These two planes are separated from each other by a distance  $3c/4$ , where  $c$  is the edge length of the unit cell along the  $c$  axis (see, for example, figures 1(a) and 2(a)). The different arrangements of SiC tetrahedra in the different SiC polytypes result in different stacking sequences of (0001) double planes along the  $[0001]$  direction. Thus, 6H- and 4H-SiC may also be considered as having, respectively, six and four double layers in their corresponding hexagonal unit cells with stacking sequences  $\dots \alpha A \beta B \gamma C \beta B \alpha A \gamma C \dots$  and  $\dots \alpha A \beta B \alpha A \gamma C \dots$  (figures 1(a) and 2(a)).

All the SiC polytypes are semiconductors with different bandgaps varying from 2.4 eV for the cubic 3C phase to 3.3 eV for the 2H-SiC. Because of their wide bandgaps, there has been much interest recently in employing single-crystal, single-polytype, SiC polytypes for fabricating high-temperature electronic devices, specially since they have many desirable electronic properties such as high electron mobility, large breakdown field, high thermal conductivity, and good corrosion and radiation resistance (see, for example, Choyke *et al.* (1997)). Based on the pioneering work of Tairov and Tsvetkov (1978), 6H- and 4H-SiC polytypes can now be grown as ingots. Since wafers of these two crystals have become commercially available, they are the two polytypes that are most often used for producing electronic devices for applications in harsh environments (e.g., high radiation flux) where Si- or GaAs-based devices do not last too long. Table 1 summarizes some of the physical properties of 6H- and 4H-SiC.

Because of the good mechanical properties of SiC, its deformation behaviour has been studied extensively in the polycrystalline form. The investigation of single-crystal SiC is more recent and has been of much interest because it sheds light on the relationship between the deformation mechanism of these tetrahedrally coordinated materials and the microstructure of deformed crystals (mainly their dislocation

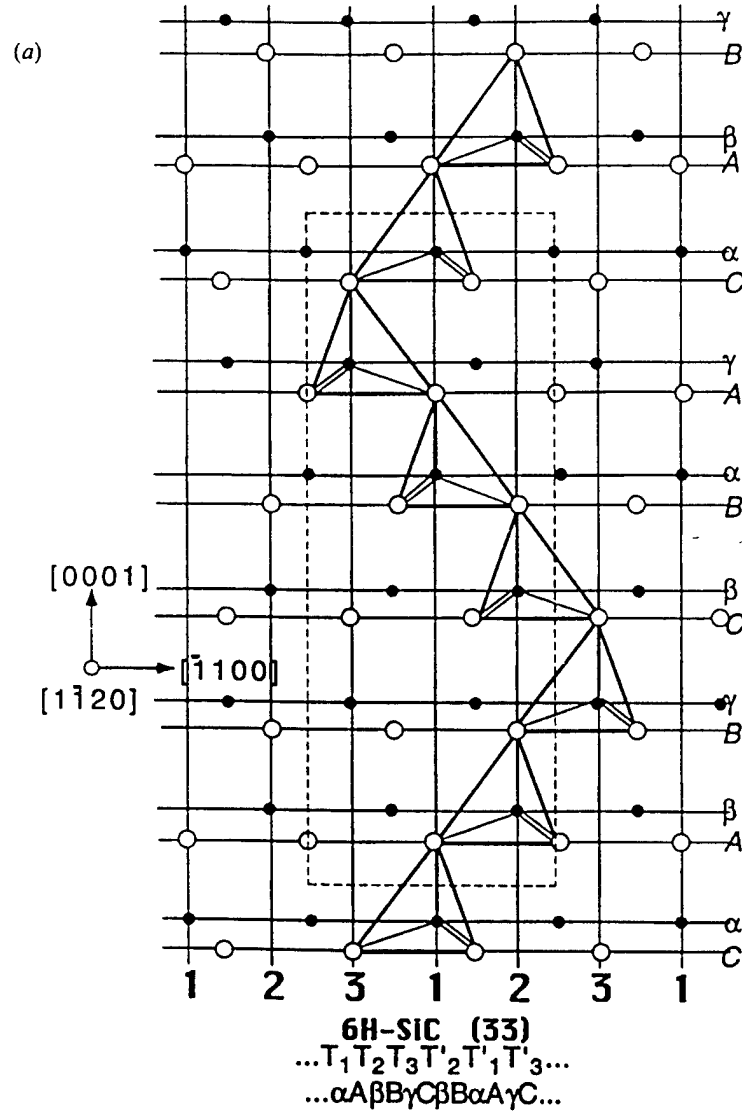


Figure 1. Tetrahedral stacking sequence of 6H-SiC (a) before and (b) after glide of a leading  $\mathbf{b}_1 = \frac{1}{3}\langle 1\bar{1}00 \rangle$  partial dislocation (Burgers vector indicated in the figure). Note that the normal (twinned) tetrahedra on the glide plane are translated by  $\mathbf{b}_1$  and also are converted to twinned (normal) tetrahedra. All the other tetrahedra above the slip plane are simply translated by  $\mathbf{b}_1$  without changing their nature. The dashed lines in (a) delineate the projection of a 6H-SiC unit cell.

structure). The dislocation structure of 3C-SiC has been studied by Stevens (1970, 1972), and that of 6H-SiC by many different groups (for example, Pilyankevich *et al.* (1982), Pilyankevich and Britun (1984), Fujita *et al.* (1986, 1987), Maeda *et al.* (1988, 1993), Suematsu *et al.* (1991), Corman (1992), Yang (1993), Yang and Pirouz (1993), Yang *et al.* (1994), Ning and Pirouz (1996) and Samant (1999)). The microstructure of single-crystal 4H-SiC has been studied to a much lesser extent (see, however, Ning *et al.* (1997), Samant (1999) and Samant *et al.* (1999)).

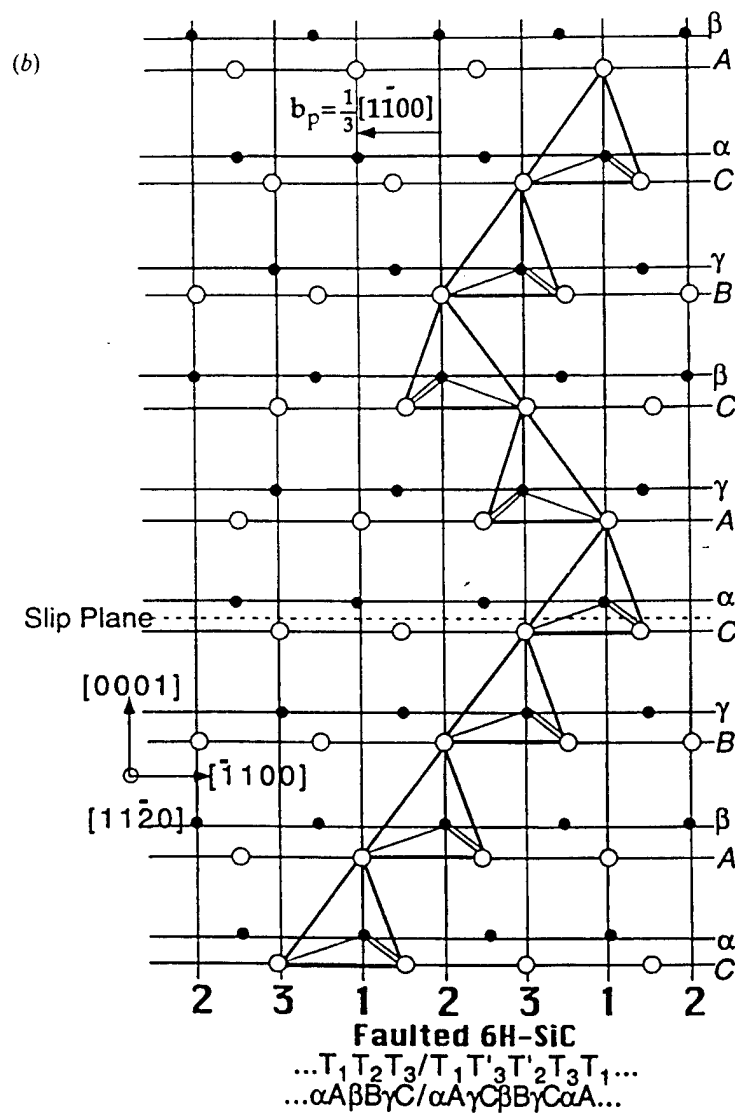
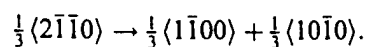
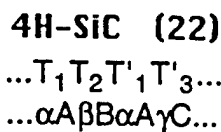


Figure 1. (Continued)

The easy slip plane of all the non-cubic (hexagonal or rhombohedral) SiC polytypes is (0001) and the dislocations have a total Burgers vector  $\mathbf{b} = \frac{1}{3}\langle 2\bar{1}\bar{1}0 \rangle$ . As in other tetrahedrally-coordinated structures, these dislocations are dissociated into two partials with Burgers vectors  $\mathbf{b}_l = \frac{1}{3}\langle 1\bar{1}00 \rangle$  and  $\mathbf{b}_t = \frac{1}{3}\langle 10\bar{1}0 \rangle$ , where subscripts l and t denote the leading and trailing partials, respectively. The dislocation dissociation is according to the following reaction (Amelinckx *et al.* 1960, Amelinckx 1979):



The partial dislocations in SiC, as in other tetrahedrally coordinated semiconductors, very probably move on the narrowly spaced 'glide' planes rather than on the



widely spaced 'shuffle' planes (Pirouz and Ning 1995). The motion of the leading partial dislocation on a particular (0001) slip plane displaces the part of the crystal on one side of the slip plane by the vector  $\mathbf{b}_1 = \frac{1}{3}(1\bar{1}00)$  with respect to the other part and, in addition, changes the nature of all the tetrahedra on that plane (normal to twinned, and vice versa). As a result, an intrinsic stacking fault is left on the (0001) slip plane. This can be seen for 6H-SiC by comparing figure 1 (a) and (b) which show



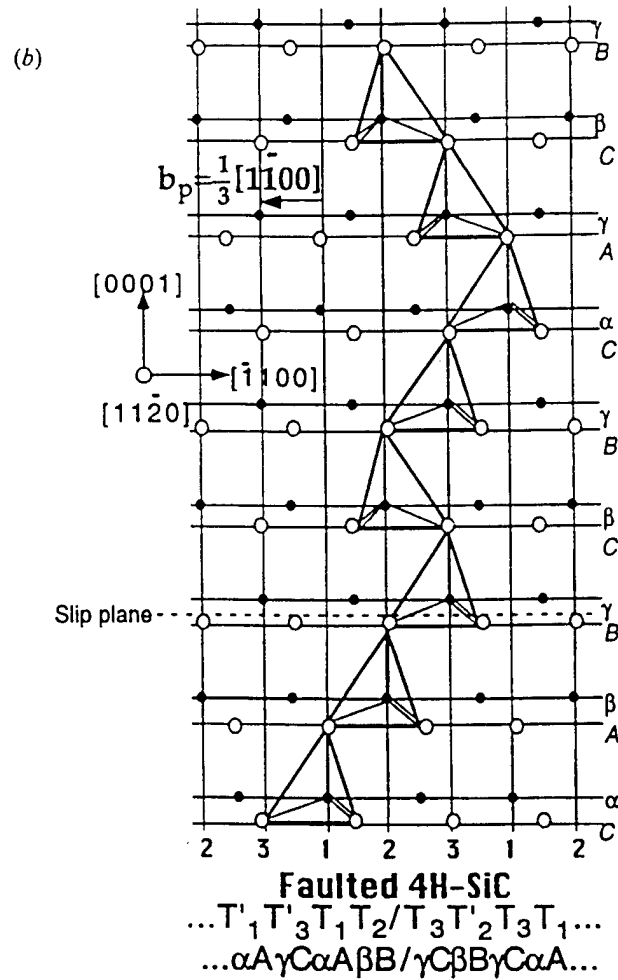


Figure 2. (Continued)

Table 1. Some important properties of 6H-SiC and 4H-SiC.

	$a$ (nm)	$c$ (nm)	Number of atoms per unit cell	Normal/twinned tetrahedra	Bandgap (eV)
4H-SiC	0.308	1.005	8	2/2	3.265
6H-SiC	0.308	1.508	12	3/3	3.023

the configuration of the tetrahedra before and after the passage of a leading partial dislocation. As can be seen, the  $\dots T_1 T_2 T_3 T_2' T_1' T_3' \dots$  stacking sequence in the perfect crystal changes to  $\dots T_1 T_2 T_3 / T_1' T_3' T_2' T_3 T_1 T_2 \dots$  in the deformed crystal; the symbol/representing the plane on which the leading partial has moved and left a stacking fault. Similarly, figure 2(a) and (b) show the change in the tetrahedral stacking sequence that takes place when a partial dislocation glides on the slip plane of a 4H-SiC crystal; in this case  $\dots T_1 T_2 T_1' T_3' \dots$  tetrahedral stacking sequence in the

perfect crystal changes to  $\dots T_1 T_2 / T_3 T_2' T_3 T_1 T_3' T_2' \dots$  after the passage of the leading partial.

As in other tetrahedrally coordinated compounds, because of the polar nature of basal planes, the core of the perfect or partial dislocations consists of only one species, i.e., silicon or carbon, and, because the partial dislocations belong to the glide plane, they are denoted as Si(g) or C(g) (Alexander *et al.* 1979). Using the technique of large-angle convergent beam electron diffraction (LACBED), it has been possible to distinguish between the different partials and show that the Si(g) partials have a smooth morphology whereas the C(g) partials tend to be zigzagged (Ning and Pirouz 1996).

A number of investigators have studied the mechanical deformation of 6H-SiC single crystals. The results of these studies show that, above  $\sim 1100^\circ\text{C}$ , plastic deformation of this material occurs by the activation of the (0001)(11 $\bar{2}$ 0) slip system with the uncorrelated motion of leading/trailing partial dislocation pairs. From the width of partial separations, Maeda *et al.* (1988) evaluated the stacking fault energy of 6H-SiC to be  $2.5 \pm 0.9 \text{ mJ m}^{-2}$ . This value is much lower than that of other tetrahedrally coordinated semiconductors (Gottschalk *et al.* 1978, Takeuchi *et al.* 1984, Takeuchi and Suzuki 1999), such as Si ( $55 \pm 7 \text{ mJ m}^{-2}$ ), GaAs ( $45 \pm 7 \text{ mJ m}^{-2}$ ), or CdS ( $8.7 \pm 1.5 \text{ mJ m}^{-2}$ ); consequently the dissociation width of dislocations in SiC tends to be much larger than in other semiconductors. Very recently, Samant (1999) has shown that 6H-SiC can be plastically deformed at temperatures as low as  $550^\circ\text{C}$  by the activation of only the  $\frac{1}{3}\langle 10\bar{1}0 \rangle$  leading partial dislocations. Further, Hong *et al.* (1999), using LACBED, have shown that these single partial dislocations have a silicon core.

In contrast to 6H-SiC, the mechanical properties and the resulting dislocation microstructure of 4H-SiC have been studied to a much lesser extent. Ning *et al.* (1997) investigated the indentation hardness of 4H-SiC over a range of temperatures and found a strong hardness anisotropy between the silicon- and carbon-terminated (0001) faces. They concluded that this hardness anisotropy arises from the different core structure of leading dislocations introduced by high-temperature indentation: the hardness of the opposite Si- and C-terminated faces was, respectively, controlled by Si(g) and C(g) partial dislocations. The more recent work of Samant (1999) used compression of single crystals oriented for easy glide. It was shown that, as in 6H-SiC, perfect dissociated dislocations dominated the microstructure of crystals deformed above  $1100^\circ\text{C}$ , while at lower temperatures the microstructure was dominated by single leading partials that appear to be all Si(g).

In the present paper we report the results of a transmission electron microscopy (TEM) study of dissociated dislocations in 6H- and 4H-SiC single crystals produced by plastic deformation at  $1300^\circ\text{C}$ . To the authors' knowledge, except for the aforementioned work of Ning *et al.* (1997) on indented 4H-SiC, there are no reports of the dislocation configuration in deformed 4H-SiC, or on the experimental determination of the stacking fault energy of this polytype. Here we have determined the stacking fault energy of the 6H-SiC and 4H-SiC, or polytypes, and compared the value obtained for 6H-SiC with that previously obtained by Maeda *et al.* (1988). Also we have used the axial next-nearest-neighbour Ising (ANNNI) model, as developed by Heine *et al.* (1992) to explain polytypism in SiC and ZnS, to estimate the stacking fault energy of 6H- and 4H-SiC and compare these with the experimentally determined values.

## §2. EXPERIMENTAL

The 6H- and 4H-SiC bulk single crystals used in this study were grown by the modified sublimation technique (the 6H-SiC was grown at Cree Research, Inc., and the 4H-SiC was grown at Northrop-Grumman Corporation). Parallelepiped specimens with nominal dimensions  $2\text{ mm} \times 2\text{ mm} \times 4\text{ mm}$  were oriented and cut for single glide such that one pair of their lateral faces was parallel to  $\{1\bar{1}00\}$ , and the (0001) basal plane made an angle of  $45^\circ$  with respect to the compression axis. The samples were compressed at  $1300^\circ\text{C}$  in ultra-high purity argon to a strain of about 4–6%. From the deformed specimens, 0.3 mm thick slices parallel to (0001) were sectioned with a diamond wheel cutter. Subsequently, the slices were ground with emery paper to a thickness of about  $100\text{ }\mu\text{m}$ , dimpled to a thickness of about  $20\text{ }\mu\text{m}$ , and ion-thinned to electron transparency at a voltage of 6 kV at an angle of  $\sim 15^\circ$ . The thin TEM foils were examined in a Philips CM20 electron microscope operating at an accelerating voltage of 200 kV.

## §3. RESULTS

Figure 3 presents typical examples of the dislocations produced in a 6H-SiC single crystal specimen deformed to a normal strain of 2.4% at  $1300^\circ\text{C}$  at a strain

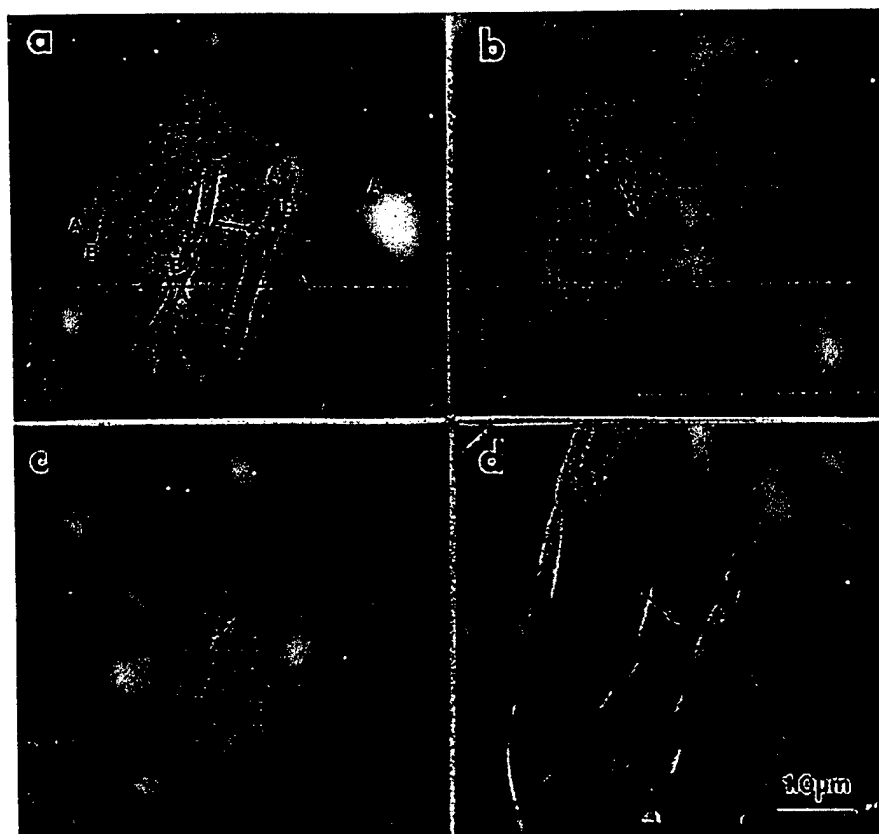


Figure 3. Dissociated dislocations in 6H-SiC introduced by compression at  $1300^\circ\text{C}$ . The bright-field figures, (a)  $g = 11\bar{2}0$ , (b)  $g = 2\bar{1}10$ , and (c)  $g = 1\bar{2}10$ , were taken close to the [0001] zone-axis while the dark-field figure, (d)  $g = 101\bar{1}$ , was taken close to the  $[\bar{1}012]$  zone axis.

rate of  $6.3 \times 10^{-5} \text{ s}^{-1}$ . The Burgers vector of the dislocation segments denoted by A and B were determined using the standard  $\mathbf{g} \cdot \mathbf{b} = 0$  invisibility criterion. The same region of the specimen was observed under 2-beam bright-field (figure 3(a-c)) and dark-field (figure 3(d)) conditions. Dislocation A is in contrast with reflections  $\mathbf{g} = 11\bar{2}0$  (figure 3(a)) and  $\mathbf{g} = 1\bar{2}10$  (figure 3(c)) and is out of contrast with reflection  $\mathbf{g} = 2\bar{1}\bar{1}0$  (figure 3(b)). This indicates that A is a partial dislocation with a Burgers vector  $\mathbf{b}_A = \frac{1}{3}[01\bar{1}0]$ . On the other hand, dislocation B is in contrast with  $\mathbf{g} = 11\bar{2}0$  (figure 3(a)) and  $\mathbf{g} = 2\bar{1}\bar{1}0$  (figure 3(b)) and is out of contrast with  $\mathbf{g} = 1\bar{2}10$  (figure 3(c)). This indicates that the Burgers vector of (partial) dislocation B is  $\mathbf{b}_B = \frac{1}{3}[10\bar{1}0]$ . Figure 3(d) shows a dark-field micrograph of the dislocation configuration in the same region taken with  $\mathbf{g} = [\bar{1}01\bar{1}]$  near the  $[\bar{1}012]$  zone axis. It shows clearly the stacking fault contrast between the two partials that lie on the same basal plane, confirming that A and B are the two partials of the same dissociated  $\mathbf{b} = \frac{1}{3}[11\bar{2}0]$  dislocation. Similar micrographs from other dislocation segments in this specimen confirmed that all the dislocations observed in the deformed 6H-SiC sample are indeed partial dislocation pairs of dissociated  $\mathbf{b} = \frac{1}{3}[11\bar{2}0]$  dislocations. Observation of many dislocations in the foil shows that the width of the stacking fault ribbon does not change greatly within the sample. At a deformation temperature of  $1300^\circ\text{C}$ , we believe that the dissociated dislocations are close to their equilibrium configuration. Table 2 summarizes the results of figure 3.

The stacking fault energy  $\gamma$  of a dissociated dislocation segment can be obtained by balancing it to the sum of the self-energies of the two partials plus their interaction energy (Amelinckx 1979). For an anisotropic hexagonal structure,  $\gamma$  is related to the separation distance  $d$  of the two partials of a dissociated dislocation by the following equation (Steeds 1973):

$$\gamma = \frac{b^2}{24\pi d} \{ (3 \sin^2 \phi - \cos^2 \phi) K_1 + (3 \cos^2 \phi - \sin^2 \phi) K_3 \}, \quad (1)$$

where  $b = |\mathbf{b}|$  is the magnitude of the Burgers vector of the *perfect* dislocation,  $\phi$  is the angle between the Burgers vector and dislocation line, and  $K_1$  and  $K_3$  are the energy factors calculated from elastic constants. The elastic constants were taken from the work of Lambrecht *et al.* (1991).

As expected, the separation distance  $d$  of the dissociated dislocations in 6H-SiC is much larger than in other tetrahedrally coordinated semiconductors. Using equation (1), the stacking fault energy of 6H-SiC was calculated; the results are plotted as a function of the angle between the Burgers vector and the dislocation line in figure 4. The two lines drawn in the figure show the theoretical values calculated from equation (1). The stacking fault energy is evaluated to be  $2.9 \pm 0.6 \text{ mJ m}^{-2}$ ; the upper and lower bound values, corresponding to a standard deviation, are  $2.4 \text{ mJ m}^{-2}$  and  $3.5 \text{ mJ m}^{-2}$  and are shown by the two lines in the figure. This value of  $\gamma$  in 6H-SiC is in good agreement with the value of  $2.5 \pm 0.9 \text{ mJ m}^{-2}$  obtained previously by

Table 2. Determination of the Burgers vector of dislocations in figure 3 produced by deformation of 6H-SiC at  $1300^\circ\text{C}$ :  $\checkmark$ , in contrast; and  $\times$ , out of contrast.

$\mathbf{g}$	$11\bar{2}0$	$2\bar{1}\bar{1}0$	$1\bar{2}10$	$\bar{1}01\bar{1}$	$\mathbf{b}$
A	$\checkmark$	$\times$	$\checkmark$	$\checkmark$	$\frac{1}{3}[01\bar{1}]$
B	$\checkmark$	$\checkmark$	$\times$	$\checkmark$	$\frac{1}{3}[10\bar{1}0]$

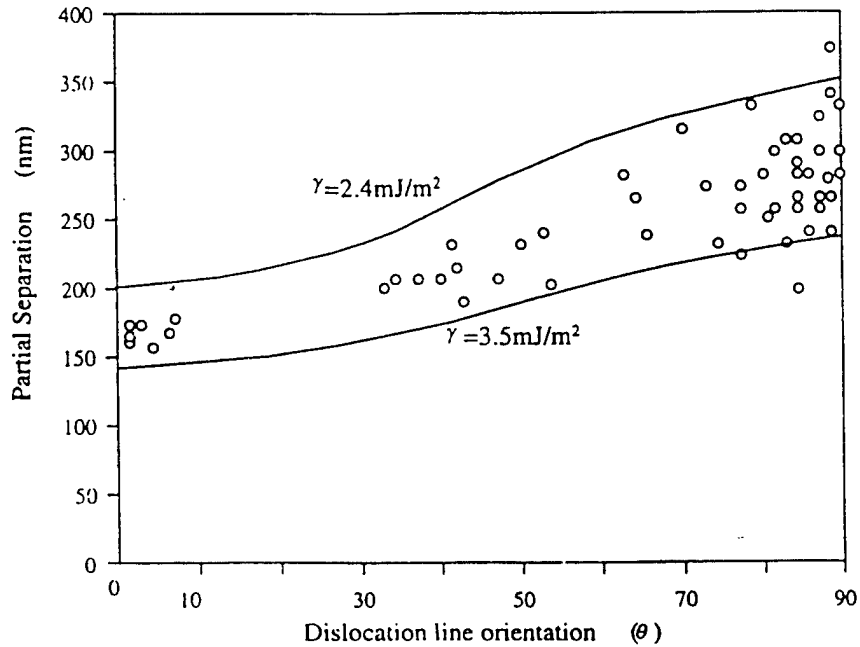


Figure 4. Separation of partial dislocations in 6H-SiC as a function of the angle between the Burgers vector and the dislocation line: the two solid lines were calculated from equation (1) assuming an upper bound value of  $\gamma = 3.5 \text{ mJ m}^{-2}$  and a lower bound value of  $\gamma = 2.4 \text{ mJ m}^{-2}$ .

Maeda *et al.* (1988) using the same TEM techniques applied to extended dislocations resulting from compression of Acheson single-crystal SiC samples at 1600°C.

For the case of 4H-SiC, the separation of partial dislocations was found to be much less than that of the dissociated dislocations in 6H-SiC. Consequently, the weak-beam dark-field technique of TEM (Cockayne *et al.* (1969) was employed to measure the separation widths of partials. Figure 5 shows pseudo-weak-beam ( $\mathbf{g}/3\mathbf{g}$  corresponding to a deviation parameter  $s$  of  $0.12 \text{ nm}^{-1}$ ) micrographs of typical dislocations produced in a 4H-SiC single-crystal sample deformed to a strain of 4.2% at 1300°C at a strain rate of  $3.0 \times 10^{-5} \text{ s}^{-1}$ . Figure 5(a) and (b) are a  $\mathbf{g}/-\mathbf{g}$  pair taken with reflections  $\mathbf{g} = \pm \bar{1}2\bar{1}0$  showing inside/outside contrast between the two partials of a dissociated dislocation segment. Figure 5(c) was taken with reflection  $\mathbf{g} = \bar{1}0\bar{1}\bar{1}$  after the specimen was tilted to near the  $[\bar{1}012]$  zone axis; it shows the contrast from the stacking fault between the two partials of the dissociated dislocation segment. Detailed  $\mathbf{g} \cdot \mathbf{b}$  contrast experiments showed that the two partials have Burgers vectors  $\mathbf{b}_1 = \frac{1}{3}[01\bar{1}0]$  and  $\mathbf{b}_2 = \frac{1}{3}[\bar{1}100]$ . A comparison of figures 5 and 3 shows clearly that the width of the stacking fault ribbon is much smaller in 4H-SiC than in 6H-SiC.

By measuring the separation of partial dislocations in micrographs such as those shown in figure 5, and using equation (1), the stacking fault energy of 4H-SiC was calculated. The solid lines in figure 6 show the theoretical values of  $d$  versus  $\theta$  corresponding to two values of stacking fault energy, an upper bound value of  $\gamma = 17.2 \text{ mJ m}^{-2}$ , and a lower bound value of  $\gamma = 12.3 \text{ mJ m}^{-2}$ . The experimental points in this figure correspond to the actual width of the partial separation ( $\Delta$ ), corrected by means of the equation proposed by Cockayne *et al.* (1969), from the experimental width ( $\Delta_{\text{obs}}$ ) at several locations along the dislocation line. The mean

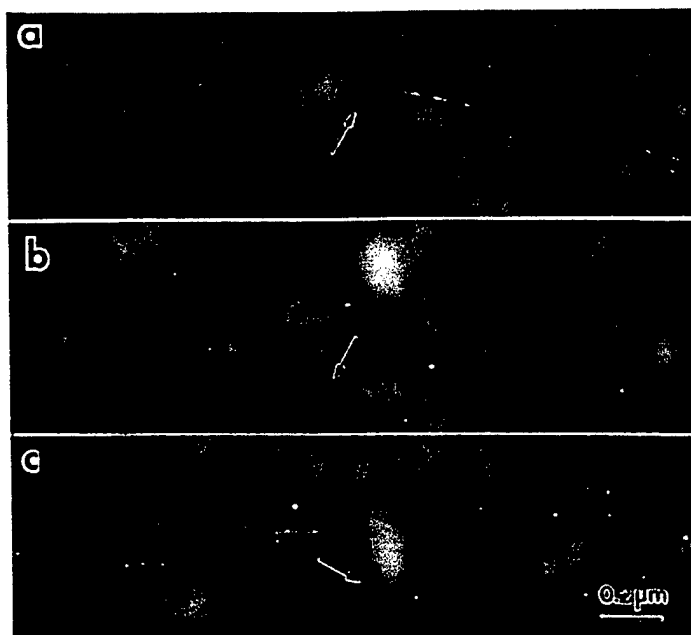


Figure 5.  $g/3g$  ( $s = 0.12 \text{ nm}^{-1}$ ) pseudo-weak-beam micrographs of a typical dissociated dislocation in 4H-SiC introduced by compression at  $1300^\circ\text{C}$ : (a)  $g = \bar{1}2\bar{1}0$  and (b)  $g = \bar{1}2\bar{1}0$  were taken near the  $[0001]$  zone axis, while (c)  $g = \bar{1}0\bar{1}1$  was taken near the  $[1012]$  zone axis.

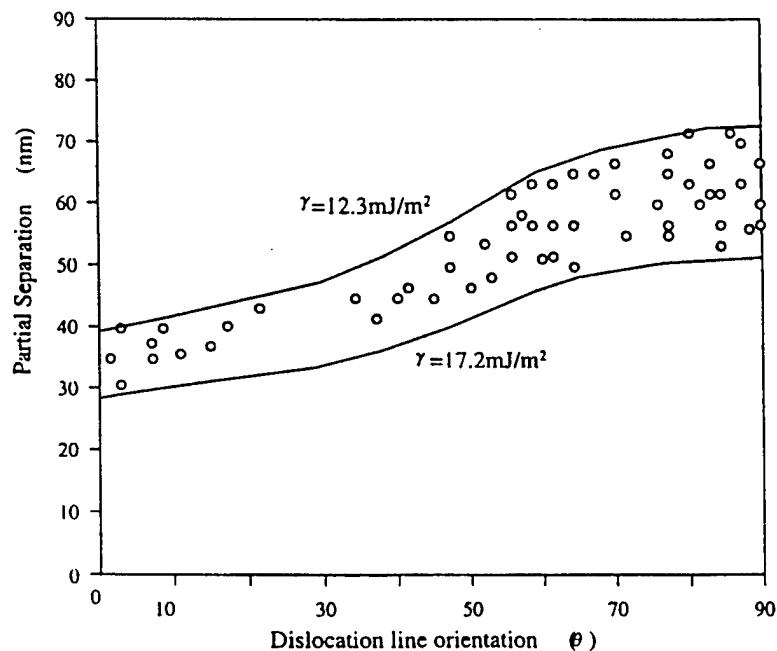


Figure 6. The separation distance of dissociated dislocations in 4H-SiC as a function of the angle between the Burgers vector and the dislocation line: the two solid lines were calculated from equation (1) assuming an upper bound value of  $\gamma = 17.2 \text{ mJ m}^{-2}$  and a lower bound value of  $\gamma = 12.3 \text{ mJ m}^{-2}$ .

value of the stacking fault energy is evaluated to be  $14.7 \pm 2.5 \text{ mJ m}^{-2}$ ; the values corresponding to the standard deviation are  $12.3 \text{ mJ m}^{-2}$  and  $17.2 \text{ mJ m}^{-2}$ . As in the case of 6H-SiC, we believe that dislocations introduced by deformation of 4H-SiC at  $1300^\circ\text{C}$  are dissociated to their equilibrium separation.

In addition to the measurement of partial separations, the stacking fault energy of 4H-SiC was estimated also from the minimum radius of extended nodes produced by the deformation process ( $\epsilon = 4.2\%$ ,  $T = 1300^\circ\text{C}$ ,  $\dot{\epsilon} = 3.0 \times 10^{-5} \text{ s}^{-1}$ ). Such an extended node, consisting of dislocation arms A, B and C, is shown in the pseudo-weak-beam image ( $s = 0.12 \text{ nm}^{-1}$ ) of figure 7. The Burgers vectors of the three arms were determined by the standard  $\mathbf{g} \cdot \mathbf{b} = 0$  invisibility criterion. Dislocation A is in contrast with the two reflections  $\mathbf{g} = \bar{1}2\bar{1}0$  (figure 7(a)) and  $\mathbf{g} = 2\bar{1}\bar{1}0$  (figure 7(b)) and out of contrast with  $\mathbf{g} = \bar{1}\bar{1}20$  (figure 7(c)). This indicates that segment A is a partial dislocation with a Burgers vector  $\mathbf{b}_A = \frac{1}{3}[\bar{1}\bar{1}00]$ . On the other hand, dislocations B and C are out of contrast when reflections  $\mathbf{g} = 2\bar{1}\bar{1}0$  (figure 7(b)) and  $\mathbf{g} = \bar{1}2\bar{1}0$  (figure 7(a)) are, respectively, used to image the node. Thus, the Burgers vectors of dislocations B and C are  $\mathbf{b}_B = \frac{1}{3}[01\bar{1}0]$  and  $\mathbf{b}_C = \frac{1}{3}[10\bar{1}0]$ , respectively. Figure 7(d) shows the node imaged with the reflection  $\mathbf{g} = \bar{1}01\bar{1}$  near the  $[\bar{1}012]$  zone axis. Similar to the case of 6H-SiC in figure 3(d), the stacking fault contrast within the extended dislocation node ABC is in contrast,

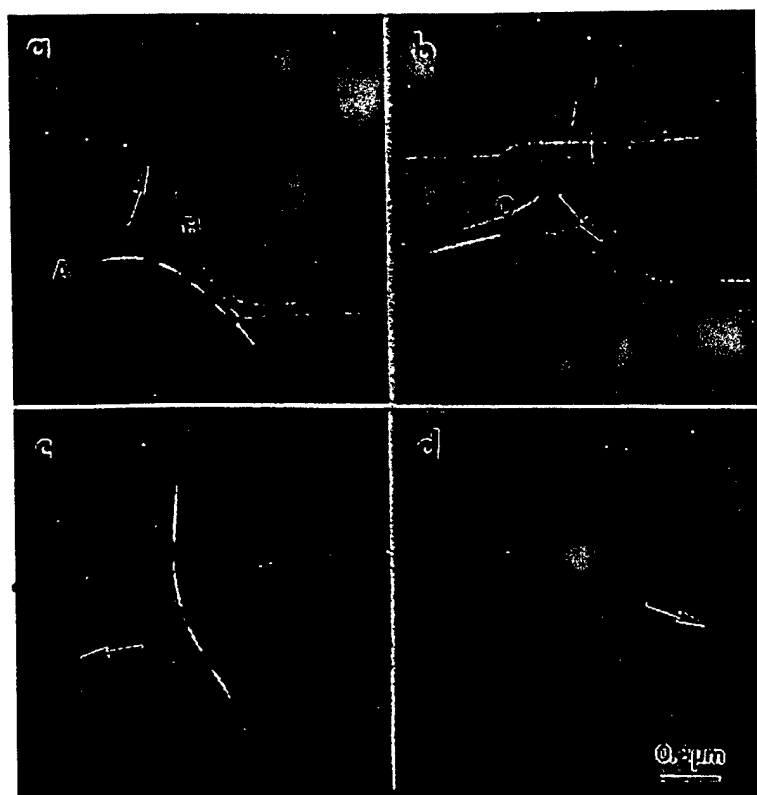


Figure 7.  $\mathbf{g}/3\mathbf{g}$  ( $s = 0.12 \text{ nm}^{-1}$ ) pseudo-weak-beam micrographs of an extended node in 4H-SiC introduced by compression at  $1300^\circ\text{C}$ : (a)  $\mathbf{g} = \bar{1}2\bar{1}0$  (b)  $\mathbf{g} = 2\bar{1}\bar{1}0$  and (c)  $\mathbf{g} = \bar{1}\bar{1}20$  were taken near the  $[0001]$  zone axis, while (d)  $\mathbf{g} = \bar{1}01\bar{1}$  was taken close to the  $[\bar{1}012]$  zone axis.

Table 3. Determination of the Burgers vector of dislocations in figure 7 produced by deformation of 4H-SiC at 1300°C: ✓, in contrast; and ×, out of contrast.

g	$\bar{1}2\bar{1}0$	$2\bar{1}\bar{1}0$	$\bar{1}\bar{1}20$	$\bar{1}0\bar{1}\bar{1}$	b
A	✓	✓	×	✓	$\frac{1}{3}[1\bar{1}00]$
B	✓	×	✓	✓	$\frac{1}{3}[01\bar{1}0]$
C	×	✓	✓	✓	$\frac{1}{3}[10\bar{1}0]$

confirming that all the three partials lie on the same (0001) basal plane. Table 3 summarizes the results of the analysis of figure 7.

According to Brown and Thölen (1964), the minimum radius of an extended dislocation node is given by:

$$\frac{\gamma_w}{Gb_p^2} = 0.055 \left( \frac{2-\nu}{1-\nu} \right) - 0.06 \left[ \frac{\nu}{(1-\nu)^2} \right] \cos 2\alpha + \left[ 0.018 \left( \frac{2-\nu}{1-\nu} \right) + 0.036 \left( \frac{\nu}{1-\nu} \right) \cos 2\alpha \right] \log_{10}(\rho/\epsilon), \quad (2)$$

where  $G$  is the shear modulus,  $b_p$  is the length of the partial dislocation Burgers vector,  $w$  is the radius of the inscribed circle in the node,  $\nu$  is Poisson's ratio,  $\alpha$  is the character of the partial at the midpoint of the node,  $\rho$  is the loop radius and  $\epsilon$  is the cutoff radius taken to be equal to  $b_p$ . Using this equation, and the elastic coefficients of Lambrecht *et al.* (1991), we obtain  $\gamma = 12.2 \pm 1.1 \text{ mJ m}^{-2}$ . This value lies within the range  $14.7 \pm 2.5 \text{ mJ m}^{-2}$  determined from the partial separations. Note that the stacking fault energy of 4H-SiC is nearly five times larger than that of 6H-SiC ( $= 2.9 \pm 0.6 \text{ mJ m}^{-2}$ ).

#### §4. DISCUSSION

##### 4.1. Energy of perfect (unfaulted) polytypes

According to Heine and coworkers (for example Cheng *et al.* (1988)), the total energy of a system of  $n$  layers of an  $n\text{H}$ - (or  $n\text{R}$ -) SiC polytype at  $T = 0 \text{ K}$  is

$$E = E_0 - \frac{1}{n} \sum_{i=1}^n \sum_{j=1}^{\infty} J_j \sigma_i \sigma_{i+j}, \quad (3)$$

where  $\sigma_i = +1$  or  $-1$  according to whether the layer has up or down spin. The up or down spin corresponds to the orientation of the triple bonds in an SiC tetrahedron (Zhdanov 1945) or, alternatively, to whether the tetrahedron is normal ( $T$ ) or twinned ( $T'$ ) (Pirouz and Yang 1993). Thus, a 4H polytype with a tetrahedral stacking sequence of  $\dots T_1 T_2 T'_1 T'_3 \dots$ , or 22 in Zhdanov notation, can be represented as  $\dots \uparrow \uparrow \downarrow \downarrow \dots$ , and a 6H polytype with a tetrahedral stacking sequence  $\dots T_1 T_2 T_2' T'_1 T'_3 \dots$ , or 33 in Zhdanov notation, can be represented as  $\dots \uparrow \uparrow \uparrow \downarrow \downarrow \downarrow \dots$ .

In equation (3),  $E_0$  is the reference energy per layer in the crystal, and the  $J_i$  are the interaction energies between  $i$ th-neighbour basal (double) planes. In this equation, spin couplings higher than third-order layers ignored are usually because the corresponding interaction energies become negligibly small. Using norm-conserving



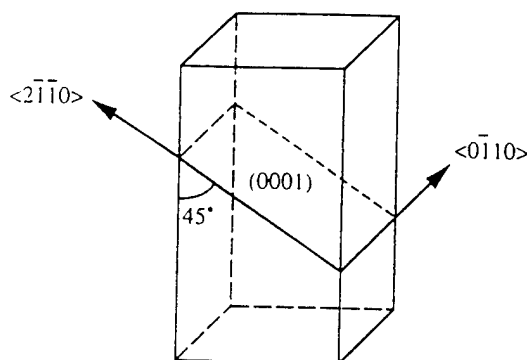


Fig. 2. Schematic of the compression specimen. Nominal specimen dimensions are  $2.0 \times 2.0 \times 4.0 \text{ mm}^3$

6H-SiC. Secondary ion mass spectroscopy (SIMS) was used to determine the oxygen (less than  $1 \times 10^{16} \text{ cm}^{-3}$ ) and nitrogen ( $\approx 5 \times 10^{16} \text{ cm}^{-3}$ ) contents. Photographic emission spectroscopy [10] revealed that the concentration of each of the common impurity elements, such as titanium, iron, aluminium, nickel and manganese, was below the detection limit of 5 ppm.

The orientation of the bulk crystal was determined by the X-ray Laue back-reflection technique and the samples were cut in an orientation as shown in Fig. 2. The samples were parallelepiped-shaped specimens with nominal dimensions  $\approx 2.0 \times 2.0 \times 4.0 \text{ mm}^3$ . After cutting, all the faces of each specimen were ground using a  $20 \mu\text{m}$  diamond-impregnated disc followed by a  $9 \mu\text{m}$  diamond polish. Each specimen then had the correct orientation for maximum resolved shear stress ( $S = 0.5$ ) for one of the three independent (0001)  $\langle 2\bar{1}10 \rangle$  primary slip systems. The Schmid factor ( $S$ ) for slip on the two other (0001)  $\langle 2\bar{1}10 \rangle$  independent (secondary) slip systems was lower ( $\approx 0.43$ ). Fig. 2 is a schematic representation of the compression samples used in the current experiments.

The samples were tested using a 1361 Instron machine equipped with an electro-mechanical actuator, in a specially machined polycrystalline SiC jig. The machine was fitted with a furnace with  $\text{MoSi}_2$  heating elements. Tests were conducted at temperatures between 550 and  $1300^\circ\text{C}$ . The temperature was monitored with a Pt-30% Rh versus Pt-6% Rh thermocouple. All the tests were conducted in an inert atmosphere of ultra-high purity (99.999%) argon gas, at three different strain rates: a fast strain rate of  $1.3 \times 10^{-4} \text{ s}^{-1}$ , an intermediate strain rate of  $6.3 \times 10^{-5} \text{ s}^{-1}$ , and a slow strain rate of  $3.1 \times 10^{-5} \text{ s}^{-1}$ . At each temperature in the range 500 to  $1300^\circ\text{C}$ , the compliance of the machine was obtained from the stress-strain curve of the system (fixture only without any sample mounted) using different loads on the load cell of the Instron and measuring the displacement response of the LVDT system.

Subsequent to the compression tests, transmission electron microscopy (TEM) samples were prepared from some of the deformed crystals. Specimens parallel to the (0001) plane were prepared from cut slices of  $\approx 300 \mu\text{m}$  initial thickness. These slices were then mechanically ground using silicon carbide paper to a thickness of  $\approx 70 \mu\text{m}$ . After further polishing using 3 and  $1 \mu\text{m}$  diamond paste, the samples were dimpled to a thickness of  $\approx 20 \mu\text{m}$  followed by ion beam thinning to electron transparency. A Philips CM20 transmission electron microscope was utilized to examine these specimens.

### 3. Experimental Results and Discussion

#### 3.1 Shear stress measurements

Fig. 3a, b are optical micrographs showing the slip traces on the (0110) front and  $\approx(2\bar{1}\bar{1}10)$  side face, respectively, of a 6H-SiC single crystal specimen deformed at a test temperature of 1300 °C and a strain rate of  $1.3 \times 10^{-1} \text{ s}^{-1}$  to a true longitudinal strain of 5.5%. Fig. 4a, b and c show the engineering stress, ( $\sigma$ ) versus engineering strain ( $\epsilon$ ) curves for some of the samples tested in uniaxial compression at various temperatures, at the fast strain rate of  $1.3 \times 10^{-1} \text{ s}^{-1}$ , the intermediate strain rate of  $6.3 \times 10^{-2} \text{ s}^{-1}$ , and the slow strain rate of  $3.1 \times 10^{-3} \text{ s}^{-1}$ , respectively. All these curves have been corrected for the machine compliance. All the samples deformed at the fast and intermediate strain rate exhibited smooth yielding. The critical resolved shear stress for the samples tested at these strain rates was assumed to be the stress value at the onset of nonlinearity in the engineering stress-strain curve. However, for the samples tested at the slow strain rate, the engineering stress-strain curves exhibited nonlinearities in the form of load drops at test temperatures of 600 °C and above. To determine the origin of these load drops, 'two-step' slow strain rate compression tests were conducted at some selected temperatures as follows. In the first step, samples were compressed at the respective temperatures to about 75% of the stress value of the first stress drop observed in the initial tests at the same strain rate and temperature. These samples were then unloaded, cooled, and carefully examined using Nomarski optical microscopy to rule-out the existence of any plastic deformation (e.g. slip traces). Since the unloading curves of these samples were also very close to the linear loading curve, one could be fairly confident that very little, if any, plastic flow had occurred. In the second step, these samples were then reloaded at the same strain rate and temperature to the point where they

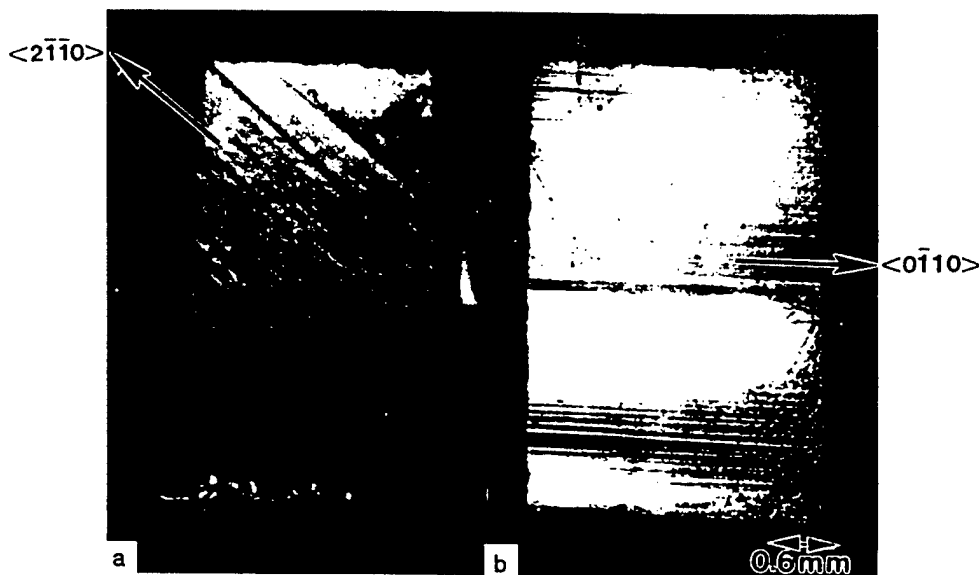


Fig. 3. Optical micrographs showing the slip traces on the a) (0110), and b)  $(2\bar{1}\bar{1}10)$  side faces of the sample deformed at a strain rate of  $1.3 \times 10^{-1} \text{ s}^{-1}$  and a test temperature of 1300 °C

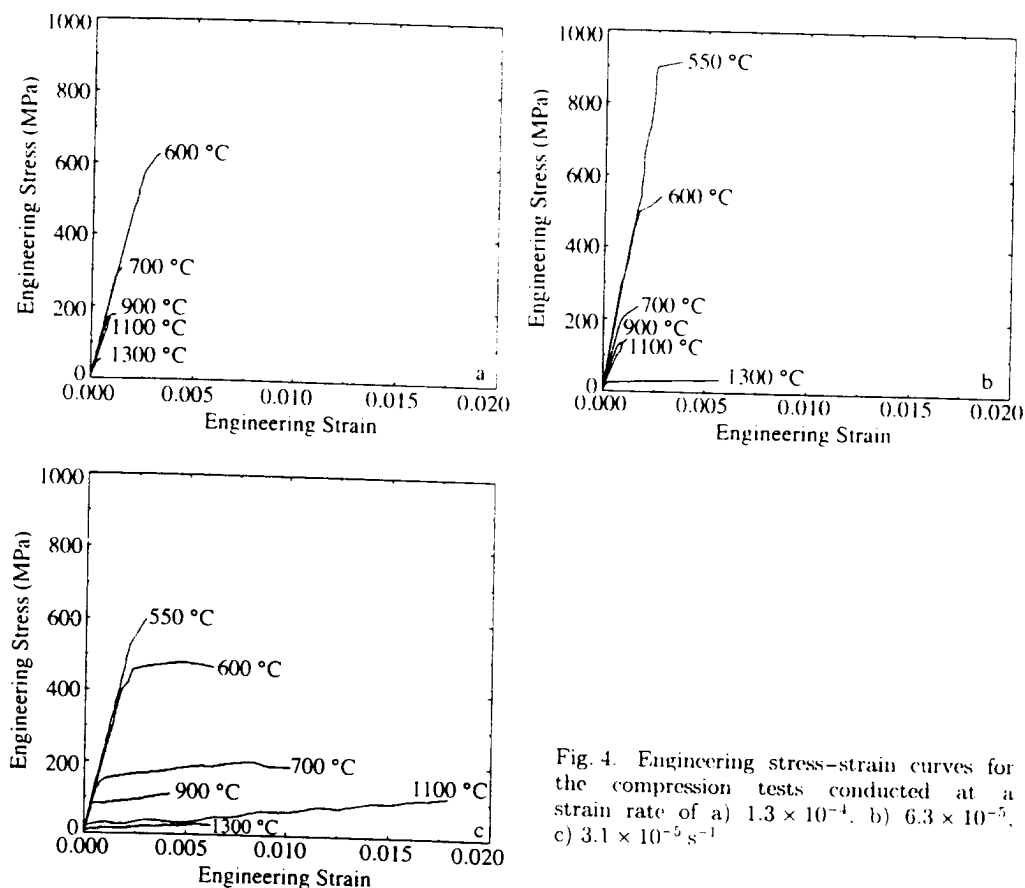


Fig. 4. Engineering stress-strain curves for the compression tests conducted at a strain rate of a)  $1.3 \times 10^{-4}$ , b)  $6.3 \times 10^{-5}$ , c)  $3.1 \times 10^{-5} \text{ s}^{-1}$ .

exhibited the first detectable load drop in the engineering stress-strain curve. After unloading and cooling the samples, they were again observed using Nomarski optical microscopy. All the samples tested in this 'two-step' fashion exhibited slip traces on their faces after the first load drop, indicating the onset of plastic flow. Thus, for the slow strain rate tests, the value of the stress at this first load drop could be assumed to be the critical resolved shear stress at that particular test temperature. For all the samples tested, there appeared to be a particular test temperature below which yielding was always accompanied by cracking, originating at the sample loading face. These temperatures were  $\approx 900$ ,  $\approx 700$  and  $\approx 600$  °C for the fast, intermediate and slow strain rates, respectively.

Fig. 5 shows the effect of test temperature on the critical resolved shear stress for the (0001)  $\langle 2\bar{1}10 \rangle$  primary slip system of 6H-SiC, determined at the three strain rates. Each data point in this figure represents one test. It is clear from Fig. 5 that the critical resolved shear stress increases sharply at test temperatures below 700 °C. In the temperature range of 700 to 1300 °C the critical resolved shear stress drops gradually.

Fig. 6 shows the effect of increasing the strain rate from  $3.1 \times 10^{-5}$  to  $6.3 \times 10^{-5} \text{ s}^{-1}$ , from  $6.3 \times 10^{-5}$  to  $1.3 \times 10^{-4} \text{ s}^{-1}$ , and from  $3.1 \times 10^{-5}$  to  $1.3 \times 10^{-4} \text{ s}^{-1}$ . It is clear from this figure that in each case, the temperature dependence of  $\Delta\tau_c$  is almost the same as

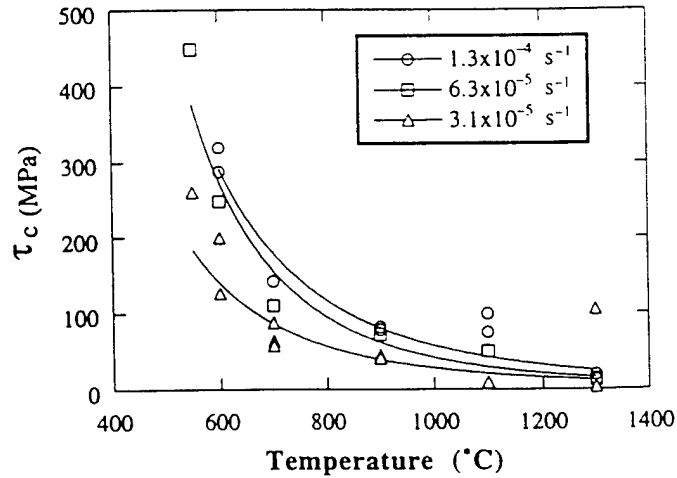


Fig. 5. Effect of test temperature on the critical resolved shear stress  $\tau_c(T)$  for the (0001)  $\langle 2\bar{1}10 \rangle$  primary slip system of 6H-SiC

the temperature dependence of the critical resolved shear stress  $\tau_c$ , i.e. it follows the trends observed in Fig. 5. The effect of the change in the strain rate  $\Delta\dot{\gamma}$  on  $\Delta\tau_c$  increases sharply at test temperatures below 700 °C. In the temperature range 700 to 1300 °C, this effect decreases gradually.

To the best of the authors' knowledge, 550 °C is the lowest temperature at which monocrystalline 6H-SiC has been plastically deformed in a 'constant' strain-rate type test. The critical resolved shear stress required to activate basal slip (at the intermediate strain rate) at this temperature is about 450 MPa, which is relatively low for deformation of such a hard material at such a low temperature.

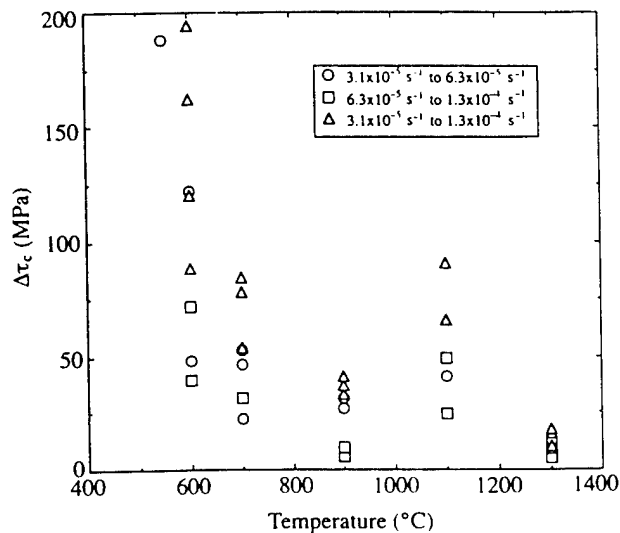


Fig. 6. Effect of increasing the strain rate from  $3.1 \times 10^{-5}$  to  $6.3 \times 10^{-5}$  s $^{-1}$ , from  $6.3 \times 10^{-5}$  to  $1.3 \times 10^{-4}$  s $^{-1}$ , and from  $3.1 \times 10^{-5}$  to  $1.3 \times 10^{-4}$  s $^{-1}$ , on the critical resolved shear stress  $\Delta\tau_c(T)$ , for the (0001)  $\langle 2\bar{1}10 \rangle$  primary slip system of 6H-SiC

### 3.2 Variations of Young's modulus with temperature

The Young's modulus of a crystal is usually determined from dynamic methods. However, since corrections of engineering stress,  $s$  and engineering strain  $e$ , to their true values  $\sigma$  and  $\epsilon$ , respectively, in the elastic regime of a crystal are not very significant, we can estimate the Young's modulus of 6H-SiC for the particular orientation under consideration from our static experiments, i.e., from the slope of the  $s$ - $e$  curves shown in Fig. 4a to c (it should be recalled that these curves have been corrected for machine and fixture compliances). This is a worthwhile exercise because, to the authors' knowledge, there are no reports of experimental variations of Young's modulus of 6H-SiC as a function of temperature. The results of this exercise are shown in Fig. 7 (open circles), where it can be seen that the Young's modulus of 6H-SiC decreases from a value of  $\approx 330$  GPa at  $550^\circ\text{C}$  to  $\approx 90$  GPa at  $1300^\circ\text{C}$ .

The only report that the authors have come across on the measurement of elastic constants of SiC as a function of temperature is the work of Li and Bradt [11] on cubic SiC. These authors estimated the three independent elastic constants ( $C_{11}$ ,  $C_{12}$ , and  $C_{44}$ ) in the stiffness constant tensor,  $C_{ij}$ , of 3C-SiC from the then available experimental data on the Young's modulus ( $E$ ), shear modulus ( $G$ ), bulk modulus ( $K$ ) and Poisson's ratio ( $\nu$ ) of high density  $\beta$ -SiC polycrystalline ceramics at different temperatures (in the range 25 to  $1000^\circ\text{C}$ ). In addition, using tensor transformations, Li and Bradt [11] estimated the five independent single crystal elastic constants ( $C_{11}$ ,  $C_{12}$ ,  $C_{13}$ ,  $C_{33}$ , and  $C_{44}$ ) of hexagonal 6H-SiC from those of cubic 3C-SiC; this was done by setting the hexagonal [0001] direction of 6H-SiC parallel to a  $\langle 111 \rangle$  direction of 3C-SiC. Hence, these authors were able to provide the variations of the elastic stiffnesses of 6H-SiC as a function of test temperature in the range quoted (25 to  $1000^\circ\text{C}$ ).

We have used the single crystal elastic constants of 6H-SiC as estimated by Li and Bradt [11], and the standard equations of Nye [12], to estimate the variations of Young's

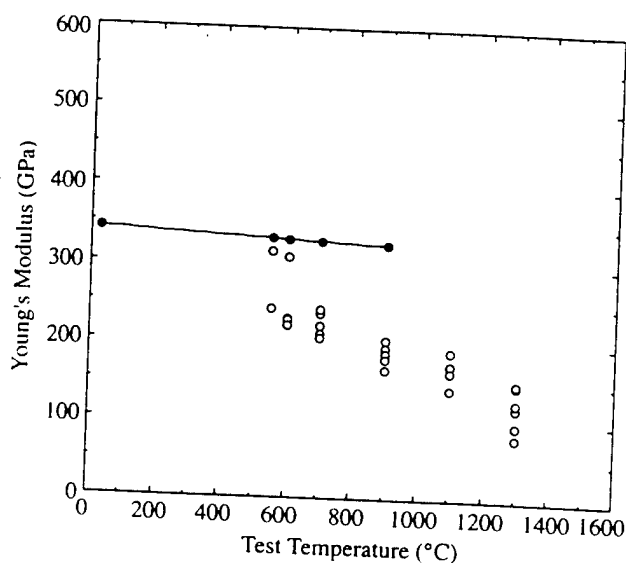


Fig. 7. Temperature variation of Young's modulus of 6H-SiC. open symbols estimated from the slope of the  $s$ - $e$  curves in Figs. 4a to c, solid symbols calculated from the elastic constants of 3C-SiC (see text)

modulus of 6H-SiC with temperature in the crystal orientation used in the present experiments. The results are also shown in Fig. 7. As seen, there is considerable deviation between the two sets of data, specially at temperatures above 900 °C (we recall that the calculated values in Fig. 7 (solid circles) are valid only up to  $\approx 1000$  °C, the maximum temperature to which Li and Bradt's [11] 3C-SiC data were measured). SiC starts becoming increasingly nonstoichiometric as the temperature increases above 1100 °C, and thus the temperature variations of the Young's modulus above this temperature may not correspond to those extrapolated from Li and Bradt's [11] data. In brief, the results shown in Fig. 7 (open circles) have been deduced from static mechanical tests and thus give only approximate values for the Young's moduli. Dynamic tests, such as acoustic techniques, need to be employed to more accurately determine the effect of test temperature on the elastic constants, including the Young's modulus, of 6H-SiC.

### 3.3 Activation enthalpy calculations

Two basic methods for the analysis of activation parameters exist in the literature [1, 13 to 17]. The first method can be derived starting from Orowan's equation [15],

$$\dot{\gamma} = \rho b v, \quad (1)$$

where  $\dot{\gamma}$  is the shear strain rate,  $\rho$  the mobile dislocation density,  $b$  the magnitude of the Burgers vector, and  $v$  the dislocation velocity.

The dislocation velocity in semiconductors can be expressed as

$$v = v_0 \exp \left( \frac{-H(\tau)}{kT} \right), \quad (2)$$

where  $\tau$  is the shear stress,  $H(\tau)$  is a stress dependent activation enthalpy,  $k$  the Boltzmann constant, and  $T$  the absolute temperature.

From equations (1) and (2) we have,

$$\dot{\gamma} = \dot{\gamma}_0 \exp [-H(\tau)/kT], \quad (3)$$

where  $\dot{\gamma}_0 (= \rho b v_0)$  is a pre-exponential factor which might be stress and temperature dependent. Taking logarithms from both sides of equation (3), differentiating with respect to  $\tau$ , and rearranging

$$\left( \frac{\partial H(\tau)}{\partial \tau} \right)_T = -kT \left( \frac{\partial \ln \dot{\gamma}}{\partial \tau} \right)_T. \quad (4)$$

The left-hand side of equation (4), i.e. the stress dependence of the activation enthalpy  $H$  is usually defined as the activation volume  $V$ ,

$$V \equiv - \left( \frac{dH}{d\tau} \right)_T. \quad (5)$$

Thus,

$$V = kT \left( \frac{\partial \ln \dot{\gamma}}{\partial \tau} \right)_T. \quad (6)$$

Fujita et al. [1] suggested a variant of the strain rate jump test for measuring the activation volume  $V$ , whereby, at a particular strain  $\gamma_1$ , during a stress-strain experi-

ment, the strain rate  $\dot{\gamma}_1$  is suddenly changed by  $\Delta\dot{\gamma}(=\dot{\gamma}_2 - \dot{\gamma}_1)$  and the resulting stress change  $\Delta\tau(=\tau_2 - \tau_1)$  is measured. The slope of the plot of  $\ln(\dot{\gamma}_1/\dot{\gamma}_2)$  versus  $\Delta\tau(=\tau_2 - \tau_1)$  should then be proportional to the activation volume  $V$ .

Once the activation volume has been determined, the activation enthalpy  $H$  can be estimated by partial differentiation of equation (3) with respect to  $T$  under a given  $\dot{\gamma}$ .

$$H = T \frac{dH}{d\tau} \left( \frac{\partial \tau}{\partial T} \right)_\gamma - \frac{kT^2}{\rho} \left( \frac{\partial \rho}{\partial T} \right)_\gamma \quad (7)$$

For strain rate jump tests of the kind described above, and using equation (5) it can be shown [1] that equation (7) reduces to

$$H = -V'T \left( \frac{\partial \tau}{\partial T} \right)_\gamma \quad (8)$$

However, since the compression tests conducted in the present study were done on different samples for each different strain rate, the assumption of identical microstructures would be inappropriate.

The second method for analyzing the activation parameters can be deduced from the following expression:

$$\dot{\gamma} = \tau_c^n \exp[-Q/kT], \quad (9)$$

where  $n$  is the stress exponent and  $Q$  the stress- and temperature-independent activation enthalpy.

For 'constant' strain rate type tests, similar to those in the present study, equation (9) can be rewritten as follows:

$$\ln \tau_c = \frac{Q}{nkT} + \frac{1}{n} \ln \dot{\gamma}, \quad (10)$$

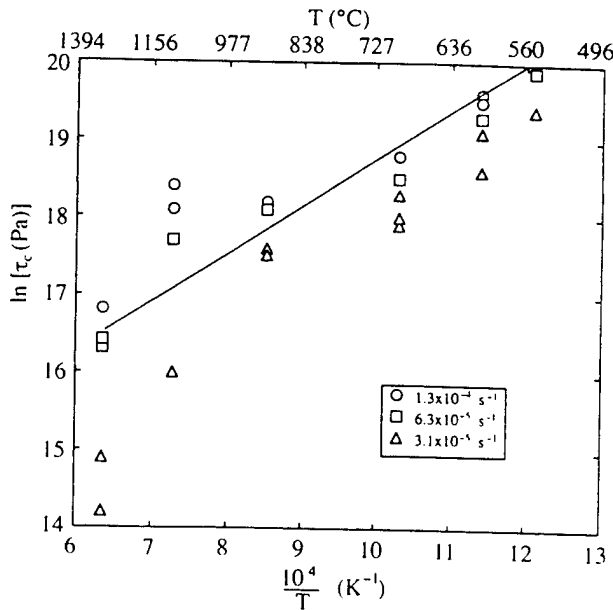


Fig. 8. A plot of  $\ln \tau_c$  versus  $1/T$  following equation (10)

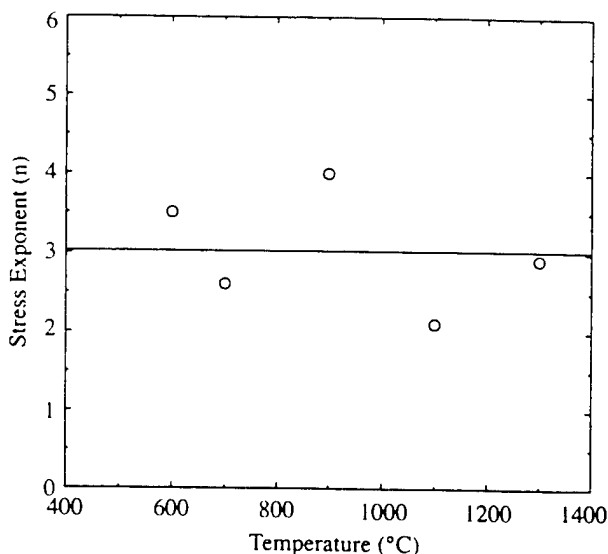


Fig. 9. A plot of the variation of the stress exponent ( $n$ ) as a function of the test temperature following equation (11)

where the second term on the right-hand side of equation (10) is a constant. Thus, according to equation (10), a plot of  $\ln \tau_c$  versus  $1/T$  should be linear with a slope of  $Q/nk$ . The stress exponent  $n$  can be calculated according to the following expression which can be obtained from equation (10):

$$n = \frac{\ln(\dot{\gamma}_1/\dot{\gamma}_2)}{\ln(\tau_{c1}/\tau_{c2})}, \quad (11)$$

where  $\tau_{c1}$  and  $\tau_{c2}$  are the critical resolved shear stresses at the two independent strain rates  $\dot{\gamma}_1$  and  $\dot{\gamma}_2$  at the same test temperature  $T$ .

Fig. 8 is a plot of the critical resolved shear stress  $\tau_c$  versus the reciprocal of the absolute temperature  $T$ . It is clear that the linear relationship predicted by equation (10) is indeed observed for the fast and intermediate strain rates over the temperature range tested (550 °C to 1300 °C). However, for the slow strain rate tests (especially at temperatures of 1100 °C and above), there is considerable deviation from linearity indicating that equation (10) can no longer be used to estimate the activation enthalpy. For the fast and intermediate strain rates at temperatures up to 1300 °C, and for the slow strain rate at temperatures below 1100 °C, the average slope,  $(Q/n)$ , is estimated to be  $(0.7 \pm 0.1)$  eV, whereas for higher temperatures at the slow strain rate, the slope is estimated to be  $(1.5 \pm 0.1)$  eV. Fig. 9 is a plot of the stress exponent ( $n$ ) versus the test temperature  $T$ , calculated using equation (11) for the same strain rates. The average value of  $n$  is estimated to be  $3.0 \pm 0.7$ . Based on this analysis, the activation enthalpy  $Q$  was evaluated to be  $(2.1 \pm 0.7)$  eV for the fast and intermediate strain rates at  $T \leq 1300$  °C, and for the slow strain rate at  $T \leq 1100$  °C. At  $T > 1100$  °C at the slowest strain rate, the activation enthalpy was determined to be  $(4.5 \pm 1.2)$  eV.

### 3.4 Transmission electron microscopy

As the curves in Fig. 8 indicate, for the fast and intermediate strain rates,  $\ln \tau_c$  varies linearly with  $1/T$  over the range of temperatures studied (550 to 1300 °C) whereas at



the slowest strain rate there is a change in the slope of the curve above  $\approx 1100^\circ\text{C}$ . For this reason, samples deformed at a temperature below ( $900^\circ\text{C}$ ) and above ( $1300^\circ\text{C}$ ) this critical value ( $\approx 1100^\circ\text{C}$ ) were selected for TEM examination and comparison of the dislocation structure in them.

Fig. 10a to c, from the sample deformed at  $1300^\circ\text{C}$ , shows a series of bright-field (BF) micrographs taken with reflections  $g_1 = 2\bar{1}\bar{1}0$ ,  $g_2 = \bar{1}2\bar{1}0$ , and  $g_3 = \bar{1}\bar{1}20$ . In Fig. 10a, taken with  $g = 2\bar{1}\bar{1}0$ , two dissociated dislocation lines have approached each other and interacted. Each of the dislocations consists of two partials. The dissociation is confirmed by Fig. 10d which was taken with the  $g_4 = 1\bar{1}01$  reflection, showing stacking fault contrast between the two partials of each dislocation. In Fig. 10b and c, one partial from each dissociated dislocation is out of contrast each time showing that the two partials of both pairs have the same Burgers vectors  $b_1 = \frac{1}{3} [1\bar{1}00]$  and  $b_2 = \frac{1}{3} [10\bar{1}0]$  where  $b_1$  and  $b_2$  are the Burgers vectors of the leading and trailing partial dislocations,

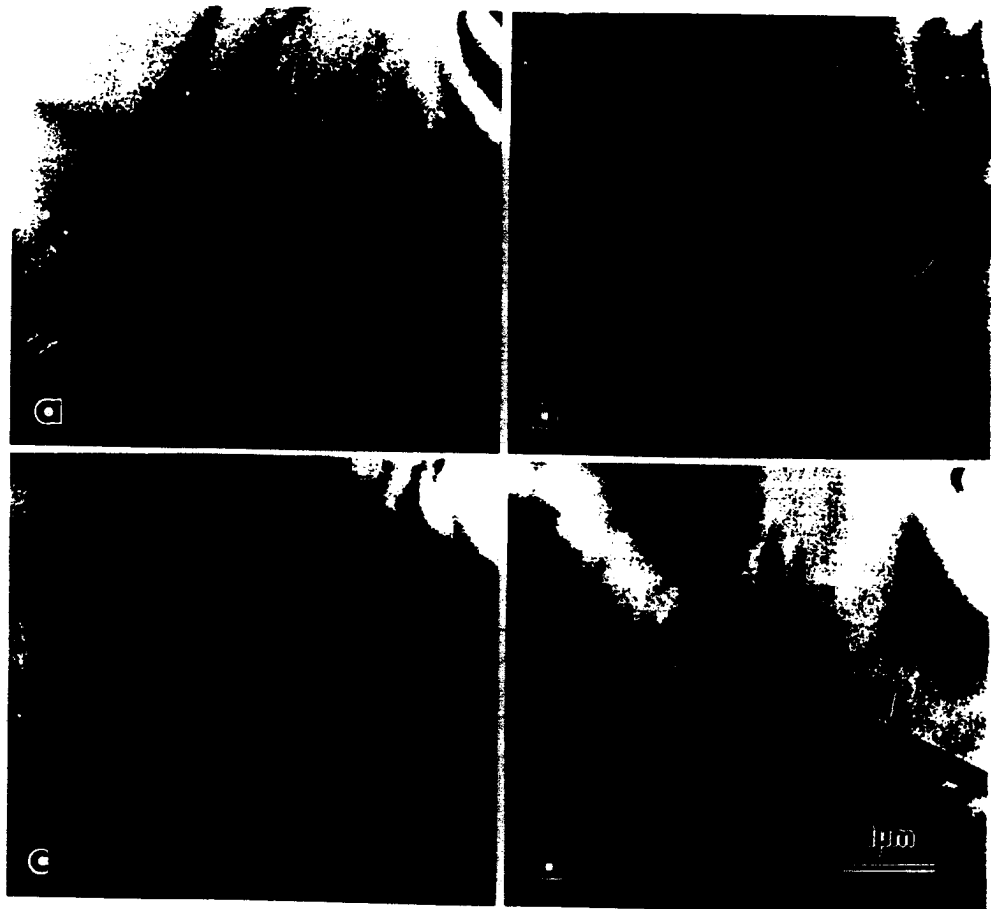


Fig. 10. Bright-field (BF) micrographs from the (0001) primary glide plane of the sample deformed at  $1300^\circ\text{C}$  at a strain rate of  $3.1 \times 10^{-5} \text{ s}^{-1}$  taken with the a)  $g_1 = 2\bar{1}\bar{1}0$ , b)  $g_2 = \bar{1}2\bar{1}0$ , c)  $g_3 = \bar{1}\bar{1}20$ , and d)  $g_4 = 1\bar{1}01$  reflections

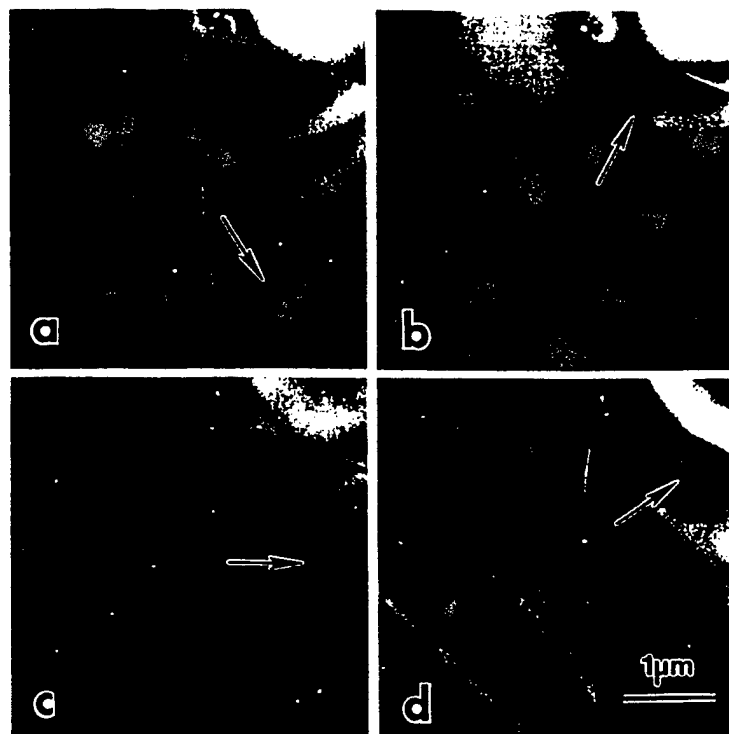


Fig. 11. Bright-field (BF) micrographs from the (0001) primary glide plane of the sample deformed at 900 °C at a strain rate of  $3.1 \times 10^{-5} \text{ s}^{-1}$  taken with the a)  $g_1 = 2\bar{1}\bar{1}0$ , b)  $g_2 = \bar{1}2\bar{1}0$ , c)  $g_3 = \bar{1}120$ , and d)  $g_4 = 10\bar{1}1$  reflections

respectively; as a result, the Burgers vector of each complete dissociated dislocation in Fig. 10 is  $b = \frac{1}{3} [2\bar{1}\bar{1}0]$  according to the following reaction:

$$\frac{1}{3} [2\bar{1}\bar{1}0] \rightarrow \frac{1}{3} [1\bar{1}00] + \frac{1}{3} [10\bar{1}0].$$

Most of the dislocations observed in this sample proved to be complete dissociated dislocations of the type shown in Fig. 10.

The other sample that was examined by TEM was the one deformed at 900 °C. As expected, the density of dislocations in this sample was much lower than the one deformed at 1300 °C. In fact, large areas had to be examined by TEM before dislocations could be found. When found, the dislocations in this sample usually appeared singly and not, like the ones seen in Fig. 10a, as pairs. This could either mean that the observed dislocations in the 900 °C deformed sample are complete and undissociated, or that they consist of a single partial with the complimentary partial not present in the viewing area. A typical dislocation in this low-temperature deformed sample is shown in Fig. 11a to c under  $g_1 = 2\bar{1}\bar{1}0$ ,  $g_2 = \bar{1}2\bar{1}0$ , and  $g_3 = \bar{1}120$  reflections, respectively. Note that the dislocation is in contrast with two reflections of the type  $g = \bar{1}2\bar{1}0$  and is out of contrast with the third one ( $g = \bar{1}120$ ). This is only consistent with a partial dislocation with  $b_p = \frac{1}{3} [1\bar{1}00]$ ; a complete dislocation of the type  $b = \frac{1}{3} [2\bar{1}\bar{1}0]$  would have been in contrast under all three reflections. Fig. 11d, taken with the reflection  $g_4 = 10\bar{1}1$  shows

stacking fault on one side of this dislocation and confirms that it is indeed a partial. The question now arises as to whether this dislocation is one of the partials (leading or trailing) of a pair where the complimentary (trailing or leading) partial is far from it and out of the viewing area, or whether the dislocation is a single leading partial that has nucleated without its complimentary trailing partial having ever been nucleated. This question cannot be answered at present but some work on 4H-SiC [18] has shown that, under certain conditions of deformation, leading partial dislocations can nucleate singly without the associated trailing partials having a chance to nucleate.

The fact that the dislocations in the sample deformed at 1300 °C consist primarily of complete (albeit dissociated) dislocations, whereas the dislocations in the sample deformed at 900 °C are primarily partials, may explain the deviation from linearity at temperatures above  $\approx 1100$  °C for the tests conducted at the slowest strain rate (see Fig. 8). Since the Burgers vectors of the complete dislocations ( $\mathbf{b} = \frac{1}{3} \langle 2\bar{1}\bar{1}0 \rangle$ ) is  $\sqrt{3}$  times larger than that of the partial dislocations ( $\mathbf{b}_p = \frac{1}{3} \langle 10\bar{1}0 \rangle$ ), the glide of perfect dislocations produces a larger strain at a particular stress. Conversely, the same strain can be produced at a lower stress when the deformation is produced via the glide of perfect rather than partial dislocations.

It is interesting to note that in Fig. 8, the slope of the  $\ln \tau_c$  versus  $1/T$  curve for the slow strain rate tests at temperatures below  $\approx 1100$  °C, is roughly the same as that of the curve for the intermediate and fast strain rate tests. It is well-known that the effect of increasing the strain rate in a deformation test is equivalent to lowering the test temperature, and vice versa. Thus, it is possible that the dislocations responsible for plastic strain in the fast and intermediate strain rate tests, like the low temperature regime (i.e. at temperatures less than  $\approx 1100$  °C) for the slow strain rate tests, are also single partials.

In [18 to 20], evidence has been presented that in semiconductors, the leading partial is the one which has a lower activation enthalpy and thus nucleates before the trailing partial dislocation, which has a higher activation enthalpy. Moreover, at lower temperatures, if the applied shear stress is not sufficiently high, the trailing partial may not nucleate at all, and the leading partial may glide singly with a stacking fault trailing behind it. Thus, in the present experiments it is possible that for the intermediate and fast strain rate tests, and also for the slow strain rate tests at temperatures lower than  $\approx 1100$  °C, the deformation takes place primarily by nucleation and glide of the more mobile leading partial dislocations only. The change at  $\approx 1100$  °C in the slope of the slow strain rate test curve (Fig. 8) may then correspond to a change in the activation enthalpy. Thus, the lower activation energy at  $T < 1100$  °C may correspond to the glide of only the leading partial dislocation, whereas the higher activation energy at  $T > 1100$  °C may correspond to the glide of a complete dislocation which is controlled by the mobility of the slower trailing partial.

It was further shown in [18 to 20] that the more mobile partial dislocations in SiC have a silicon core [Si(g)] while the less mobile partial dislocations have a carbon core [C(g)]. The fact that the activation enthalpy of  $(2.1 \pm 0.7)$  eV for the fast and intermediate strain rate tests calculated from Fig. 8 and equations (9) to (11), is approximately the same as that for glide of dislocations in elemental silicon [13], suggests that, in this temperature-strain rate regime, we might in fact be measuring the activation enthalpy for glide of the Si(g) partial dislocation in SiC, and that this partial has approximately the same activation enthalpy as that of the leading partial dislocation in elemental silicon. After all, the activa-

tion enthalpy for the glide of Si(g) dislocations in both SiC and Si is primarily determined by the strength of the Si-Si bond in the reconstructed dislocation core [21].

Additional deformation tests need to be conducted in the 1100 to 1300 °C temperature regime at the slow strain rate, in order to determine whether the  $\ln \tau_c$  versus  $1/T$  curve is linear with a higher slope in this temperature regime. In addition, TEM experiments are continuing to determine the nature of the dislocations in the samples deformed at the intermediate and fast strain rates.

#### 4. Conclusions

1. The critical resolved shear stress  $\tau_c$  for basal slip in 6H-SiC increases sharply at test temperatures below 700 °C and drops gradually in the 700 to 1300 °C temperature range.

2.  $\tau_c$  varies between 5 and 450 MPa in the temperature range of 1300 to 550 °C and a strain rate range of  $3.1 \times 10^{-5}$  to  $1.3 \times 10^{-4} \text{ s}^{-1}$ .

3. In the easy slip orientation chosen in the present study, 6H-SiC can be plastically deformed to relatively large plastic strains at test temperatures as low as 550 °C, via the application of modest resolved shear stresses (450 MPa at the intermediate strain rate) on the basal plane.

4. From all the tests, the stress exponent,  $n$ , was estimated to be  $3.0 \pm 0.7$ . For the intermediate and fast strain rates at temperatures up to 1300 °C, and also for the slow strain rate at temperatures below  $\approx 1100$  °C, the activation enthalpy was estimated to be  $(2.1 \pm 0.7) \text{ eV}$ . In contrast, for the slow strain rate at temperatures above  $\approx 1100$  °C, the activation enthalpy was estimated to be  $(4.5 \pm 1.2) \text{ eV}$ .

5. At the slow strain rate of  $3.1 \times 10^{-5} \text{ s}^{-1}$ , deformation possibly occurs by dissociated complete dislocations above  $\approx 1100$  °C and by single leading partial dislocations below  $\approx 1100$  °C.

6. The Young's modulus of 6H-SiC, as determined from experimental engineering stress-strain curves, decreases from  $\approx 330 \text{ GPa}$  at 550 °C to  $\approx 90 \text{ GPa}$  at 1300 °C.

**Acknowledgements** The authors wish to thank Dr. Calvin Carter of Cree Research Inc. for providing the bulk 6H-SiC crystal used in this study. This work was supported by subcontract number 95-SPI-420757-CWRU from the Silicon Carbide Consortium and contract number DE-FG02-93ER45496 from the Department of Energy.

#### References

- [1] S. FUJITA, K. MAEDA, and S. HYODO, *Phil. Mag.* **A55**, 203 (1987).
- [2] H. SUEMATSU, T. SUZUKI, T. ISEKI, and T. MORI, *J. Amer. Ceram. Soc.* **74**, 173 (1991).
- [3] J. W. YANG, T. SUZUKI, P. PIROUZ, J. A. POWELL, and T. ISEKI, Stress-Induced Polytropic Transformation in SiC, in: *Wide Band Gap Semiconductors*, Eds. T. D. MOUSTAKAS, J. I. PANKOVE, and Y. HAMAKAWA, Materials Research Society, Pittsburgh, PA 1992 (pp. 531 to 536).
- [4] G. S. CORMAN, *J. Amer. Ceram. Soc.* **75**, 3421 (1992).
- [5] X. J. NING and P. PIROUZ, Kink and Crack Interfaces in Low-Temperature-Deformed 6H-SiC Single Crystals, in: *Structure and Properties of Interfaces in Ceramics*, Eds. D. A. BONNELL, U. CHOWDHRY, and M. RÜHLE, Materials Research Society, Pittsburgh, PA 1994 (pp. 157 to 162).
- [6] D. FELDMAN, J. PARKER, W. CHOYKE, and L. PATRICK, *Phys. Rev. A* **170**, 698 (1986).
- [7] S. NAKASHIMA, H. KATAHAMA, Y. NAKAKURA, and A. MITSUISHI, *Phys. Rev. B* **33**, 5721 (1986).

- [8] H. NIENHAUS, T. KAMPEN, and W. MÖNCH, *Surf. Sci.* **324**, L328 (1995).
- [9] Z. FENG, C. TIN, R. HU, and K. YUE, *Semicond. Sci. Technol.* **10**, 1418 (1995).
- [10] Standard Recommended Practice for Photographic Photometry in Spectrochemical Analysis, Modified ASTM Standard E116, in: *Ann. Book of ASTM Standards*, American Society for Testing and Materials, Philadelphia, PA 1996.
- [11] Z. LI and R. C. BRADT, Thermal Expansion and Elastic Anisotropies of SiC as Related to Polytype Structure, in: *Ceramic Transactions: Silicon Carbide '87*, The American Ceramic Society, Inc., Westerville, OH 1989 (p. 313 to 339).
- [12] J. F. NYE, *Physical Properties of Crystals*, Clarendon Press, Oxford 1957.
- [13] J. RABIER and A. GEORGE, *Rev. Phys. Appl.* **22**, 1327 (1987).
- [14] B. ESCAIG, J. L. FARVACQUE, and D. FERRÉ, *phys. stat. sol. (a)* **71**, 329 (1982).
- [15] M. OMRI, C. TETE, J.-P. MICHEL, and A. GEORGE, *Phil. Mag.* **A55**, 601 (1987).
- [16] U. F. KOCKS, A. S. ARGON, and M. F. ASHBY, in: *Progress in Materials Science*, Vol. 19, Ed. B. CHALMERS, J. W. CHRISTIAN, and T. B. MASSALSKI, Pergamon Press, Oxford 1975.
- [17] G. SHOECK, *phys. stat. sol.* **8**, 499 (1965).
- [18] X. J. NING, N. HUVEY, and P. PIROUZ, *J. Amer. Ceram. Soc.* **80**, 1645 (1997).
- [19] X. J. NING, T. PEREZ, and P. PIROUZ, *Phil. Mag.* **A72**, 837 (1995).
- [20] X. J. NING and P. PIROUZ, *J. Mater. Res.* **11**, 884 (1996).
- [21] P. PIROUZ and X. J. NING, Partial Dislocations in Semiconductors: Structure, Properties and Their Role in Strain Relaxation, in: *Microscopy of Semiconducting Materials*, Inst. Phys. Conf. Ser., Vol. 146, Bristol 1995 (pp. 69 to 77).

## On deformation and fracture of semiconductors

P Pirouz\*, A V Samant\*, M H Hong\*, A Moulin\*\* and L P Kubin\*\*

\*Department of Materials Science and Engineering, CWRU, Cleveland, Ohio 44106, U.S.A.

\*\*LEM, CNRS-ONERA, B.P. 72, Av. de la Division Leclerc, 9322 Châtillon Cedex, France.

**ABSTRACT:** Recent experiments on deformation of semiconductors show an abrupt change in the variation of the critical resolved shear stress with temperature. This implies a change in the deformation mechanism at a critical temperature  $T_c$ . In the cases examined so far in our laboratory and elsewhere, this critical temperature appears to coincide approximately with the brittle-ductile transition temperature of the material. In this paper, we describe TEM investigations that have been performed on the wide bandgap semiconductor, SiC, deformed at temperatures below and above  $T_c$  in order to understand the change of mechanism. Based on these deformation and TEM experiments, suggestions are made as to the different mechanisms operating at low and high temperatures in semiconductors, and a possible relation between  $T_c$  and the brittle-ductile transition temperature in these materials.

### 1. INTRODUCTION

Recently, Suzuki *et al.* (1998, 1999a,b) have re-measured the variation of yield stress,  $\tau_y$ , of a few semiconductors (InP, GaAs, and InSe) as a function of temperature,  $T$ , and find a break at a critical point ( $\tau_c, T_c$ ) in the  $\tau_y(T)$  plot. Instead of a single curve with a smooth increase in the slope of the  $\tau_y(T)$  plot with decreasing temperature, the new  $\tau_y(T)$  plots appear to consist of two segments with different slopes. This transition appears perhaps more clearly in a plot of  $\ln(\tau_y)$  versus  $1/T$ , usually linear with a slope proportional to the activation energy for dislocation glide in the material. In the new experiments of Suzuki *et al.* (1999a), the  $\ln[\tau_y(1/T)]$  plot is separated into two straight lines with different slopes joined at  $T_c$ . Similar results were found by Samant (1999) in two wide bandgap semiconductors, 4H and 6H SiC. In all cases mentioned, the slope of the  $\ln[\tau_y(1/T)]$  linear plot is smaller in the low-temperature regime ( $T < T_c$ ) than that in the high-temperature regime ( $T > T_c$ ). Also, intriguingly, in every case, this critical transition temperature in  $\tau_y(T)$  or  $\ln[\tau_y(1/T)]$  is close to the brittle-ductile transition (BDT) temperature,  $T_{BDT}$ , of the semiconductor (Pirouz *et al.* 1999).

### 2. EXPERIMENTAL RESULTS

#### 2.2. Temperature-Dependence of the Yield Stress

The yield stress,  $\tau_y$ , of two SiC polytypes, 4H-SiC and 6H-SiC, was measured in the temperature range ~550-1300°C under different strain rates. The most relevant results to the present work occur at the slowest strain rate,  $3.1 \times 10^{-5} \text{ s}^{-1}$ , for both polytypes. The results are shown in Fig. 1(a) and 1(b) in terms of a plot of  $\ln(\tau_y)$  versus  $1/T$ . It can be seen that each plot is divided into two linear regimes with different slopes separated at a critical temperature,  $T_c \approx 1100 \pm 100^\circ\text{C}$ . The fact that the plots are linear indicates that the kink pair mechanism can

be applied to both regimes, albeit with different activation energies for dislocation glide. In the low-temperature regime,  $550^{\circ}\text{C} < T < T_c$ , the slope of the plot for both 4H-SiC and 6H-SiC corresponds to an activation energy for dislocation glide of  $2.1 \pm 0.7$  eV. In contrast, in the high-temperature regime,  $T > T_c$ , the slope of the plots for both materials corresponds to an activation energy of  $4.8 \pm 1.8$  eV. It is noteworthy that an activation energy of  $\sim 2$  eV corresponds to that for dislocation glide in elemental silicon while an activation energy of  $\sim 4$  eV corresponds to that for dislocation glide in diamond. Interestingly, the cores of the two  $30^{\circ}$  partials of a dissociated screw dislocation in SiC are Si(g) and C(g).

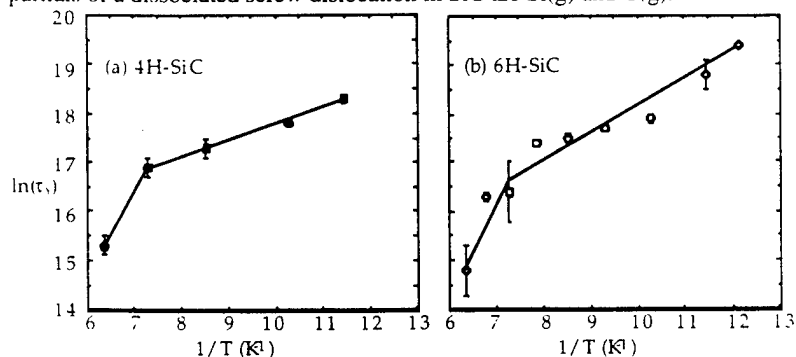
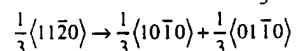


Fig. 1.  $\ln(\tau\gamma)$  versus  $1/T$  for (a) 4H-SiC, (b) 6H-SiC.

## 2.2. TEM of the Deformed Samples

The dislocation configurations of the deformed 4H-SiC and 6H-SiC crystals were investigated by TEM. From samples deformed above  $T_c$  ( $1300^{\circ}\text{C}$  for 4H and  $1350^{\circ}\text{C}$  for 6H-SiC) and below  $T_c$  ( $750^{\circ}\text{C}$  for 4H-SiC and  $900^{\circ}\text{C}$  for 6H-SiC), slices were cut parallel to the primary slip plane, (0001). From these slices, three TEM specimens each were prepared and investigated in a Philips CM20 at 200 kV using bright-field (BF), weak-beam dark-field (WB) and LACBED. The results of these experiments were as follows. The dislocations in all the samples deformed above  $T_c$  (three each for 4H-SiC and 6H-SiC) were  $\frac{1}{3}\langle 11\bar{2}0 \rangle$  total dislocations, albeit dissociated into two  $\frac{1}{3}\langle 1\bar{1}00 \rangle$  partials according to the following reaction:



This is shown in Fig. 2 for both 4H- and 6H-SiC.



Fig. 2. BF TEM micrographs of dislocations in (a) 4H-SiC, (b) 6H-SiC induced by deformation at  $T > T_c$ .

By contrast, in all the TEM specimens of 4H and 6H-SiC deformed at temperatures below  $T_c$  that have been investigated, the dislocations were predominantly, but not exclusively,  $\frac{1}{3}\langle 10\bar{1}0 \rangle$  single leading partials, bordered on one side by a stacking fault (Fig. 3).

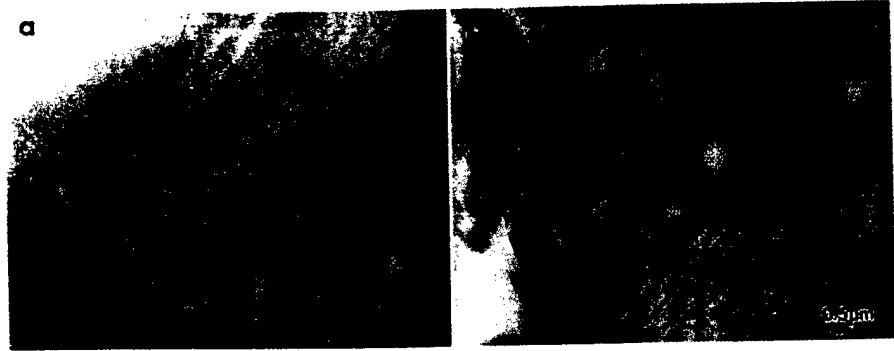


Fig. 3. BF TEM micrographs of single leading dislocations in (a) 4H-SiC, (b) 6H-SiC induced by deformation at  $T < T_c$ .

In no case was it possible to observe the trailing partial, i.e. the stacking fault either disappeared in the hole within the foil, or extended to the thicker parts of the specimen where the contrast became too weak to be observed. The nature of the single partial in the case of deformation at  $T < T_c$  was determined by the LACBED technique (Ning and Pirouz 1996). In the three cases examined, the partial was found to have a silicon core in 4H-SiC (Fig. 4).

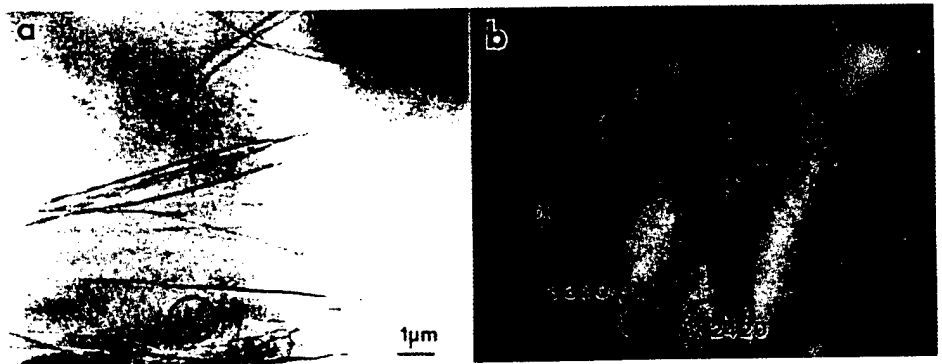


Fig. 4. Partial dislocations in 4H-SiC (a) BF (b) LACBED of the circled segment.

### 3. DISCUSSION

#### 3.1. The transition in the yield stress versus temperature curves

It may be assumed that to nucleate a dislocation half-loop at a surface (or at a crack tip), the applied stress must overcome primarily the attractive image force and that this is easier at an edge heterogeneity, such as a surface step (or a ledge at a crack tip). Recently, Brochard *et al.* have compared the nucleation of the leading and trailing Shockley partial dislocations from a surface step in tetrahedrally coordinated cubic materials (Brochard, Junqua and Grilhé 1998a) taking into account the possibly different mobilities of the two partials of a dissociated dislocation (Brochard, Rabier and Grilhé 1998b). They found that both the mobility of the partial as well as the average friction force (=velocity/mobility) opposing its motion are important in the nucleation of that partial, and that over a wide range of the  $\tau$ - $\gamma$  plane (where  $\gamma$



is the stacking fault energy), the stress necessary to nucleate a partial dislocation of higher mobility is lower. Although the model of Brochard *et al.* (1998b) does not take into account any activation energy, it is expected that thermal activation will decrease the stresses required for dislocation nucleation, and that the value of the activation energy will be different for the two partials. Conversely, it can be said that at a fixed value of stress, the two partials will be nucleated at different temperatures, with the more mobile dislocation having a lower activation energy and nucleating at a lower temperature.

We therefore propose that, at temperatures below  $T_c$ , only the more mobile dislocations, assumed to have a lower activation energy, are nucleated (as the leading partials), and deformation occurs primarily by their glide on different planes. This is despite the fact that creation of a stacking fault (of energy  $\gamma$ ) by the leading partial creates an additional force ( $=\gamma/b$ ) for the creation of the trailing partial. In fact, we propose that the trailing partials only start to nucleate at the critical temperature  $T_c$  when the thermal energy becomes sufficient. Thus,  $T_c$  in Fig. 1, and in the  $\tau_y(T)$  plots of Suzuki (1999), is identified with the temperature at which a transition in the deformation mode of the material takes place: deformation by glide of single leading partials at  $T < T_c$  versus glide of total dislocations at  $T \geq T_c$ . This may be valid for all the tetrahedrally coordinated materials with a deep Peierls valley.

### 3.2. Brittle-Ductile Transition (BDT)

Since in the five semiconductors for which a transition in the plot of  $\tau_y(T)$  has been observed, the transition temperature,  $T_c$ , roughly coincides with the BDT, it is possible that  $T_c$  and  $T_{BDT}$  are also related. To expand on this point, we shall start with a brief description of the Hirsch and Roberts (HR) model for the BDT (Hirsch, Roberts and Samuels 1989, Hirsch and Roberts 1991) that is able to explain most of the experimental features observed in the fracture of silicon (Samuels and Roberts 1989). Two important features of the BDT in semiconductors are that, for a given geometry: (i) the value of the transition temperature in dislocation-free and non-prestrained crystals is very sharp, and (ii) the strain-rate dependence of  $T_{BDT}$  has an activation energy close to that of the dislocation velocity in the material.

The HR model is based on the shielding of the crack front by the dislocations nucleated there (Lin and Thomson 1986). It can be explained by means of Fig. 5(a) that shows a crack front under Mode III (Hirsch *et al.* 1989), or Mode I loading (Hirsch and Roberts 1991). Under the applied stress intensity factor  $K$ , dislocations can be nucleated only at special sites, e.g. X and Y, along the crack front. Dislocation loops of Burgers vector,  $b$ , are emitted when  $K$  reaches a critical value  $K_N$  for the first loop, and  $K_o$  for the subsequent loops. The value of  $K_o$  is assumed to be very close to  $K_{lc}$ , the critical stress intensity factor, and much larger than that of  $K_N$ ; typically  $K_N \approx 0.2K_{lc}$  and  $K_o \approx 0.9K_{lc}$ . The dislocation loops so formed shield the crack tip and reduce the effective stress intensity factor on it to a lower value

$$K_{eff} = K - \sum K_d = K - \sum_j \frac{\mu b}{(2\pi x_j)^{1/2}} \quad (\text{for the simpler case of Mode III}),$$

where  $K_d$  is the

shielding effect of a dislocation loop (summed over all the loops),  $\mu$  is the shear modulus, and  $x_j$  is the distance of the  $j$ th dislocation from the crack tip.

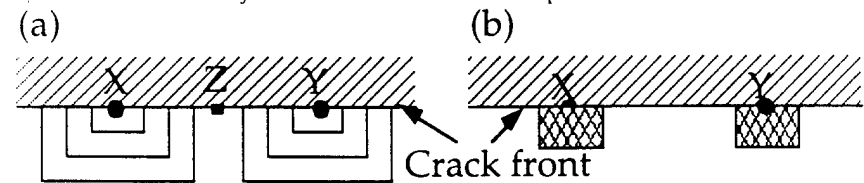


Fig. 5. Nucleation of (a) total, (b) partial dislocations at special sites (shown by solid circles) along a crack front; the solid square is a point in the initially dislocation-free zone.

The main feature of the HR model is that the crack front will propagate catastrophically if the increasing (under constant  $\dot{K}$ ) applied stress intensity factor  $K$  increases  $K_{eff}$  to the critical value,  $K_{lc}$ , unless the emitted dislocations shield the whole of the crack front, i.e., points X and Y (that are shielded from the start of dislocation nucleation), as well as points such as Z (that are not initially shielded). It is important that sites, such as Z, that are initially in a dislocation-free zone, become shielded by the expanding dislocation loops around points X and Y. In this case, the effective stress intensity factor,  $K_{eff}$ , becomes less than  $K_{lc}$  everywhere along the crack tip, for all values of the applied stress intensity factor up to the value at which macroscopic yield takes place. According to the HR model, the sharp yield point in silicon arises because of nucleation events, whereas the strain-rate dependence of  $T_{BDT}$  is explained by the time taken for the nucleation events to occur along the crack front, and the time taken for the expanding dislocation loops to shield all the points along the crack front from reaching  $K_{lc}$ .

Using the same equations and terminology as the HR model, let us now consider a crack tip under an increasing  $K$  at temperatures lower than  $T_c$ . In this case, it is suggested that only leading partial dislocation loops, with a Burgers vector,  $b_l$ , can be nucleated at heterogeneities (e.g., ledges) along the crack front, e.g., at sites such as X and Y in Fig. 5(b). At each such site, a partial dislocation loop is able to nucleate only once after which it will expand until the resolved shear stress on it due to the applied stress intensity factor,  $K$ , is balanced by the line tension/stacking fault/image stresses. Inevitably, the leading partial will drag a stacking fault behind it (shown shaded inside the loops in Fig. 5(b)) and, more importantly, shut off the source leaving a single partial loop that will not be able to effectively shield the crack tip. As a result, the shielding of the crack tip is very limited and the effective stress intensity factor,  $K_{eff}$ , on the crack tip (given by  $K_{eff} = K - K_d = K - \mu b_l / \sqrt{2\pi x}$  for Mode III) is nearly the same as the applied  $K$ . Because of the lack of effective shielding, the crack front will propagate catastrophically as soon as  $K_{eff}$  reaches  $K_{lc}$  under the increasing  $K$  (at a constant  $\dot{K}$ ).

At a temperature higher than  $T_{BDT}$  [Fig. 5(a)], a trailing partial immediately follows the nucleation of the leading partial to form a total dislocation loop, with a Burgers vector  $b$ . Now, however, since the stacking fault has been removed by the trailing partial, the source can remain active and further dislocation loops can form and expand as long as the back stress of the initial dislocation loops does not reduce the stress to a value below that required for nucleation. The situation is now somehow similar to that described by Hirsch and Roberts (1991). Under these conditions, an avalanche of total dislocation loops form that can shield the crack tip effectively, maintaining  $K_{eff}$  at a value less than  $K_{lc}$  up to the value at which macroscopic yield takes place (i.e. to the value of  $K$  corresponding to the shear stress  $\tau_c$ ).

However, if, as we suggest,  $T_c$  does in fact coincide with  $T_{BDT}$ , then nucleation, rather than mobility, of dislocations probably controls the BDT, in some ways, similar to the original Rice-Thomson model (1974). To clarify this point, consider Model B in Hirsch and Roberts (1991), i.e. the case where the starting crystal is basically dislocation-free (corresponding to the experiments of Michot and George (1989), and Brede and Haasen (1988)).

In the HR model, it is assumed that dislocations are emitted at a few special sites along the crack tip (e.g. at ledges) spaced  $d_{crit}^i$  apart at values of  $K = K_N < K_{lc}$ . Subsequently, loops emitted from these sites help to activate nucleation from other, more difficult, sites along the crack front because of the anti-shielding stresses ahead of these dislocation loops. The separation between these secondary nucleation sites is assumed to be  $d_{crit}^f$  ( $\ll d_{crit}^i$ ). In this model, the condition for the BDT is that the loops from the original sources must have traversed a distance  $(d_{crit}^i - d_{crit}^f)$ . This is when the applied  $K$  reaches  $K_{lc}$  (with  $K_{lc}$  just below  $K_{lc}$ ) such that the dislocations nucleated at the secondary sources have time to traverse  $d_{crit}^f$  and shield the whole crack front before the applied  $K$  reaches  $K_{lc}$ . Since the effective shielding of the crack tip depends on how quickly a sufficient number of dislocation loops can form and expand to allow the shielding of the crack tip, dislocation velocity,  $v = A\tau^m \exp(-U/kT)$ , plays a predominant role in this model. As Hirsch and Roberts (1991) show, the slope of the

linear plot of  $\ln(\dot{K})$  versus  $1/T_{BDT}$  is the same as the activation energy for dislocation glide.  $U$ , and  $T_{BDT}$  will depend on the strain-rate because the dislocation velocity is stress-dependent.

Within the present speculation, the sudden formation of an avalanche of full dislocations at  $T_c (=T_{BDT})$  releases the stored elastic energy required for further propagation of the crack. The  $\dot{K}$ -dependence of  $T_c$  comes from the assumption that nucleation of a (partial) dislocation depends on the rate of change of shear stress with time,  $\dot{\tau}$ . This is not unreasonable because the upper yield point,  $\tau_y^u$ , in semiconductors, which is probably also controlled by the start of dislocation nucleation events in the crystal, is a sensitive function of the strain rate,  $\dot{\epsilon}$ , and thus of  $\dot{\tau}$ . A simple starting point is to assume that the time,  $t$ , for a partial dislocation half-loop to nucleate from the crystal surface under an applied shear stress,  $\tau$ , is given by  $t = (1/v_o) \exp(\Delta E - \tau\Omega/kT)$ , where  $\Omega$  and  $v_o$  are the atomic volume and vibration frequency, respectively. Equating  $t$  with the time  $(K_{lc}/\dot{K})$  to reach  $K_{lc}$  gives the  $\dot{K}$ -dependence of  $T_{BDT}$ ; a linear variation of  $\ln(\dot{K})$  with  $1/T_{BDT}$  with a slope  $(\Delta E - \alpha K_{lc}\Omega)$  where  $\tau = \alpha K$  ( $\alpha$  is a geometrical factor). Thus, the present model suggests an approximate equivalence of the stress-dependent activation energy for dislocation nucleation,  $(\Delta E - \tau\Omega)$ , with  $U$ .

#### 4. CONCLUSION

It is proposed that deformation of semiconductors at low temperatures ( $T < T_c$ ) takes place by the nucleation and glide of single leading partials dragging a stacking fault behind them. This, together with the low mobility of the partial dislocations at low temperatures, gives rise to very limited plasticity. Also, the very limited shielding of crack tips results in a brittle behaviour at temperatures below  $T_c$ . Above the critical temperature,  $T_c$ , both partials can be nucleated and deformation of the semiconductor takes place by the glide of total dislocations. In this case, plasticity is extensive and, provided that the dislocations are sufficiently mobile, crack tips can be shielded resulting in a ductile behaviour.

#### ACKNOWLEDGEMENTS

This work was supported by grant number FG02-93ER45496 from the DoE and subcontract number 95-SPI-420757-CWRU from the SiC Consortium. Thanks are due to Dr. Calvin Carter, Jr. (of Cree Research, Inc.) and Dr. Don Hobgood (previously of Northrop-Grumman) for providing single-crystal samples of 6H-SiC and 4H-SiC, respectively.

#### REFERENCES

- Brede, M and Haasen, P, 1988, *Acta Metall.*, **36**, 2003-2018.
- Brochard, S, Junqua, N and Grilhé, J, 1998a, *Phil. Mag. A*, **77**, 911-922.
- Brochard, S, Rabier, J and Grilhé, J, 1998b, *Eur. Phys. J. - AP*, **2**, 99-105.
- Hirsch, P B and Roberts, S G, 1991, *Phil. Mag. A*, **64**, 55-80.
- Hirsch, P B, Roberts, S G and Samuels, J, 1989, *Proc. R. Soc. Lond. A*, **421**, 25-53.
- Lin, I-H and Thomson, R, 1986, *Acta Metall.*, **34**, 187-206.
- Michot, G, 1988, *Crystal Properties and Preparation*, **17-18**, 55.
- Michot, G and George, A, 1989, *Inst. Phys. Conf. Ser.*, **104**, 385-396.
- Ning, X J and Pirouz, P, 1996, *J. Mater. Res.*, **11**, 884-894.
- Pirouz, P, Samant, A, Hong, M, Moulin, A and Kubin, L, 1999, *J. Mater. Res.* In press.
- Rice, J R and Thomson, R, 1974, *Phil. Mag.*, **29**, 73-97.
- Samant, A V, Ph.D. thesis, Case Western Reserve University (1999).
- Samuels, J and Roberts, S G, 1989, *Proc. R. Soc. Lond. A*, **421**, 1-23.
- Suzuki, T, Nishisako, T, Taru, T and Yasutomi, T, 1998, *Phil. Mag. Lett.*, **77**, 173-180.
- Suzuki, T, Yasutomi, T, Tokuoka, T and Yonenaga, I, 1999b, *Phil. Mag. A*, In press.
- Suzuki, T, Yasutomi, T, Tokuoka, T and Yonenaga, I, 1999a, *phys. stat. sol. (a)*, **171**, 47.

## DEFORMATION-INDUCED DISLOCATIONS IN 4H-SiC AND GaN

M. H. HONG\*, A. V. SAMANT\*, V. ORLOV\*, B. FARBER\*, C. KISIELOWSKI\*\*,  
P. PIROUZ\*

\*Department of Materials Science and Engineering, Case Western Reserve University,  
Cleveland, OH, 44106-7204.

\*\*Lawrence Berkeley Laboratory, Berkeley, CA.

### ABSTRACT

Bulk single crystals of 4H-SiC have been deformed in compression in the temperature range 550-1300°C, whereas a GaN thin film grown on a (0001) sapphire substrate was deformed by Vickers indentation in the temperature range 25-800°C. The TEM observations of the deformed crystals indicate that deformation-induced dislocations in 4H-SiC all lie on the (0001) basal plane but depending on the deformation temperature, are one of two types. The dislocations induced by deformation at temperatures above ~1100°C are complete, with a Burgers vector, **b**, of  $\frac{1}{3}\langle 11\bar{2}0 \rangle$

but are all dissociated into two  $\frac{1}{3}\langle 10\bar{1}0 \rangle$  partials bounding a ribbon of stacking fault. On the other hand, the dislocations induced by deformation in the temperature range 550<T<~1100°C were predominantly single leading partials each dragging a stacking fault behind them. From the width of dissociated dislocations in the high-temperature deformed crystals, the stacking fault energy of 4H-SiC has been estimated to be  $14.7 \pm 2.5 \text{ mJ/m}^2$ . Vickers indentations of the [0001]-oriented GaN film produced a dense array of dislocations along the three  $\langle 11\bar{2}0 \rangle$  directions at all temperatures. The dislocations were slightly curved with their curvature increasing as the deformation temperature increased. Most of these dislocations were found to have a screw nature with their **b** parallel to  $\langle 11\bar{2}0 \rangle$ . Also, within the resolution of the weak-beam method, they were not found to be dissociated. Tilting experiment show that these dislocations lie on the  $\{1\bar{1}00\}$  prism plane rather than the easier (0001) glide plane.

### INTRODUCTION

SiC, GaN, and alloys of the latter, are wide bandgap semiconductors showing considerable promise for high-temperature and optoelectronic applications [1,2]. Recent advances in crystal growth have resulted in the production of single-crystal, single polytype, SiC boules [3] and very-nearly single crystalline GaN thin films [2]. In spite of their widespread interest, the deformation behavior and microstructure of these materials have not been studied in sufficient detail.

The most common polytypes of SiC are 6H and 4H; these are now produced commercially in boule form and are available as wafers. The stable ambient form of GaN has a 2H structure, and thin films of the metastable 3C (cubic) polytype can also be grown by CVD on certain substrates. All the polytypes of SiC and GaN are tetrahedrally coordinated and consist of two variants of a basic tetrahedron: normal, *T*, and twinned, *T'*; each of these variants can occupy three spatial positions, *T*<sub>1</sub>, *T*<sub>2</sub>, and *T*<sub>3</sub> (or *T'*<sub>1</sub>, *T'*<sub>2</sub>, and *T'*<sub>3</sub>) (for details, see, e.g. [4, 5]). They predominantly exhibit hexagonal symmetry, denoted by H in the Ramsdell notation [6], e.g. 2H (wurtzite), 4H, 6H or, in general, 2*n*H (where *n* is an integer), or rhombohedral symmetry, denoted by R in the Ramsdell notation, e.g. 15R or, in general, (2*n*+1)R. The 3C (zincblende) polytype is a subset of the rhombohedral polytypes and is unique in that it consists of only one tetrahedral variant (either all normal, *T*, or all twinned, *T'*, tetrahedra) and additionally exhibits cubic (C) symmetry. Fig. 1 shows the  $\langle 11\bar{2}0 \rangle$  projected structure of 4H-SiC and 2H-GaN with tetrahedral sequences ...*T*<sub>1</sub>*T*<sub>2</sub>*T'*<sub>1</sub>*T'*<sub>2</sub>... (periodicity of four) and ...*T*<sub>1</sub>*T'*<sub>1</sub>... (periodicity of two), respectively. The structure of each polytype can also be considered in terms of stacking of widely-spaced double planes  $\alpha A$ ,  $\beta B$  and  $\gamma C$  where  $\alpha$ ,  $\beta$ ,  $\gamma$  represent basal planes of carbon or nitrogen (silicon or gallium) atoms and *A*, *B*, and *C* represent interleaved parallel planes consisting of silicon or gallium (carbon or nitrogen) atoms. Thus, the structure of 4H-SiC and 2H-GaN may also be

369

Mat. Res. Soc. Symp. Proc. Vol. 572 © 1999 Materials Research Society

described in terms of the stacking sequences  $\dots\alpha A\beta B\alpha A\gamma C\dots$  and  $\dots\alpha A\gamma C\dots$ , respectively. Note that all SiC and GaN polytypes are polar along the c-axis: the  $[0001]$  direction is distinct from the opposite  $[000\bar{1}]$  direction.

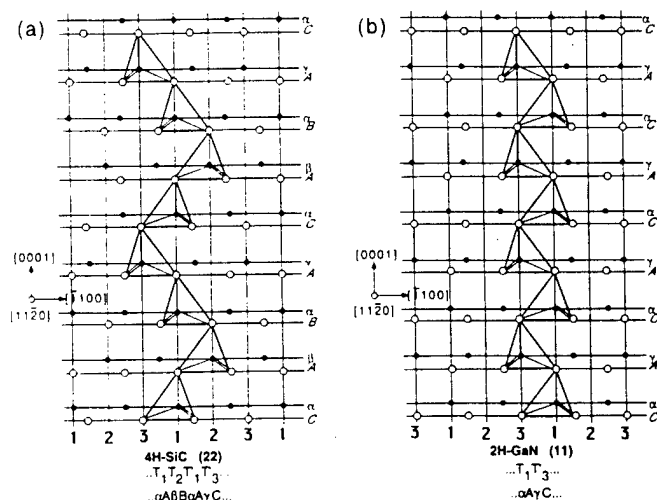


Fig. 1. The structure of (a) 4H-SiC and (b) 2H-GaN

The aim of this work is to investigate the deformation-induced microstructure of bulk 4H-SiC single crystals and a 2H-GaN thin film as a function of temperature using transmission electron microscopy (TEM). The dislocation structure is discussed based on the differences in the core structure of partials as well as the slip planes on which the dislocations lie.

## EXPERIMENTAL PROCEDURES

The bulk 4H-SiC single crystals used in this study were grown by the modified sublimation technique [3]. Parallelepiped specimens with nominal dimensions  $2\times 2\times 4\text{ mm}^3$  were oriented and cut for single glide such that one pair of their lateral faces was parallel to  $\{1\bar{1}00\}$ , and the  $(0001)$  basal plane made an angle of  $45^\circ$  with respect to the compression axis. The samples were compressed at  $550\text{--}1300^\circ\text{C}$  in ultra-high purity argon to a strain of  $\sim 4\text{--}6\%$ . On the other hand, the GaN film was grown by molecular beam epitaxy (MBE) on a  $(0001)$  sapphire substrate and was deformed by Vickers indentation in the temperature range  $25\text{--}800^\circ\text{C}$ . The indentation diagonals were aligned along the  $\langle 11\bar{2}0 \rangle$  and  $\langle 1\bar{1}00 \rangle$  directions on the  $(0001)$  surface of the film. From the deformed samples,  $0.3\text{ mm}$  thick slices parallel to  $(0001)$  plane were sectioned with a diamond wheel cutter. Subsequently, the slices were ground with emery paper to a thickness of  $\sim 100\text{ }\mu\text{m}$ , then dimpled to a thickness of  $\sim 20\text{ }\mu\text{m}$ , and ion-milled to electron transparency at a voltage of  $5\text{ kV}$  at an angle of  $\sim 15^\circ$ . GaN thin films were prepared by back-side thinning with the foil surface normal to the  $[0001]$  direction from the sapphire substrate side. The thin TEM foils were examined in a Philips CM20 electron microscope operating at an accelerating voltage of  $200\text{ kV}$ .

## RESULTS AND DISCUSSION

The easy slip plane of hexagonal and rhombohedral polytypes is (0001) and the dislocations have a perfect  $\mathbf{b} = 1/3\langle 11\bar{2}0 \rangle$  Burgers vector [7]. As in other tetrahedrally-coordinated structures, these dislocations are dissociated into two partials with Burgers vectors  $\mathbf{b}_l = 1/3\langle 10\bar{1}0 \rangle$  and  $\mathbf{b}_t = 1/3\langle 01\bar{1}0 \rangle$ , where the subscripts  $l$  and  $t$  denote the leading and trailing partials, respectively. The dislocations dissociate as follows:

$$1/3\langle 11\bar{2}0 \rangle = 1/3\langle 10\bar{1}0 \rangle + 1/3\langle 01\bar{1}0 \rangle$$

In tetrahedrally coordinated compounds, because of the polarity along the [0001] axis, the core of the perfect or partial basal dislocations consists of only one species, i.e. silicon (gallium) or carbon (nitrogen), and, because the partial dislocations belong to the glide plane, they are denoted as Si(g) [Ga(g)] or C(g) [N(g)] [8].

### 4H-SiC

Fig. 2 shows typical bright-field (BF) micrographs of 4H-SiC deformed in compression. Both micrographs in this figure were obtained using the  $\mathbf{g} = \bar{1}01\bar{1}$  reflection near the  $[\bar{1}012]$  zone axis. Samant [9] has recently shown that plastic deformation of 4H-SiC above  $\sim 1100^\circ\text{C}$  takes place by the activation of the (0001) $\langle 11\bar{2}0 \rangle$  slip system with the uncorrelated motion of partial dislocations. This is clearly shown in Fig. 2(a) where dissociated dislocations, consisting of a pair of leading/trailing partials bounding a ribbon of intrinsic stacking fault, are observed. Standard strain contrast experiments indicate that, as expected, the Burgers vectors of the partials are, respectively, parallel to  $\langle 1\bar{1}00 \rangle$  and  $\langle 10\bar{1}0 \rangle$  directions.

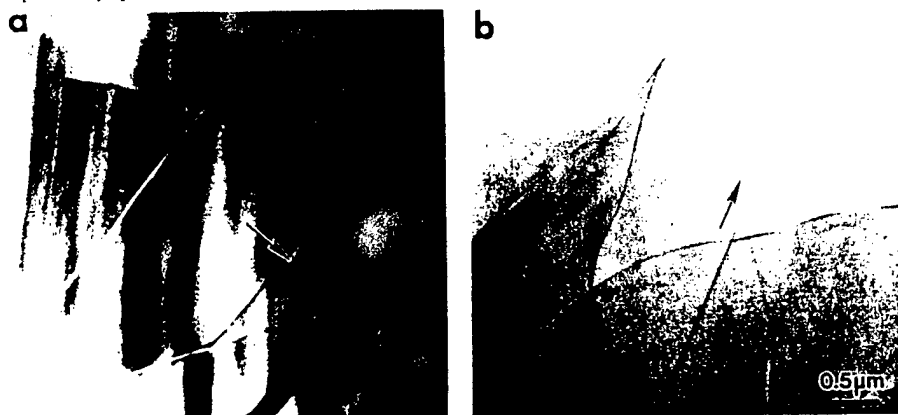


Fig. 2. TEM micrograph of 4H-SiC deformed in compression (a) at  $1300^\circ\text{C}$  and (b) at  $700^\circ\text{C}$

From the width of partial separation, the stacking fault energy of 4H-SiC has been estimated to be  $14.7 \pm 2.5 \text{ mJ/m}^2$ ; this value is nearly five times larger than that ( $2.9 \pm 0.5 \text{ mJ/m}^2$ ) of 6H-SiC obtained by the same techniques [10].

Fig. 2(b) shows a BF micrograph of dislocations induced by deformation at  $700^\circ\text{C}$ . In this case, the microstructure is dominated by single leading partials without the associated trailing partials; each partial drags a stacking fault. The Burgers vectors of the single leading partials are all parallel to the  $\langle 1\bar{1}00 \rangle$  directions, and LACBED experiments on three different segments have shown that they have a silicon core (i.e. they are Si(g) partials) [11]. Thus, it appears that in the 4H-SiC single crystals, deformation proceeds by nucleation and glide of single leading Si(g) partials at low-temperatures ( $< \sim 1100^\circ\text{C}$ ), whereas it proceeds by the generation and glide of total, although dissociated, dislocations at high temperatures ( $> \sim 1100^\circ\text{C}$ ). It has already been argued

[12] that only the leading partials, with a silicon core, nucleate at low temperatures ( $< \sim 1100^\circ\text{C}$ ), and a higher temperature ( $> \sim 1100^\circ\text{C}$ ) is required to nucleate the associated carbon-core trailing partials whereby the glide of leading/trailing pairs (i.e., dissociated dislocations) will carry out the plastic deformation: at a certain applied shear stress, the activation barrier for nucleation of trailing partials is higher than that of the leading partials. Since the formation of the same partial dislocation from the same source cannot occur more than once on the same glide plane, plastic deformation of the crystal can take place to a very limited extent at low temperatures. On the other hand, once thermal activation is sufficient to from the trailing partial, repeated dislocation multiplication can take place from the same source on the same planes, and plastic deformation will proceed by the glide of total dislocations. At these temperatures, the crystal will be ductile and large strains are obtained [12].

## 2H-GaN

Fig. 3 shows a (a) plan-view and (b) cross-sectional micrograph of the as-grown GaN specimen (before deformation). As shown by various authors (see, e.g., [13, 14]) there is a high density of threading dislocations in such films: some are those connected to misfit dislocation segments, and some generated to accommodate the tilt and twist misorientation of neighboring domains in the granular structure of the film. The plan-view micrograph in Fig. 3(a), with the inserted  $[0001]$  SADP, shows the typical cell structure of the film with the grain boundary dislocations defining the cell boundaries. They are mostly aligned along the  $\langle 11\bar{2}0 \rangle$  directions that are the Peierls valleys in non-cubic tetrahedrally-coordinated crystals. The cross-sectional micrograph in Fig. 3(b) shows that the thickness of the GaN film deposited on the  $(0001)$  sapphire substrate is approximately  $2\ \mu\text{m}$ . The dislocations in this micrograph are mostly parallel to the  $c$ -axis, i.e., to the growth direction. Standard  $g \cdot b = 0$  invisibility criterion shows that most of the dislocations are  $a$ -type edge dislocations with a Burgers vector parallel to the  $[11\bar{2}0]$  direction. The SADP obtained from an aperture covering both the 2H-GaN and the sapphire substrate shows the orientation relationship to be  $[11\bar{2}0]_{\text{GaN}} // [1100]_{\text{sap}}$ ,  $(1\bar{1}00)_{\text{GaN}} // (11\bar{2}0)_{\text{sap}}$ .

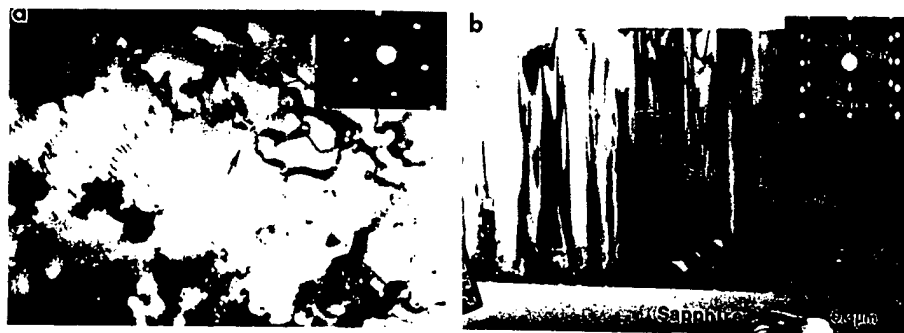


Fig. 3. (a) plan-view and (b) cross-sectional micrograph of the as-grown 2H-GaN.

Fig. 4 shows micrographs taken under different reflections from the same region of a specimen indented at  $450^\circ\text{C}$ . From these, and micrographs taken under other reflections, the Burgers vectors of dislocations were determined. Practically all the dislocations appear under reflections of the type  $g = 11\bar{2}0$  shown in Fig. 4(a). In this micrograph, the short segments are projections of threading dislocations (lying along the  $c$ -axis) in the film, while the dislocations denoted by symbols A and B, aligned along the  $\langle 11\bar{2}0 \rangle$  directions, are newly-generated (presumably by indentation) dislocations that are parallel to the  $(0001)$  plane of the film. Dislocations denoted by A are in contrast when imaged with reflections of the type  $g = 1\bar{1}00$  (Fig. 4(b)), while they are out of contrast when imaged with reflections of the type  $g = 1010$  (Fig. 4(c)). On the other hand, dislocations denoted by B are out of contrast when imaged with reflections of

the type  $g = \bar{1}100$  (Fig. 4(b)) and are in contrast with reflections of the type  $g = \bar{1}010$  (Fig. 4(c)). These and other micrographs indicate that dislocations A and B have Burgers vectors parallel to  $[11\bar{2}0]$  and  $[1\bar{2}10]$  directions, respectively. Since the line directions of dislocations A and B are parallel to their Burgers vectors, it is concluded that all the indentation-induced dislocations have a perfect screw character.

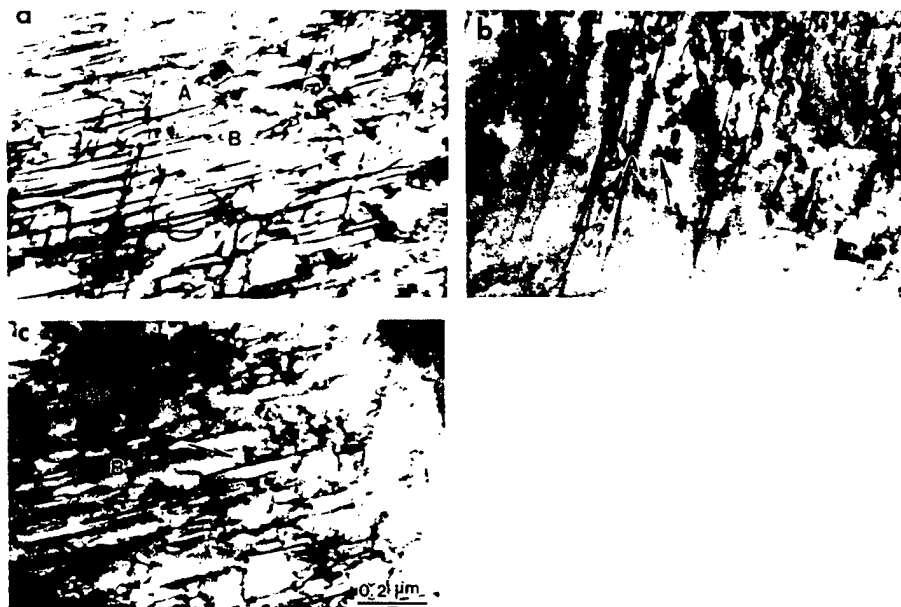


Fig. 4. TEM micrograph of a 2H-GaN indented at 450°C; imaged by reflection (a)  $g = 11\bar{2}0$ , (b)  $g = 1100$  and (c)  $g = 1010$

Since two different polytypes (2H and 3C) have often been observed in GaN, it would be expected that this material has a relatively low stacking fault energy and, consequently, that, as in 4H-SiC, all the basal dislocations in the GaN film would be dissociated into two partials. Indeed, recent weak-beam TEM of GaN powder deformed by pulverization shows that basal dislocations in this material are dissociated into two partials with a width of 3-8 nm, corresponding to a stacking fault energy of  $\sim 20 \text{ mJ/m}^2$  [15]. However, this is not the case in the present experiments: despite many attempts using the weak beam technique of TEM, no evidence of dissociation was found for any of the dislocations in the deformed film that were parallel to the basal plane. An example is shown in Fig. 5 which is a  $g/3g$  weak-beam micrograph (with  $g = 11\bar{2}0$ ) from a GaN film indented at 300°C; all the dislocations appear as single lines and not as pairs.

One possibility for the non-dissociation of basal  $1/3\langle 11\bar{2}0 \rangle$  screw dislocations in Fig. 4 could be that they actually lie on the  $\{1\bar{1}00\}$  prism planes. Unlike the basal plane, the stacking fault energy on the prism planes is quite likely very high and the perfect dislocations, if dissociated at all on these planes, would have a small dissociation width (less than the resolution of the weak beam technique,  $\sim 2.5 \text{ nm}$ ). In order to check for this, extensive tilting experiments were carried out in the microscope and the changes in the shapes of individual kinked dislocations were noted with tilting. Figure 6 shows a typical example observed with the incident beam (a) nearly normal (tilted by  $\sim 5^\circ$ ) to the basal plane and (b) after tilting the foil approximately  $35^\circ$  away from position (a). Care was taken that the same region of the foil was imaged during the tilt. In (a), a super-kink pair is arrowed on an otherwise straight dislocation. In Fig. (b), the same super-kink pair has widened considerably after the foil has been tilted by  $\sim 35^\circ$  about the  $\langle 11\bar{2}0 \rangle$  axis. This clearly



indicates that the dislocation is not lying on the basal plane (in which case, the super-kink pair would have shrunk with the tilt) and the results are consistent with the fact that it lies on the prism plane. This sort of experiment was performed on five? kinked dislocation segments lying parallel to the basal plane and, in all cases, the dislocations were found to lie on one of the three  $\{1\bar{1}00\}$  prism planes.

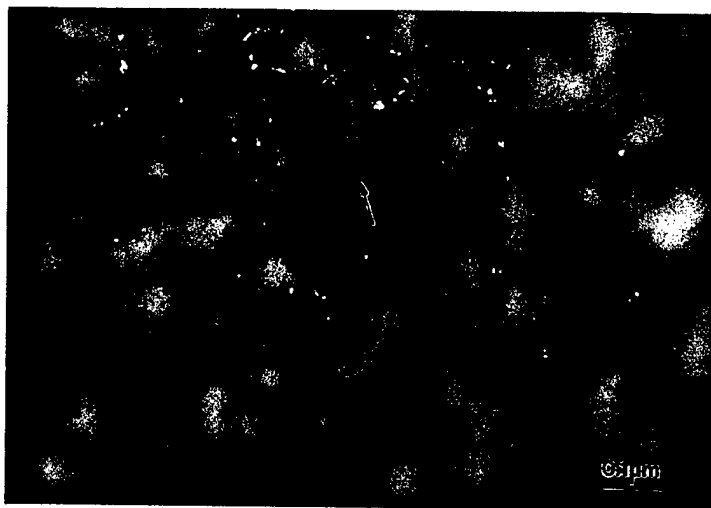


Fig. 5. Weak-beam TEM micrograph of the 2H-GaN deformed at 300°C using reflection  $g = 1\bar{1}\bar{2}0$  close to the  $[0001]$  zone axis

Two possibilities may account for these unexpected results. Under the complex stress field of the indentation, the  $1/3\langle 1\bar{1}\bar{2}0 \rangle$  screw dislocations may have nucleated on  $(0001)$  basal planes, where they would be dissociated; subsequently, they could have cross-slipped onto the prism planes by the Friedel-Escaig mechanism. More likely, however, the deformation-induced dislocations were probably nucleated on the prism planes from the sample surface because of large shear stresses on these planes induced by the indentation.

## CONCLUSIONS

The deformation-induced dislocations in 4H-SiC are all basal dislocations and are divided into two types. For deformations performed above  $\sim 1100^\circ\text{C}$ , the dislocations are predominantly dissociated perfect dislocations, while in crystals deformed below  $\sim 1100^\circ\text{C}$ , the dislocations are predominantly single leading partials without their corresponding trailing partials. From the width of the dissociated dislocations, the stacking fault energy of 4H-SiC has been estimated to be  $14.7 \pm 2.5 \text{ mJ/m}^2$ .

In the GaN film, Vickers indentation produced a dense array of dislocations on the  $\{1\bar{1}00\}$  prism planes; these dislocations lie along the three  $\langle 1\bar{1}\bar{2}0 \rangle$  Peierls valleys on these planes. Most of these dislocations were found to have a screw character and, because of the high stacking fault energy on the prism planes, they were not dissociated.

## ACKNOWLEDGEMENTS

This work was supported by grant number FG02-93ER45496 from the Department of Energy, and subcontract number 95-SPI-420757-CWRU from the Silicon Carbide consortium.

Thanks are due to Dr. Don Hobgood (previously of Northrop-Grumman) for providing a single crystal of 4H-SiC.

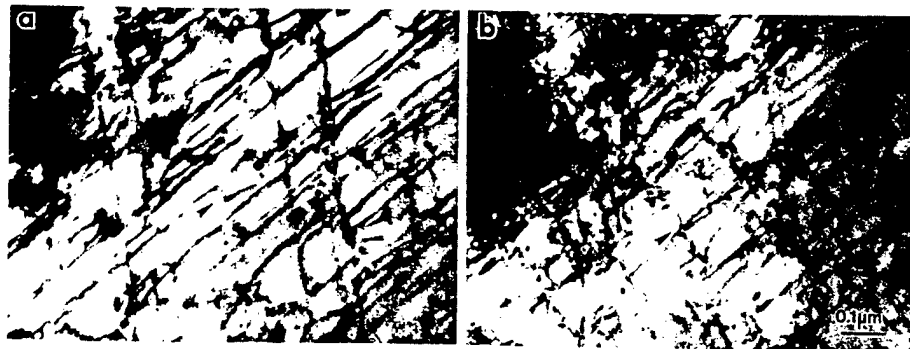


Fig. 6. TEM micrograph of deformed 2H-GaN (a) before and (b) after tilting around the  $[11\bar{2}0]$  axis

## REFERENCES

1. W. J. Choyke, H. Matsunami and G. Pensl (edited), *Silicon Carbide, A Review of Fundamental Questions and Applications to Current Device Technology*, (Akademie Verlag GmbH Volume I and II, Berlin, 1997).
2. S. Nakamura and G. Fasol, *The Blue Laser Diode*, (Springer-Verlag, Berlin-Heidelberg, 1997).
3. Y. M. Tairov and V. F. Tsvetkov, *J. Crystal Growth* **43**, 209-212 (1978).
4. P. Pirouz and J. W. Yang, *Ultramicroscopy* **51**, 189-214 (1993).
5. P. Pirouz, *Solid State Phenomena* **56**, 107-132 (1997).
6. L. S. Ramsdell, *Am. Mineralogist* **32**, 64-82 (1947).
7. P. Pirouz, "Extended Defects in SiC and GaN Semiconductors", in *Proceedings of the International Conference on Silicon Carbide, III-Nitrides and Related Materials*, edited by G. Pensl, H. Morkoç, B. Monemar and E. Janzén (Trans Tech Publications Ltd. **264-268**, Zurich, Switzerland, 1998), pp. 399-408.
8. H. Alexander, P. Haasen, R. Labusch and W. Schröter, Foreword to *J. Phys. (Paris)* **40**, Colloque C6 (1979).
9. A. V. Samant, *Effect of Test Temperature and Strain-Rate on the Critical Resolved Shear Stress of Monocrystalline Alpha-SiC*, Ph.D. Thesis, Case Western Reserve University, 1999.
10. M. H. Hong, A. V. Samant and P. Pirouz, *Phil. Mag. A* (1999). In press.
11. X. J. Ning and P. Pirouz, *J. Mater. Res.* **11**, 884-894 (1996).
12. P. Pirouz, A. V. Samant, M. H. Hong, A. Moulin and L. P. Kubin, *J. Mater. Res.* (1999). In press.
13. B. Heying, X. H. Wu, S. Keller, Y. Li, D. Kapolnek, B. P. Keller, S. P. Denbaars and J. S. Speck, *Appl. Phys. Lett.* **68**, 643-645 (1996).
14. X. J. Ning, F. R. Chien, P. Pirouz, J. W. Yang and M. Asif Khan, *J. Mater. Res.* **11**, 580-592 (1996).
15. S. Takeuchi and K. Suzuki, *Phil. Mag. Lett.* (1999). In press.

# On temperature dependence of deformation mechanism and the brittle-ductile transition in semiconductors

P. Pirouz,<sup>a)</sup> A.V. Samant, and M.H. Hong

*Department of Materials Science and Engineering, Case Western Reserve University,  
Cleveland, Ohio 44106-7204, U.S.A.*

A. Moulin and L.P. Kubin

*LEM, CNRS-ONERA, B.P. 72, 29, Av. de la Division Leclerc, 92322 Châtillon Cedex, France*

(Received 19 October 1998; accepted 5 April 1999)

Recent deformation experiments on semiconductors have shown the occurrence of a break in the variation of the critical resolved shear stress of the crystal as a function of temperature. These and many other examples in the literature evidence a critical temperature at which a transition occurs in the deformation mechanism of the crystal. In this paper, the occurrence of a similar transition in two polytypes of SiC is reported and correlated to the microstructure of the deformed crystals investigated by transmission electron microscopy, which shows evidence for partial dislocations carrying the deformation at high stresses and low temperatures. Based on these results and data in the literature, the explanation is generalized to other semiconductors and a possible relationship to their brittle-ductile transition is proposed.

## I. INTRODUCTION

The plastic deformation of semiconductors has been the subject of many studies, leading to a large amount of experimental data. It is generally agreed that the mobility of dislocations in these crystals is governed by the Peierls mechanism and can be described by kink pair nucleation and migration.<sup>1-4</sup> The kink diffusion model<sup>5</sup> has thus provided a basis for rationalizing the experimental results. This mechanism results in a strong temperature dependence of the flow stress, which has been mainly studied for temperatures above the brittle-ductile transition (BDT) temperature,  $T_{BDT}$ .

In addition to deformation behavior, the BDT of elemental and compound semiconductors has also been extensively studied, particularly in the case of silicon<sup>6-9</sup> where it has been found to be very sharp for dislocation-free crystals and to extend over a temperature range of up to about 200 °C in crystals initially containing dislocations.<sup>10</sup> In general, an important feature of the BDT temperature is that it sensitively depends on the strain rate<sup>11</sup> and, in semiconductors, this dependence has the same activation energy as the one associated with dislocation mobility (for a review, see George<sup>12</sup>). This has led to several models that relate the BDT to the mobility of the dislocations emitted by sources located at,<sup>7,13</sup> or close to,<sup>9,10</sup> the crack tip.

The lower temperature limit (set by the onset of brittle fracture) for experimental studies of the plastic behavior

of semiconductors can be bypassed under certain experimental conditions, for instance, by prestraining the specimen (which provides a supply of dislocations and enhances the plasticity of the crystal at low temperatures) and/or by using a confining pressure (that counteracts and reduces the tensile stresses at the crack tips). In addition, the lower the strain rate, the easier it is to initiate thermally-activated processes such as dislocation nucleation and glide, and the easier it is to perform deformation experiments at lower temperatures. These conditions have been employed by researchers to study the deformation behavior of several semiconductors over a wide temperature range below the BDT. As shown in Sec. II, these experiments have revealed a transition between two deformation regimes, characterized by a break in the temperature dependence of the yield stress. The experimental results on SiC reported here, as well as results on other semiconductors from the literature, seem to indicate that this break occurs at a temperature close to the  $T_{BDT}$ .

In parallel, transmission electron microscopy (TEM) observations of the dislocation microstructure in deformed semiconductors have provided evidence for a different transition. In Sec. III, it is shown that in SiC and in other elemental or compound semiconductors, partial dislocations may be responsible for the plastic strain rate at low temperatures, approximately below  $T_{BDT}$ . This is in contrast with the usual high-temperature behavior where both partials constituting total (perfect) dislocations are mobile under stress, and the latter are responsible for plastic deformation of the crystal.

<sup>a)</sup>e-mail: pirouz@cwmsd.mse.cwru.edu

Compared to the low-stress/high-temperature regime, the influence of two other factors on the dissociation state of perfect dislocations is enhanced in the high-stress/low-temperature regime. The first factor is the different resolved shear stresses on the  $\frac{1}{6}\langle 11\bar{2} \rangle$  Shockley partials of a  $\frac{1}{2}\langle 1\bar{1}0 \rangle$  perfect dislocation (or  $\frac{1}{3}\langle 10\bar{1}0 \rangle$  partials of a  $\frac{1}{3}\langle 11\bar{2}0 \rangle$  dislocation in hexagonal/rhombohedral crystals), which, under certain favorable orientations, induce an increase of the splitting width—an effect sometimes known as the “Escaig effect.”<sup>14,15</sup> The second factor that is enhanced at low temperatures is any difference in the intrinsic mobility of the leading and trailing partials (say, due to their different core structures); this also can result in a widening or shrinking of the stacking fault width. Although there is experimental evidence for such effects, as discussed in Sec. IV, they have not been modeled to date.

The objective of the present paper is to suggest a model that identifies the three transitions mentioned above and explains both the break in the stress/temperature curves and the BDT in terms of a transition in the nature of the mobile dislocations, total or partial. This model is presented in Sec. IV. Several arguments supporting it, and discrepancies to be clarified, are discussed in the concluding section.

## II. EXPERIMENTAL EVIDENCE FOR A BREAK IN THE STRESS-TEMPERATURE PLOTS

In general, a plot of the critical resolved shear stress,  $\tau_y$ , as a function of absolute temperature,  $T$ , in semicon-

ductors follows a variation shown schema Fig. 1(a). As shown in this figure, the extrapolation curve to 0 K gives the Peierls stress,  $\tau_p$ , for the under consideration. The shape of this  $\tau_y(T)$  has been widely discussed by Suzuki and coworkers on the basis of the Peierls mechanism. These authors state that the  $\tau_y(T)$  of all the tetrahedrally coordinated materials lies on a universal normalized plot of  $\tau_y/kT/Gb^3$ , where  $G$  is the shear modulus and  $b$  is the magnitude of the Burgers vector of dislocations in the material.

A different way to represent the variations of the critical resolved shear stress of the semiconductor with respect to temperature is to plot  $\ln(\tau_y)$  versus  $1/T$ , as suggested by the Arrhenius model. In this case, Orówan's equation for the plastic strain rate,  $\dot{\gamma}$ , gives a linear plot with a slope that is proportional to the stress-independent activation enthalpy,  $H$ , for the glide of dislocations responsible for crystal deformation. Specifically:

$$\ln \tau_y = \frac{H}{nkT} + \frac{1}{n} [\ln \dot{\gamma} - \ln A],$$

where  $n$  is related to the stress exponent of the dislocation velocity and  $A$  is a constant (see, Ref. 4).

Recently Suzuki *et al.*<sup>19</sup> have plastically deformed single crystals under confining pressure for a range of temperatures from ~500 K down to ~50 K. The BDT temperature,  $T_{BDT}$ , of InP is typically around 100 K (a value that is sensitive to strain rate and initial dislocation density), most of the new measurements confirm the plasticity of InP in the brittle regime: previous

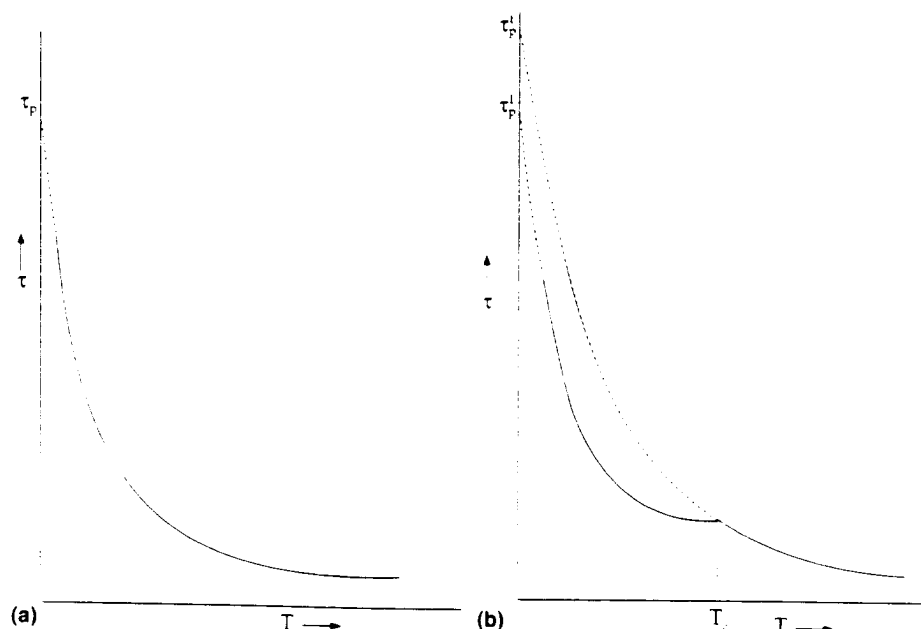


FIG. 1. Schematic variation of the critical resolved shear stress,  $\tau_y$ , with temperature,  $T$ . (a) The usual plot reported for semiconductors.  $\tau_p$  is obtained by extrapolation to  $T = 0$  K. (b) The plot of new measurements showing a break in the curve at a critical temperature,  $T_c$ . Extrapolation to  $T = 0$  K gives two Peierls stresses,  $\tau_p^1$  and  $\tau_p^2$ .

urements, e.g., those of Gall *et al.*,<sup>20</sup> were all done under atmospheric pressure in the ductile regime. The significant point about the data of Suzuki *et al.*<sup>19</sup> is the appearance of a break at a critical temperature,  $T_c$  ( $\approx 420$  K) in the  $\tau_y(T)$  plot and the near coincidence of this point with the BDT of the material. Such a break is shown schematically in Fig. 1(b) with extrapolation of each section of the curve to two new values of Peierls stress, denoted as  $\tau_p^l$  and  $\tau_p^h$ .

Similar results have been presented more recently for GaAs and InSe<sup>21,22</sup> with breaks in their  $\tau_y(T)$  plots at critical temperatures,  $T_c$ , also close to the BDT temperature of these materials. For all three of the crystals (InP, GaAs, and InSe) deformed by Suzuki *et al.*,<sup>22</sup> there are also changes of slope in the  $\ln(\tau_y)$  versus  $1/T$  plots at the same temperatures,  $T_c$ , at which there are breaks in the  $\tau_y(T)$  plots. The different slopes of the  $\ln \tau_y(1/T)$  plots on the two sides of the transition thus correspond to two different activation enthalpies,  $H_i$  and  $H_j$ , for dislocation glide in the high-temperature ( $T > T_c$ ) and low-temperature ( $T < T_c$ ) regimes, respectively.

Plastic deformation of two wide band gap semiconductors, 4H- and 6H-SiC, in the temperature range 550–1300 °C at a slow strain rate ( $\sim 10^{-4}$  s<sup>-1</sup>) also exhibits a break at a temperature  $T_c$  in their  $\tau_y(T)$  plots and a corresponding change in the slope of their  $\ln(\tau_y)$  versus  $1/T$  plots [Figs. 2(a) and 2(b)].<sup>23–25</sup> In the two linear regimes of these figures, the slope of the straight lines is different with the high-temperature regime ( $T > T_c$ ), giving a larger activation energy for dislocation glide as compared to the low-temperature regime ( $T < T_c$ ).<sup>24,25</sup> From Fig. 2, the breaks in the  $\ln \tau_y(1/T)$  plots of 4H-SiC and 6H-SiC are at  $T_{cl}^{4H} \approx T_{cl}^{6H} \approx 1100 \pm 100$  °C, which is close to the BDT of these two materials.

Looking back in the literature for deformation data of semiconductors, one comes across other  $\tau_y(T)$  data that appear to show a break, or change of slope, at (or close to) the BDT of the material. Thus, inspection of the  $\tau_y(T)$  data of intrinsic ( $10^{13}$  cm<sup>-3</sup> phosphorus-doped) silicon given by Castaing *et al.*<sup>26</sup> for the temperature range  $\sim 300$ – $1100$  °C (Fig. 2 of their paper) also clearly shows a break (change of slope) at  $T_c \approx 650$  °C close to the BDT of intrinsic silicon at the particular strain rate used in their experiments ( $2 \times 10^{-5}$  s<sup>-1</sup>). Similarly, Demenet<sup>27</sup> deformed Si under hydrostatic pressure in the range 350–550 °C and combined his data with literature values for higher temperatures ( $> 600$  °C) to obtain a  $\ln(\tau_y)$  versus  $1/T$  plot. Again, this plot shows a break at  $\sim 600$  °C, separating two linear regimes, one with a lower slope in the high-stress/low-temperature regime and the other with a higher slope in the low stress/high-temperature regime.

In the case of GaAs, as mentioned before, recent experiments of Suzuki *et al.*<sup>21,22</sup> show a clear change of slope in the  $\ln(\tau_y)$  versus  $1/T$  plot. However, as also

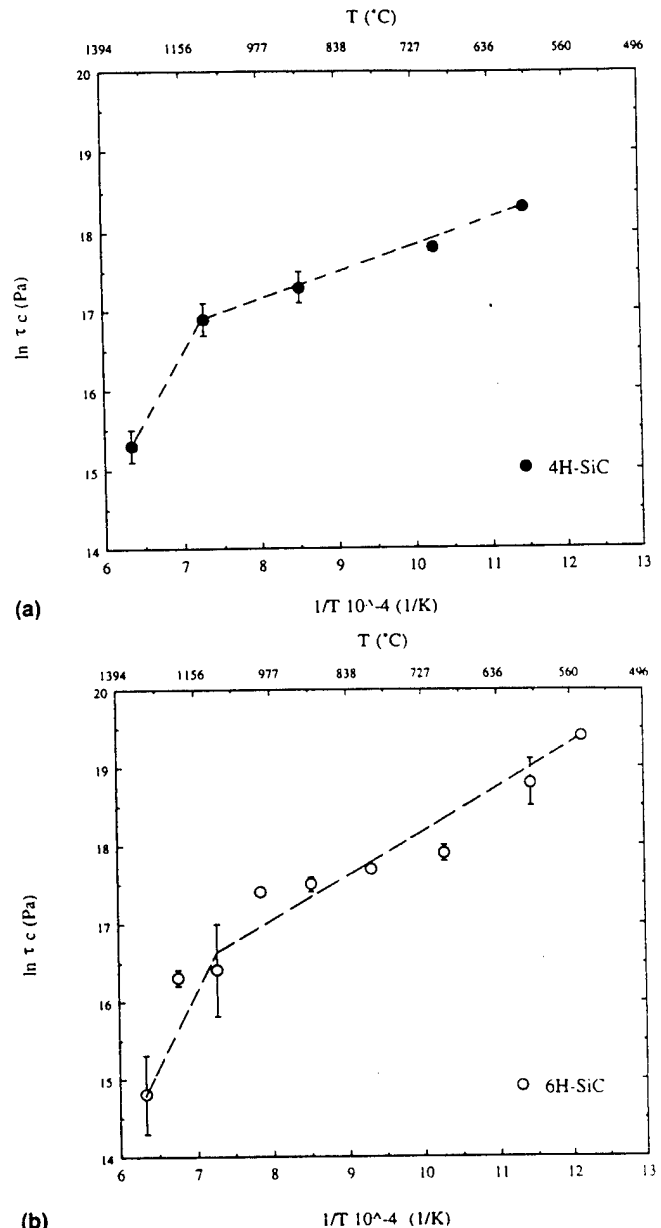


FIG. 2.  $\ln(\tau_y)$  versus  $1/T$  plots in (a) 4H-SiC and (b) 6H-SiC at a strain rate of  $\dot{\epsilon} \approx 1.3 \times 10^{-5}$  s<sup>-1</sup>. Note the change in slope of the linear plots at a critical temperature,  $T_c$  ( $\pm \Delta T$ ), and a critical stress.

noted,<sup>19</sup> even the earlier deformation experiments of Boivin *et al.*,<sup>28</sup> show a clear transition at a critical temperature,  $T_c \approx 400 \pm 20$  K, which is close to the BDT of GaAs. Thus, in Fig. 5 of the latter paper,<sup>28</sup> a distinct change of slope can be observed at this temperature. It is significant that, in this case (and also in the recent results of Suzuki *et al.*<sup>21,22</sup>), the activation energy for glide of dislocations [obtained from the slope of the  $\ln(\tau_y)$  versus  $1/T$  curve] above the transition temperature is appreciably higher than that for temperatures below  $T_c$ .

A break in the  $\tau_y(T)$  plot, or a change in the slope of  $\ln(\tau_y)(1/T)$  plot, very probably indicates a change in the deformation mechanism operating at temperatures below

and above  $T_c$ . Suzuki *et al.*<sup>19,21,22</sup> have suggested that the reason for the break in the  $\tau_y(T)$  curves of the three semiconductors that they have studied could be due to a change of the slip plane on which the dislocations glide. This is based on an earlier suggestion by Duesbery and coworkers<sup>29-32</sup> that at temperatures below the BDT, dislocations in semiconductors may belong to the shuffle set, whereas at temperatures above  $T_{BDT}$ , dislocations belong to the glide set. This is an unlikely possibility because extensive TEM studies on plastically deformed semiconductors have shown that, not only glide dislocations in all semiconductors are dissociated,<sup>33-35</sup> but also the lower the deformation temperature, the wider is the separation of partials of the dissociated dislocations, and the greater is the degree of uncorrelated kink nucleation and migration of the two partials.<sup>36</sup> It is also well known that it would be very difficult (and, energetically very costly) for shuffle dislocations to dissociate, and even more difficult for shuffle partials to move.<sup>2,37,38,32</sup>

### III. PARTIAL AND PERFECT DISLOCATIONS

#### A. Previous observations

The dominance of partial—rather than total—dislocations in the microstructure of low-temperature plastically deformed semiconductors can be seen in many works. Thus, preliminary TEM investigations of Castaing *et al.*<sup>26</sup> on [100] silicon crystals deformed in compression at low temperatures revealed a microstructure dominated by microtwins and extended stacking faults, indicating that the deformation was dominated by partial dislocation motion. This is consistent with the work of Wessel and Alexander<sup>39</sup> who deformed silicon under high stresses and low temperatures by a two-stage technique and investigated the resulting deformed material by TEM. The microstructure consisted of straight dissociated dislocations along  $\langle 110 \rangle$  Peierls valleys mostly with nonequilibrium dissociation widths. The same results were found by Boivin *et al.*<sup>28</sup> in *p*-type GaAs where, depending on the relative orientation of the compression axis with respect to the crystal, there was a high density of wide stacking faults and twins, indicating deformation by uncorrelated motion of partial deformations.

On the other hand, there are also reports of total dislocations dominating the microstructure of high-stress/low-temperature deformed semiconductors. Thus, Boivin *et al.*<sup>28</sup> found the microstructure of glide bands in intrinsic and *n*-type GaAs deformed at low temperatures to consist of *total* dislocations, mostly with a screw character and dissociated to their equilibrium separation. Similarly, in what appears to be a preliminary TEM investigation of one of their low-temperature (300 K) deformed InP crystals, Suzuki *et al.*<sup>19</sup> found the microstructure to be dominated by screw dislocations lying

along the  $\langle 110 \rangle$  Peierls valleys and dissociated to their equilibrium width (corresponding to a stacking fault energy of 15 mJ/m<sup>2</sup>). In addition, optical micrographs of the deformed sample side surfaces by the same authors showed profuse cross-slipping: a dislocation is able to cross-slip only when it is perfect and has a screw character. It should be noted, nevertheless, that, using the Escaig mechanism,<sup>14,15</sup> it can be shown that in compound semiconductors a dissociated screw dislocation segment can cross-slip if a fast partial trails a slow leading partial.<sup>40-42</sup> Similar results have been obtained by Branchu *et al.*<sup>43</sup> for low-temperature (between 20 and 200 °C) deformation of InSb. In this case, TEM investigation of the deformed crystals showed that at temperatures above ~50 °C, the dominant deformation mechanism was glide of total dislocations, while at room temperature, the deformation could be attributed to partial dislocations.

In general, then, TEM investigations of semiconductors deformed at low temperatures have shown the dominance of the microstructure by either perfect or partial dislocations, depending, apparently, on the orientation of the crystal with respect to the compression axis.<sup>44-46</sup> Thus, deformation of cubic crystals oriented for single glide ( $\langle 213 \rangle$  orientation), or those with  $\langle 110 \rangle$  orientation, produces a microstructure that is reportedly dominated by perfect dislocations, whereas in a deformed  $\langle 100 \rangle$ -oriented crystal the reported dislocations are predominantly single partials with, sometimes, a significant density of twin bands. Following Wessel and Alexander,<sup>39</sup> these results have been interpreted in terms of the orientation dependence of the different resolved shear stresses acting on the leading and trailing partial dislocations.<sup>44-46</sup> Calculation of the Schmid factors for the different Burgers vectors of the leading and trailing partials of a dissociated dislocation shows that for  $\langle 213 \rangle$  and  $\langle 110 \rangle$  orientations,  $\tau_l > \tau_r$ , whereas for the  $\langle 100 \rangle$  orientation,  $\tau_l > \tau_r$ , where  $\tau_l$  and  $\tau_r$  are the resolved shear stresses on the leading and trailing partials, respectively. This interpretation correctly explains the experimental results in the cases where the mobilities of the two partials are known (compare with Sec. IV. A).

#### B. TEM observations on SiC

In the case of 4H- and 6H-SiC, TEM investigations have been performed for crystals deformed below  $T_c$  (700 °C for 4H and 900 °C for 6H-SiC) and above  $T_c$  (1300 °C for both 4H-SiC and 6H-SiC). The results of these experiments are shown in Figs. 3 and 4; in both crystals, for deformations below  $T_c$ , the microstructure is dominated by a *single* leading partial [Figs. 3(b) and 4(b)] without the associated trailing partial appearing in the electron-transparent regions of the TEM foil (it

should be noted, nevertheless, that, occasionally, dissociated *perfect* dislocations were also observed). On the other hand, for deformation temperatures above  $T_c$ , the microstructure is dominated by perfect dislocations that are dissociated into two partials bounding a ribbon of stacking fault [Figs. 3(a) and 4(a)].

#### IV. PROPOSED MODEL

##### A. Emission and mobility of partial dislocations

The results on SiC appear to indicate that the transition in deformation mechanism of this material at  $T_c$  may have to do with a change in the mode of glide in the crystal. Specifically, it appears that in the low-temperature regime ( $T < T_c$ ) deformation proceeds by the nucleation and glide of single *partial* dislocations, whereas in the high-temperature regime ( $T > T_c$ ) deformation proceeds by the formation and glide of *perfect*, albeit dissociated, dislocations. We shall now assume that this is true for all semiconductors and attempt to explain the discrepancies that may exist. Subsequently, we shall argue that the critical temperature,  $T_c$ , at which a transition in the deformation mechanism of the semiconductor occurs, can be identified with the BDT temperature,  $T_{BDT}$ , of the crystal.

Experimentally, it has been found that, in practically all semiconductors, there is an asymmetry in the mobility of the two partials of a dissociated dislocation with the leading partial being more mobile in screw (30/30) and mixed  $+120^\circ$  (90/30) dislocations.<sup>2,3</sup> The asymmetry in the mobility of the two partials of a dissociated dislocation is not surprising in a compound semiconductor, XY,

as the core of the partials always consists of the same atom species X or Y, and, at least for screw dislocations, the two partials have different cores  $X(g)$  and  $Y(g)$ .<sup>47</sup> Since the dangling bonds in the core of partial dislocations can be eliminated by reconstruction, the formation and migration energy of the kinks in the two partials is different because of the different X–X and Y–Y bonding energies.<sup>3,47,48,49</sup> In elemental semiconductors (Si, Ge, and diamond), the cores of the partials consist of the same species, but their reconstructed atomic structure depends on their character. Thus, the many experimental results that show an asymmetry in the mobility of the two partials<sup>39</sup> can be explained for the  $\pm 120^\circ$  (90/30 or 30/90) mixed dislocations but is not easily explicable for the screw (30/30) dislocations. One possibility is that, in the latter case, the leading partial is always moving into a perfect crystal, while the trailing partial is moving into a faulted structure.<sup>39,50</sup> It is possible that the formation and migration of kinks in a faulted structure are more difficult than in a perfect lattice, thus requiring higher activation energies.

We now turn to the production of mobile dislocations during plastic flow, considering essentially the operation of surface sources. Bulk (Frank–Read) sources are discussed in more detail in Sec. IV. C and lead to similar conclusions. The different mobilities of the two partials indicate that their formation energies are also probably different and that the leading partial has a lower formation activation energy than the trailing partial.<sup>24,25,42,51,52</sup> The dominance of a single partial dislocation in the microstructure of crystals deformed below  $T_c$  suggests that only the leading partial is nucleated in the crystal, presumably because there is not sufficient thermal energy to

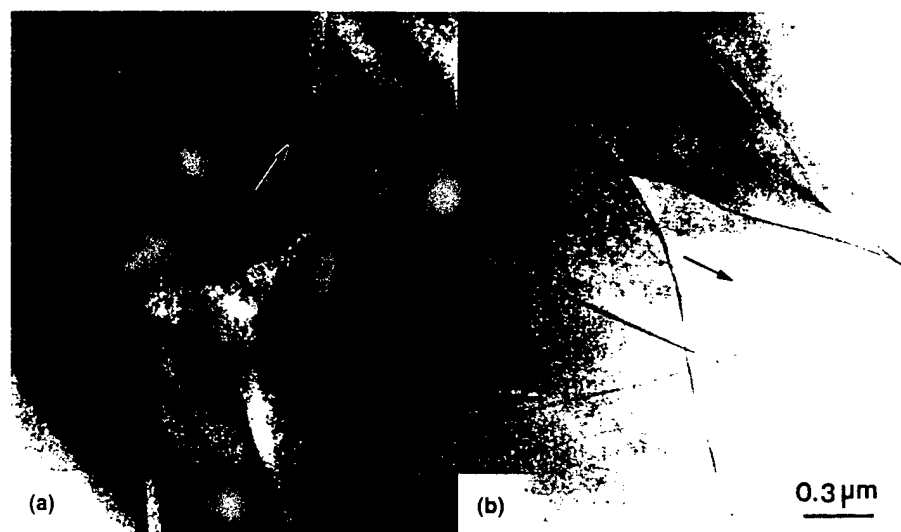


FIG. 3. Bright-field TEM micrographs of the microstructure of deformed 4H-SiC at (a) 1300 °C, in which the  $\frac{1}{2}\langle 11\bar{2}0 \rangle$  dislocations are predominantly dissociated into a pair of partials (left-hand side) bounding a ribbon of stacking fault with approximately their equilibrium width; and (b) 700 °C, in which the dislocations are predominantly single  $\frac{1}{2}\langle 10\bar{1}0 \rangle$  leading partials (left-hand side) with no associated trailing partials in the thin regions of the TEM foil.

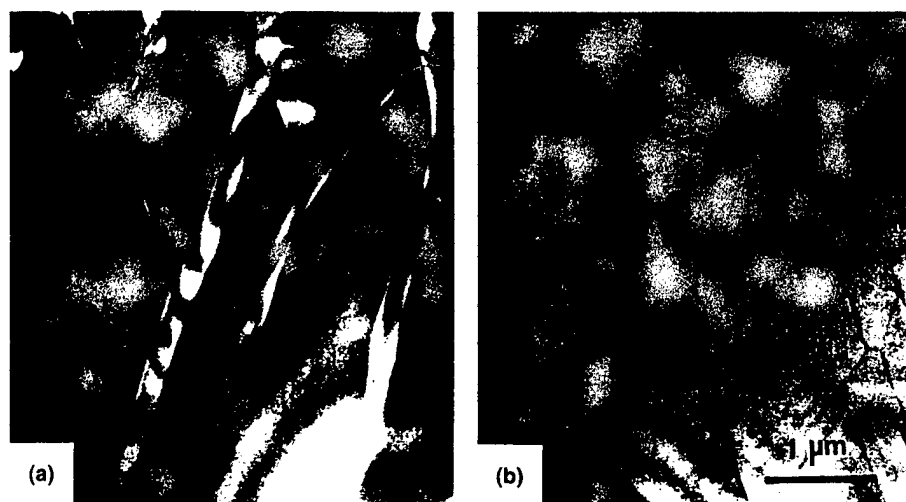


FIG. 4. Bright-field TEM micrographs of the microstructure of deformed 6H-SiC at (a) 1300 °C, in which the  $\frac{1}{3}\langle 11\bar{2}0 \rangle$  dislocations are predominantly dissociated into a pair of partials (left-hand side) bounding a ribbon of stacking fault with approximately their equilibrium width; and (b) 900 °C, in which the dislocations are predominantly single  $\frac{1}{3}\langle 10\bar{1}0 \rangle$  leading partials (right-hand side) with no associated trailing partials in the thin regions of the TEM foil.

nucleate the corresponding trailing partial with the higher activation energy<sup>42</sup>; besides the core structure of the trailing partial, this activation energy would, presumably, also depend on the stacking fault energy of the crystal.

The modeling of dislocation nucleation in crystals, and in particular in silicon, has recently become a focus of interest again.<sup>53–62</sup> In most cases, nucleation of perfect dislocations from a crack tip or from the surface of a strained heteroepitaxial layer has been considered. However, Rice<sup>55</sup> employed the Peierls concept to calculate the critical load required to nucleate partial dislocations from a crack tip in an FCC crystal. These 0 K calculations (in the absence of thermal fluctuations) considered the different Schmid factors on nucleation of the two partials of a  $+120^\circ$  dissociated dislocation for a particular crystal geometry. Using a different technique, Brochard *et al.*<sup>61</sup> have calculated the critical stress required for nucleation of leading/trailing partial dislocations from a surface step and, more recently, have included the effect of the different mobility of these partials in their calculations.<sup>62</sup> However, they have not as yet extended their calculations to finite temperatures in order to estimate the activation energies for nucleation of the different partials at a given applied stress.

It should be noted that a stacking fault always drags behind a leading partial, and thus the nucleation and motion of the latter on a certain slip plane in the crystal prevents the formation of the same partial from the same source on that plane. This argument applies to both bulk<sup>50</sup> and surface<sup>42</sup> sources. As a result, crystal shear is highly inefficient in the low-temperature regime and plastic deformation of the crystal can take place to a very limited extent. Not only is the Burgers vector of a partial much smaller than a perfect dislocation but also once a

partial is nucleated from a source, the operation of the source is practically shut off at least for all pinned non-screw dislocation segments. (In the case of pinned screw dislocation segments, twins may start forming by repeated cross-slip processes.<sup>50</sup> However, even if twinning does occur, this is a much more limited mode of deformation as compared to the motion of perfect dislocations.) At a certain critical temperature,  $T_c$ , thermal energy becomes sufficient to nucleate the trailing partial (as well as the leading partial of course). In this case, the motion of the trailing partials on the slip planes clean up any left-over stacking faults on those planes and the existing sources start operating rapidly again. Moreover, the shearing of the crystal takes place much more efficiently. The same sources can multiply repeatedly on the same slip planes and produce many dislocations, the motion of each of which can shear the crystal through a full Burgers vector. Hence, any applied stress on the crystal will be relaxed by the efficient formation and glide of perfect (dissociated) dislocations above  $T_c$  and the crystal becomes plastically deformable (ductile). On the other hand, the very limited plasticity of the crystal below  $T_c$  prevents the relaxation of the applied stress and results in its build up. Any crack nucleus is then susceptible to rapid growth by the propagation of the crack tip under a resolved tensile stress on it. Thus, according to this argument, the slope of the  $\ln(\tau_p)$  versus  $1/T$  plot in the  $T < T_c$  regime gives the activation energy for glide of the leading partial dislocation, and the slope of this plot at  $T > T_c$  gives the activation energy for glide of the slow trailing partial (which effectively controls the mobility of the perfect dislocation). Correspondingly,  $\tau_p^l$  and  $\tau_p^t$  in Fig. 1(b) are the Peierls stresses for the leading and trailing partial dislocation, respectively.



## B. BDT

The same argument applies for generation of dislocation half-loops from stress concentrations at a crack tip.<sup>63,64</sup> This is schematically shown in Fig. 5(a) for a crack tip that is subject to the simple case of mode I loading, i.e., a tensile stress,  $\sigma$ , normal to the crack surfaces, or a corresponding stress intensity factor,  $K_I$ , at the crack tip. In this figure, slip planes  $S$  are also shown that intersect the crack tip and the few ledges on the crack faces that are, presumably, the most likely sites for dislocation nucleation. At temperatures below the BDT, only a leading partial dislocation half-loop can be emitted from each source, which will subsequently shut off that source [Fig. 5(a)]. In this case, the crack tip blunting, or its shielding,<sup>65</sup>  $\sum K_I^{dis}$ , by the few partial dislocations, is negligible, and the effective stress on the crack tip,  $K_I^{eff}$  ( $= K_I - \sum K_I^{dis}$ ), is nearly equal to the applied stress-intensity factor,  $K_I$ . Consequently, as the applied stress is increased and  $K_I^{eff}$  ( $\approx K_I$ ) reaches the critical stress intensity factor,  $K_{Ic}$ , the crack propagates, leading to the fracture of the material. On the other hand, at or above the BDT, when full dislocations can be nucleated by the stress concentration [Fig. 5(b)], the crack tip source will operate repeatedly on the same slip plane and an avalanche of full dislocation half-loops will be emitted by the existing sources. These dislocations are collectively able to blunt the crack tip (if they are screw and are able to cross-slip around the crack profile), or more importantly, shield it from the tensile stress (if they are edge and move away from the crack) and prevent the crack from propagating.<sup>65</sup> In other words, in this case the shielding,  $\sum K_I^{dis}$ , becomes significant and will be able to maintain the effective stress-intensity factor,  $K_I^{eff}$ , below  $K_{Ic}$ .

We should also add that the nucleation of perfect dislocations by itself is not sufficient to shield the crack and stop it from propagating. Once a (full) dislocation is nucleated at a source, it must be able to move away rapidly enough to let the source operate continuously and generate other dislocations. In fact, the mobility of dislocations must be high enough that a sufficient number of dislocations can form in a short enough time frame that the crack is shielded effectively before it has a chance to run away. Thus, the present model does not contradict the dependence of the BDT on dislocation mobility through the rate of expansion of a crack tip shielding zone of dislocations emanating from the crack tip.

From the above discussion, the present model predicts that, at temperatures below BDT, only a few leading partial dislocations with their associated stacking fault would be present at a crack tip. Whether there is sufficient contrast produced by a few partial dislocations to enable their observation by TEM or x-ray techniques to provide enough resolution to observe the few partials is

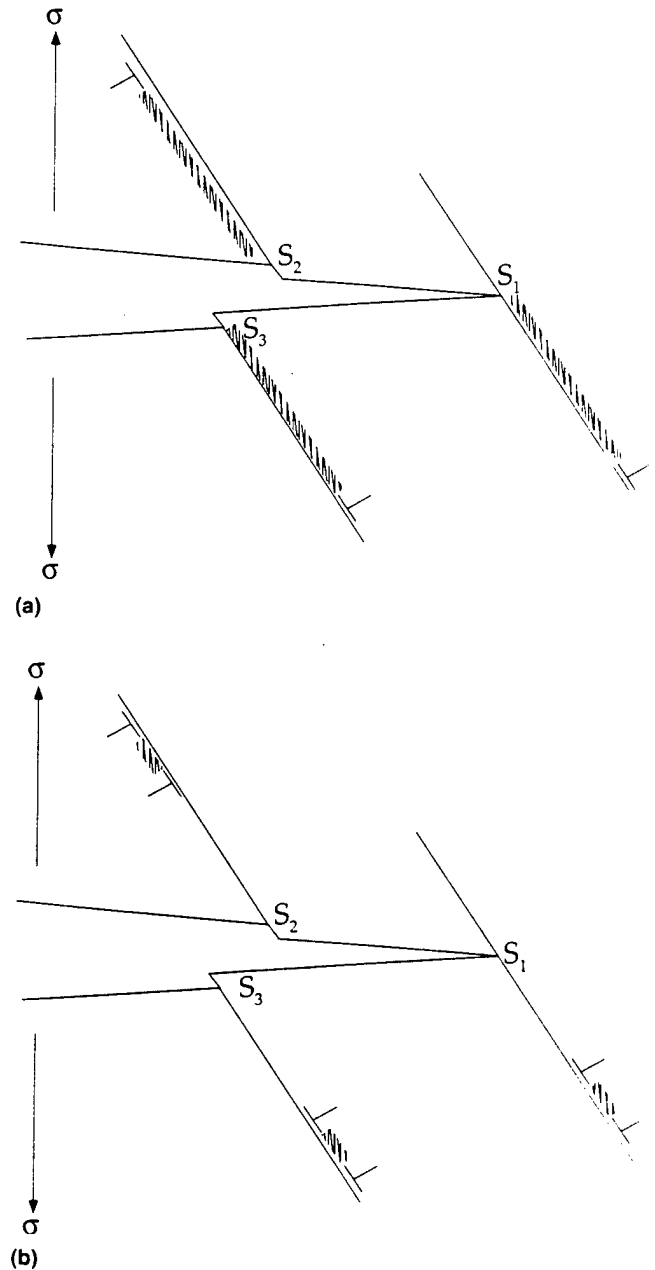


FIG. 5. Schematic projection of a crack tip under mode I loading with an intersecting slip plane: (a) at  $T < T_{BDT}$ , emission of a single partial dislocation loop shuts off the source(s); and (b) at  $T \geq T_{BDT}$ , emission of the associated trailing partial cleans the glide plane(s), thus enabling continuous operation of the source(s).

questionable. On the other hand, only perfect dislocations should be observed at temperatures above the BDT. The few experimental data that are available for the most investigated element, silicon (e.g., x-ray observations by George<sup>12</sup>) and *in situ* TEM observations by Chiao and Clark,<sup>66</sup> are not inconsistent with these predictions. In addition, as far as the authors are aware, no observations contradicting these predictions are available for other semiconductors. Further, it is well established that the temperature and strain rate dependence of the BDT, in

silicon,<sup>6–9</sup> germanium,<sup>67</sup> and GaAs<sup>68</sup> at least, are practically the same as those associated with dislocation mobility in the high-temperature/low-stress regime. Within the present context, this confirms that any significant amount of plasticity recorded at crack tips stems from the motion of perfect dislocations. We shall come back to the effect of the initial dislocation density on the BDT after discussing some recent simulations in silicon.

### C. Frank–Read sources in silicon

It is known from many studies that dislocation multiplication occurs by surface sources in crystals containing an initial density of dislocations smaller than a critical value (about  $10^6 \text{ m}^{-2}$ , according to Alexander and Haasen<sup>1</sup>) and by volume (Frank–Read) sources for pre-strained crystals or crystals containing a large density of grown-in dislocations. Moulin<sup>69</sup> has recently simulated the operation of a Frank–Read source in silicon using three-dimensional mesoscopic simulations that fully take into account the self-energy and interaction between dislocations.<sup>70,71</sup> As part of his simulations, Moulin considers the formation of the first loop from a dissociated screw dislocation segment by a Frank–Read mechanism [Fig. 6(a)]. The evolution of the process may be followed by changes in two parameters [Fig. 6(b)]:  $d_1$  (separation between the initial leading and trailing partials) and  $d_2$  (separation between the re-formed leading and trailing partials) as a function of temperature,  $T$ , and the resolved applied shear stress,  $\tau_{\text{appl}}$ . Figure 6(c) shows the evolution of  $d_1$  and  $d_2$  as a function of temperature for a source length of  $1 \mu\text{m}$  at an applied stress of  $\tau_{\text{appl}} = 400 \text{ MPa}$  when the stress axis on the crystal is along a  $[100]$  direction. Under this particular geometry, the intersection of the two curves  $d_1(T)$  and  $d_2(T)$  corresponds to a critical temperature,  $\sim 900 \text{ K}$ , where a transition occurs. (This transition can be viewed as equivalent to the one studied by Wessel and Alexander,<sup>39</sup> but now it is defined in dynamic conditions and for dislocation sources, not for infinite straight segments.) At lower temperatures, faulted loops form by the expansion of only the leading partial [left-hand inset to Fig. 6(c)], whereas at higher temperatures, perfect loops form by the expansion of both the leading and the trailing partials [right-hand inset to Fig. 6(c)]. This critical temperature ( $\sim 900 \text{ K}$ ) falls in the range of the BDT of silicon.<sup>10</sup> It should be noted, however, that the problem of the nucleation of the partials (compare with Sec. IV. A) was not considered by Moulin, since these results only deal with the case where both partials are already present. It is also interesting that the intersection point (and thus the transition temperature) shifts with the source length.<sup>69</sup> Since in a dislocated crystal the source length is inversely proportional to the square root of the dislocation density, this effect is in some ways equivalent to the experimental dependence of BDT on the initial dislocation density in the crystal.

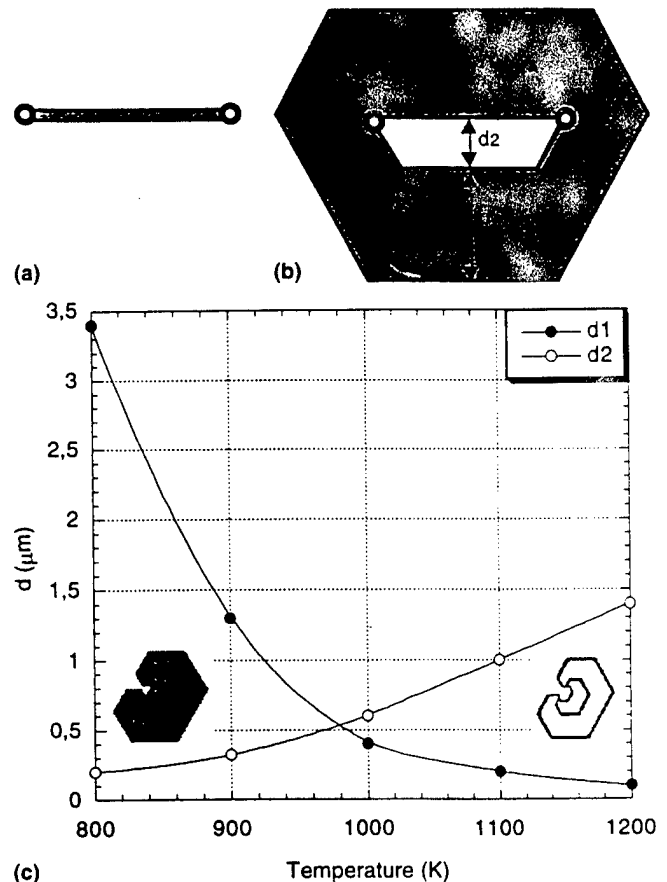


FIG. 6. The definitions of  $d_1$  and  $d_2$  in a Frank–Read source: (a) initial pinned segment of a dissociated screw dislocation, (b) after expansion of the leading partial, and (c) variations of  $d_1$  and  $d_2$  with temperature,  $T$ , in a Frank–Read source starting from a pinned dislocation segment of  $1\text{-}\mu\text{m}$  length under an applied stress of  $\tau_{\text{appl}} = 400 \text{ MPa}$ . The inset shows the formation of perfect loops for  $T > T_c$  and faulted loops for  $T < T_c$ .

However, in addition to uncertainties related to the assumed initial microstructure, two effects must be considered. One is the influence of orientation—since the one used here,  $[100]$ , favors the extension of the stacking fault ribbon—and the other is the effect of the intrinsic difference in partial dislocation velocities that appears to affect, to some extent, the transition in the source mode of operation. Hence, the present simulation results are essentially qualitative.

## V. DISCUSSION AND CONCLUDING REMARKS

### A. Velocity and mobility of partial dislocations

The transition observed in the simulation experiment of Fig. 6(c) can be explained in part by the occurrence of two different velocity regimes, as predicted within the framework of the diffusing kink mode.<sup>5</sup> In short, based on the mean-free-path of kinks on a dislocation segment of length  $L$ , one can define a transition between a low-

stress/high-temperature domain, where dislocation velocities are independent of the segment's length, and a high-stress/low-temperature regime, where the velocity is proportional to the length.<sup>5</sup> Since the activation energy ( $E_l + E_m$ ) for glide of a length-dependent segment is smaller by  $\sim E_l$  than that ( $2E_l + E_m$ ) of a length-independent segment ( $E_l$  and  $E_m$  are, respectively, the kink formation and migration energies), it follows that the activation enthalpy should be larger at low temperatures. However, this would induce a break in the  $\tau_Y(T)$  plots in a sense opposite to the one that is experimentally observed. This discrepancy can be attributed to the fact that the simulations do not account for the intrinsic difference in the mobility of partial dislocations—a difference that increases with decreasing temperature.<sup>72</sup> In fact, not much is known about these effects, even in silicon, but it is clear that there is no obvious correlation between the break in the  $\tau_Y(T)$  curves and the transition between the two types of velocity laws.

Finally, another possible explanation for the break in the  $\tau_Y(T)$  plot could arise from a breakdown of the hypothesis that kinks move in a diffusive manner along the secondary Peierls valleys. Indeed, at high stresses, the probability for reverse jumps of the kinks (i.e., jumps in a direction opposite to that of the applied stress) becomes vanishingly small. In such a case, the activation enthalpy for kink migration would depend on stress in a nonlinear manner—unlike the case of kink diffusion regime where the kink velocity is proportional to the applied stress. This possibility was actually discussed by Suzuki *et al.*<sup>22</sup> in their latest paper. However, these authors considered only mobile *perfect* dislocations since their experiments were performed along the  $\langle 123 \rangle$  axis—an orientation not favorable for dissociation under the Escaig effect. In any case, whether or not this change in the velocity law occurs at low temperatures—and superimposes on the different mobilities of partial dislocations—it does not modify the substance of the model presented here.

## B. Prestrained versus dislocation-free crystals

A question that remains to be answered is the observation of both leading and trailing partials in some of the crystals deformed in the brittle regime, e.g., silicon deformed in a  $\langle 110 \rangle$  orientation for which the resolved shear stresses tend to constrict the stacking fault ribbon. With the exception of a few cases for silicon, the crystals tested under high-stress/low-temperature conditions have not been dislocation free. In fact, sometimes (e.g., experiments of Wessel and Alexander on Si<sup>39</sup>), the dislocation density is intentionally increased in the crystal by predeformation at a high temperature (in the ductile regime) and with low stress to prevent fracture of the crystal when the second stage of deformation at low-temperature (brittle regime) and high stress is applied. In

other cases, there is usually an initial density of dislocations that have been usually introduced (again in the ductile regime) in the crystal during its solidification and growth. In any case, these pre-existing dislocations (intentionally or nonintentionally introduced) are usually perfect, albeit dissociated into leading/trailing pairs. Hence, application of high stresses at low temperatures (and under low strain rates, or with a superimposed hydrostatic pressure that prevents fracture of the crystal by counteracting the tensile stresses on pre-existing crack nuclei) will lead to motion of dissociated pairs. In general, under such conditions, nonequilibrium widening or narrowing of dissociated dislocations occurs during glide, as demonstrated by Wessel and Alexander.<sup>39</sup> In addition to the relative mobilities of the leading and trailing partials, this depends sensitively, as mentioned before, on the crystal orientation.<sup>39</sup> According to the present model, however, new dislocations can also be generated in the low-temperature deformation stage, although these will be single leading partials. There are, thus, two competing mechanisms for generating dislocations at low temperatures, and the final microstructure consists of a mixture of dissociated perfect dislocations (from the initial dislocation content, and new loops generated from nonscrew Frank–Read sources) together with some single leading partials that are generated by deformation below  $T_c$ . The relative amounts of dissociated perfect versus single (leading) partial dislocations depends on the initial dislocation density of the crystal (pre-existing or intentionally introduced in the ductile regime) and the temperature, stress, and duration of the low-temperature deformation (which controls the fraction of single partials nucleated in the brittle regime). Similarly, during the deformation of a dislocation-free crystal in the brittle regime (say, under a large hydrostatic pressure), it is expected that all the dislocations in the crystal would be single partials. It also follows that in fracture tests, the BDT temperature will be very sharp for a dislocation-free crystal (all sources shut off after they have emitted one single leading partial), whereas it would be rather diffuse for a crystal containing pre-existing dislocations, as is found experimentally.<sup>10,73</sup> In the latter case, the temperature range,  $\Delta T$ , over which the BDT extends would depend on the initial dislocation density. Another consequence of the model is that plastic deformation of a *truly dislocation-free* bulk crystal, with well-polished sample surfaces, should be practically impossible at low temperatures even under very high hydrostatic pressures because of the very limited plasticity (all the dislocation sources shut off quickly after emission of a leading partial). The situation will of course be different if new sources are continually introduced (say, at the surface); this is what takes place in an indentation test where a superimposed compressive hydrostatic component is present. Then, plasticity is provided exclusively

by the formation and motion of leading partials and microtwins.

## ACKNOWLEDGMENTS

The work at Case Western Reserve University, was supported by grant No. FG02-93ER45496 from the Department of Energy, and subcontract No. 95-SPI-420757-CWRU from the Silicon Carbide Consortium. Thanks are due to Dr. Calvin Carter, Jr. (of Cree Research, Inc.) and Dr. Don Hobgood (previously at Northrop-Grumman) for providing single-crystal samples of 6H-SiC and 4H-SiC, respectively.

## REFERENCES

- H. Alexander and P. Haasen, in *Solid State Physics*, edited by F. Seitz, D. Turnbull, and H. Ehrenreich (Academic Press, New York and London, 1968), Vol. 22, p. 27.
- H. Alexander, in *Dislocations in Solids*, edited by F.R.N. Nabarro (Elsevier Science Publishers B., Amsterdam, 1986), Vol. 7, p. 114.
- A. George and J. Rabier, *Rev. Phys. Appl.* **22**, 941 (1987).
- J. Rabier and A. George, *Rev. Phys. Appl.* **22**, 1327 (1987).
- J.P. Hirth and J. Lothe, *Theory of Dislocations*, (McGraw-Hill, New York, 1968).
- C.St. John, *Phil. Mag.* **32**, 1193 (1975).
- M. Brede and P. Haasen, *Acta Metall.* **36**, 2003 (1988).
- J. Samuels and S.G. Roberts, *Proc. R. Soc. Lond. A* **421**, 1 (1989).
- P.B. Hirsch, S.G. Roberts, and J. Samuels, *Proc. R. Soc. Lond. A* **421**, 25 (1989).
- P.B. Hirsch and S.G. Roberts, *Phil. Mag. A* **64**, 55 (1991).
- J.F. Knott, *Fundamental of Fracture Mechanics*, (Butterworths, London, 1979).
- A. George, *Solid State Phenomena* **59-60**, 251 (1998).
- A.S. Argon, *Acta Metall.* **35**, 185 (1987).
- B. Escaig, in *Dislocation Dynamics*, edited by A.R. Rosenfield, G.T. Hahn, A.L. Bement, Jr., and R.I. Jaffee (MacGraw-Hill London, 1968), p. 655.
- B. Escaig, *J. Physique* **29**, 225 (1968).
- T. Suzuki, H. Koizumi, and H.O.K. Kirchner, *Phil. Mag. A* **71**, 389 (1995).
- T. Suzuki, I. Yonenaga, and H.O.K. Kirchner, *Phys. Rev. Lett.* **75**, 3470 (1995).
- H.O.K. Kirchner and T. Suzuki, *Acta Mater.* **46**, 305 (1997).
- T. Suzuki, T. Nishisako, T. Taru, and T. Yasutomi, *Phil. Mag. Lett.* **77**, 173 (1998).
- P. Gall, J.P. Peyrade, R. Coquill  , F. Reynaud, S. Gabillet, and A. Albacette, *Acta Metall.* **35**, 143 (1987).
- T. Suzuki, T. Yasutomi, T. Tokuoka, and I. Yonenaga, *Phil. Mag. A* In press (1998).
- T. Suzuki, T. Yasutomi, T. Tokuoka, and I. Yonenaga, *Phys. Stat. Sol. (a)* **171**, 47 (1999).
- A.V. Samant, Ph.D. Thesis, Case Western Reserve University (1999).
- A.V. Samant, W.L. Zhou, and P. Pirouz, *Phys. Stat. Sol. (a)* **166**, 155 (1998).
- A.V. Samant, M. Hong, and P. Pirouz (1998, unpublished).
- J. Castaing, P. Veyssi  re, L.P. Kubin, and J. Rabier, *Phil. Mag. A* **44**, 1407 (1981).
- J.F. Demenet, *Etude du Silicium a Basse et Moyenne Temperature Sous Forte Contrainte*, Th  se d'etat, Universit   de Poitiers (UFR Sciences fondamentales et appliquees), No. 457 (1987).
- P. Boivin, J. Rabier, and H. Garem, *Phil. Mag. A* **61**, 647 (1990).
- E. Kaxiras and M.S. Duesbery, *Phys. Rev. Lett.* **70**, 3752 (1993).
- B. Jo  s, Q. Ren, and M.S. Duesbery, *Phys. Rev. B* **50**, 5890 (1994).
- Q. Ren, B. Jo  s, and M.S. Duesbery, *Phys. Rev. B* **52**, 13223 (1995).
- M.S. Duesbery and B. Jo  s, *Phil. Mag. Lett.* **74**, 253 (1996).
- H. Gottschalk, G. Patzer, and H. Alexander, *Phys. Stat. Sol. (a)* **45**, 207 (1978).
- S. Takeuchi, K. Suzuki, K. Maeda, and H. Iwanaga, *Phil. Mag. A* **50**, 171 (1984).
- S. Takeuchi and K. Suzuki, *Phys. Stat. Sol. (a)* **171**, 99 (1999).
- H.-J. M  ller, *Acta. Met.* **26**, 963 (1978).
- F. Louchet and J. Thibault-Desseaux, *Rev. Phys. Appl.* **22**, 207 (1987).
- P. Pirouz and X.J. Ning, in *Proceedings of Microscopy of Semiconducting Materials*, edited by A.G. Cullis and A. Staton-Bevan (Inst. Phys. Conf. Ser. No. **146**, Bristol, England, 1995), p. 69.
- K. Wessel and H. Alexander, *Phil. Mag.* **35**, 1523 (1977).
- J. Rabier and P. Boivin, *Phil. Mag. A* **61**, 673 (1990).
- P. Pirouz and P.M. Hazzledine, *Scripta Metall. Mater.* **25**, 1167 (1991).
- P. Pirouz, in *Twinning in Advanced Materials*, edited by M.H. Yoo and M. Wuttig (The Minerals, Metals, and Materials Society, Pittsburgh, PA, 1994), p. 275.
- S. Branchu, H. Garem, J. Rabier, and J.L. Demenet, *Phys. Stat. Sol. (a)* **167**, 89 (1998).
- P. Grosbras, J.L. Demenet, H. Garem, and J.C. Desoyer, *Phys. Stat. Sol. (a)* **84**, 481 (1984).
- J.L. Demenet, J. Rabier, and H. Garem, in *Proceedings of Microscopy of Semiconducting Materials*, edited by A.G. Cullis and P.D. Augustus (Inst. Phys. Conf. Ser. No. **87**, Bristol, England, 1987), p. 355.
- J.L. Dement, P. Grosbras, H. Garem, and J.C. Desoyer, *Phil. Mag. A* **59**, 501 (1989).
- H. Alexander, P. Haasen, R. Labusch, and W. Schr  ter, *J. Phys. (Paris)* **40**, Colloque C6 (1979).
- P. Pirouz, *Scripta Metall.* **23**, 401 (1989).
- P. Pirouz, in *Proceedings of Microscopy of Semiconducting Materials*, edited by S.G. Roberts, D.B. Holt, and P.R. Wilshaw (Inst. Phys. Conf. Ser. No. **104**, Bristol, England, 1989), p. 49.
- P. Pirouz, *Scripta Metall.* **21**, 1463 (1987).
- X.J. Ning, T. Perez, P. Pirouz, *Phil. Mag. A* **72**, 837 (1995).
- X.J. Ning, N. Huvey, and P. Pirouz, *J. Am. Ceram. Soc.* **80**, 1645 (1997).
- G. Sch  ck, *Phil. Mag. A* **63**, 111 (1991).
- G. Sch  ck and W. P  schl, *Phil. Mag. A* **64**, 931 (1991).
- J.R. Rice, *J. Mech. Phys. Solids* **40**, 239 (1992).
- J.R. Rice and G.E. Beltz, *J. Mech. Phys. Sol.* **42**, 333 (1994).
- G. Xu, A.S. Argon, and M. Ortiz, *Phil. Mag. A* **72**, 415 (1995).
- G. Xu, A.S. Argon, and M. Ortiz, *Phil. Mag. A* **75**, 341 (1997).
- J. Gril  h  , *Europhys. Lett.* **23**, 141 (1993).
- N. Junqua and J. Gril  h  , *Phil. Mag. Lett.* **75**, 125 (1997).
- S. Brochard, N. Junqua, and J. Gril  h  , *Phil. Mag. A* **77**, 911 (1998).
- S. Brochard, J. Rabier, and J. Gril  h  , *Eur. Phys. J.* **75**, 99 (1998).
- A. Kelly, W.R. Tyson, and A.H. Cottrell, *Phil. Mag.* **15**, 567 (1967).
- J.R. Rice and R. Thomson, *Phil. Mag.* **29**, 73 (1974).
- R. Thomson, in *Solid State Physics*, edited by H. Ehrenreich and D. Turnbull (Academic Press, New York, 1986), Vol. 39, p. 1.
- Y.-H. Chiao and D.R. Clarke, *Acta Metall.* **37**, 203 (1989).

67. F.C. Serbena and S.G. Roberts, *Acta. Metall. Mater.* **42**, 2505 (1994).
68. K. Maeda and S. Fujita, in *Lattice Defects in Ceramics*, edited by S. Takeuchi and T. Suzuki (Jap. J. Appl. Phys. Series 2, Tokyo, 1989), p. 25.
69. A. Moulin, *Etude de la Plasticité du Silicium à une Échelle Méso-scopique par Simulation Numérique Tridimensionnelle*, Thèse de doctorate, École Centrale de Paris, (1997).
70. A. Moulin, M. Condat, and L.P. Kubin, *Acta. Mater.* **45**, 2339 (1997).
71. A. Moulin, M. Condat, and L.P. Kubin, *Phil. Mag.*, in press (1998).
72. K. Yasutake, S. Shimizu, M. Umeno, and H. Kawabe, *J. Appl. Phys.* **61**, 940 (1987).
73. P.D. Warren, *Scripta Metall.* **23**, 637 (1989).

## An optical and transmission electron microscopy study of deformation-induced defects in 6H-SiC

By A. V. SAMANT, X. L. WEI and P. PIROUZ

Department of Materials Science and Engineering, Case Western Reserve University, Cleveland, Ohio 44106, USA

[Accepted 23 January 1998]

### ABSTRACT

Deformation tests were conducted on 6H-SiC in an orientation favourable for activation of the  $(2110)(0001)$  slip system. Tests were conducted at temperatures between 550 °C and 1400 °C and at a strain rate of  $3.1 \times 10^{-3} \text{ s}^{-1}$ . Subsequent to the deformation tests, optical and transmission electron microscopy were used to study the deformation-induced defects such as stacking faults, deformation kinks, and cracks. Based on these observations, a mechanism for the formation of deformation kinks, and nucleation and propagation of cracks, and the temperature dependence of this mechanism is proposed.

### §1. INTRODUCTION

Owing to its potential as a wide bandgap semiconductor, there has recently been an increased interest in the mechanical behaviour and the structure-property relationships of monocrystalline silicon carbide (Fujita *et al.* 1987, Suematsu *et al.* 1991, Corman 1992, Yang *et al.* 1992, Ning and Pirouz 1994, Samant *et al.* 1998). These studies have involved primarily 6H-SiC because of the recent successes in new and improved methods of growing bulk monocrystals of this polytype (Tairov and Tsvetkov 1978). Studies on the effects of test temperature and strain rate on the yield stress of monocrystalline 6H-SiC (Fujita *et al.* 1987, Samant *et al.* 1998) have shown that in an orientation favourable for activation of the  $(21\bar{1}0)(0001)$  primary slip system, these crystals can be deformed to relatively large plastic strains via the application of modest resolved shear stresses on the basal plane. The present paper reports the results of optical and transmission electron microscopy studies on the deformation-induced kinks and cracks in these crystals.

### §2. EXPERIMENTAL PROCEDURE

The 6H-SiC bulk single crystal was obtained from Cree Research Inc. (Durham, North Carolina, USA), and was grown along the  $[0001]$  direction by the modified sublimation technique (Tairov and Tsvetkov 1978). The orientation of the bulk crystal was determined by the X-ray Laue back-reflection technique and the samples were cut in an orientation as shown schematically in figure 1. After cutting, all the faces of each sample were ground using a 20  $\mu\text{m}$  diamond-impregnated disc followed by a 9  $\mu\text{m}$  diamond polish. Each specimen then had the correct orientation for maximum resolved shear stress (i.e. Schmid factor,  $S = 0.5$ ) for the  $[1210](0001)$  primary slip system. The Schmid factors for slip on the other two equivalent slip systems, e.g.  $[2110](0001)$  and  $[1120](0001)$ , were lower ( $\approx 0.43$ ). The samples were tested in compression in a manner described elsewhere (Samant *et al.* 1998) at

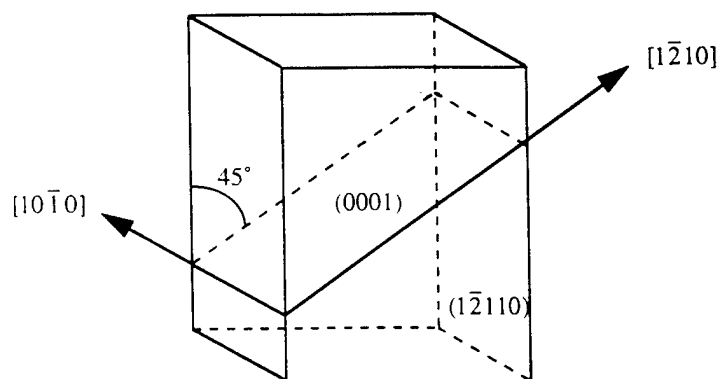


Figure 1. Schematic of the compression sample. Nominal specimen dimensions are 2.0 mm  $\times$  2.0 mm  $\times$  4.0 mm.

various temperatures ranging from 550 C to 1400 C and at a slow strain rate of  $3.1 \times 10^{-5} \text{ s}^{-1}$ . Subsequent to the compression tests, transmission electron microscopy (TEM) specimens were prepared from the crystals deformed at test temperatures of 1300 C and 1400 C. Foils parallel to the  $(10\bar{1}0)$  planes were prepared from slices of  $\sim 500 \mu\text{m}$  initial thickness, cut from the deformed crystals. These slices were then mechanically ground using 9  $\mu\text{m}$  diamond paste to a thickness of  $\sim 130 \mu\text{m}$  and, after further polishing with 3  $\mu\text{m}$  diamond paste, they were dimpled to a thickness of  $\sim 30 \mu\text{m}$  followed by ion beam thinning to electron transparency. A Philips CM20 transmission electron microscope was utilized to study these samples.

### §3. RESULTS

Figure 2 is an optical micrograph showing the slip traces on (a)  $(10\bar{1}0)$  and (b) the  $(12\bar{1}10)$  side faces of a 6H-SiC single crystal sample deformed at a test temperature of 1300 C to a true longitudinal strain of 8%. As expected, the slip traces correspond to the intersection of the sheared  $(0001)$  primary slip planes of 6H-SiC with the sample faces.

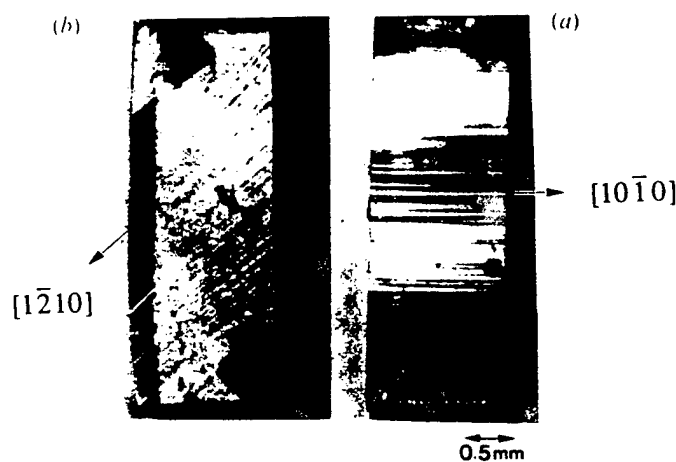


Figure 2. Optical micrograph showing the slip traces on (a) the  $(10\bar{1}0)$  and (b) the  $(12\bar{1}10)$  face of the sample deformed at a test temperature of 1300 C.

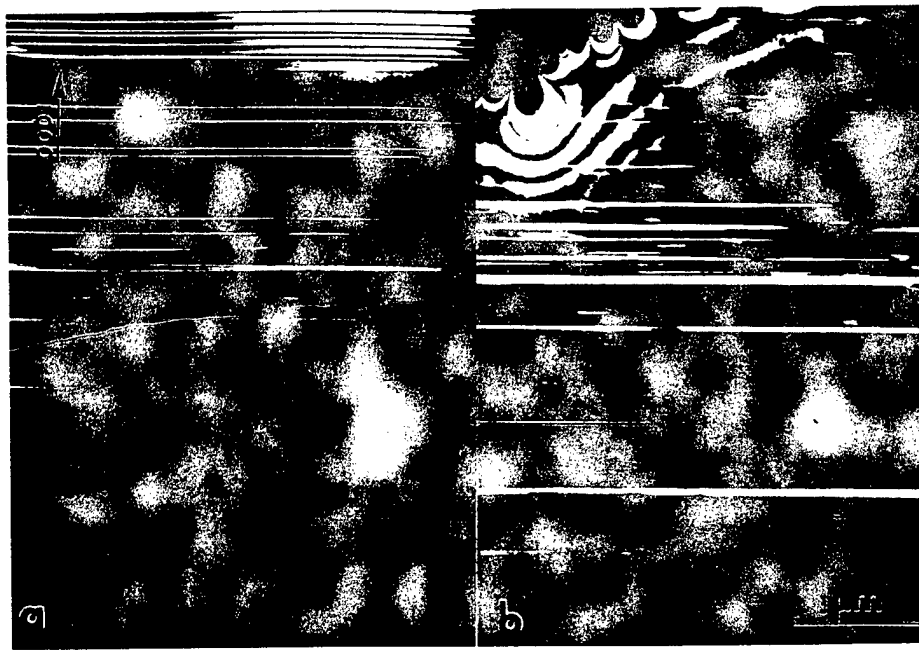


Figure 3. Dark-field transmission electron micrographs of the sample deformed at (a) 1300 C and (b) 1400 C obtained using the  $\mathbf{g} = 0110$  reflection near the  $[2110]$  zone axis. Each white band is a stacking fault ribbon on the (0001) plane. Note the large number of short ribbons, especially in (b), bounded at the ends by leading and trailing partial dislocations.

Figures 3 (a) and (b) are dark-field transmission electron micrographs of the samples deformed at 1300 C and 1400 C respectively, recorded using the  $\mathbf{g} = 0110$  reflection near the  $[2110]$  zone axis. A high density of stacking fault ribbons lying on the basal (0001) planes is observed in both these samples. Each ribbon is the result of wide dissociation of a  $\frac{1}{3}[1210]$  dislocation into two  $\frac{1}{3}\langle 1\bar{1}00 \rangle$  partials. This was confirmed by  $\mathbf{g} \cdot \mathbf{b} = 0$  analysis, in which the bands in these figures went out of contrast under  $\mathbf{g} = 0006$  and  $\mathbf{g} = 1120$  reflections, confirming that they have a translation vector parallel to  $[1100]$ . In some cases, both partials are in the field of view (the stacking fault ribbon is terminated at both ends), while in others, one or both partials are out of view (the stacking fault ribbon is terminated on one end only, or the ribbon crosses the whole field of view). It can be seen that many more short stacking fault ribbons are present in the sample deformed at the higher test temperature of 1400 C. The short ribbons in figure 3(b) have widths ranging from 130 nm to 300 nm, corresponding to a stacking fault energy between 3.5 and 1.5 mJ m<sup>-2</sup> respectively, with most of the ribbons having widths corresponding to a stacking fault energy of 2.6 mJ m<sup>-2</sup>. This is close to the value (2.5 mJ m<sup>-2</sup>) determined by Maeda *et al.* (1988) which they quote as the equilibrium stacking fault energy of 6H-SiC.

Figure 4 is a dark-field transmission electron micrograph of another area of the sample shown in figure 3(b), obtained using the same diffraction conditions. Two deformation kinks, labelled as I and II, are marked with arrows in figure 4; these are separated by a distance of about 7  $\mu$ m. The boundaries of the kinks are heavily faulted and further investigations were focused on kink I.



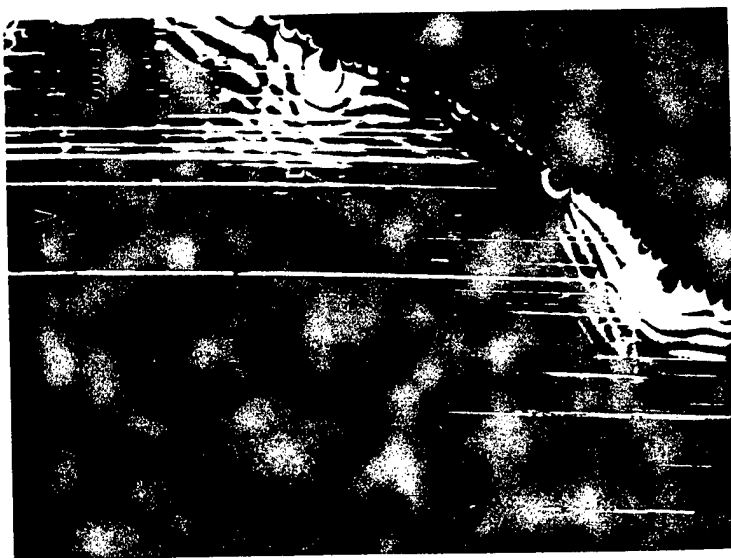


Figure 4. Dark-field transmission electron micrograph of the sample deformed at 1400 °C obtained using the  $\mathbf{g} = 01\bar{1}0$  reflection near the  $[2\bar{1}\bar{1}0]$  zone axis. Two deformation kinks, labelled as I and II, can be observed.

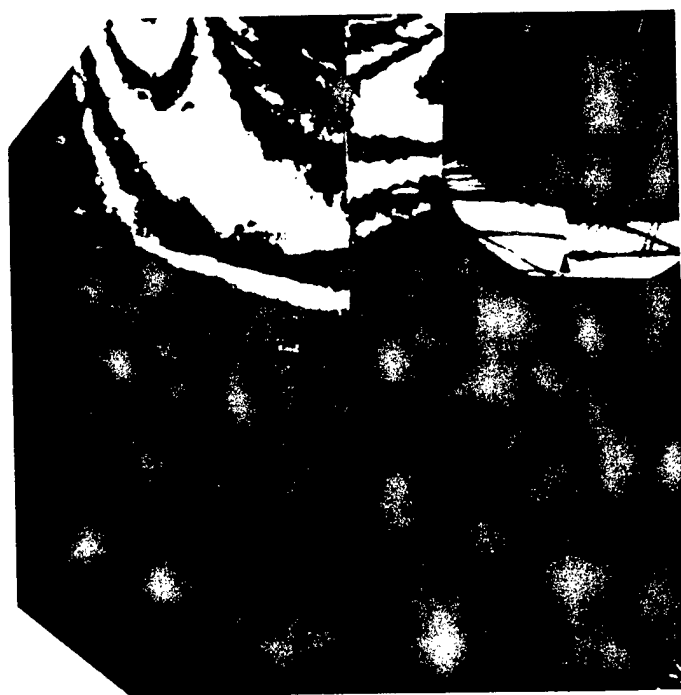


Figure 5. Dark-field transmission electron micrograph of the sample deformed at 1400 °C obtained using the  $\mathbf{g} = 0006$  reflection near the  $[10\bar{1}0]$  zone axis. A kink (labelled I in figure 4) passes vertically near the centre of the micrograph. The inset shows a bright-field LACBED pattern of a region intersecting the kink.

Figure 5 is a higher magnification view of kink I of figure 4, obtained using the  $\mathbf{g} = 0006$  reflection near the  $[1010]$  zone axis. The difference in contrast on either side of the kink indicates that there is a change of orientation across the kink. Large-angle convergent beam electron diffraction (LACBED) was utilized to determine the orientation of the two sides of kink I. The bright-field LACBED pattern, shown in the inset of figure 5, was obtained after tilting the specimen a few degrees away from the  $[1010]$  zone axis. The two arrows in this inset indicate the defocused shadow image of the deformation kink. The high order Laue zones (HOLZ) in the inset of figure 5 clearly indicate that the kink lies on the  $(1\bar{2}10)$  plane. The discontinuities in the HOLZ lines across the deformation kink revealed a  $\sim 5^\circ$  angle of rotation between the two sides of the kink.

Figure 6 is a higher magnification dark-field transmission electron micrograph of kink I obtained using the same diffraction conditions as those used in figures 3 and 4. The areas A and B marked in figure 6 indicate regions on the left and right hand side of the kink respectively. The  $\sim 5^\circ$  rotation of the deformation bands, which are parallel to the  $(0001)$  basal planes, can be clearly seen in this micrograph.

Figure 7 was obtained using the  $\mathbf{g} = 01\bar{1}0$  reflection near the  $[2\bar{1}\bar{1}0]$  zone axis. The reversal of contrast in regions A and B between figures 7(a) and (b) was obtained by exploiting the difference in the orientation of these two areas (discussed above).

Figure 8 is an optical micrograph of the  $(10\bar{1}0)$  face of a sample, compressed at a temperature of 950 °C to a true longitudinal strain of 17.9%, showing a  $(1\bar{2}10)$  prism plane crack. It is remarkable that, even at such a low temperature, the crack has not propagated to catastrophic failure: the upper portion of the sample is still intact. The crystal is also heavily kinked, as indicated by the bent slip traces.

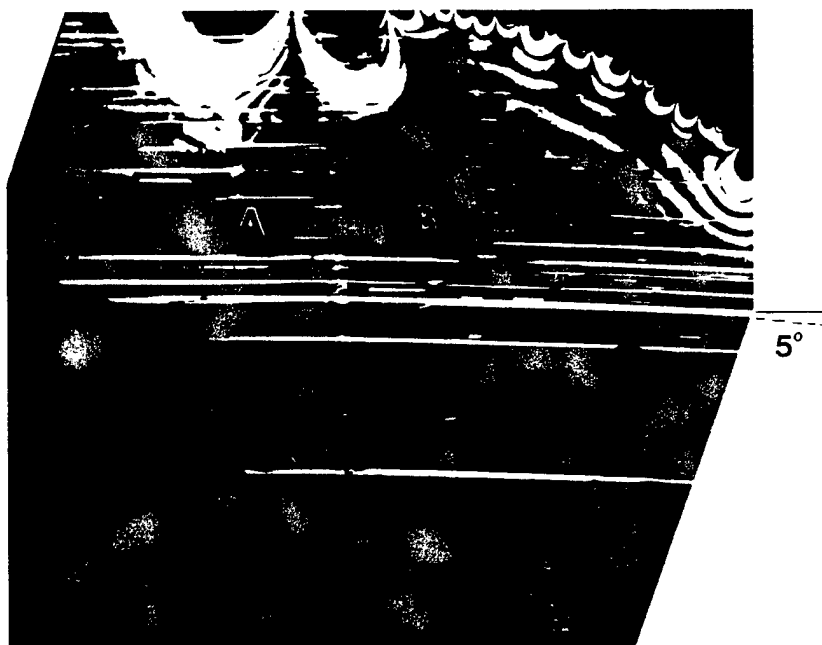


Figure 6. Dark-field transmission electron micrograph of the region containing kink I obtained using the  $\mathbf{g} = 01\bar{1}0$  reflection near the  $[2\bar{1}\bar{1}0]$  zone axis. Note the  $\sim 5^\circ$  rotation of the deformation bands (parallel to  $(0001)$  basal planes) on crossing the kink.

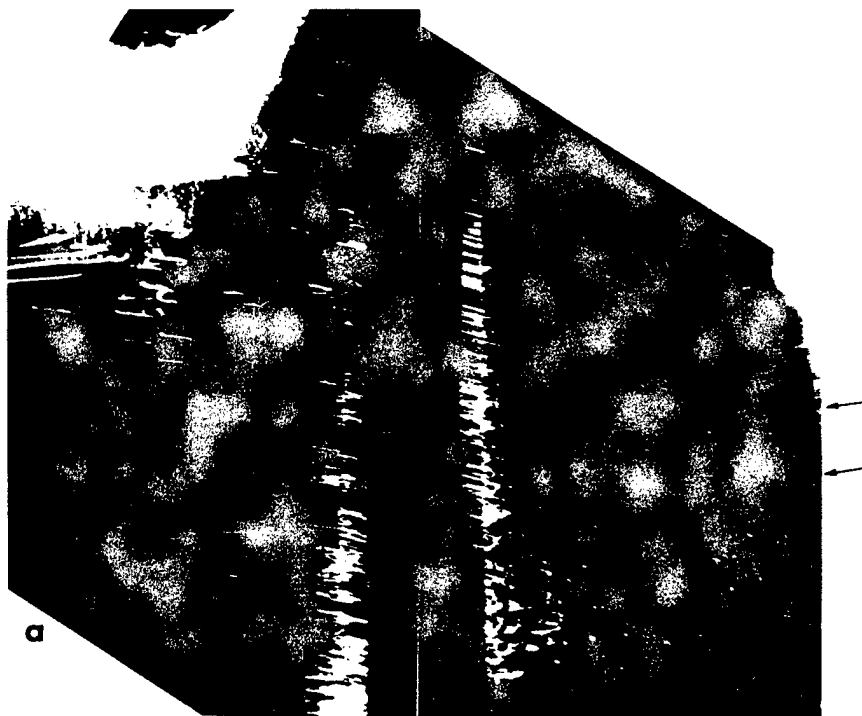


Figure 7. Dark-field transmission electron micrographs of the sample deformed at 1400 C obtained using the  $g = 0110$  reflection near the  $[2110]$  zone axis of (a) region A and (b) region B of figure 6. Note the high density of dislocations on both sides of the kink. The arrows indicate what appears to be dislocation pile-ups against the kink.

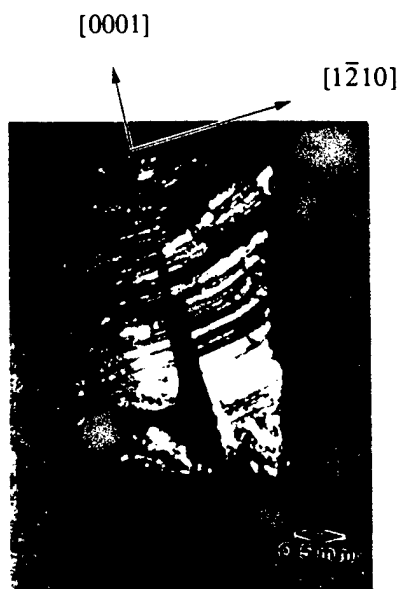


Figure 8. Optical micrograph showing the slip traces and prism crack on the  $(1010)$  face of the sample deformed at a test temperature of 950 C. Note the curved slip traces indicating the change in orientation of the crystal on either side of the crack which propagated along the kink.



Figure 9. Optical micrograph showing slip traces and cracks parallel to the compression axis on the  $(10\bar{1}0)$  face of a sample deformed at a test temperature of 550 °C.

Figure 9 is an optical micrograph of the  $(10\bar{1}0)$  face of a sample compressed at the very low temperature of 550 °C to a true longitudinal strain of 0.3%. This sample shows slip traces which do not appear to be kinked as are those seen in the specimen shown in figure 8 where the compression was carried out at a higher temperature (950 °C) to a true longitudinal strain of 17.9%. The sample in figure 9 does, however, have two cracks, both of which appear to have nucleated and propagated in a direction parallel to the applied compressive stress (i.e. they have propagated in a direction perpendicular to the maximum tensile stress, as expected in a brittle solid).

#### §4. DISCUSSION

Ning and Pirouz (1994) proposed a mechanism for the formation of deformation-induced cracks and kinks in 6H-SiC crystals at low deformation temperatures. In their paper, it was suggested that a  $(1\bar{1}00)\frac{1}{3}\langle 11\bar{2}0 \rangle$  prism dislocation acts as a barrier to the glide of partial basal dislocations, i.e.  $(0001)\frac{1}{3}\langle 01\bar{1}0 \rangle$  leading partials. Under the applied stress, the partial dislocations accumulate at their intersection with the  $\{1100\}$  plane on which the prism dislocation lies, and eventually nucleate a crack on this plane. Once a prism-plane crack is formed, further incoming partial dislocations glide out of the crack surface each forming a demi-step at the crack plane. This causes an accumulation of demi-steps of the same sense on neighbouring planes, which eventually results in the rotation of one part of the crystal with respect to the other, thus forming a kink on the  $\{1100\}$  plane in the 6H-SiC crystal deformed at lower temperatures. In the current experiments, however, specimens exhibited kinked slip traces on their  $\{10\bar{1}0\}$  faces even when no basal-plane or prism-plane cracks were detected. TEM on the samples deformed at test temperatures between 1300 °C and 1400 °C (discussed above) did not reveal the presence of any cracks. The fact that optical microscopy had shown these specimens to be kinked leads us to believe that, in the present deformation experiments, the formation of kinks

preceded the nucleation and propagation of cracks, and the above-mentioned mechanism cannot apply in this case.

Suematsu *et al.* (1991) suggested that deformation kinks present in the 6H-SiC samples on which they had performed compression experiments, formed because of the inevitable stress concentrations and inhomogeneous nature of their deformation tests. We believe the same type of inhomogeneities may also be at the origin of the deformation kinks in our experiments, and this is what will now be discussed.

Recently, Castaing and co-workers (Rivière and Castaing 1997, Castaing *et al.* 1997) considered the evolution of the sample shape during compression of a single crystal in which only single slip is activated (figure 10). In figure 10(a), the set of crystallographic planes parallel to the slip plane is shown in the undeformed crystal: initially this set makes an angle of  $45^\circ$  with respect to the end compression faces of the specimen. In general, during a compression test of a parallelepiped crystal, in which only single slip is activated, deformation is not homogeneous in the specimen but, rather, is concentrated in a sheared band, leaving two triangular regions undeformed. During deformation, if the end faces of the crystal are free to move, then the specimen changes shape, becoming distorted as in figure 10(b). The shape of the sample in this figure is due to shear of the central portion on the slip planes and the motion of the two triangular regions parallel to the compression faces in order to keep up with this shear. The slip planes remain parallel, however, in all three regions of the deformed sample. However, if the end faces are prevented from motion by frictional forces, then glide on the slip planes is accompanied by a rotation of these planes as in figure 10(c). As seen in this figure, only one kinked band forms which consists of the central portion of the sample, separated by two deformation kinks on the two sides of the crystal. In the actual case, however, the deformation is much more inhomogeneous and the shape evolution is correspondingly more complex: as a result, a series of kinked bands may form throughout the sample.

Once a deformation kink is formed, further straining increases the tensile stress along the  $[1210]$  direction and a microcrack nucleates at the kink plane where the interatomic bonds are severely distorted (i.e. weakened). Following nucleation, the

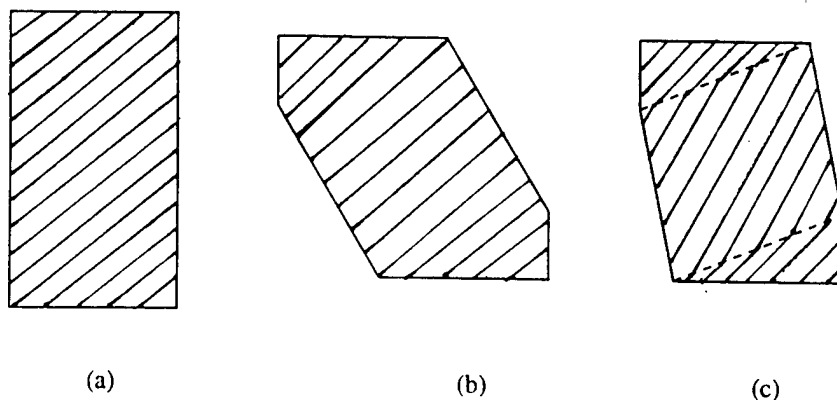


Figure 10. (a) Undeformed parallelepiped crystal with the primary set of slip planes making an angle of  $45^\circ$  with respect to the compression axis. (b) the shape change of the crystal after compression assuming that only the central portion deforms by slip and that the end faces are free to move and (c) the shape change of the crystal after compression assuming that only the central portion deforms by slip and that the end faces cannot move. The slip planes in the central portion rotate producing two deformation kinks.

crack then propagates along the kink plane. The specimen shown in figure 8 exhibits inhomogeneous deformation, which probably provided the stress concentration necessary to nucleate and propagate the crack. Note that the sample has fractured on a plane parallel to (1210) (i.e. the prism plane), which is the plane on which the 'kink' occurs.

The fracture behaviour at lower temperatures, however, appears to be different from that just discussed. This is apparent by comparing figures 8 and 9, and they lead us to believe that there are two possible mechanisms leading to the formation of cracks as a consequence of deformation of a crystal in the chosen orientation. At higher test temperatures (e.g. above 900 °C), there is sufficient thermal activation for dislocation glide to take place; in this case, the crystal exhibits kinking due to the presence of frictional forces between the deformation fixture, and the end faces of the sample that prevents the free motion of the sample and thus gives rise to inhomogeneities in the deformation process. As observed in figure 8, on further plastic deformation, the crystal then nucleates cracks along the kink plane, which acts as a large pre-existing flaw.

On the other hand, at the lower test temperatures (e.g. 550 °C), there is insufficient thermal activation for dislocation glide and there is hardly any slip in any part of the crystal (including the central section, figure 10(b)). Thus, the crystal is unable to develop kinks, the formation of which requires a substantial amount of inhomogeneous deformation. At these low temperatures (e.g. 550 °C) the crystal will develop cracks from other pre-existing flaws such as polishing damage or other internal defects such as voids etc. On further straining, these cracks will propagate on any suitable plane which is perpendicular to the maximum tensile stress (in the manner observed in figure 9) after little plastic deformation. In other words, at lower test temperatures, the 6H-SiC crystal will cleave as a brittle solid under an applied compressive stress, exhibiting cracks on a suitable plane on which the atomic bonds are subjected to the maximum tensile stress.

Further deformation tests need to be conducted to determine the critical temperature below which the formation of kinks is preceded by the formation of cracks of the kind seen in figure 9. Deformation tests above this critical temperature would also help determine the critical strain (at a particular temperature) above which further straining leads to the formation of deformation kinks and to the nucleation and propagation of prism-plane cracks (along these kinks).

## §5. CONCLUSIONS

- (1) The deformation appears to occur heterogeneously by dislocations which are widely dissociated and produce long stacking faults on basal planes. Because of the wide separation of the two partials, they are uncorrelated and the deformation very likely takes place by independent nucleation and propagation of leading and trailing partial dislocations.
- (2) Deformation kinks were observed in the samples deformed at or above 950 °C, where slip traces were more visible indicating higher dislocation mobility. The origin of the deformation kinks is probably related to the frictional constraints imposed on the 6H-SiC in which only one single slip plane, (0001), is available.
- (3) For the sample deformed at 1400 °C, LACBED revealed that the deformation kinks lie on the (1210) planes. LACBED on one of the deformation kinks also revealed a  $\sim 5^\circ$  angle of rotation between its two sides.

- (4) Current results suggest that at low temperatures (e.g.  $\sim 550^\circ\text{C}$ ), cracks are nucleated and propagate in a direction perpendicular to the maximum tensile stress, after little plastic deformation. At higher temperatures (e.g. above  $\sim 900^\circ\text{C}$ ), however, when dislocation glide becomes possible, the formation of  $\{1210\}$  prism-plane cracks is preceded by the formation of kinks.

#### ACKNOWLEDGMENTS

The authors wish to thank Dr Calvin Carter of Cree Research Inc. for providing the bulk 6H-SiC crystal used in this study. They also acknowledge useful discussions with Dr Jacques Castaing on the evolution of the sample shape during deformation. This work was supported by subcontract number 95-SPI-420757-CWRU from the Silicon Carbide Consortium and contract number DE-FG02-93ER45496 from the Department of Energy.

#### REFERENCES

- Castaing, J., Mitchell, T. E., and Dominguez-Rodriguez, A., 1997, *Scripta mater.*, **38**, 45.  
 Corman, G. S., 1992, *J. Am. Ceram. Soc.*, **75**, 3421.  
 Fujita, S., Maeda, K., and Hyodo, S., 1987, *Phil. Mag. A*, **55**, 203.  
 Maeda, K., Suzuki, K., Fujita, S., Ichihara, M., and Hyodo, S., 1988, *Phil. Mag. A*, **57**, 573.  
 Ning, X. J., and Pirooz, P., 1994, *Structure and properties of Interfaces in Ceramics*, Materials Research Society Proceedings, Vol. 357, Edited by D. A. Bonnell, U. Chowdhry and M. Rühle, (Pittsburgh, PA: Materials Research Society), pp. 157–162.  
 Rivière, J. P., and Castaing, J., 1997, *J. Am. Ceram. Soc.*, **80**, 1711.  
 Samant, A. V., Zhou, W. L., and Pirooz, P., 1998, *Phys. Stat. Sol. (a)*, **166**, 155.  
 Suenatsu, H., Suzuki, T., Iseki, T., and Mori, T., 1991, *J. Am. Ceram. Soc.*, **74**, 173.  
 Tairov, Y. M., and Tsvetkov, V. F., 1978, *J. Crystal. Growth*, **43**, 209.  
 Yang, J. W., Suzuki, T., Pirooz, P., Powell, J. A., and Iseki, T., 1992, *Wide Band Gap Semiconductors*, Materials Research Society Proceedings, Vol. 242, edited by T. D. Moustakas, J. I. Pankove and Y. Hamakawa (Pittsburgh, PA: Materials Research Society), pp. 531–536.